Precision spectroscopy and optomechanics of single trapped ions in the weak-binding limit

Maximilian Herrmann

München 2008

Precision spectroscopy and optomechanics of single trapped ions in the weak-binding limit

Maximilian Herrmann

Dissertation
an der Fakultät der Physik
der Ludwig–Maximilians–Universität
München

vorgelegt von
Maximilian Herrmann
aus London

München, den 13. 11. 2008

Meinen Eltern und Melanie gewidmet

Zusammenfassung

Gegenstand der vorliegenden Arbeit sind Experimente mit einzelnen, in Radiofrequenzfallen gespeicherten Ionen im Regime nicht aufgelöster Seitenbänder.

Zentrales Ergebnis ist eine im Rahmen dieser Arbeit neu entwickelte Methode für höchstauflösende Laserspektroskopie an einzelnen Ionen im Grenzfall schwacher Bindung. Sie erlaubt es, mittels sympathischer Kühlung von Ionenketten und räumlich aufgelöster Detektion starke Dipolübergänge mit bis dato unerreichter Genauigkeit zu vermessen. Neben einer ausführlichen theoretischen Untersuchung der Methode wurde zur Demonstration ihrer Leistungsfähigkeit eine Absolutfrequenzmessung eines astrophysikalisch relevanten Übergangs an einzelnen Magnesium Ionen durchgeführt. Dabei konnte die Genauigkeit der Linienmitte knapp 400fach gegenüber dem Literaturwert verbessert werden und die Eignung für hochpräzise Lebensdauermessungen wurde gezeigt. Es wurde erstmalig eine Auflösung von besser als 1% der Linienbreite in diesem Regime erreicht (0.4%), wie für anpruchsvolle Anwendungen, etwa in der Kernphysik, vonnöten. Die Resultate sind lediglich durch Linienbreite und -form des verwendeten Farbstofflasers limitiert, und nicht durch die Methode selbst. Theorie und Experiment zeigen, dass der Methode noch weitaus größeres Potential innewohnt und dass sie Genauigkeiten auf dem Niveau 10^{-4} der Linienbreite und besser ermöglicht. Potenzielle Anwendungen hierfür finden sich in einer Reihe von Gebieten, von der Atomphysik über die Astrophysik bis hin zur Kernphysik.

Ein zweiter Themenkreis befaßt sich mit Ionen als harmonischen Oszillatoren und untersucht die mechanische Wechselwirkung von Licht und Materie. Als Modellsystem dient hierbei ein einzelnes, schwach gebundenes Ion, dass mit zwei Laserstrahlen wechselwirkt. Dieses einfache System zeigt eine überraschende Fülle von interessanten Phänomenen, die sowohl theoretisch als auch experimentell untersucht wurden. Es konnte gezeigt werden, dass ein einzelnes Ion unter bestimmten Bedingungen einen regenerativen Oszillator darstellt, also ein laserähnliches System mit Schwellwertverhalten und Verstärkungssättigung. Darüberhinaus konnte Bistabilität und Hysterese beobachtet werden. Die hierfür entwickelte Theorie erlaubt überdies ein tieferes Verständnis einer in Ionenfallenexperimenten weitverbreiteten Diagnosetechnik, der sogenannten optischen Säkularanregung.

Schließlich wird der Stand eines laufenden, äußerst vielversprechenden Projekts präsentiert: Präzisionspektroskopie des 1S-2S Übergangs in He$^+$. Eine erfolgreiche Messung dieser zwei Photonen Resonanz verspricht einzigartige Tests der Quantenelektrodynamik gebundener Zustände. Allerdings ist das Experiment sehr anspruchsvoll, da alle relevanten Wellenlängen im extremen Ultraviolett bei 61 nm und darunter liegen. Neben einer detaillierten Machbarkeitsstudie werden erste experimentell erreichte Meilensteine vorgestellt.

Die gesamte bei den Experimenten verwendete Apparatur wurde im Rahmen dieser Arbeit entwickelt und aufgebaut.

Abstract

This thesis reports on experiments with single ions stored in radio frequency traps in the limit of unresolved motional sidebands.

The main result is the idea, theory and experimental demonstration of a new spectroscopy method for ions in the weak-binding limit. By virtue of sympathetic cooling of a chain of ions and spatially resolved detection, strong dipole transitions can be measured with unprecedented accuracy. To demonstrate the method, the absolute frequency of an astrophysically relevant transition in single magnesium ions was measured. The accuracy of the line center presents a nearly 400fold improvement over previous results. This is the first demonstration of an accuracy exceeding 1% of the linewidth in this regime (0.4%) as required for demanding applications such as in nuclear physics. Furthermore, the suitability of the approach for precision measurements of the linewidth and thus the lifetime of the excited state could be demonstrated. The results are only limited by the large linewidth of the dye laser used, not by the method, and both theory and the experiment indicate that significant improvements are possible, promising accuracies on the level of 10^{-4} of the linewidth and below. As a new method enabling orders of magnitude greater accuracy in a previously hardly explored regime, widespread applications are expected, ranging from laboratory astrophysics to nuclear physics and atomic physics.

A second set of experiments explores the optomechanical interaction of light with weakly bound ions and studies a single ion interacting with two laser beams. Despite its simplicity this system shows a surprising wealth of interesting phenomena. Under certain conditions the ion constitutes a regenerative oscillator, that is, a laser-like system with a threshold and saturable gain. Moreover, bistability and hysteresis were observed. A theoretical framework is developed that describes all the observed phenomena remarkably accurate and with no adjustable parameters. Furthermore, the theoretical study of this "single ion regenerative oscillator" elucidates the mechanism of a technique wide-spread in the ion trapping community, the so-called optical secular scan.

Finally, the status of a very promising ongoing project is summarized: Precision spectroscopy of the 1S-2S transition in trapped He$^+$ ions. This transition lies deep in the extreme ultraviolet near $61\,\mathrm{nm}$ and is thus experimentally challenging but will allow to uniquely test the theory of bound state QED. Both a detailed study of the feasibility is presented as well as important experimental milestones that have been achieved so far.

The entire apparatus used for these experiments was developed and built as part of this thesis.

Contents

Introduction

Nature's captivating beauty challenges scientists that try to grasp and quantify it with over-whelming complexity. Taming this complexity by finding few, simple and universal laws is an elaborate art. However, very rarely we are lucky enough to encounter systems that are so simple and pristine that they hardly require approximations and allow us to test the very fundamentals of the scientific world view.

Single trapped ions are an example for such a pristine system. They are the closest approximation to an unperturbed particle floating at rest in free space ever realized. Harmonically bound in the field free region of a radio frequency trap and under ultra-high vacuum conditions, a trapped ion is extremely well isolated from external perturbations. This allows to perform spectroscopy with highest precision and allows to study elusive quantum phenomena such as entanglement. Moreover, a trapped ion is a very pure realization of a harmonic oscillator - the ion can be viewed as a point particle suspended from an essentially mass- and frictionless spring.

The work presented in this thesis explores the spectroscopy and the optomechanical aspect: A new spectroscopy method for a regime previously inaccessible for high precision spectroscopy, the weak-binding limit, is proposed, studied theoretically and demonstrated experimentally. The new method is shown to enable orders of magnitude greater accuracy than traditional approaches. A second set of experiments explores the optomechanics of a single trapped ion. Under certain conditions the ion constitutes a regenerative mechanical oscillator and shows a number of interesting effects including bistability and hysteresis. A surprisingly simple theoretical description is developed that accounts for all the observed phenomena.

All absolute frequency measurements on single trapped ions so far have been performed in the strong-binding limit where the interaction of a laser with an electronic transition can be decoupled from the interaction with its motional state. In contrast, in the weak-binding regime this is not possible which leads to systematic line shape distortions that limit the accuracy. A new spectroscopy method based on sympathetic cooling of a chain of trapped ions and spatially resolved detection is demonstrated that allows to observe essentially unperturbed Voigt profiles with high signal-to-noise ratio. To demonstrate the technique an absolute frequency measurement of an astrophysically relevant transition in trapped magnesium ions is performed, which is the first absolute frequency measurement on a single trapped ion in the weak-binding limit. Thanks to the new approach both the line center as well as the linewidth can be measured with unprecedented accuracy: The spectroscopy reaches an absolute accuracy of $160\,\mathrm{kHz}$ on a $42\,\mathrm{MHz}$ wide line, a nearly 400fold improvement over previous results. Furthermore, the Gaussian and Lorentzian contribution to the linewidth could be determined with high resolution which shows the suitability of this approach for precision lifetime measurements. The results obtained were not limited by the method and further improvements are possible. The demonstrated technique is expected to be useful to a broad community, ranging from laboratory astrophysics to nuclear physics.

The development of micromechanical oscillators, such as nanospheres or microtoroids, that combine both high mechanical and high optical quality factors have recently attracted con-

siderable attention. A wealth of interesting phenomena has been observed in such systems, including the generation of frequency combs and sideband cooling. These developments renewed interest in the study of the mechanical interaction of light with matter. In this light we revisit the interaction of a laser with a mechanical oscillator at the most basic level. In particular, we study a trapped ion interacting with two laser beams which can be viewed as a harmonic oscillator driven and damped by nonlinear, stochastic forces. We find a behaviour analogous to a laser with a threshold for oscillation and saturable gain: The ion is a regenerative oscillator. Despite the simplicity of the system we also find complex phenomena such as bistability and hysteresis. Further, a common misconception is resolved: A laser detuned to the high frequency side of a transition (blue detuned) does not necessarily heat the motion but can rather provide gain for a coherent oscillation of the ion. The analysis of this "single ion regenerative oscillator" (SIRO) furthermore leads to a deeper understanding of an important and widespread technique, the optical secular scan. Secular scans are used to non-destructively analyze the mass and/or motional spectrum of a sample of trapped ions, based on the fact that each ion species oscillates in the trap with a characteristic frequency proportional to its charge-to-mass ratio. Excitation of the oscillation with an external RF field leads to a readily detectable change in the fluorescence rate. The theoretical framework of the SIRO elucidates the mechanism and allows to find the optimum conditions for such scans.

The second part of this thesis summarizes progress towards a very promising albeit ambitious goal, namely two-photon frequency-comb spectroscopy on trapped He^+ in the extreme ultraviolet (XUV). Precision spectroscopy on simple systems like hydrogen or helium allows to uniquely confront theory with experiment and has played an important role in the development of physics. Theory, i.e. bound-state QED, is well developed and can make extremely accurate predictions. On the other hand, hydrogenic systems are experimentally well accessible and have narrow two-photon transitions that allow for spectroscopy with highest precision. This fruitful interplay is the basis for a famous track record in physics, namely 1S-2S spectroscopy in hydrogen. For three decades the accuracy has improved exponentially (about a factor 10 every three years) and the relative accuracy has now reached a level of about 10^{-14}. However, further progress turns out to be very challenging. Even worse, already now the accuracy cannot be used to confront theory: One of the parameters that enters into the calculations, the proton charge radius, is only poorly known and limits the accuracy of the theoretical prediction to a level of about 10^{-11}. Here, the He^+ ion comes into play. Roughly speaking, most of the systematic uncertainties that plague the hydrogen experiment can be traced back to the fact that spectroscopy is performed on an atomic beam, i.e. that the atoms are moving. In contrast, the He^+ ion is charged and can therefore be trapped, which automatically removes most, if not all systematic uncertainties that currently impede progress. Moreover, the charge radius issue is far less pronounced and projected experimental uncertainties will allow to test higher-order QED corrections which are currently not accessible in hydrogen. A detailed analysis of the feasibility of the experiment shows that albeit possible, it is very challenging and quite different compared to the vast majority of trapped ion spectroscopy experiments: i) All relevant wavelengths are deep in the XUV where currently no suitable cw laser sources exist. No refractive optics are available (e.g. lenses) and the best normal incidence mirrors reflect on the order of $30\,\%$. ii) For this reason, standard cooling and detection techniques such as Doppler cooling and shelving fail and the ions cannot be "seen", i.e. imaged directly. iii) The 1S-2S transition can be ionized by the clock laser, so the spectroscopy is destructive and requires frequent reloading. However, important progress

has been made. A major breakthrough was achieved in 2005 when C. Gohle (MPQ) and R. Jason Jones (JILA) demonstrated high repetition rate XUV frequency combs. Baklanov and Chebotaev showed in 1975 theoretically that under certain conditions a frequency comb can drive a two-photon transition much like a cw laser. For this reason, the extension of the frequency comb technique from the infrared into the XUV is the long sought-after quasi cw light source for high precision spectroscopy in the XUV. Since this first demonstration of XUV frequency combs second generation systems have been developed that are capable of delivering close to a microwatt at $60.8\,\mathrm{nm}$, a 10^5fold improvement over the first systems. Although this is still an order of magnitude short of power levels useful for spectroscopy, the giant leap from first to second generation systems raises hope that suitable systems will be available in the not-too-distant future. In the envisioned experiment the cooling and detection issue is solved as follows: A second, directly laser coolable ion species is co-stored with the He^+ ions and sympathetically cools them. Successful excitations will be accompanied by ionization, so on resonance He^{++} ions accumulate in the trap. The He^{++} ions are then detected via secular excitation with unity efficiency and essentially no background. This strategy is the result of a thorough study of the feasibility of the experiment which was conducted as part of this thesis. Also experimentally small first steps towards the spectroscopy goal could be taken: Both sympathetic cooling of light ions (most likely helium) by laser cooled Mg^+ ions and the detection method based on secular excitation were demonstrated.

This dissertation is organized as follows: The first chapter reviews important basics about ion trapping for later reference. The second chapter describes in detail the design and performance of the two ion trap systems that have been constructed as part of this thesis. The new spectroscopy method for the weak-binding limit together with the metrology on single Mg^+ ions is presented in chapter three. Chapter four presents theory and experiments on the single ion regenerative oscillator. Finally, chapter five is a collection of co-authored papers that summarize the progress towards XUV frequency comb spectroscopy on 1S-2S in He^+.

1. Fundamentals of ion trapping

"After all we are not experimenting with single particles as much as we can raise Ichtyosauria in the zoo."

This famous quote by Erwin Schrödinger dates back to 1952. Although the extinct aquatic lizard could not be resurrected to date, 26 years later, in 1978, two independent groups simultaneously observed single, trapped, and laser cooled ions [1, 2]. It was Wolfgang Paul's and others work on the dynamics of particles subject to oscillating electric multipole fields that triggered the evolution from quadrupole mass filters to ion traps and let Hans Dehmelt's dream of a "single particle floating at rest in free space'" come true. Radio frequency ion traps (Paul traps) are remarkable devices that allow to confine a sample of atomic or molecular ions extremely well isolated from external perturbations for long times. Modern ion traps can store millions as well as single ions, which can be as hot as $\sim$100'000 K or cooled to the quantum mechanical ground state of motion (corresponding to $\sim \mu$ K). Ultra-high vacuum systems that achieve pressures below 10 nPa have become standard, so that a trapped ion will collide with background gas atoms only about once in five minutes. This allows to store an ion for days. These exciting achievements are not only of aesthetic appeal. Trapped ions are ideal systems for spectroscopy with highest precision. They allow long interactions times and the suppression of many systematic uncertainties, including first and second order Doppler shifts, collisional shifts, etc.. Indeed, the most precise measurements ever made were performed on trapped atomic ions. A recent frequency comparison of the clock transitions of a single aluminum ion and a single mercury ion achieved an accuracy of a few parts in 10^{17} [3]. Apart from spectroscopy, the absence of external perturbations make trapped ions ideal systems to study such elusive phenomena as entanglement. Experiments on trapped ions demonstrated quantum gates for the first time and thus paved the way towards quantum computing [4, 5]. The technologies developed along these lines are currently being applied to perform quantum simulations [6], an idea which goes back to R. Feynman [7]. A rather unexpected but extremely
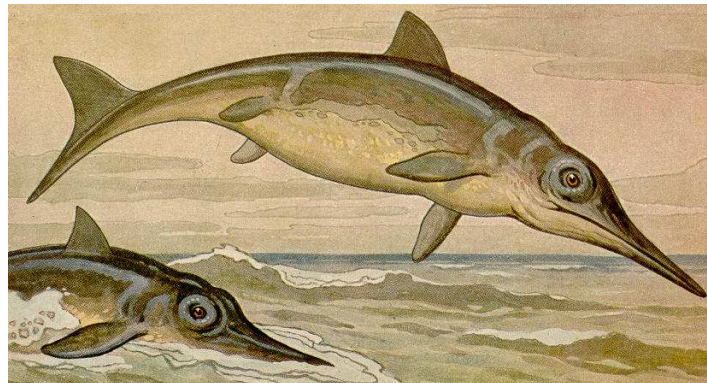

Figure 1.1.: *Ichthyosaurus*

useful application of the techniques developed for quantum computing is the use of quantum logic for spectroscopy. The aforementioned precision measurement on a single aluminum ion relied on this method.

1.1. RF Traps

Radio frequency (RF) traps are based on alternating quadrupolar electric fields (see Fig. 1.2) of well chosen frequency and amplitude that can generate (on average) a harmonic restoring force in all three dimensions. At first sight this might seem surprising, since one could
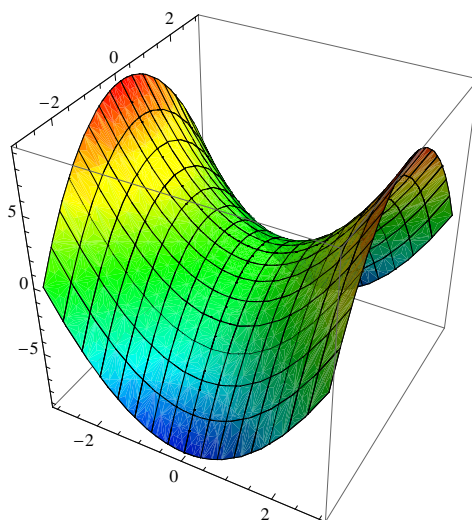

Figure 1.2.: *A quadrupolar potential.*

assume that the net force from rapidly alternating fields would average to zero. The origin of the resulting ponderomotive force is the nonlinearity of the potential. This can also be understood from an analog to optics: Along a chosen axis, the quadrupolar field will be focusing or defocusing, depending on the phase of the alternating field. The resulting force on the ion is similar to the action of a periodic arrangement of focusing and defocusing lenses on a beam of light. If the relative focal lengths (RF amplitudes) and distances (frequency) are chosen appropriately, the lens system can be focusing in total.

In a RF trap the ions oscillate around a minimum or node of the trapping field. Depending on their temperature (their residual kinetic energy) the ions will therefore occupy a more or less field-free region of the trap (this statement will be quantified in the next section). Possible adverse effects from the trapping fields can thus be minimized by cooling the ions. This is in contrast to Penning traps which use a combination of static electric and magnetic fields for confinement, where the latter is present in the whole trapping volume. Of course, in some cases this is desirable, e.g. if the magnetic moment of a trapped particle is being studied, like in the famous g-2 experiments on single trapped electrons [8], but often the magnetic field is bothersome and limits the accuracy of a precision measurement.

The dynamics of charged particles in RF traps have been studied extensively both classically and quantum mechanically. The following sections review the most important facts for later reference.
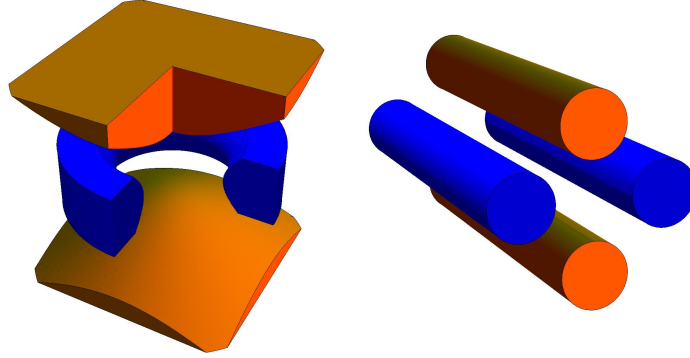
Figure 1.3.: *Electrode structures of a three dimensional (left) and an ideal linear 4-rod (right) Paul trap. Trapping voltages are applied to the electrodes shown in orange, while the blue electrodes are grounded.*

1.1.1. Basic dynamics

RF traps achieve three dimensional harmonic confinement by rapidly alternating quadrupolar fields. Writing the time dependent potential as

$$\varphi(x, y, z, t) = \frac{1}{2}(U_{\mathrm{dc}} + U_{\mathrm{rf}}\cos(\Omega t)) \cdot (\alpha x^2 + \beta y^2 + \gamma z^2) \tag{1.1}$$

then the Laplace equation $\Delta\varphi = 0$ imposes following restriction on α, β and γ:

$$\alpha + \beta + \gamma = 0. \tag{1.2}$$

Two frequent choices are $\alpha = \beta = -2\gamma$ and $\alpha = -\beta, \gamma = 0$. The first corresponds to a trap with three dimensional RF confinement, the second to a so-called linear trap, where the ion is confined radially by RF fields and axially by DC fields. Examples are shown in Fig. 1.3. The equations of motion decouple with respect to different directions, so it is sufficient to consider the problem in one dimension only. For a particle of mass m and charge Q we find

$$\ddot{x} = -\frac{Q}{m}\frac{\partial\Phi}{\partial x} = -\frac{\alpha Q}{m}(U_{\mathrm{dc}} + U_{\mathrm{rf}}\cos(\Omega t))x\,. \tag{1.3}$$

If the electrodes are equipotential surfaces α equals $1/2r_0^2$, where r_0 is the size of the trap, measured as the distance from the trap axis to the closest electrode surface. This equation is a Mathieu type differential equation and can be transformed to its standard form by introducing the following, dimensionless, parameters:

$$a = \frac{4QU_{\mathrm{dc}}}{mr_0^2\Omega^2}, \qquad q = \frac{2QU_{\mathrm{rf}}}{mr_0^2\Omega^2}, \qquad \xi = \frac{\Omega t}{2} \tag{1.4}$$

The parameters a and q characterize the amplitudes of the static and dynamic part of the quadrupole field respectively, and ξ measures time in units of the radio frequency cycle. With this the equation of motion is recast into

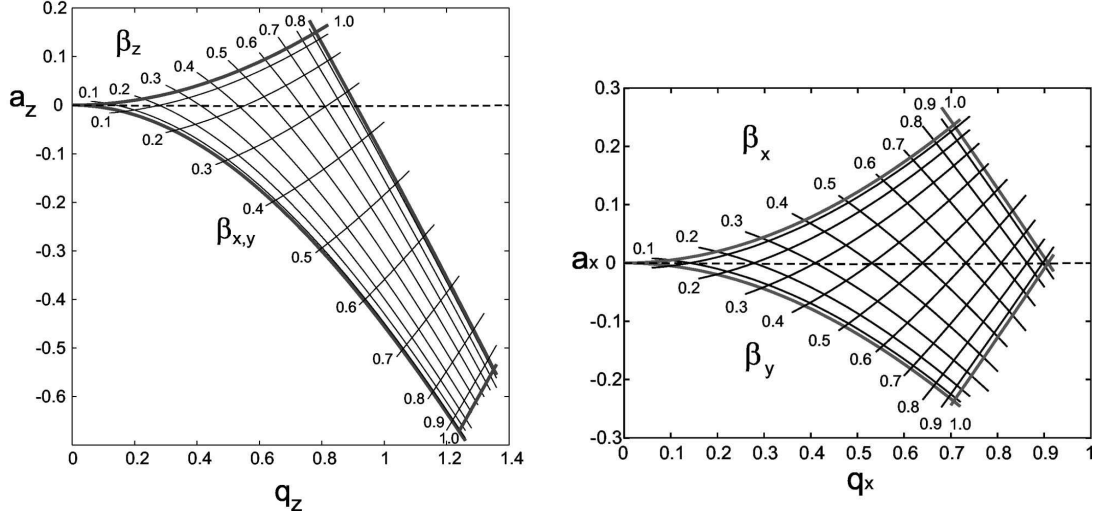$$\frac{d^2x}{d\xi^2} + [a - 2q\cos(2\xi)]x = 0. \tag{1.5}$$

Figure 1.4.: *Stability diagrams for an ion stored with 3 dimensional confinement (left) and for a linear trap (right) (taken from [9]). For $a = 0$ the range of stability extends in both cases to $q = 0.908$. For the linear trap, the apex is at $(q, a) = (0.706, 0.237)$.*

The coefficients of this differential equation are periodic, so, according to the Floquet theorem, the solutions will exhibit the same periodicity.

The general solution reads

$$x(\xi) = A e^{i\beta\xi} \sum_{n=-\infty}^{\infty} C_{2n} e^{i2n\xi} + B e^{-i\beta\xi} \sum_{n=-\infty}^{\infty} C_{2n} e^{-i2n\xi}. \qquad (1.6)$$

The coefficients β, called "Mathieu characteristic exponent", and C_{2n} can be obtained by different methods, e.g. by a recursion relation that is found by substituting the solution into the Mathieu equation. They depend only on a and q, whereas A and B depend on the initial conditions. Inspection of equation 1.6 shows, that solutions are stable, i.e. the trajectory remains bounded, if and only if the characteristic exponent β is real and not an integer. Depending on the trap geometry (e.g. linear or spherical) different regions in the $a - q$ plane correspond to stable solutions. This is shown in Fig. 1.4 for both three-dimensional and two-dimensional RF confinement. The number of stability islands is infinite and the regions shown are the regions that contain $(a, q) = (0, 0)$. These lowest stability regions are the ones commonly used in ion trapping experiments, although the higher regions have been studied and characterized, too. For $a = 0$ the range of stability extends to $q = 0.908$. On the low end there is no hard limit for q - practical limitations will be discussed in the next paragraph.

For small (a, q), more precisely for $(|a|, q^2) \ll 1$, the Mathieu characteristic exponent β can be approximated by

$$\beta \cong \sqrt{a + q^2/2}. \qquad (1.7)$$

Most ion trapping experiments are indeed operated at low (a, q), so this approximation is well justified in practice. A comparison of Eq. 1.7 with the exact values of β is shown in Fig. 1.5. With this, the general solution of Eq. 1.6 can be, to lowest order, simplified to

$$x(t) \cong x_0 \cos(\frac{\beta}{2}\Omega t)[1 - \frac{q}{2}\cos(\Omega t)], \qquad (1.8)$$

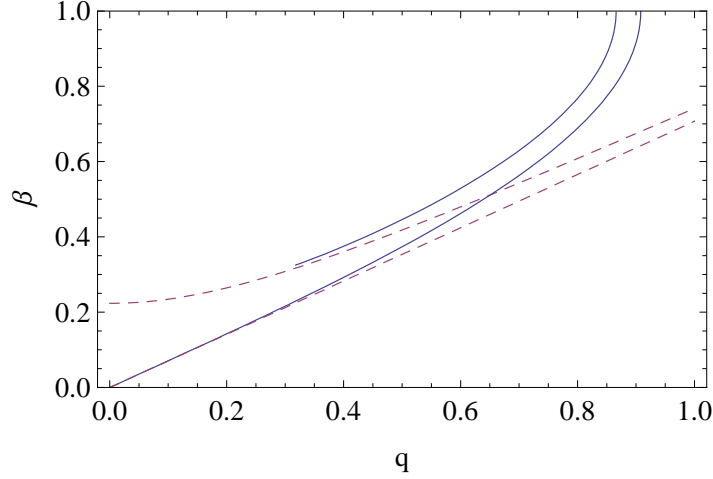where x_0 depends on the initial conditions and a possible phase has been neglected for clarity.

Figure 1.5.: *The Mathieu characteristic exponent β (solid line). The dashed lines are calculated according to the approximation of Eq. 1.7. The lower line pair is calculated for a=0, the upper line pair for a=0.05.*

This form is very instructive and shows the general behaviour of a trapped ion clearly. The ion oscillates with two superimposed motions: First, a slow oscillation with large amplitude and a frequency of $\omega_s = \Omega \beta/2$, called "secular frequency". And, second, a fast quiver at the trap radio frequency Ω. Its amplitude depends on the position of the ion. At the origin it is zero and at the turning points of the secular motion its amplitude is maximal, but $q/2$ times smaller than the amplitude of the secular motion. This fast, driven motion is called micromotion. Figure 1.6 shows sample trajectories inside and outside the regime where the approximation $(|a|, q^2) \ll 1$ is valid. A useful relation between the secular frequency ω_s and the trap frequency Ω reads for $a = 0$

$$\omega_s = \frac{q\Omega}{2\sqrt{2}}. \tag{1.9}$$

For typical trapping conditions ($q \sim 0.1 \dots 0.2$) the secular frequency is about 1/20th of the trap frequency.

Excess micromotion can occur if the ions are shifted from the trap center by stray electric fields or if there is a phase difference between two opposing electrodes of the trap. This can lead to large Doppler shifts, heating and exposes the ion to the trapping fields. Stray electric fields can be compensated by additional electrodes, a phase difference between the electrodes cannot. An excellent account of the various adverse effects of excess micromotion together with a description of methods for detection and compensation can be found in [10]. If we neglect micromotion, the ion can be thought of moving in a three dimensional harmonic well. This is called "pseudo-potential approximation"

$$\Phi = \frac{1}{2}m\omega_s^2 x^2. \tag{1.10}$$

From this we can derive the potential well depth, that is, the maximum kinetic energy an ion can have and remain stored. This is simply the value of the potential at the electrode
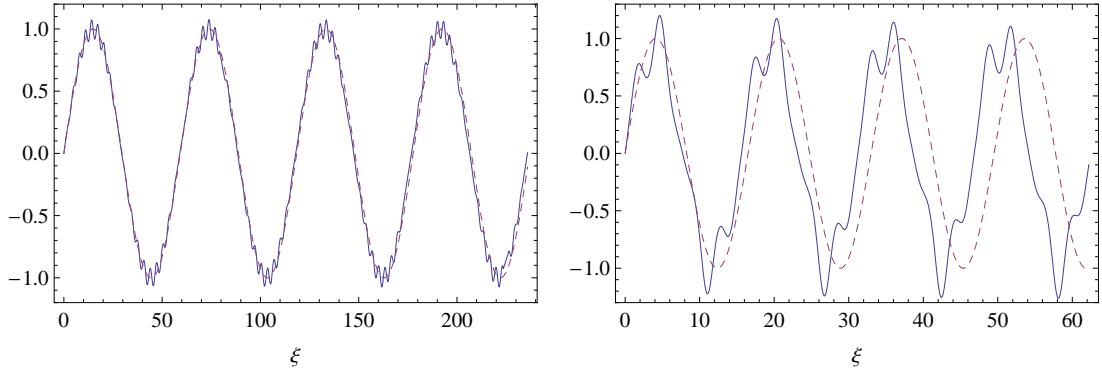
Figure 1.6.: *Trajectories (1-D) of a trapped ion (solid) compared to the pseudo-potential approximation (dashed) with $(|a|, q^2) \ll 1$. The left figure is calculated for $q = 0.15$ and $a = 0$. The ion oscillates at the secular frequency with micromotion superimposed. Note, how the amplitude of the micromotion increases as the distance to the axis increases. The right figure is calculated for $q = 0.5, a = 0.02$, so the condition $(|a|, q^2) \ll 1$ is not fulfilled.*

surfaces

$$D = \frac{1}{2} m \omega_s^2 r_0^2 = \frac{Q q U_{\text{rf}}}{8} \tag{1.11}$$

Typical trap depths are in the eV range, or, correspondingly on the order of 10^5 K. This is remarkably high - traps for neutral atoms are typically less than 1 K deep. With Eq. 1.11 we can also find the lower bound on q given by the kinetic energy of a laser cooled ion due to its temperature. For $T = 1$ mK and trapping parameters typical for the ion traps described in this thesis q_{min} is on the order of 10^{-5}. However, static electric stray fields E displace the ion from the trap center by [10]

$$\Delta x \simeq \frac{QE}{m \omega_s^2}. \tag{1.12}$$

If we require that the displacement should be smaller than the trap dimensions we obtain an upper bound on stray fields of less than $E \ll 1\,\mu\text{V/cm}$. Such low values are very hard to reach in practice. In general, the minimum obtainable q is therefore given by the ability to avoid and compensate electric stray fields.

1.2. Laser cooling

For many ion trapping experiments laser cooling is an essential technique. Apart from the aesthetic appeal of bringing isolated atomic particles to rest, a number of adverse effects are reduced: The ions are better localized and hence less exposed to trapping fields, second order Doppler shifts are reduced, collisions are minimized etc.. The usage of radiation pressure for cooling has been proposed by T.W. Hänsch [11] for free particles and by D.J. Wineland [12] for bound particles and demonstrated only three years later [1, 2].

The key idea behind laser cooling is to ensure an asymmetry in the absorption-emission cycle such that the momentum of the atom is reduced. In Doppler cooling this idea is realized by illuminating an atom with a narrow band cw laser tuned below resonance ("red detuned") of a cycling transition. Due to the first order Doppler effect atoms moving against the propagation direction of the laser have a higher probability to absorb a photon than atoms moving away

from the laser source. Absorption of a photon leads to a reduction of the momentum of the atom by $\Delta p_{\text{abs}} = \hbar k$. The emission process on the other hand is symmetric, so the average momentum transfer from the decay of the excited state is zero $\langle \Delta p_{\text{em}} \rangle = 0$. Thus, the average net effect of one absorption-emission cycle is to reduce the momentum component pointing towards the laser source by $\hbar k$. A collection of free atoms can be cooled in three dimensions by directing six mutually orthogonal laser beams at them ("optical molasses"). For trapped atoms or ions it is sufficient to use only one laser beam at an oblique angle to the trap axes.

The argument given so far suggests that the ions will cool to zero momentum. However, this is not the case. The random emission kicks cause the atom to undergo a random walk in momentum space, similar to Brownian motion. This implies that although $\langle p \rangle$ equals zero, $\langle p^2 \rangle$ does not. To derive the cooling limit of a trapped ion, two different regimes need to be distinguished. The oscillation of the ion around the trap center modulates the phase of the cooling laser. Therefore, the ion sees a spectrum that consists of a carrier and sidebands due to first order Doppler effect which are separated by ω_s. If the natural linewidth Γ of the cooling transition exceeds the secular frequency, then the motional sidebands of the trapped ion are not resolved and the cooling dynamics closely resemble the cooling of a free atom or ion. This regime is called "Doppler cooling". If the motional sidebands are resolved, they can be addressed individually by the cooling light, thus allowing "resolved sideband cooling". This regime is experimentally more demanding but allows to achieve lower temperatures, down to the quantum mechanical ground state of motion. All experiments described in this thesis have been performed with Doppler cooled ions, which is the regime we will limit the following discussion to.

Before deriving the limiting temperature in Doppler cooling, it should be noted that strictly speaking, the quantity "temperature" is ill-defined for a single ion. Following convention, temperature is defined as the kinetic energy associated with the root-mean-square velocity of an ion $T = \langle E_{\text{kin}} \rangle / k_b = m \langle v^2 \rangle / 2 k_b$. Besides, the concept of temperature is not that far-fetched. It can be shown that after laser cooling the harmonic oscillator states of the ion $E_n = (n + 1/2)\hbar\omega_s$ will be populated according to a thermal distribution [13].

If we neglect micromotion, the limiting temperature in Doppler cooling is derived as follows. The secular cycle averaged cooling or heating power $\langle P_l \rangle$ due to the interaction with a laser beam reads [14]

$$\langle P_l \rangle = \langle Fv \rangle = \langle \dot{p}v \rangle = \langle \hbar k \, g(s, \Delta - kv_0 \cos(\omega_s t)) \, v_0 \cos(\omega_s t) \rangle, \qquad (1.13)$$

Here, $\hbar$ denotes Planck's constant, k the wave vector, s is the dimensionless saturation parameter that measures the intensity in units of the saturation intensity, Δ is the detuning, v_0 the velocity amplitude, and g represents a Lorentzian line shape function that gives the scattering rate.

$$g(s, \Delta) = \frac{\Gamma s}{2(1 + s + (\frac{2\Delta}{\Gamma})^2)}. \qquad (1.14)$$

Spontaneous emission heats the motion on average by

$$\langle P_h \rangle = \langle (1 + \xi) \frac{\hbar^2 k^2}{2m} g(s, \Delta - kv_0 \cos(\omega_s t)) \rangle, \qquad (1.15)$$

where m is the ion's mass and $\xi = 2/5$ is a factor that takes the non-isotropic emission pattern of dipole radiation into account. In a steady state heating and cooling balances $P_l = P_h$. Solving this equation for v_0 gives the ion's temperature $T = m \langle v^2 \rangle / 2 k_b$, where
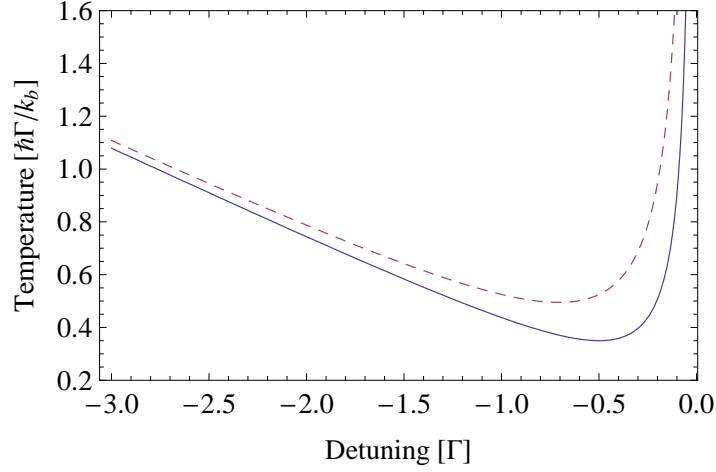
Figure 1.7.: *Doppler cooling limit as a function of detuning the cooling laser. The full line is calculated for $s \to 0$, the dashed line for $s = 1$.*

$\langle v^2 \rangle = v_0^2/2$ for a harmonic oscillation. In the final stages of cooling the velocity of the ion will be small and simple analytic solutions can be found if the cooling force is linearized. Including the detuning and the intensity of the cooling laser the temperature reads [9]

$$T = \frac{\hbar\Gamma}{8k_b}(1 + \xi)\left((1 + s)\frac{\Gamma}{2\Delta} + \frac{2\Delta}{\Gamma}\right). \tag{1.16}$$

The temperature as a function of detuning is shown in Fig. 1.7 for a saturation parameter of $s = 1$ and $s \to 0$. The minimum temperature is obtained for a detuning of $\Delta = -\sqrt{1 + s}\,\Gamma/2$ and reads

$$T_{\min} = \frac{\hbar\Gamma}{4k_b}(1 + \xi)\sqrt{1 + s} > \frac{7\hbar\Gamma}{20k_b} \tag{1.17}$$

Remarkably, the temperature depends on the linewidth only. A typical order of magnitude is mK, for the ^{24}Mg$^+$ D2 transition the Doppler limit is $0.72\,$mK ($\Gamma=41.5\,$MHz).

1.3. Many ions

1.3.1. Trapping many ions

So far we considered the dynamics of a single ion in one dimension only. However, ion traps can easily store millions of ions with densities on the order of $n = 10^9\,1/\text{cm}^3$. Such extremely dilute non-neutral plasmas (the density corresponds to a pressure of $10^{-8}\,$mbar) show a variety of interesting effects. A surprising phenomenon is that trapped ions can undergo a phase transition between a "liquid" and a "solid" state, called Wigner crystallization. Below a certain temperature the potential energy of the trap together with the mutual Coulomb repulsion of the ions dominates over the kinetic energy so they arrange on a regular grid. More precisely, if we treat the trapped ions as a one component plasma characterized by the ratio of Coulomb- to thermal energy Γ_c

$$\Gamma_c = \left(\frac{4\pi}{3}\right)^{\frac{1}{3}} \frac{Q^2\,n}{4\pi\,\epsilon_0\,k_b T}, \tag{1.18}$$
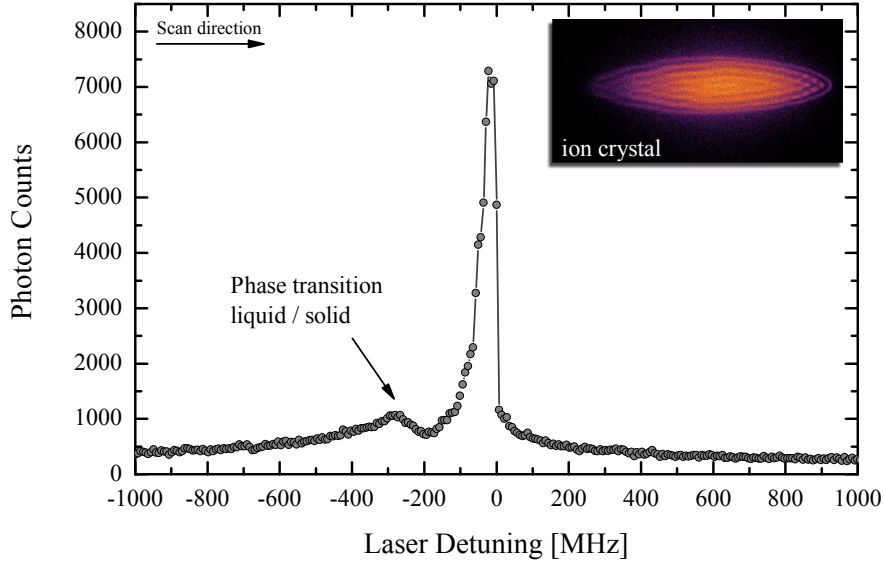
Figure 1.8.: *Phase transition observed in the 6-rod trap introduced later in this thesis. The plot shows the fluorescence intensity of a sample of about 10^5 trapped magnesium ions as the cooling laser is swept from low to high frequencies. As the laser approaches the resonance the temperature of the crystal is steadily reduced. At a detuning of about -250 MHz, corresponding to a temperature of about 5 mK, the trapped ions undergo a phase transition from a "liquid" to a "solid" state causing a dip in the fluorescence. The inset shows an image of an ion crystal. As the laser approaches the resonance cooling becomes less efficient and finally the ions are driven out of the trap, visible as a sharp decrease in fluorescence.*

then it can be shown [15] that for $\Gamma_c > 170$ a phase transition occurs. For typical ion trap parameters (i.e. densities) the freezing temperature is around 10 mK. In a linear RF trap the ion plasma has the shape of a prolate spheroid, both in the liquid and in the solid state. Phase transitions of trapped ions were first observed in the group of H. Walther at MPQ in 1987 [16]. An example measured in our lab is shown in Fig. 1.8. The agreement with Eq. 1.18 is surprisingly good. The typical ion-ion distance inferred from images is about 30 μm which implies a freezing point around 5 mK. Indeed, the phase transition occurs at a detuning of $\Delta = -2\pi\,250\,\mathrm{MHz}$ where Eq. 1.16 predicts a temperature of 5 mK.

A further important effect that occurs only in a large collection of ions is RF heating. For a single ion no energy can be transferred from the trapping fields to the secular motion of the ion: The motion of the ion (Eq. 1.8) has frequency components at ω_s and $\Omega \pm \omega_s$ but not at Ω. However, the situation is quite different if a large number of ions is stored. Then, during collisions, the spectrum of the motion can have an overlap with Ω so the ion can gain energy from the trapping field. Another way of viewing this mechanism has been suggested in [17] and was coined "instability heating". Due to the fluctuating Coulomb forces of the other ions present in the trap, a particular ion acquires a time-varying effective mass. During collisions the effective mass can become so small that the associated q parameter exceeds the stability limit of $q = 0.908$. Thus, for a brief moment of time, the trajectory grows exponentially until the motion stabilizes again at higher temperature.
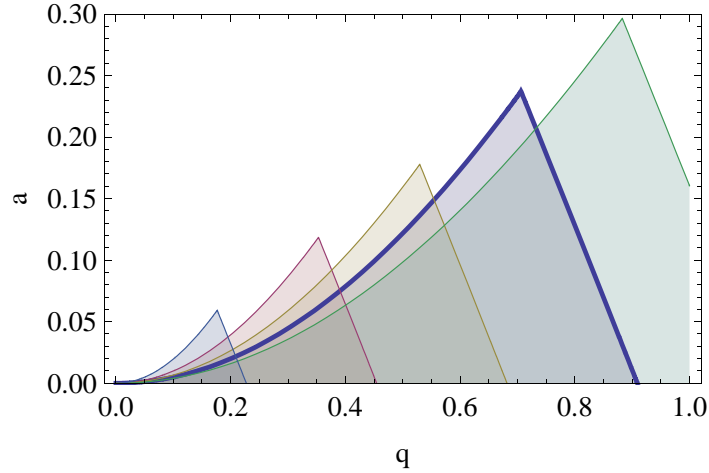
Figure 1.9.: *Stability diagram for ions with Q/m=(1, 1/2, 1/3, 1/4, 1/5). The smallest "triangle" corresponds to Q/m=1. (a, q) values are given for Q/m=1/4 (thick line).*

RF heating thus becomes stronger as the distance to the trap axis increases (due to stronger fields and larger micromotion amplitudes) and at high values of q.

1.3.2. Trapping multiple species

Many applications, including the spectroscopy experiments presented later in this thesis, require trapping different species simultaneously.

Figure 1.9 shows the stability diagram for a number of different masses (Q/m ratios), where the axes are labeled with the a and q parameters for Q/m=1/4 (e.g. He^+). The diagram illustrates the mass selectivity of an ion trap clearly. For each Q/m ratio there is a parallelogram type area around the apex of the stability "triangle" that is stable for this Q/m ratio only. Further, regions exist that are stable only for certain combinations of Q/m ratios. To give an example, consider the species $^{24}Mg^+$, $^4He^+$ and $^4He^{++}$ (this particular combination will be relevant to the envisioned He^+ 1S-2S spectroscopy). There are regions that are stable for all three species individually (near the apex) or together (e.g. $q = (0.05, 0.3, 0.6), a = 0$), for both the He ions only, or for $^{24}Mg^+$ and $^4He^+$ but not for $^4He^{++}$. Inspection of the stability diagram shows that lighter species can be removed by e.g. increasing q (i.e. the RF voltage U_{rf}) and, for appropriate q, heavier species by increasing a (i.e. the DC offset U_{dc}).

Empirically, it is favorable to operate the ion trap with a Mathieu q-parameter in the range $(0.05, 0.6)$, so the trap stays reasonably steep and RF heating is bridled. Since q is proportional to $1/m$ this implies that feasible mass ratios are smaller than, say, 1:10. If only a string of crystallized ions is stored in a linear trap and stray fields are well compensated, significantly larger mass ratios are possible.

If different ion species are stored in a trap, they will be confined with different strengths. Light ion species are bound with high secular frequencies, heavy ions with low secular frequencies. If all ions have roughly the same temperature, the light species will therefore occupy a smaller volume around the center of the trap (see Eq. 1.10) and displace the heavier ions. If the ions are sufficiently cold, this results in a shell structure with heavy ions surrounding light ions as illustrated in Fig. 1.10.
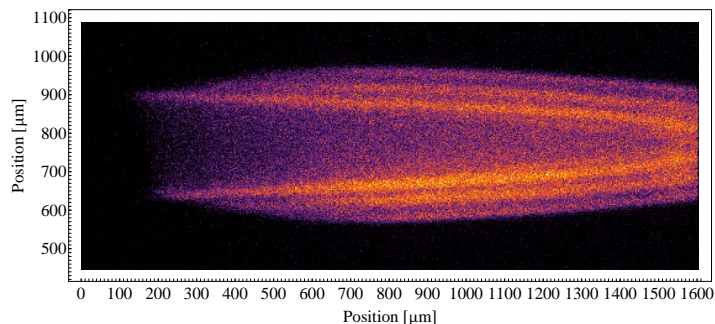
Figure 1.10.: *Ion crystal with multiple species observed in the 6-rod trap. The fluorescing $^{24}Mg^+$ ions form shells around non-fluorescing lighter species stored in the center. Further species heavier than magnesium are responsible for the dark edge in the left part of the image.*

1.3.3. Sympathetic cooling

For the majority of atomic ions and all molecular ions direct laser cooling is very challenging if not impossible either because no suitable laser source exists or the ion possesses no suitable cycling transition. In this case the ion of interest can be cooled indirectly by co-storing a different ion species that can be directly laser cooled. Energy is transferred via the mutual Coulomb interaction. This very useful technique with widespread applications is called "sympathetic cooling".

The most important parameter that governs the cooling dynamics is the mass ratio of the cooled to the uncooled ion. The range of masses that can be cooled sympathetically by a certain laser cooled ion depends critically on the number of ions and the phase, liquid or crystalline. If a large number of ions is to be cooled it is important to ensure that the coolant ions have similar mass. Otherwise the laser cooled and the sympathetically cooled ions segregate. The lighter species accumulates in the center of the trap as described above and couples only weakly to the heavier species that has been displaced from the center. In addition, the heavier species is exposed to the trapping fields and thus experiences stronger RF heating. These limitations due to segregation are of course absent if only a string of different ion species is to be cooled in a linear trap, so much larger mass ratios are feasible if only a small number of cold ions is to be cooled.

Not only the mass ratio and thus the degree of segregation and RF heating influences the cooling dynamics but also the "sign", that is whether a species lighter or heavier than the laser-cooled ion is to be cooled. In general, cooling a lighter species, i.e. mass ratios smaller one is more challenging than cooling heavier species. Drastically simplified, imagine a hot, light particle bouncing of a heavy, laser-cooled particle: The velocity of the heavy ion will hardly change. Since laser cooling is essentially a viscous damping force, the small change in velocity implies inefficient cooling. This naive picture has been confirmed experimentally and with molecular dynamics simulations:

Early MD simulations by [18] claim that for *liquid phase* ions in a linear trap only ions heavier than 0.53 times the mass of the laser cooled ion are cooled sympathetically. A later study by [17] confirms this result for the parameters that had been used in [18]. However, they find that this is actually no hard limit and virtually any mass ratio can be cooled, provided the q parameter of the laser cooled ion is lowered accordingly. This is a general notion common to most experimental and computer studies of sympathetic cooling found in

the literature: The larger the asymmetry in the masses, the lower the q value needs to be.

The group of S. Schiller at the university of Düsseldorf studied sympathetic cooling of light species in the *solid phase* both by simulations [19] and experimentally [20]. For crystallized samples of two ion species the cooling dynamics are quite different due to reduced RF heating. MD simulations show that H_2^+ ions can be at least partially crystallized by laser cooled $^9Be^+$ ions, corresponding to a mass ratio of 0.2 [19]. This was also shown experimentally [20]. The temperature of the molecular ions was inferred from MD simulations that showed that the sympathetically cooled ions thermalize to within a factor two with the laser cooled ions. In this thesis H_2^+ ions embedded in cold $^{24}Mg+$ crystals were observed. If the MD simulations remain valid for our (very similar) ion trap, this implies the successful cooling of an even smaller mass ratio of 0.08.

The cooling of heavier species is not limited by the dynamics of sympathetic cooling but rather by the experimental difficulties of trapping unequal masses. Here, the record is set by successful cooling of $^{12}C_{60}^+$ fullerenes ($m = 720\,u$) by thirty times lighter $^{24}Mg^+$ ions to $14\,K$ [21].

2. The apparatus

This chapter provides a detailed description of the design and performance of the two ion trap systems used for the experiments described in this thesis. The discussion includes the ion traps, RF electronics, vacuum system, imaging system, laser system and ion creation. All systems were set up from scratch. The chapter is written in the spirit of this experience and I hope it will be useful to novices in this field.

2.1. Ion traps

This section begins with general considerations concerning the design of an ion trap and discusses geometries, materials and field calculations. Finally, the two ion traps that were used in the experiments are introduced. The 6-rod trap is a design of Hans Schüssler[1] and Kunihiro Okada[2] that offers a large harmonic trapping volume for up to a million ions and good laser access. The linear endcap trap was designed as part of this thesis and also offers excellent optical access, but is smaller and thus steeper and provides 9 segments to store and move ions. As such it is a versatile tool for experiments on a small number of ions.

2.1.1. Geometries

RF traps are based on alternating quadrupolar fields. In general, a specific field configuration may be produced by charging electrodes whose shapes are equipotential surfaces. In the case of quadrupolar fields this would correspond to hyperboloids of revolution. Indeed, the first ion traps traps were built from electrodes that closely resemble that shape (see Fig 1.3). However, such electrodes are hard to manufacture and only offer limited optical access. On the other hand it is quite easy to generate a quadrupolar field *locally*. If one expands the electric field of an electrode structure that is at least reflection symmetric around the origin, it will be quadrupolar to lowest order. Therefore it is possible to trap ions with rather exotic electrode geometries, provided one works close to the center by e.g. cooling and/ or trapping a small number of particles. Figure 2.1 illustrates this quite dramatically: It shows an ordinary paper clip trapping lycopod spores. The first question in the design procedure that therefore needs to be addressed is whether a large harmonic trapping volume is required. If only a single ion or a string of ions needs to be stored, one gains great freedom in the design of the electrodes. Trapping large particle numbers on the other hand requires large harmonic trapping volumes that can only be generated by hyperboloidal or similar electrode shapes.

The actual design should pay attention to the following boundary conditions:

- Optical access. Good optical access is mandatory to admit the laser beams and to efficiently collect scattered photons.

---

[1]Texas A&M University (College Station, Tx, USA)
[2]Sophia University, Tokyo, Japan
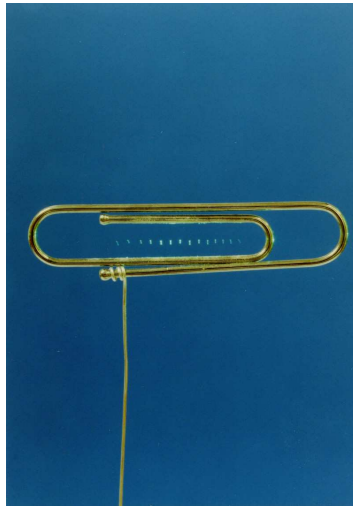
Figure 2.1.: *Paperclip ion trap with lycopod spores. Courtesy of T.W. Hänsch.*

- Mechanical stability. The trap should be machined precisely to ensure good control over the fields. Imperfections can cause excess micromotion that cannot be compensated, e.g. if in a linear trap opposing electrodes aren't strictly parallel. It should also be taken into account that typically a few watt RF power will be dissipated in the electrodes which therefore expand slightly during operation. Finally, the trap may be exposed to vibrations from the vacuum system.

- Capacitance. For several reasons, detailed in the section on the tank circuit (Sec. 2.2), the capacitance should be minimized.

- Vacuum compatibility. This limits the range of materials that can be used. Further, so-called virtual leaks must be avoided, e.g. tapped blind holes require extra venting holes (see also Sec. 2.3).

- Insulators. The trap assembly will likely include electrical isolators which can charge up during operation, e.g. by an electron gun used for ion creation and/or by UV laser beams which can create photoelectrons. Such patch potentials can severely perturb the trapping fields. This can be avoided by ensuring that insulating surfaces are as far away from the trapping region as possible and that there is no line-of-sight connection to the ion.

- Segmentation. Although not mandatory, it has proven very useful to separate the loading and experimental zone. The atomic oven used for ion loading may coat the electrodes which leads to contact potentials and possibly heating. A spatially separated experimental zone efficiently avoids these effects.

A large variety of traps with non-hyperboloidal geometries has been demonstrated, ranging from merely two opposing needles [22] to sophisticated surface chip traps with an intricate architecture of multiple trapping regions [23, 24, 25]. A very popular design for a linear trap with favorable properties is the so-called 4-rod trap, depicted in Fig. 1.3 and briefly discussed in Sec. 2.1.3.

2.1.2. Materials

The ideal electrode material should be a good electrical and hence thermal conductor, UHV compatible, non-magnetic, well machineable and have a low tendency to form oxide layers. Surface contaminations e.g. from oxide layers can be problematic in at least two ways: First, non-conducting patches can statically charge and thus perturb the trapping potential. Second, patches can fluctuate (thermally activated) which is currently believed to be the dominant source of heating and decoherence. This issue is discussed in more detail in the next paragraph. Frequent choices are stainless steel and (gold-plated) copper, but also more exotic materials like beryllium, tungsten and molybdenum have been used. In general, electrodes made from chemical elements tend to be excellent concerning certain properties (e.g. conductivity, contact potentials,...) but are much harder to machine in comparison to alloys like stainless steel. As mentioned above, machining precision is important for good control over the trapping potentials. To illustrate the tradeoffs consider copper vs. stainless steel: Copper is an excellent conductor but poorly machineable and corrodes rapidly developing layers of different oxides. The problems associated with corrosion can be overcome by electroplating with gold, but this takes the risk of embedding contaminants from the electroplating bath with possibly adverse effects for the electric, magnetic and vacuum behavior (frequently a ferromagnetic nickel layer serves as primer). Also does electroplating not faithfully reproduce the shape of the parent electrode. Stainless steel on the other hand is excellently machineable but a poor conductor and may exhibit residual magnetic fields. Other materials have been used to solve specific problems. At NIST in Boulder, CO, USA, a trap designed to store beryllium ions was also machined from beryllium to avoid contact potentials from the atomic oven. Molybdenum is a further, particularly interesting candidate. It is not "noble" and hence as corrosion resistant as e.g. gold or platinum, but at temperatures below $600\,°C$ it also hardly oxidizes. Further, even if an oxide layer grows, it will be thin (due to the hardness of Mo) and conducting. It therefore also offers a surface quality comparable to gold or platinum, but is more practicable: cheaper, harder than gold but still machineable, and has a very low thermal expansion coefficient.

Heating

It has been observed that the motion of trapped ions is incoherently excited (heated) at a rate of about 0.1-10 phonons per ms, which is an important source for decoherence. The heating rate increases strongly as the distance to the closest surface decreases ($\propto d^{-4}$) [26] and can be suppressed by cooling the electrodes [22, 27]. The origin of this heating is not entirely clear, but is generally accepted to be due to fluctuating patches. This assumption gives the correct scaling with distance and temperature. Other sources of heating, like Johnson noise or collisions with background gas atoms have been shown to be significantly weaker than the observed rates [26]. An open question is what the patches microscopically actually are. Although widely believed that they are surface contaminations, this has not been shown conclusively yet. Most ion traps have been cleaned and "baked" for ultra high vacuum conditions. In addition, in the recent years separate loading and trapping zones have become standard as well as efficient photoionization that minimizes the contaminations from the atomic oven. What if the meticulous cleaning and baking actually was sufficient and surface contaminations are not the origin? Could the material itself be responsible for the heating and if so, is there an optimum "quiet" material? A possible mechanism compatible with the

"patch" assumption would be fluctuating defects and/ or grain boundaries. Defects and grains are present in every metal and are subject to thermally activated diffusion, which in turn leads to electric field noise. An important observation supporting this assumption was made in the group of I. Chuang (MIT) [27]: The heating rate of a surface trap made from silver depended sensitively on the annealing procedure and thus on its micro- i.e. grain structure. To test this hypothesis we compared measured heating rates with respect to the electrode material. To this end we collected 16 published and unpublished heating rates from traps made from six different materials [26, 28, 27, 29, 30, 22]. The data, mostly given in phonons per ms, was made comparable by scaling the heating rates to a common secular frequency of $10\,\mathrm{MHz}$ and trap size of $1\,\mu\mathrm{m}$. Hereby, the heating rate was assumed to scale $\propto \omega^{-2}$ [30] and d^{-4} [26]. In a next step the "activity" of the material was quantified as follows: Diffusion processes require a certain activation energy which is provided by the thermal bath. If, e.g. a vacancy moves from one lattice position to the next, a material specific energy Q is required. Since this energy is provided by the thermal bath, the diffusion rate is proportional to $\exp\left(-Q/k_b T\right)$. This implies that for constant temperature the activity of the material decreases exponentially as the activation energy increases. The comparison of different materials is complicated by the fact that various diffusion processes exist that have different activation energies. However, they are correlated. For example, the melting temperature and lattice energy depend linearly on each other, and the self-diffusion constant that describes the diffusion of point defects depends linearly on the melting point ("Van Liempt law"). Therefore, the lattice energy and self-diffusion are correlated linearly. For this reason the heating rates observed in traps made from different materials were compared with respect to the lattice energy. The result is shown in Fig. 2.2. The trend is obtained by averaging all results belonging to one material and surprisingly clearly shows the expected exponential decrease in heating rate as the lattice energy increases. Of course, this is only an indication and no proof. The individual data points scatter by orders of magnitude so that a number of cases can be found that even oppose the trend. Nonetheless, the presented trend together with the dependence on the micro structure observed in silver surface chip traps are a strong indication that the material and its grain structure contribute significantly to the anomalous heating, but further investigations are necessary to corroborate or falsify this hypothesis.

2.1.3. Field calculations

The performance of a trap can be predicted quite accurately by numerically calculating the electric fields generated by a given electrode geometry. A number of software packages utilizing different methods exist for this purpose, including finite element (FEM, e.g. Comsol Multiphyics), finite difference (FDM, e.g. SIMION) and boundary element methods (BEM, e.g. CPO). The different solvers have been compared in [31]. Finite element and finite difference software packages can be applied to simulate a variety of phenomena (heat conductance, mechanical stress, etc.) but are slower and less accurate than the boundary element method that is limited to the solution of electrostatic problems. The traps considered in this thesis were simulated with Simion (FDM) and CPO (BEM). Indeed, CPO turned out to be significantly faster and more accurate.

   The pseudo potential and related quantities like secular frequencies etc. are derived from simulations with the following basic steps: First, the static potential of the ion trap is simulated for a voltage U_{rf}. Then, the curvature of the potential in the trapping region is determined by fitting a quadratic function to the data: $\rho(x) = c_0 + c_2 x^2$. The polynome ρ
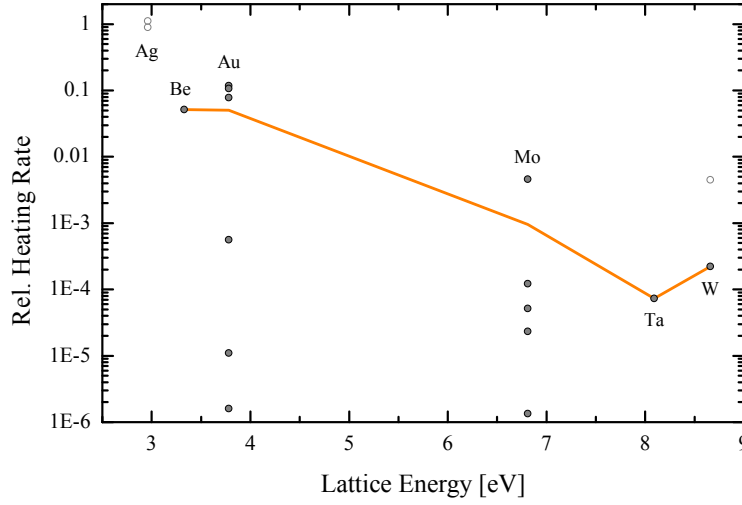
Figure 2.2.: *Overview of normalized heating rates as a function of material/ lattice energy (Nov. 2008 [26, 28, 27, 29, 30, 22]). The orange trend is generated by averaging all results for a particular material. Data points shown as open circles have badly defined surfaces and are not included in the trend.*

is even due to the reflection symmetry of an ion trap and can include higher order terms to quantify anharmonicities ($\rho'(x) = c_0 + c_2 x^2 + c_4 x^4 + c_6 x^6 + \dots$). Finally, this curvature is used to calculate the ponderomotive pseudo potential as follows:

The time averaged (pseudo-) potential $\Phi(\vec{r})$ is related to the time varying "true" potential $\varphi(\vec{r}, t) = V(\vec{r})\cos(\Omega t)$ by [32]

$$\Phi = \frac{Q^2}{4m\Omega^2}|\nabla V(\vec{r})|^2 \tag{2.1}$$

With $V(\vec{r}) = \rho(x)$ it follows:

$$\Phi = \frac{Q^2 c_2^2}{m\Omega^2}x^2. \tag{2.2}$$

From comparison with Eqs. 1.10, 1.9 and 1.4 we find that for an ideal trap $c_2 = U_{\mathrm{rf}}/(2r_0^2)$. The ratio of c_2 to this value is the trap efficiency $\kappa = 2c_2 r_0^2/U_{\mathrm{rf}}$ or voltage loss factor $L = \kappa^{-1}$. The latter highlights the fact that a non-ideal trap behaves much like an ideal trap, except a L times higher voltages is required to obtain the same stability parameter and secular frequency. With this, the dynamics of a "real" trap are calculated either from Eq. 2.2 directly or by multiplying Eqs. 1.4 with κ. For example, the secular frequency for $a = 0$ reads

$$\omega_s = \frac{\sqrt{2}Qc_2}{m\Omega} = \frac{\kappa Q U_{\mathrm{rf}}}{mr_0^2\Omega} \tag{2.3}$$

The efficiency κ for non-hyperboloidal electrodes is typically between $10\,\%$ and $40\,\%$ but can be close to 1 for a trap built from four rods with appropriately chosen diameter and spacing as shown in Fig. 1.3.

Non-hyperbolic electrode structures generate a field that is harmonic only locally around the node. The anharmonicities of different trap geometries can be compared quantitatively
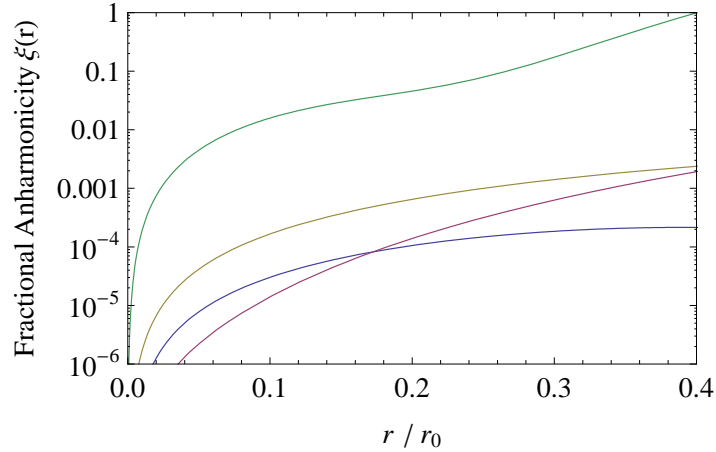
Figure 2.3.: *Fractional anharmonicities for different ion trap geometries, as defined in Eq. 2.4. From top to bottom the curves show calculations for: The endcap trap (green), the 6 rod trap (ochre), a 4 rod trap with $b = 0.5$ (lilac) and an ideal 4 rod trap with $b = 1.16$ (blue).*

with the following function and the coefficients of ρ':

$$\xi(r) = \sum_{i=2}^{\infty} \frac{c_{2i}}{c_2} \left(\frac{r}{r_0} \right)^{2i-2}. \tag{2.4}$$

The most frequently used non-hyperbolic ion trap geometry is a linear trap with a symmetric arrangement of 4 rods. Such a trap is characterized by the size r_0 and the radius of the rods $r' = br_0$. For $b > 0.5$ the efficiency κ exceeds 90%. A particular interesting value of b is 1.16, where the anharmonicities $\xi(r)$ are minimized [33]. Such a trap is called "ideal 4-rod trap". A slight disadvantage of the ideal 4-rod trap is its limited optical access. The solid angle for observation is limited by the electrodes to 1.4%. However, this corresponds to imaging with a f/2 lens, which is sufficient for many applications. A comparison of the anharmonicities of the traps used in this thesis with 4 rod traps with $b = 0.5$ and $b = 1.16$ is shown in Fig. 2.3. From the maximum diameter of ion crystals observed in both the 6 rod and endcap trap it appears that fractional anharmonicities up to a few percent still allow to prepare $\sim 10\,\mathrm{mK}$ cold ions.

2.1.4. The 6-rod Trap

The 6-rod trap was designed by K. Okada[3] and H. A. Schüssler[4]. It's open electrode structure provides excellent optical access and a large sufficiently harmonic trapping volume. Thanks to its size ($r_0 = 1.4\,\mathrm{mm}$) it allows to trap a substantial number of ions; we observed up to 10^6 Mg$^+$ ions. A schematic of the electrode structure is shown in Fig. 2.4, an image of the assembled trap in Fig. 2.6. The trapping voltage is applied to two rods of $3\,\mathrm{mm}$ diameter separated by $5.8\,\mathrm{mm}$ (center-to-center), so $r_0 = 1.4\,\mathrm{mm}$. Four grounded rods of $2\,\mathrm{mm}$ diameter are placed symmetrically around the RF electrodes with an edge length of $10.485\,\mathrm{mm}$. All rods have a length of $20\,\mathrm{mm}$. Together, they form one segment of the trap; in total the trap has three segments. With two further electrodes at either end ions can be stored in each of the three

---

[3]Sophia University, Tokyo, Japan
[4]Texas A&M University (College Station, Tx, USA)
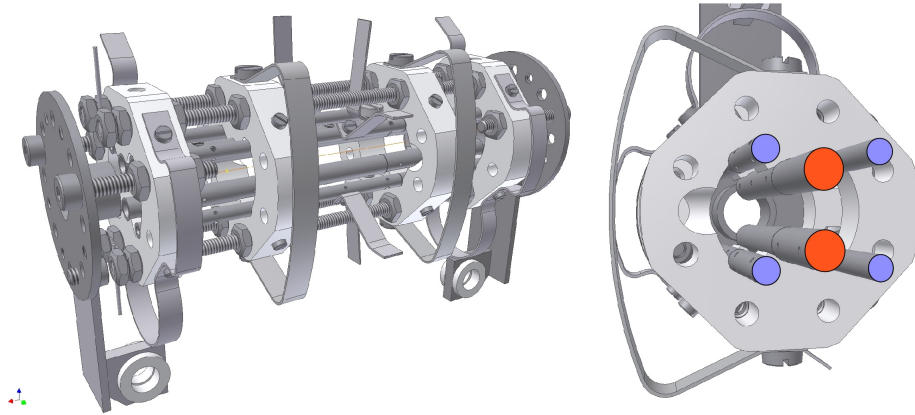
Figure 2.4.: *Electrode structure of the 6-rod trap. The left image shows the assembled trap, the right image a cut-away view of the electrodes. The radio frequency is applied to the two larger rods (diameter 3 mm, separated by 2.8 mm) marked orange. The four surrounding rods (diameter 2 mm, blue) are grounded. Ions can be stored in each of the three 20 mm long segments.*
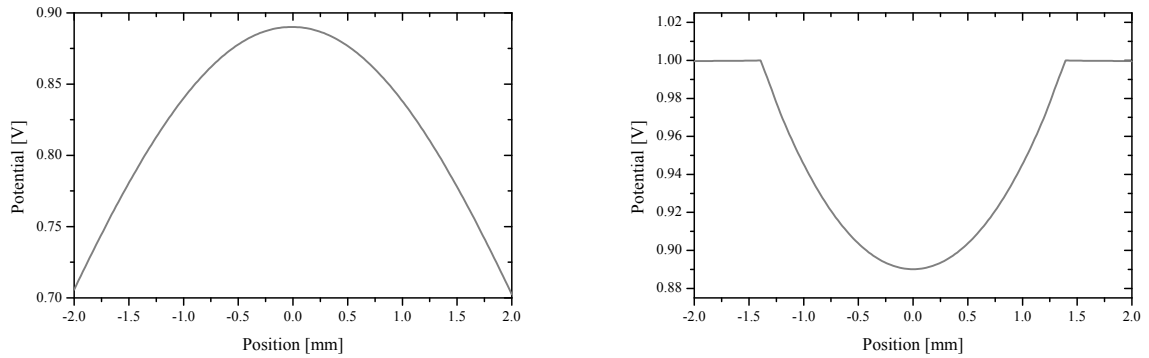
Figure 2.5.: *Calculated radial potential of the 6-rod trap. The left plot shows the open, "optical" axis, the right plot the direction of the RF electrodes ("trap axis"). The trap efficiency is $\kappa = 21\%$.*

segments. This design offers excellent optical access: The opening angle of the electrodes is $71°$, significantly larger than the approx. $27°$ an "ideal" 4-rod trap offers. However, this open structure reduces the trap efficiency. The simulated curvature of the potential calculated for $U_{\mathrm{rf}} = 1\,\mathrm{V}$ along the trap's radial principal axes are $c_2 = 0.05386\,\mathrm{V/mm^2}$ ("trap" axis) and $c_2 = 0.05361\,\mathrm{V/mm^2}$ ("optical" axis), which corresponds to a trap efficiency of $\kappa = 21\%$, see Fig. 2.5. The capacitance of the trap has been calculated to $3\,\mathrm{pF}$ per segment, so it is $9\,\mathrm{pF}$ in total. A slightly inconvenient feature of the design are the rather large ceramic rings that hold the electrodes. When ions were loaded using the electron gun they charged up significantly and displaced the ions from the trap center. Discharging took on the order of minutes.

2.1.5. The endcap trap

The endcap trap was designed to be a versatile tool for the storage of single ions and offers multiple trapping zones and excellent optical access. Its principle is illustrated in Fig. 2.7. The trapping field is generated by applying both RF and DC signals to two opposing electrodes
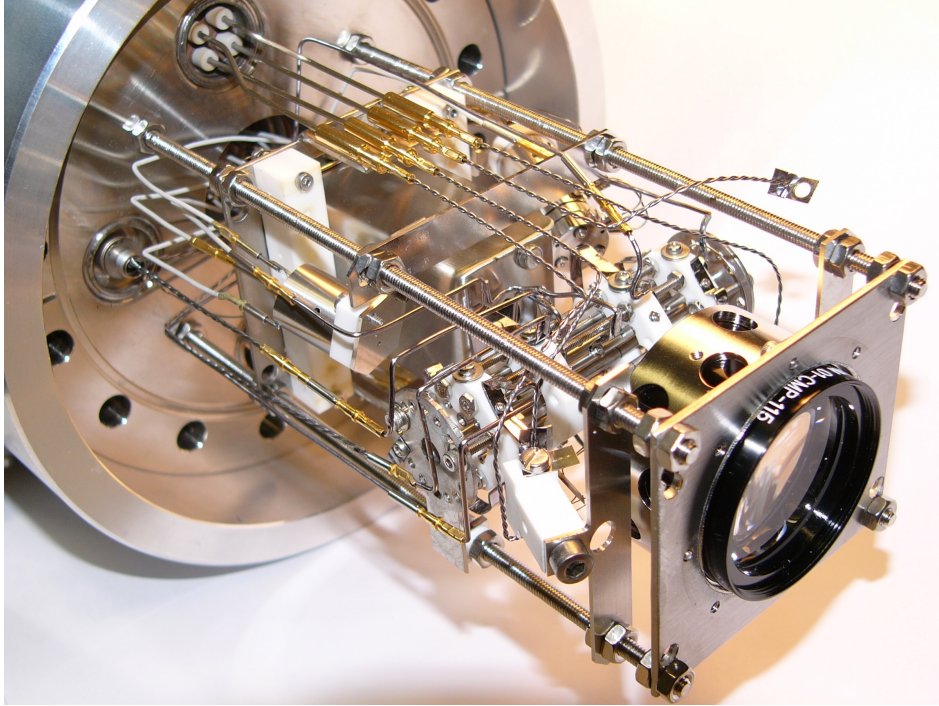
Figure 2.6.: *Image of the 6-rod trap mounted on a CF63 flange. The imaging lens is clearly seen. A channeltron is installed on the opposite side of the trap.*

indicated in orange while four bars with a triangular cross section (blue) are grounded. DC offsets applied to the RF trapping voltage serve two purposes: Applied to an electrode pair that stores ions this gives a nonzero Mathieu stability parameter a, e.g. for mass selectivity. Applied to neighbouring electrodes the DC voltages allow to adjust the axial confinement or shuttle ions between the segments. The RF electrodes are 1 mm wide and separated by 1 mm, so $r_0 = 0.5$ mm. The grounded electrodes are positioned such that the opening angle is $90°$. Their horizontal distance to the RF electrodes is 0.2 mm. Ions can be stored in 9 segments of two different lengths. Short segments are 1 mm long, long segments have a length of 5 mm. Two adjacent segments are separated by 0.5 mm.

The trap is constructed according to a tongue-and-groove principle to ensure good alignment of the electrodes, as illustrated in Figs. 2.7 and 2.8. Further, care was taken that no electrical insulators have a line-of-sight connection to the trapping region. The entire trap is made from stainless steel (304L) that has been individually selected for low magnetic susceptibility. If parts need to be electrically insulated machineable ceramic (Macor) and polyimide (an ultra high vacuum compatible plastic, also known as Vespel or Kapton) is used. The bars that serve as ground electrodes hold a precisely milled Macor structure that serves as mold for the electrodes. These are milled individually (and can thus be exchanged individually) and fit into the Macor grooves free from float. A second ground electrode bar holding a plain Macor bar serves as matching part, the two structures are connected with screws. Two such assemblies mounted opposing each other constitute the trap. BEM simulations give a trap efficiency of about 34%. The coefficients c_2 for $U_{\rm rf} = 1$ V are 0.57636 V/mm^2 horizontally and 0.58266 V/mm^2 vertically, see Fig. 2.10. The capacity of the entire trap has been calculated to 16.5 pF. An individual electrode pair has a capacity ranging from 1.0 pF (center electrode

view from imaging system

cutaway view from right side
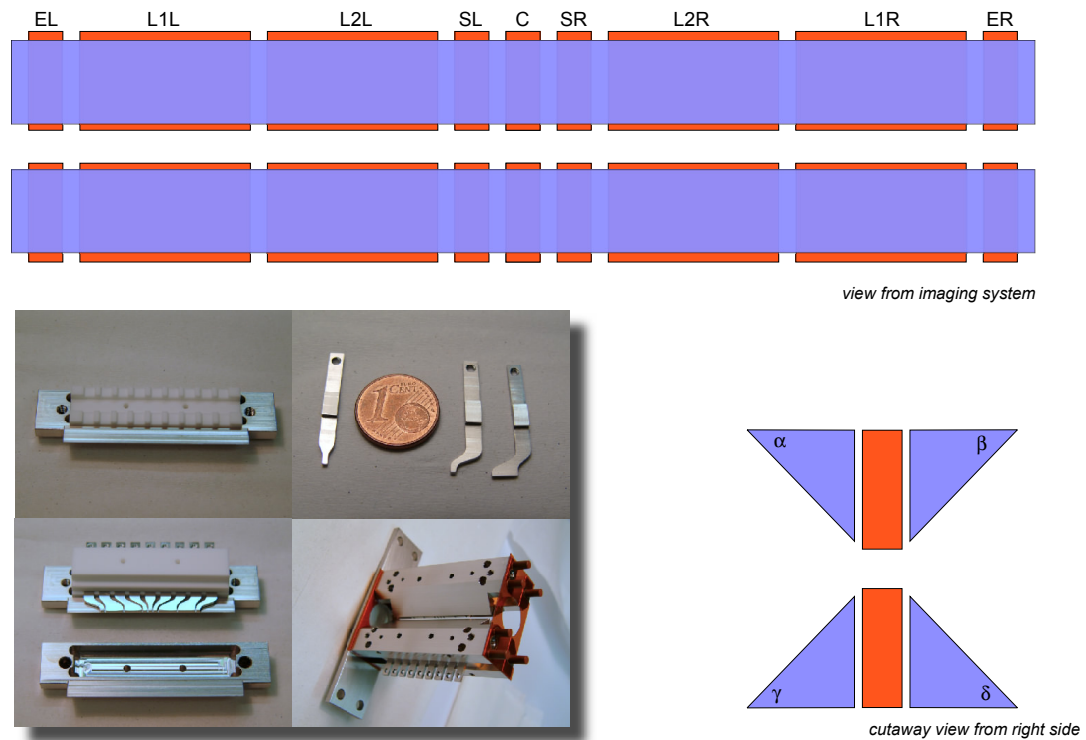
Figure 2.7.: *Simplified schematic of the endcap trap. Radio frequency and DC voltages for trapping are applied to the electrodes coloured orange. For the compensation of stray fields DC offsets can be applied to the blue electrodes that are held at RF ground otherwise. The images in the inset visualize the tongue-and-groove construction principle. The top left image shows how the ground electrodes hold a precisely milled Macor structure that in turn holds the individually machined electrodes (top right). The resulting structure is "sandwiched" together with a second ground electrode and Macor element (bottom left). Two such electrode "bars" form the trap (bottom right). The brown plastic parts are made from Vespel, an UHV compatible and electrically insulating material. Fig. 2.8 shows this in more detail. Abbreviations assigned to the 9 segments are shown above the axial view. The Mg^+ absolute frequency measurement was e.g. performed in "L2L": loading segment no. 2 left.*
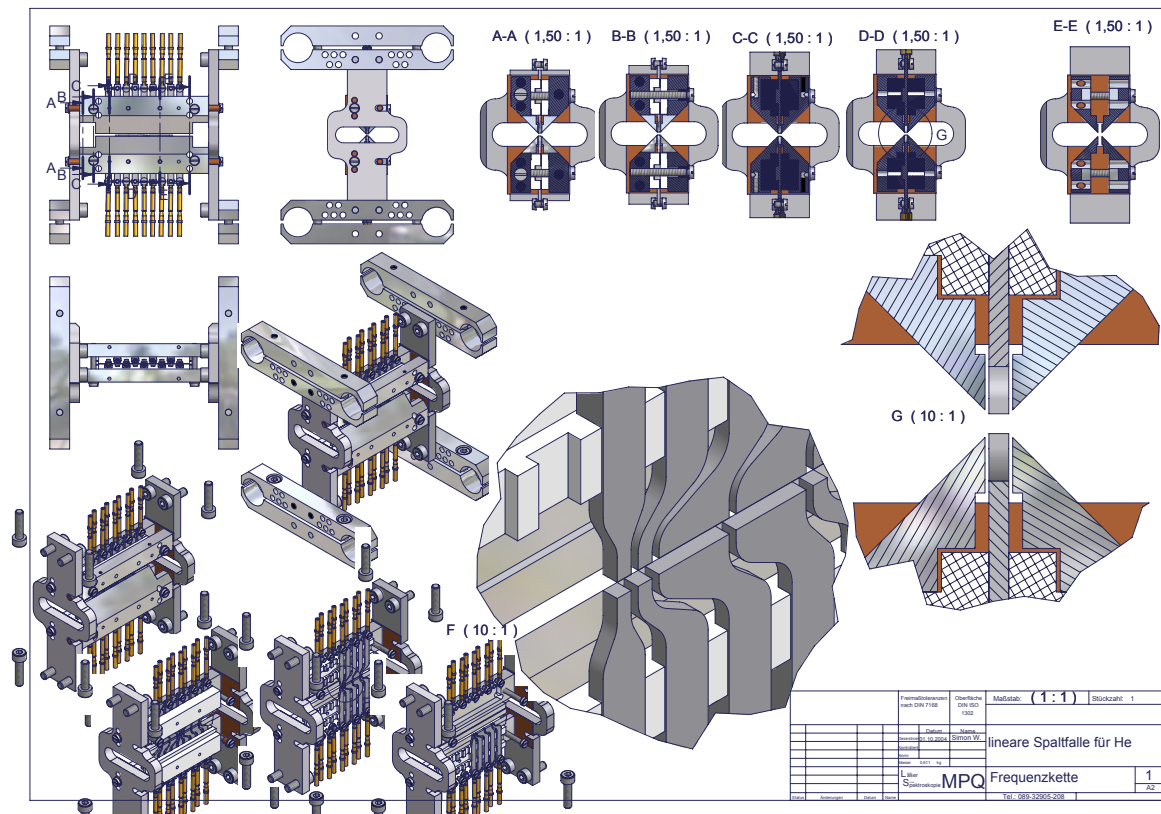
Figure 2.8.: *Technical drawing of the endcap trap. The short electrodes have an edge length of 1 mm, the dimensions of the long electrodes are 1 mm × 5 mm. All electrodes are separated axially by 0.5 mm, an opposing electrode pair is 1 mm apart. The ground electrodes (triangular cross section) are separated from the RF electrodes by 0.2 mm.*
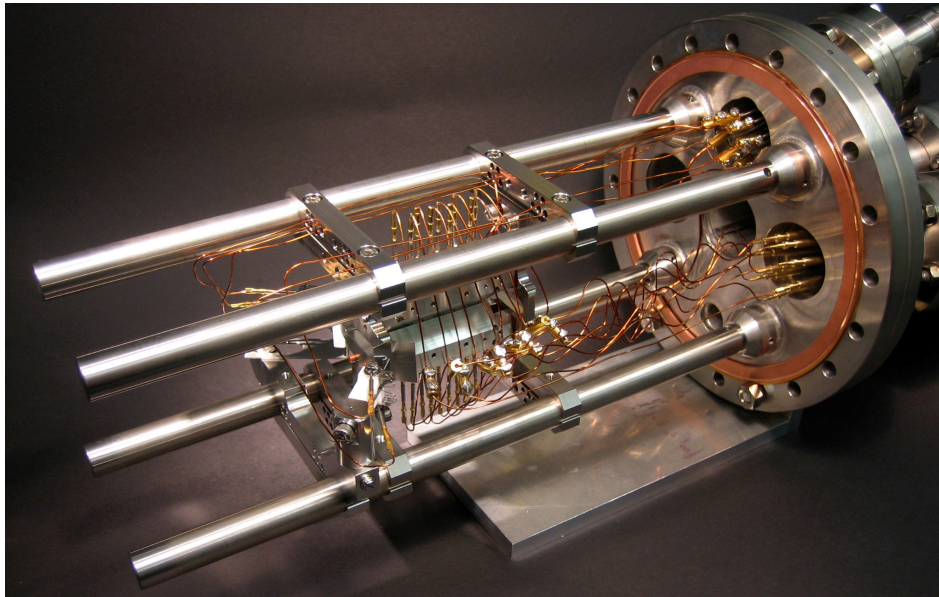
Figure 2.9.: *Image of the assembled endcap trap. Note the wiring that was optimized to minimize stray capacitance and differential phase shifts both within an electrode pair and between neighboring segments. The atomic oven and electron gun are visible to the left.*

C) to $2.8\,\mathrm{pF}$ (loading electrodes L1L and L1R). In the metrology experiments described in this thesis, only one electrode pair (L2L) was connected, which gives a soft axial RF confinement, see Fig. 2.11. The potential is very flat (relative variation 10^{-4} in the trapping region) and here the calculations do not agree well with observations. For radial secular frequencies of $1\,\mathrm{MHz}$ the measured axial frequency was about $70\,\mathrm{kHz}$, while simulations predict $5\,\mathrm{kHz}$. Apart from numerical errors this might indicate electrode misalignment.

2.2. Tank circuits

Most ion traps are operated with radio frequencies in the 6-60 MHz regime with extremes reaching down to $50\,\mathrm{Hz}$ and up to $250\,\mathrm{MHz}$. The applied voltages usually range from tens of Volts up to a few kilovolts. Providing these voltages directly from a signal source and an amplifier is a formidable task. Note, that $1\,\mathrm{kV}$ at a typical source impedance of $50\,\Omega$ corresponds to $20\,\mathrm{kW}$. Further, a RF trap is a capacitive load with typical capacitances around 5-50 pF and will therefore in general not be impedance matched with the amplifier ($50\,\Omega$) and hence reflect most of the power. The generally adopted, elegant solution to this problem is to design a resonant parallel LC circuit with the trap as capacitor. Such a tank circuit serves three purposes:

- Impedance matching
- Voltage enhancement
- Filtering (bandpass)

The following sections summarize basic properties of a tank circuit, give practical design guidelines and report on the performance of the two circuits used in the trapping experiments.
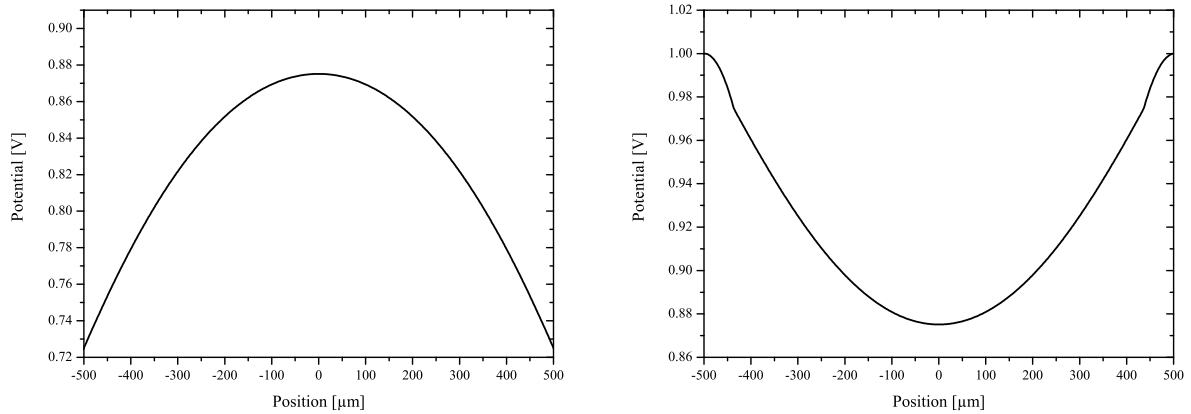
Figure 2.10.: *Calculated radial potential of the endcap trap. The left plot shows the horizontal, the right plot the vertical direction. Both plots have been calculated in the center of a loading segment.*
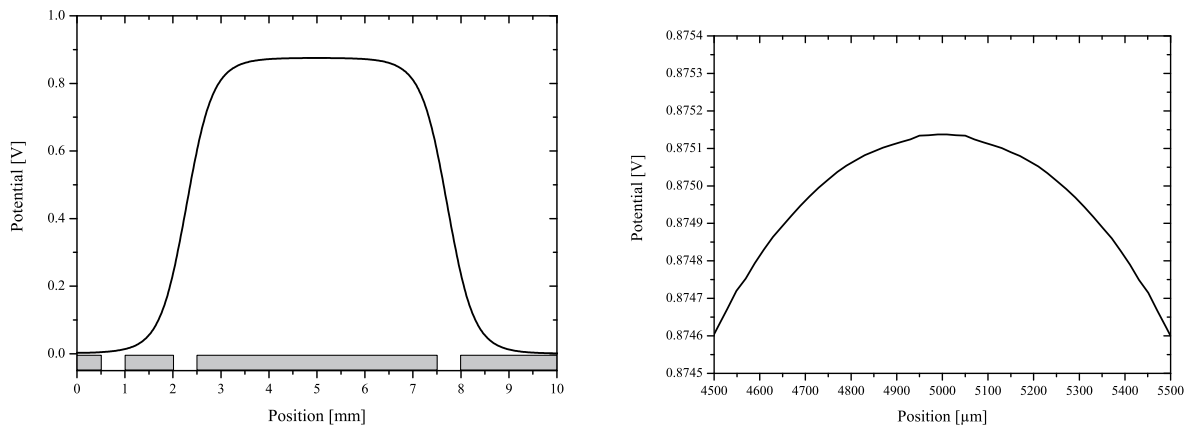
Figure 2.11.: *Calculated axial potential of the endcap trap. The left plot shows an overview with the position of the electrodes indicated, the right plot a magnification of the ion trapping region. The small "kinks" in the magnified plot are due to numerical errors.*

2.2.1. Basic properties
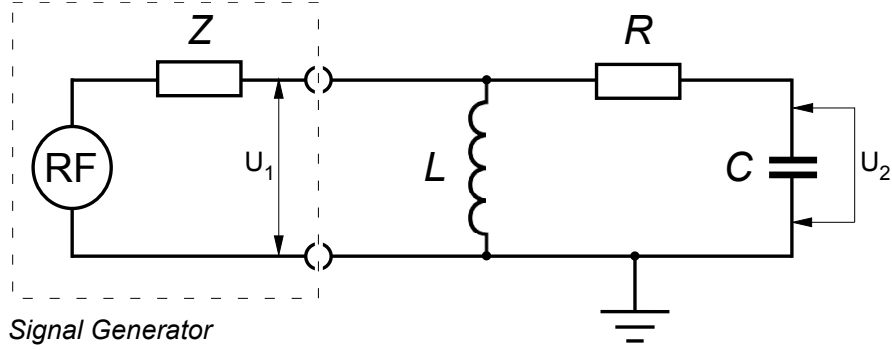
Figure 2.12.: *Schematic of a LCR circuit including a signal source of impedance Z. The impedance matching network (often a transformer realized as a single loop of wire around the primary coil) is not shown.*

Figure 2.12 shows a simplified schematic of a tank circuit. A signal source with an impedance Z provides an output voltage U_1. The tank circuit itself comprises a coil with inductance L which is connected to the trap of capacitance C to form a parallel LCR circuit. Losses are lumped into the series resistor R. The signal source is connected to the circuit using an impedance matching circuit, the details of which are discussed later. For the moment we only require it to ensure that the impedance of the tank circuit matches the source impedance Z. The resonant frequency ($\omega_0 = 2\pi\, f_0$) of the circuit reads

$$\omega_0 = \sqrt{\frac{1}{LC} - \left(\frac{R}{2L}\right)^2}. \tag{2.5}$$

The ability of the circuit to store energy is quantified by the quality factor Q which is defined as 2π times the stored energy divided by the dissipated energy per cycle

$$Q = 2\pi \times W_s/W_d. \tag{2.6}$$

This definition is equivalent to $Q = \omega_0/\Delta\omega_0$, where $\Delta\omega_0$ is the full-width at half maximum of the power. For an isolated LCR circuit (power source disconnected) Q reads

$$Q = \frac{1}{R}\sqrt{\frac{L}{C}} \tag{2.7}$$

From the definition of the quality factor we can now derive the voltage enhancement η, that is the voltage across the trap U_2 versus the input voltage U_1. In steady state the stored energy is constant and reads

$$W_s = \frac{1}{2}CU_2^2 \tag{2.8}$$

If we require impedance matching, we know that the dissipated power equals the input power $P = U_1^2/2Z$. This implies that the circuit dissipates an energy of

$$W_d = P\tau = \frac{U_1^2}{2Zf} \tag{2.9}$$

per cycle. Plugging the last two equations into the definition of Q we find for the voltage enhancement

$$\eta = \frac{U_2}{U_1} = \sqrt{\frac{Q_{\text{crit}}}{Z\omega C}} = \sqrt{\frac{Q_{\text{crit}}\omega_0 L}{Z}} = \sqrt{\frac{\sqrt{4L^2 - CLR^2}}{4CRZ}}. \tag{2.10}$$

Note that the value for Q in this equation is the "critical" Q_{crit} since we assumed impedance matching in Eq. 2.9. In the case of perfect impedance matching Q_{crit} is exactly one half of the unloaded Q, which is measured if the circuit is strongly undercoupled. The equations show, that besides minimizing ohmic losses it is advantageous to design the trap and circuit such that it has minimal capacitance. This is important to reach high resonant frequencies ($\Omega \propto 1/\sqrt{C}$), obtain good filtering ($Q \propto 1/\sqrt{C}$) and efficient voltage enhancement ($\eta \propto C^{-3/4}$).

2.2.2. Design guidelines

Frequency

As a first step, the desired resonant trap frequency Ω needs to be specified. This follows for example from the required secular frequency of the ions. Then Ω follows from $\Omega = 2\sqrt{2}\omega_s/q$, which for typical values of q (0.1…0.2) is about 10-20 times the secular frequency. In general, high trap frequencies tend to be advantageous. Assuming $(a, q) =$const. high secular frequencies $\propto \Omega$ imply well separated motional sidebands, further, adverse effects due to micromotion are minimized: For an electric stray field of given strength, the amplitude and kinetic energy of the micromotion scale $\propto \Omega^{-2}$. Finally, the heating due to fluctuating patch potentials scales $\propto \omega_s^{-1} \propto \Omega^{-1}$ [30]. On the other hand, high trap frequencies become increasingly technically challenging. The required drive power, which equals the power dissipated in the trap, scales $\propto \Omega^4$ and even under UHV conditions electric breakdown can occur.

From a technical point of view an important distinction between two different frequency domains needs to made: Tank circuits can be designed from conventional lumped components or as a special quarter wave resonator ("helical resonator"). The first regime, where standard coils and capacitors may be used, ranges up to about 25 MHz. This (soft) limit can easily be understood by estimating the minimum inductance and capacitance the circuit will exhibit. Straight wire of 1 mm diameter has an inductance of about 1.5 μH per meter, so it will be hard to keep the total inductance below, say, 2μH. If this wire is one centimeter above a grounded surface (e.g. the vacuum vessel) it will further contribute with a stray capacitance of about 15 pF per meter. The capacitance of the trap will typically exceed 5 pF so the total capacitance easily adds up to more than 20 pF. The resonance frequency of this "minimal", (20 pF, 2 μH), LC circuit is $f_r = 1/2\pi\sqrt{L\,C} = 25$ MHz. Both ion traps described are operated around $\Omega \sim 2\pi\,10$ MHz, so only "lumped circuit" designs will be discussed.

Wiring

In order to minimize ohmic losses radio frequency litz[5] should be used where ever possible, since the skin depth of copper at 10 MHz is only 21 μm. However, this is only possible outside the vacuum chamber, since litz is not suitable for UHV due to possible virtual leaks. In the tank circuits described below, the replacement of all solid wire outside the vacuum

---

[5]RF litz is different from ordinary litz: Here, every single strand is insulated to minimize losses from skin and proximity effect. Otherwise litz is only braided to enhance its mechanical flexibility.

by litz resulted in a two times higher Q factor. As shown above, the capacity of the circuit should be minimized, too. To this end, special attention should be paid to maximize the distance of the RF carrying wires to any grounded surface. UHV feedthroughs, especially multipin feedthroughs can have annoyingly high capacitances (10 pF-100 pF). When connecting the trap, care should be taken that the wiring does not introduce unintentional phase-differences between opposing electrodes. This could be caused by unequal lengths or differing stray capacitances. Even small phase-differences cause sizeable micromotion that cannot be compensated. Fig. 2.9 shows the wiring of the endcap trap.

Inductors

From all components, the primary coil is the most critical. In most cases the quality factor of the coil will limit the total quality of the circuit, which is the reciprocal sum of the Q factors of the components $1/Q = \sum_i 1/Q_i$. Even for "optimum" coils as described below it is hard to exceed a Q of, say, 500. In comparison, the Q value of a ceramic capacitor is typically around a few thousand. Designing a high Q coil requires paying attention to the following: No suitable ferrites exist in the range of frequencies above ~ 10 MHz, so the coil should be an air coil[6]. Eddy currents caused by the current itself (skin effect) and by the magnetic fields of a neighboring winding (proximity effect) increase the ohmic losses. At low frequencies the proximity effect can be neglected and close winding is favorable because this simply minimizes the length of the wire. At high frequencies an increasingly loose winding is preferable. The distinction between "low" and "high" is involved, but for the application described here the proximity effect dominates and is up to ten times larger than the skin effect. Further, the self capacitance of the coil should be taken into account. It increases linearly with diameter and aspect ratio ($\alpha = l/D$, where l is length and D diameter) and causes the coil to have a self resonant frequency which marks the maximum frequency up to which it is useful. Broadly speaking this shows that the coil should be short, loosely wound and of large diameter, where the latter is limited by the self resonant frequency and/ or practicability. In [34] the optimum geometry has been determined, with the following result assuming constant inductance and volume: The optimum aspect ratio is $\alpha = 0.7$, the optimum winding density, defined as the ratio of wire diameter d to wire spacing s (center to center) $\delta = d/s$, is $\delta = 0.6$. Empirically, for coils made of solid round copper wire, a quality factor of

$$Q \sim 41 D \sqrt{f} \tag{2.11}$$

may be expected, where the diameter D is in units of centimeters and the frequency f is given in MHz. The use of RF litz will lead to a higher Q. The inductance of a coil with such a geometry can be estimated to within 10% by

$$L \sim \frac{\pi \mu_0 D n^2}{4.6} \tag{2.12}$$

where n is the number of windings.

Capacitors

Capacitors should have low loss (sometimes called "tan δ") and withstand high voltages. For radio frequency applications silvered mica and certain ceramics (e.g. "C0G") are the most

---

[6]RF Ferrites specified for such high frequencies do exist, but due to their losses air coils are preferable

suitable dielectrics. Vacuum capacitors have the lowest losses, but are bulky and expensive. In general the Q factors are so high (a few thousand), that the exact choice is uncritical.

Resistors

High voltage carbon film resistors turned out to be most suitable for this application. Other resistor types (e.g. metal film, wire wound) can have rather large stray capacitances and therefore short cut the RF. In addition, together with their stray inductance cumbersome resonances can occur.

Coupling

To achieve impedance matching the source needs to be coupled to the tank circuit appropriately. Two coupling methods have been used: First, the RF signal wire is soldered to the primary coil directly ("galvanic coupling"). By choosing the position (close to ground corresponds to weak coupling and vice versa) the coupling strength can be tuned continuously. The advantage of this method is its mechanical stability. On the other hand it is not easy in practice to identify the optimum position. A second method is to place a current loop around the coil. Its magnetic field will have some overlap with the magnetic field of the coil and hence provide an inductive coupling. After choosing roughly the right diameter, the coupling can be fine-tuned by twisting the angle of the loop relative to the axis of the coil. This allows to achieve an extremely good coupling, limited only by the sensitivity of the measurement method.

Methods to optimize the coupling include maximizing the voltage on the trap electrode, or measuring the reflected power e.g. using a directional coupler. The first method is very easy to implement but is not very accurate and requires paying special attention to the perturbations introduced by the voltage probe. Signal generators and amplifiers are quite sensitive to reflected power, so measuring it using a directional coupler is by far the superior method.

Characterization

The tank circuit is then conveniently characterized as follows: First, the inductance of the coil is measured e.g. by attaching a well known capacitor to it and determining the resonance frequency. In a second step the trap is attached and the resonance frequency ω_0 and -width $\Delta\omega_0$ are measured, from which the quality factor $Q = \omega/\Delta\omega_0$ is inferred. Thereby the coupling should be minimized. The quality factor in the impedance matched case ("critical coupling") will then be exactly $1/2$ of the measured value $Q_{\mathrm{crit}} = Q/2$. Care should be taken that the measurement does not perturb the tank circuit, e.g. by using an ultra low capacitance probe or an antenna. From the measured values of L, ω_0 and Q the remaining parameters are calculated as follows:

$$C \quad = \quad \frac{16Q_{\mathrm{crit}}^2 - 1}{16L\omega_0^2 Q_{\mathrm{crit}}^2} \tag{2.13}$$

$$R \quad = \quad \frac{L\omega_0}{\sqrt{Q_{\mathrm{crit}}^2 - \frac{1}{16}}} \tag{2.14}$$

2.2.3. Results

6-rod trap

The tank circuit (see Fig. 2.13) resonates at $\Omega = 2\pi\,11.86\,\text{MHz}$ with a quality factor of 65. Together with the measured inductance of the primary coil of $L = 1.595\,\mu\text{H}$ this gives a voltage enhancement of $\eta = 12.4$. This has been confirmed by the measurement of secular frequencies of the trapped ions. DC offsets for axial confinement or to apply an a-value can be applied to the three segments individually by RC low-pass filters. The total capacitance amounts to $C = 113\,\text{pF}$, mainly given by the multipin vacuum feedthroughs. Losses correspond to a resistance of $R = 1.8\,\Omega$. Coupling is achieved inductively by a loop around the primary coil. The reflected power is typically $P_r/P_{in} < -30\,\text{dB}$.
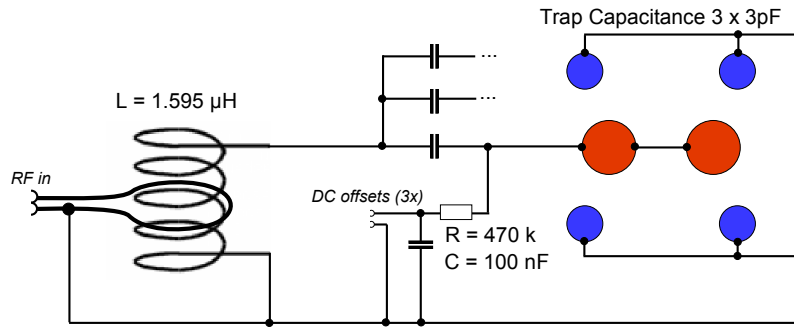
Figure 2.13.: *Schematic of the tank circuit of the 6-rod trap.*

Endcap trap

The primary coil of the endcap trap is 5 cm in diameter with 8 windings of litz over a length of 32 mm, wound on a hollow teflon body. Its inductance was measured to be $L = 3.39\,\mu\text{H}$, the quality of the isolated coil is $Q = 812$. The latter is significantly higher than the value of $Q = 615$ as predicted by Eq. 2.11 due to the usage of litz vs. solid wire. The circuit features 9 RC low-pass filters that allow to apply DC offsets to all segments individually (Fig. 2.14). Silvered mica capacitors and carbon film resistors provide low-loss decoupling of RF and DC signals. In total, the circuit resonates at $\Omega = 2\pi\,8.1\,\text{MHz}$ and has a critical quality factor of 30 (~ 60 for weak coupling). This gives a voltage enhancement of $\eta = 10$, a total capacitance of $C = 114\,\text{pF}$ and losses corresponding to $R = 2.9\,\Omega$. The calculated capacitance of the trap is 16.5 pF, so the circuit picks up 98 pF stray capacitance, which is 11 pF per segment, mainly caused by the multipin vacuum feedthrough. The RF signal is coupled to the circuit inductively with a single loop around the primary coil, which allows to minimize reflections below the isolation of the directional coupler ($P_r/P_{in} < -60\,\text{dB}$).

The experiments on spectroscopy and regenerative oscillations described in the next two chapters required only one trapping region. For these applications the trap and tank circuit was used in a second configuration where only one segment (L2l) was connected and all DC offsets were disconnected. In this mode the total capacitance is reduced to $C = 30\,\text{pF}$ and the tank circuit resonates at $\Omega = 2\pi\,15.83\,\text{MHz}$. The critical quality factor is measured to be 46 which gives a voltage enhancement of $\eta = 18$.
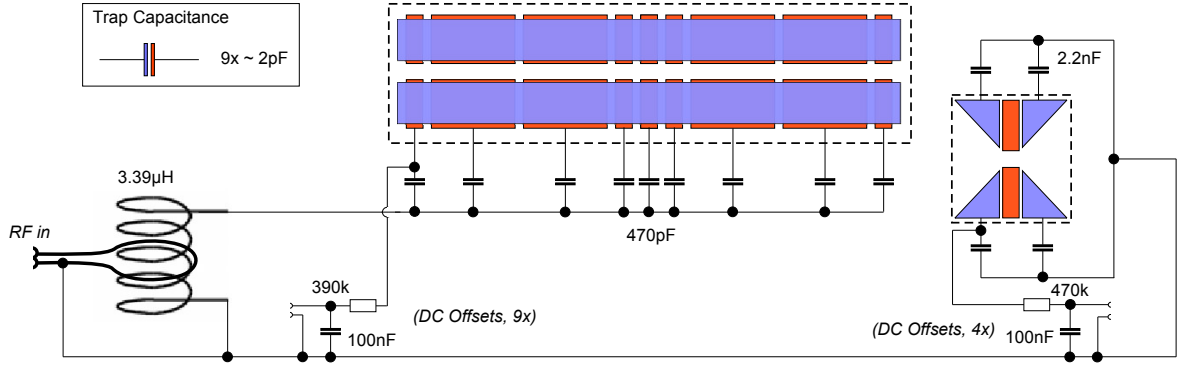
Figure 2.14.: *Schematic of the tank circuit of the endcap trap.*

2.3. Vacuum system

Ultra high vacuum, that is a pressure below 10^{-9} mbar, is a crucial prerequisite for an ion trapping experiment. This minimizes adverse collisions with background gas particles that can lead to heating (decoherence) or to chemical reactions. The latter is particularly important, since photo-assisted chemical reactions are the dominant loss mechanism for trapped alkaline earth ions (Be^+, Mg^+, ...): During laser cooling, the ion will spend some time in the excited state. If it then collides with a hydrogen molecule from the background gas, there is a high probability that it will form a hydride (e.g. $Mg^{+*}+H_2 \rightarrow MgH^{+}+H$). In general, the resulting molecule will remain trapped, but, will not interact with the laser light anymore. Depending on the residual partial hydrogen pressure, a sample of trapped ions will therefore become increasingly "polluted" with molecular ions.

This section describes the vacuum system of both ion traps in detail, including hardware (pumps and components), cleaning and baking procedures and performance. Although the SI Unit of pressure is Pa (N/m^2) we specify pressures in mbar ($=100$ Pa), which is customary in this field.

2.3.1. Preliminaries: design, materials, cleaning and baking

In order to reach the lowest pressures great care needs to be taken in choosing appropriate materials that are introduced into the vacuum system. Further, meticulous cleaning and finally careful baking are necessary.

The final pressure of the system will be given by the ratio of gas load to pumping speed. The gas load is caused by the vapor pressure of the materials used, absorbed water and hydrocarbons on the surfaces and diffusion through the walls (hydrogen!). Proper choice of the materials used will take care of the first and the last point. The second point requires minimizing the surface area (by design and smooth surfaces), cleaning and finally heating the apparatus while it is being pumped ("baking"). Without baking surface adsorbed water and hydrocarbons will make it hard to achieve a pressure below 10^{-8} mbar. Careful design is further necessary to avoid so-called "virtual leaks": This could be, for example, a simple thread. If it has no extra venting hole, a small volume is created inside the vacuum chamber that can hardly be pumped. Even after baking a tiny amount of water can be left that will prevent achieving low pressure. Welded parts must have their welded seam on the vacuum side for the same reason, even though this might be challenging in some situations.

Suitable materials must therefore have a very low vapor pressure, a smooth surface and must be "bakeable", that is withstand temperatures of 200 °C-400 °C. Frequent choices include, but are not limited to: A wide range of metals and alloys, such as stainless steel (304L), copper, gold, aluminum and tantalum, further certain ceramics and glass. Special UHV compatible plastics exist, e.g. polyimide (Vespel®, Kapton®, both by DuPont), and even some adhesives have turned out to be suitable (e.g. Epotek 301, 353ND, H77, H35-175MPV). Materials that should be avoided include brass and zinc (careful: nuts, screws and washers!). Teflon has an excellently low vapor pressure but is suitable only at first sight because it cannot be baked. Soldering should be avoided, but, if necessary, special UHV solders are available. Wiring should only be done with solid wires, litz has a big surface and can be an annoying source of virtual leaks.

The following cleaning procedure gives good results while being moderately time consuming. The use of powder-free (Nitrile) gloves throughout the procedure is of course mandatory.

- Scrub with soap. Parts from the machine shop will be full of oil and turnings, the same applies for screws, nuts and bolts.

- Immerse in ultrasonic bath with strong degreaser.

- Rinse with distilled water. Demineralised water is suitable, too.

- Clean with methanol (Uvasol®). Either by wiping or in ultrasonic bath. Acetone is a better solvent, but sometimes leaves some residue behind.

- Rinse with distilled water.

- Blow dry with hot air. Do not wipe the parts dry, otherwise dust particles accumulate.

The vacuum system should be assembled shortly after cleaning. The parts attract dust, even if covered. Ideally, the parts are still warm after blow drying, which reduces the amount of water introduced. Seals are fastened using a torque wrench. A little high-temperature compatible anti-seize (e.g. molybdenum disulfide) on the screws facilitates re-tightening and loosening.

Baking the apparatus means heating it to 200 °C-400 °C for about one week while pumping on it. The apparatus can either be heated by building an oven made from fire clay around it, or, by wrapping heating bands, stone wool and aluminum foil around it. Most vacuum systems will be made of stainless steel which is a very poor thermal conductor. For this reason the "oven" method has the clear advantage of more uniform heating. Due to size and other restrictions this may not be possible for every apparatus. If done carefully, the "wrapping" method works equally well, although great care needs to be taken to keep temperature gradients small. The weakest parts of a vacuum system are in general the vacuum windows (more precisely the solder of the glass-metal transition). Bad temperature monitoring and inhomogeneous heating (spatially and in time) can lead to a hot-spot near a window and subsequently to its failure. Other than that, the temperature should be as high as possible, again typically limited by the vacuum windows. This is because vapor pressures increase exponentially with temperature, so the amount of water and hydrocarbons removed will grow exponentially with temperature. Heating the apparatus up or cooling it down must be done carefully, that is the heating rate must be limited to the maximum specified rate of the most sensitive component. These are usually the vacuum windows and should be heated/ cooled

slower than $1\,\mathrm{K/min}$. As an example, this is the baking procedure of the endcap trap using the "wrapping" method:

- Pump the system for about one week. Leak check. If everything is well cleaned and all seals are tight, a pressure around $10^{-8}\,\mathrm{mbar}$ with the turbo pump alone is achieved.

- "Bake" the electron gun and atomic oven by operating them with increasing currents until pressure settles.

- Gradually heat up the system. The pressure can rise to $10^{-5}\,\mathrm{mbar}$ or more. The ion pump including magnet is heated, too.

- Operate (hot) ion pump with increasing voltage. Repeatedly operate ("flash") titanium sublimation pump (TSP) according to specification ($47\,\mathrm{A}$ for $1\,\mathrm{min}$ in our case, every $3\,\mathrm{mins}$).

- After 3-7 days the pressure will drop to $10^{-7}\,\mathrm{mbar}$. Cool down.

- After cooling down, a pressure around $10^{-10}\,\mathrm{mbar}$ will be reached. Close all-metal angle valve.

- Flash TSP. Within a day the pressure will drop into the low $10^{-11}\,\mathrm{mbar}$ regime.

- About one-two weeks after cooling down, the pressure will have further dropped below $10^{-11}\,\mathrm{mbar}$.

The baking procedure for the 6-rod trap is very similar.

2.3.2. Endcap trap

Vacuum chamber

The vacuum chamber consists of the following main parts:

- A CF150 double cross serves as main experiment chamber. It is attached to the optical table using four ceramic feet, so it is thermally and electrically decoupled.

- Two custom made CF150 flanges are connected to the experiment chamber which hold the ion trap (see Fig. 2.9), allow laser access and provide a direct gas inlet over a precision leak valve.

- A custom made CF150 "re-entry window" allows to position imaging optics only $63\,\mathrm{mm}$ away from the trap center.

- A CF150 tube with three connectors ($1\times$CF63, $2\times$CF40) sits on top of the experiment chamber. The ion pump and TSP are attached to the CF150 port. The turbo and backing pump are attached to an all metal angle valve which is connected to the CF63 port. The ion gauge is connected to a CF40 port.

The CF150 tube also houses two "baffles" which prevent ions from the ion pump to enter the experiment chamber, without reducing the conductivity significantly.

The ion trap is centered in the double cross. Four vacuum windows allow laser access either axially or enclosing an angle of $15°$ with respect to the axis. Ions trapped in segment C are located $333\,\mathrm{mm}$ from the axial laser access window and $262\,\mathrm{mm}$ from the "angled" port. Both distances are measured from the front (=air side) surface of the vacuum window.

Pumps

The vacuum system utilizes four different types of pumps to achieve the lowest possible pressure as follows (see also table 2.3): A Varian SH100 scroll pump serves as backing pump with a pumping speed of $1.4\,l/s$ and provides an oil-free vacuum with a base pressure of $6.6\times10^{-2}\,$mbar. It should be noted that the scroll pump used is oil- but not "particle-free". Abrasion of the teflon fitted bearings can cause dust to accumulate in the foreline which may be blown into the vacuum vessel upon venting. The teflon particles can be problematic for high voltage applications, as we experienced by dust-induced short cuts in a channeltron. This problem can be avoided by a careful venting procedure or by using newer, oil- and particle-free pumps [7]. The foreline vacuum is monitored with a Pirani type gauge. Ultra-high vacuum is then achieved with three different pumps: A $345\,l/s$ turbo pump (DN100CF) evacuates the chamber to a base pressure of about $10^{-10}\,$mbar. The specified pumping speed is not reached in our system for two reasons: First, the base pressure of the backing pump is too high, for optimum performance the foreline pressure should be below $10^{-2}\,$mbar. Second, the pump is not attached to the vacuum vessel directly, but to an all-metal angle valve with reduced opening (DN63CF). It has a conductivity of $C \sim 100\,l/s$, so the net pumping speed is only $(\sum_i 1/C_i)^{-1} \sim 78\,l/s$. The angle valve allows to separate the foreline vacuum system from the main experimental chamber which is pumped by an ion pump and a titanium sublimation pump (combined in a Varian VacIon Plus 300). Once the system has been pumped down and baked, the valve is closed and the main chamber is pumped by the ion pump and the TSP only. This has several advantages: Vibrations from the scroll and the turbo pump are eliminated, the hydrogen load is minimized (turbo pumps have bad compression ratios for light species) and in the event of a power shortage the chamber is not vented. The ion pump has a pumping speed of $240\,l/s$ and is operated at the lowest voltage setting. The titanium sublimation pump is crucial to achieve pressures below $10^{-10}\,$mbar. At such low pressures the residual gas consists mainly of hydrogen which is pumped by the TSP extremely effectively: The nominal pumping speed is $1580\,l/s$. The pumping speed can be increased by water or cryo-cooling the TSP. The ion pump is operated permanently, the titanium layer in the TSP is renewed ("flashed") only about once or twice a year.

Result

The entire system is depicted in Fig. 2.15. The ion gauge is specified down to $5 \times 10^{-11}\,$mbar, and reads "under range". As this thesis was written, the TSP had not been flashed for more than a year.

2.3.3. 6-rod trap

The vacuum system is similar to the one of the endcap trap. The major difference is that there is no TSP installed. Also, the pumping speed of the ion pump is significantly lower. For this reason the vacuum is not "pinched off" by an all-metal angle valve, but pumped permanently by the turbo pump as well.
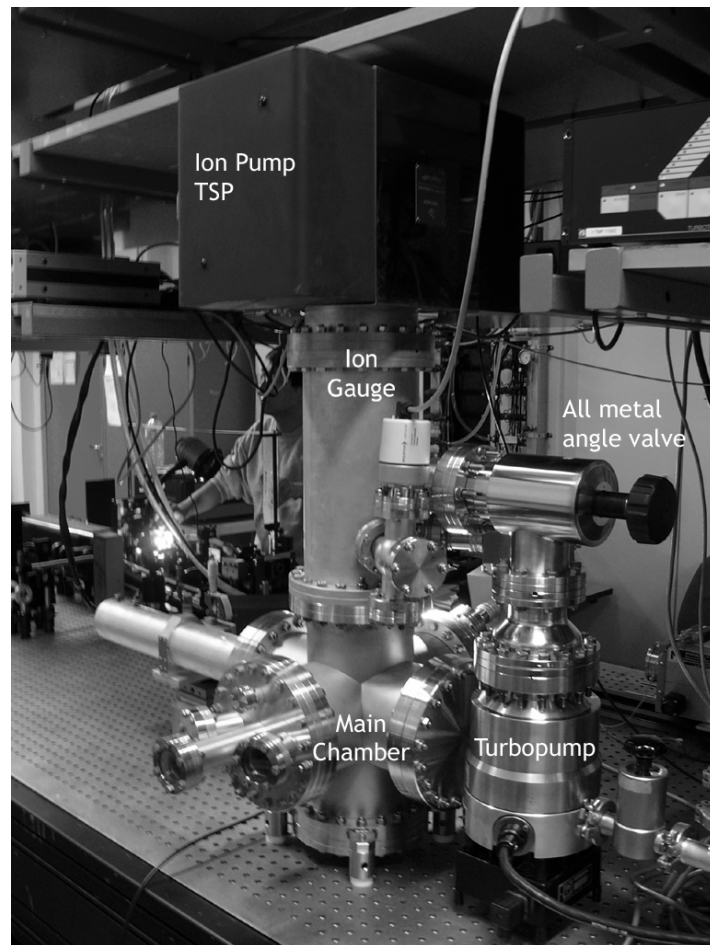
---

[7]e.g. Pfeiffer XtraDry

Figure 2.15.: *Image of the endcap trap vacuum system.*

Vacuum chamber

The vacuum chamber consists of a single, custom made stainless steel chamber with all necessary ports. The trap is held on a CF63 flange, ions are observed through a CF40 fused silica window, such that optics can be placed 85 mm away from the trap axis. Laser beams enter and exit the chamber through four CF16 windows. A four-way port that holds the pumps is attached to a CF63 flange at the bottom of the chamber.

Pumps

As in the endcap trap an oil free scroll pump (Varian SH100) serves as backing pump. The foreline pressure is measured by a Pirani type gauge. A turbo pump (Leybold TurboVac 150) with a pumping speed of 145 l/s is attached to the chamber over a CF40 all metal angle valve. The pumping speed is increased by cascading a second small turbo pump (Leybold TurboVac 50, 55 l/s) that lowers the foreline pressure. An ion pump (Leybold IZ12) is connected to the main chamber directly and provides an extra 40 l/s pumping speed. The pressure in the experiment chamber is monitored with a Bayard-Alpert gauge (Leybold Ionivac IE414).

Results

A pressure down to 2×10^{-10} mbar could be achieved. This is limited by two factors: First, no TSP is installed and second, the all-metal angle valve reduces the pumping speed of the turbo pump to about 37 l/s due to its low conductance of 50 l/s.

2.4. Imaging system

In most ion trapping experiments the measured signal, in one way or another, will be scattered photons - whether it is a spectroscopy experiment, a quantum computer or a study of a trapped one-component plasma. The imaging system is therefore a crucial part of the setup, that should collect photons efficiently and with high signal-to-noise ratio and is often required to resolve single ions.

2.4.1. Lens

A typical ion trap imaging system consists of either one or two lenses. The two-lens system has the advantage that it allows to place an aperture at the Fourier (intermediate image) plane to spatially filter the image. In this way stray light photons that enter the imaging system from outside the field of view are efficiently suppressed and therefore the observed signal-to-noise ratio is enhanced. It further facilitates large magnifications with a compact footprint. The disadvantage is that the two lenses need to be carefully aligned with respect to each other in order to minimize resolution degrading abberations, and the field stop needs to be positioned accurately in the focal plane, otherwise it introduces field distortions, such as barrel and pincushion distortion. To efficiently collect photons emitted by the ion the first lens should have a low f/♯ (the ratio between focal length f and diameter D), typically f/2 or f/1, and a short focal length so the size stays reasonable. The focal length on the other hand should not be too short (microscope objective) since the lens is an insulating surface with adverse affects for trapping if it is too close to the ions. Typical choices are in the range $f_0 = 20 \ldots 75$ mm. If single ions should be resolvable the resolution must at least exceed the ion-ion distance
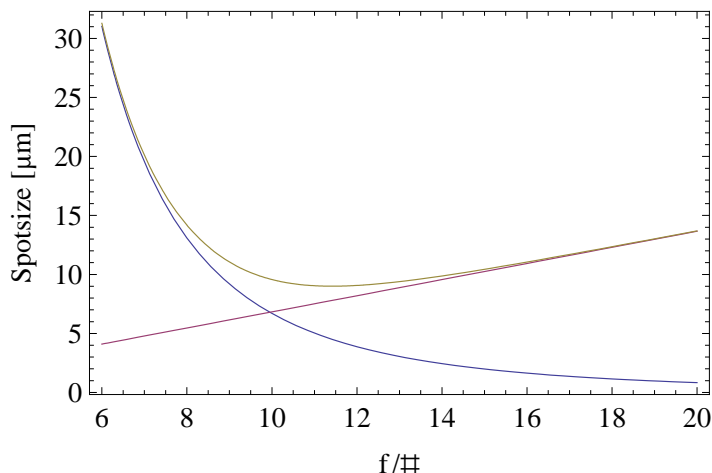
Figure 2.16.: *Focused spot size (resolution) of a 100 mm plano convex lens focusing 280 nm light as a function of opening. The dashed lines show the spot size due to spherical abberation (decreasing) and diffraction (increasing), the solid line the resulting spot size.*

of a stored crystal, which is typically on the order of $10\,\mu$m. Since only one wavelength is imaged, the resolution of the optics will be limited by monochromatic abberations, most importantly spherical abberation and coma. Spherical abberations occur because the lens surfaces of a spherical lens deviate from the ideal shape and are not e.g. paraboloidal as would be ideal for focussing collimated light. The effect is proportional to $f/\sharp^{-3}$ and can be minimized by blocking rays with low $f/\sharp$ by an aperture stop placed in front of the lens[8]. Of course this reduces the amount of collected light and increases the diffraction limited spot size: $d = 2.44\lambda f/\sharp$. Figure 2.16 illustrates this trade-off and shows the resulting spot size for a plano-convex lens as a function of $f/\sharp$. Coma causes off-axis points to be imaged as structures that resemble the tail of comet and scales $\propto f/\sharp^{-2}$. Objectives that have been corrected for both these effects are called aplanatic. Achromatic lenses exhibit also much smaller spherical abberation and coma than singlet lenses, although, as the name suggests, they have been designed to minimize chromatic abberations. Commercial or home-built "condensers" (often simply two plano-convex lenses with the curved surfaces facing each other) are a cost-effective alternative with often sufficient performance.

A costly high quality lens is required in experiments where high resolution imaging and efficient photon counting are required simultaneously. Otherwise, as in our experiments, following strategy can be adopted: For photon counting purposes the imaging resolution is not relevant, so the full aperture is used. For high resolution imaging the lens is stopped down to obtain maximum resolution at the cost of longer exposure times.

A further choice that can be made is whether the first lens is placed in the vacuum system or outside. Placing the lens in the recipient allows to place it very close to the trap. Keeping $f/\sharp$ constant it therefore can be rather small and hence cheap. The obvious disadvantage is that the lens cannot be adjusted without opening the vacuum vessel. Further, if spatial filtering and a second lens are to be employed, the alignment relative to the first lens is cumbersome in practice. An imaging system located entirely outside the vacuum vessel solves these problems but requires careful design of the recipient and possibly expensive custom

---

[8]The spot size due to transversal spherical abberation for a plano convex lens is $0.067f \cdot f/\sharp^{-3}$
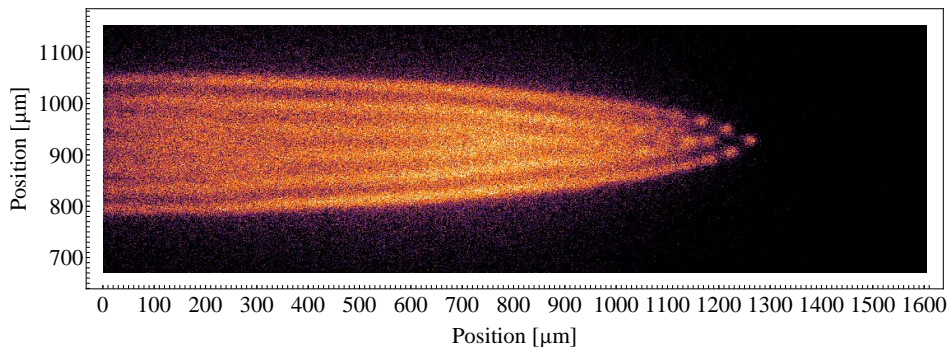
Figure 2.17.: *Image of a large ion crystal stored in the 6-rod trap. This image was taken in a "one lens" configuration.*

made vacuum components. Also will in general the minimum distance to the trapped ions be larger, so comparatively bigger and more expensive optics are necessary. Our practical experience with both approaches showed that an imaging system located entirely outside the vacuum system is clearly the better choice.

2.4.2. 6-rod trap imaging

The imaging system of the 6 rod trap consists of a two element, f/1, condenser lens made from fused silica (Melles Griot 01-CMP-115, f=35 mm). A broad band UV anti-reflection coating improves transmission and reduces ghosting. It is placed in vacuum close to the trap, and images onto an electron multiplied CCD (EMCCD) camera (Andor DUV A-DV885 LC-VP). The EMCCD chip has 1004x1002 square pixels of $8\,\mu$m edge length. The quantum efficiency at $280\,$nm is specified to be 28%. Each pixel has a full-well capacity of about 20000 e$^-$. Read noise amounts to $0.01\,$e$^-$/px, the dark current to $0.01\,$e$^-$/(px·s). To enhance the signal-to-noise ratio a $1\,$mm thick Schott UG-11 UV bandpass filter ("solar-blind") is mounted just in front of the chip. It has a transmission of 64.8% at $280\,$nm and blocks visible wavelengths effectively (optical density>5), except a region around $720\,$nm where it transmits up to 27%[9].

We tried to chose the smallest magnification that still allows to resolve single ions. A small magnification gives a large field of view and better signal-to-noise ratio since the light of an ion is not dispersed over many pixels[10]. The lens is optimized for a magnification in the range $m = -3\cdots-15$. If we assume a magnification of $m = -8$ a typical ion-ion distance of $10\,\mu$m translates to ten pixels between the ions. The focal length of the lens is specified to be $f = 35\,$mm. This implies, that the condensers first principle plane should be mounted $(m+1)/mf = 39.4\,$mm away from the trap axis. The lens is positioned using a caliper, which works quite well in practice. A measurement of the true magnification gave $m = -7.6$, corresponding to a distance of $39.6\,$mm. An aperture stop placed outside the vacuum, close to the window, is used to improve the image quality by blocking low f/♯ rays. The resolution is maximized by closing the aperture to about $2\,$mm diameter, which corresponds to f/9. The observed full width at half maximum of an imaged ion is about 5 pixels, so the resolution is roughly $5\,\mu$m. As example, an imaged ion crystal is shown in Fig. 2.17.

---

[9]The residual transmission in the red turned out not to be problematic. An Asahi interference filter that does not transmit in the red did not improve the observed signal-to-noise ratio.

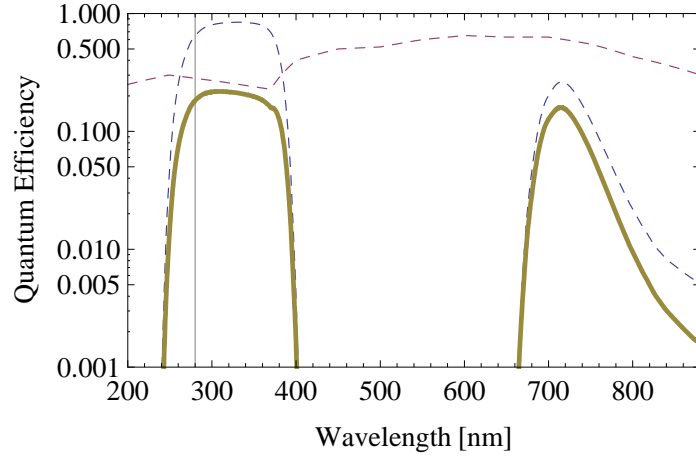[10]Because of read-noise this gives a better SNR than binning.

Figure 2.18.: *Quantum Efficiency of the imaging system of the 6-rod trap. The two dashed lines show the transmission of the Schott UG11 solar blind filter (with two transmission bands) and the quantum efficiency of the EMCCD camera (flat curve), respectively. The solid line gives the total response, which is 18.3% at 280 nm. Including solid angle (4.2%), 7.7×10^{-3} fluorescence photons are detected.*

We also worked with a second configuration where two lenses were used. The condenser lens was positioned to obtain a magnification of $m = -5$ and imaged onto a field stop to suppress stray light. The second lens was a home-built condenser made from two $f = 100$ mm plano-convex lenses with an effective focal length of 52 mm. It magnified the intermediate image a further factor $m = -4$, so the total magnification was $m = -20$. The imaging system was used rarely in this configuration. In practice, the slightly better stray-light reduction was outweighed by the tedious alignment.

In total, up to about 7.7×10^{-3} of the emitted photons are detected. The solid angle covered by a cone of opening angle ω reads $\Omega = 4\pi \sin^2(\omega/4)$. The condenser covers about $47.2°$, corresponding to 4.2% solid angle. The UG11 solar blind filter transmits about 64.8% at 280 nm, and the specified quantum efficiency of the EMCCD camera is 28.2%. With these values one obtains a maximum count rate per Mg^+ ion of 1 MHz. The spectral quantum efficiency is shown in Fig. 2.18.

2.4.3. Endcap trap imaging

The imaging system of the endcap trap is quite different to the system described above. First, a 60 mm diameter "re-entry" window made of 6 mm thick fused silica (uncoated) allows to place a lens *outside* the vacuum system as close as 56 mm to the trap axis. Second, a Quantar 2601B single photon camera is used for imaging which has a seven times lower spatial resolution than the EMCCD camera, so higher magnification is required. The sensor surface is circular with a diameter of 25 mm and has a spatial resolution of about $56\,\mu$m. We slightly oversample by digitizing the output with a resolution $512{\times}512$ pixels, which corresponds to a pixel size of $49\,\mu$m. We therefore chose a much higher magnification of $m = -100$. The imaging optics consists of two lenses and two apertures that are all integrated into an aluminum tube. This simplifies the alignment considerably and in particular ensures good centering. The first lens is a f/2 4-lens condenser optimized for a magnification of $m = -5$ (B. Halle Nachfl.). According to specification it is diffraction limited from f/3 onwards.

The maximum theoretical resolution is therefore about $0.7\,\mu$m at $280\,$nm. An aperture is placed just behind the condenser that allows to balance image quality and photon collection efficiency. A further aperture, whose opening corresponds to the field of view, is placed in the image plane of the condenser and suppresses stray light. A Newport U-13x microscope objective magnifies the intermediate image a factor $m = -20$ to obtain a total magnification of $m = -100$. To further reduce stray light, the inside of the tube is lined with black felt. The imaging tube is mounted on three (XYZ) translational stages with digital displays, which has proven to be very convenient in practice, e.g. to find the ions. A black, cardboard photography bellow provides a light-tight and flexible connection to the single-photon camera. The latter is very sensitive and may be destroyed by exposure to lab level light. For this reason it is protected by a shutter and an UG11 solar blind filter mounted directly in front of the imaging tube. The entire system is shown in Fig. 2.19.
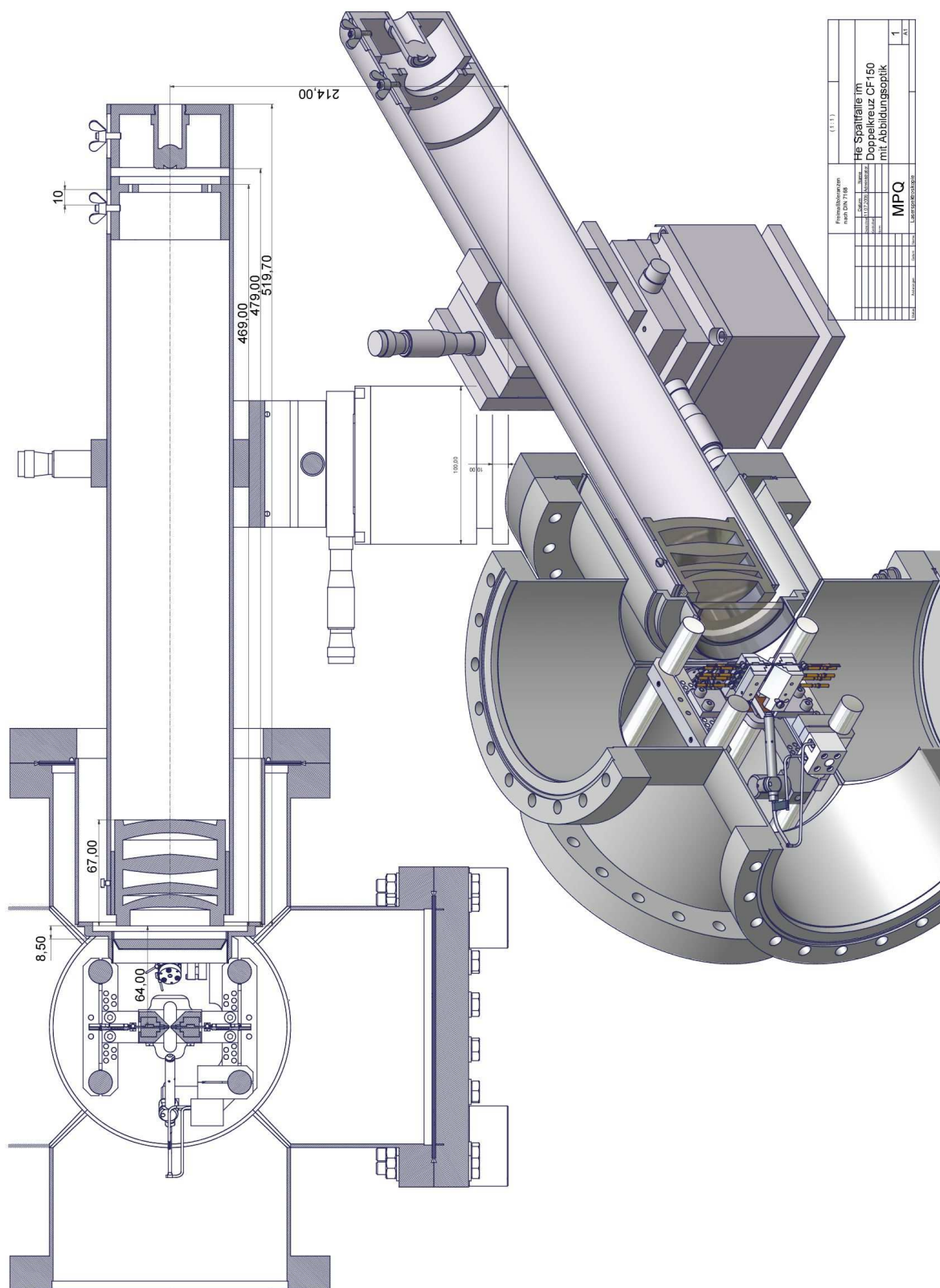
Figure 2.19.: *Overview of the imaging system of the endcap trap. The re-entry window allows to position the imaging tube very close to the trapped ions.*
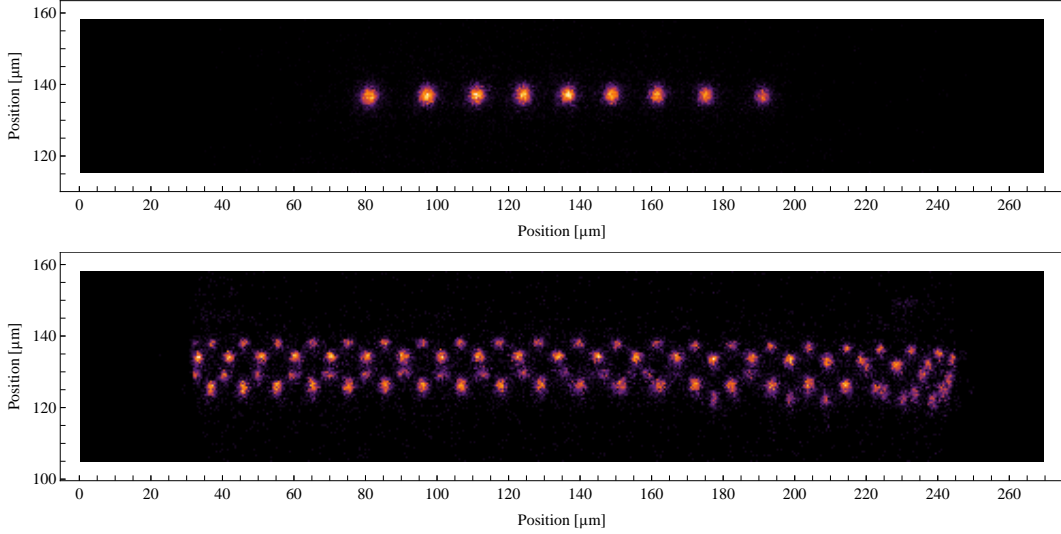
Figure 2.20.: *Images of a chain of nine $^{24}Mg^+$ ions and of a part of a very long ion crystal stored in the endcap trap.*

To calibrate the length scale we loaded two ions and measured both the ion-ion separation $\Delta x'$ in pixels and the center-of-mass frequency ω_s. From the latter the true distance in meters can be calculated and related to $\Delta x'$, thus yielding a conversion factor for pixels to μm. Two ions of charge Q and mass m confined in a trap with secular frequency ω_s are separated by

$$\Delta x = \sqrt[3]{\frac{e^2}{2\pi\varepsilon_0 m\omega_s^2}}. \tag{2.15}$$

For the endcap trap imaging system we measured $1\,\mathrm{px}=0.526\,\mu$m. This implies that the measured magnification of the system is $93\times$, in reasonable agreement with the design goal of $100\times$. We observe ions within a circle of $215\,\mu$m in diameter. The ions observed have a full-width half maximum of about 5 pixels. This corresponds to a resolution of about $2.6\,\mu$m. Two sample images are shown in Fig. 2.20. The condenser covers about $3.8\,\%$ solid angle, the transmission of the UG11 filter is, as above, $64.8\,\%$ and the (specified) quantum efficiency of the single photon camera is $25.5\,\%$. In total, the detection efficiency is about 6.2×10^{-3}. The maximum count rate per Mg$^+$ ion is therefore about $810\,\mathrm{kHz}$. The spectral quantum efficiency is shown in Fig. 2.21.

2.4.4. EMCCD vs SPC

The two camera types used acquire images in a fundamentally different way and thus have characteristic strengths and weaknesses.

A photon striking a pixel of the CCD chip will create an electron with a certain quantum efficiency (28.2% in our case). During the exposure time the photoelectrons accumulate together with electrons generated by thermal noise ($0.01\,\mathrm{e}^-/\mathrm{px}{\cdot}\mathrm{s}$). The image is then read out by subsequently shifting rows of pixels to a shift register where the charge of each pixel is then amplified and digitized. During the shifting process excess electrons can be generated, a noise source called clock-induced charge. When the accumulated charges are converted to

Figure 2.21.: *Quantum Efficiency of the imaging system of the endcap trap. The two dashed lines show the transmission of the Schott UG11 solar blind filter (with two transmission bands) and the quantum efficiency of the single photon camera (flat curve), respectively. The solid line gives the total response, which is 16.5% at 280 nm. Including solid angle (3.8%), 6.2×10^{-3} fluorescent photons are detected.*

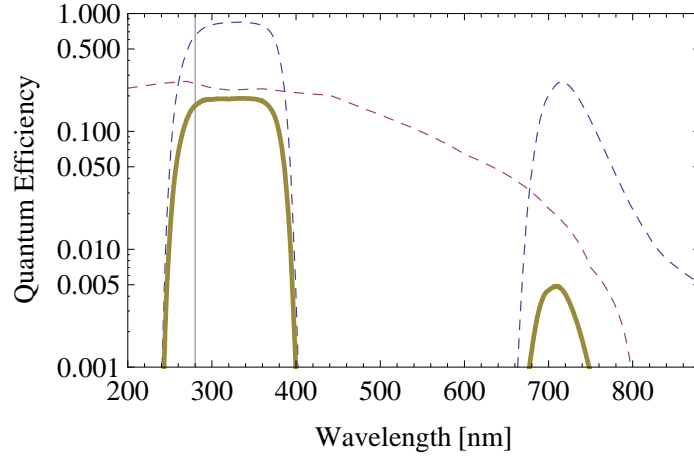a voltage, the on-chip preamplifier adds read noise ($\sim 25\,\mathrm{e}^-$), which is the most important and often dominating noise mechanism. It can be reduced by introducing a gain register, where the photoelectrons are multiplied by shifting them violently with high voltages. By impact ionization an avalanche of electrons is generated, in close analogy to an avalanche photo detector. Since the number of read noise electrons stays constant, it is reduced relatively to below one electron. Such devices are called electron multiplied CCDs (EMCCDs). The operational principle has following experimental implications: A CCD cannot provide accurate timing information. An image is integrated and then read at a frame rate $\ll 1\mathrm{kHz}$. The signal-to-noise ratio is maximized for low frame rates because this minimizes read noise.

The single-photon camera operates entirely different. It has a circular (in our case about 23 mm in diameter) detector surface. A photon that impinges on the surface creates an electron which is subsequently multiplied by a micro channel plate (MCP). The multiplied charge then strikes a resistive surface which leads to a position dependent voltage. The MCP has a dead time that limits the maximum rate of detected photons to about 100 kHz. Further, this causes the detector not to be strictly linear. If a second (or more) photon(s) enters the MCP during its dead time it is not recorded. However, every photon creates a prompt signal with a timing resolution of about 100 ps. The dark-count rate is extremely low, only about 50 Hz over the entire detector surface at room temperature. Cooling can further reduce the dark-count rate to $< 10\,\mathrm{Hz}$. If it is digitized according to the spatial resolution of the position sensitive surface with 512px $\times$ 512px, this corresponds to a dark-count rate of only $2 \times 10^{-4}\,(\mathrm{s{\cdot}px})^{-1}$. This is about a factor 10 lower than the best (EM)CCD cameras. In addition, there is no read noise. The dynamic range is about 40 dB (=100 kHz/10 Hz).

In brief, the single-photon camera offers a better signal to noise ratio at very low light levels, faster (prompt) read out and timing information. On the other hand the dynamic range is limited and its linearity is poor. At moderate to high levels of light and low frame rates, read noise can effectively be neglected and the CCD camera is advantageous if no timing information is necessary. These differences are evident in the dark regions around imaged

ions. The dark regions imaged by the EMCCD camera are noisier than those imaged by the SPC camera, whereas the (bright) ions themselves show comparable (low) noise.

2.5. Laser system

The experiments presented in this thesis are performed with ^{24}Mg$^+$ ions that are laser cooled on the D2 ($3s_{1/2} - 3p_{3/2}$) transition at 279.6 nm. One of the reasons for choosing this ion was the possibility to generate this wavelength with a convenient all-solid state laser system. Recently, Yb fiber lasers have become available that emit 2 W and more at 1120 nm with a specified linewidth below 100 kHz. With two subsequent resonant second harmonic generation stages (SHG, developed by Frank Markert as part of his diploma thesis [35] and published in [36]) we are able to convert up to 10% of the infrared light into the UV. In total, this gives us a turn-key all solid state laser system providing up to a 200 mW of narrow band UV light. This is plentiful: The saturation intensity of the D2 transition is

$$I_s = \frac{2\pi^2 c\hbar\Gamma}{3\lambda^3} = 2480 \, \text{W/m}^2, \tag{2.16}$$

so if the beam is focused to a diameter of $2w_0 = 0.5$ mm less than 0.5 mW saturate the transition.

However, the operating wavelength at 1120 nm is near the long wavelength end of the Yb gain profile and thus technically challenging. Unfortunately we had our share of the bad luck several groups around the world had using similar fiber lasers: Both our fiber lasers (from two different companies) failed and could not be repaired by the manufacturer. We therefore installed a dye laser that serves three purposes. It can replace the fiber laser by generating 560 nm, simply omitting the first SHG stage. Second, without changing the dye it can be tuned to provide light for photoionization: Neutral Mg atoms are ionized by two 285 nm photons, which can be generated by frequency doubling 570 nm. Finally, it can be tuned to excite the D1 transition ($3s_{1/2} - 3p_{1/2}$) at 280 nm which is outside the tuning range of the fiber laser.

2.5.1. The fiber laser

The fiber laser (Koheras Boostik) utilizes Yb as gain medium and emits up to 2 W of single-frequency and single-mode light at 1118.54 nm. The total output power is about 2.2 W due to an additional 200 mW of amplified spontaneous emission (ASE) that gives a broad incoherent background peaked about 50 nm below the signal. The linewidth is specified to be 100 kHz or less. The output fiber is not polarization maintaining, so the output is in general elliptically polarized. A combination of a $\lambda/4$ and $\lambda/2$ wave plate transforms the output to linear polarization. After turning on the laser the polarization changes due to thermal and other effects, but after about one hour it returns to the previous' day polarization state and remains there, given the fiber has not been moved. Due to its sensitivity to back-reflections a 60 dB optical isolator is placed just after the wave plates. The output wavelength can be controlled by changing the temperature or by applying a voltage to a piezo which dilates the oscillator fiber. The piezo has a tuning range of 64 GHz which is sufficient to scan across all Mg$^+$ isotopes: The splitting ^{24}Mg$^+ - \ ^{26}$Mg$^+ \cong 3$ GHz. The tuning sensitivity of the piezo has been measured to be 719 MHz/V.
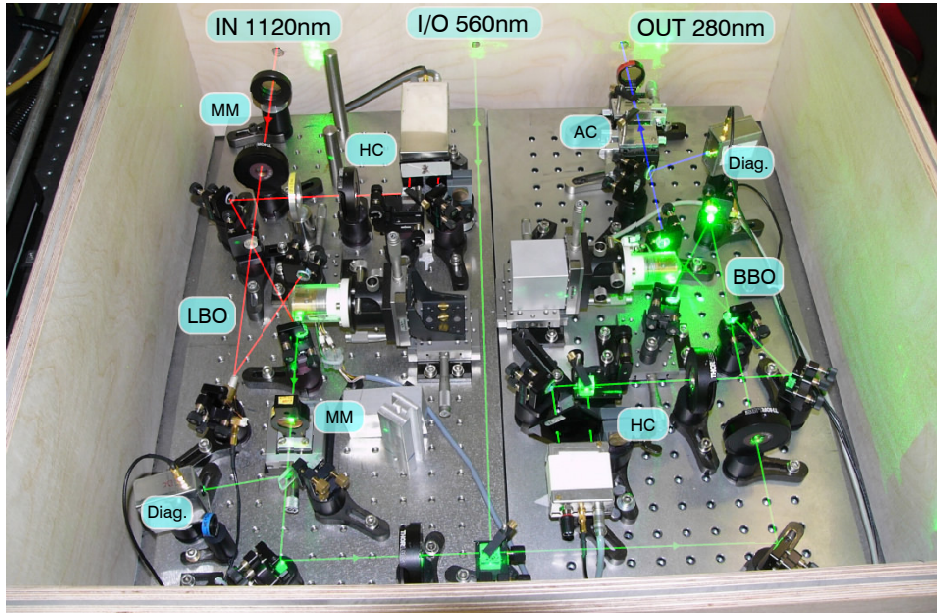
Figure 2.22.: *Image of the two second-harmonic generation cavities used to generate light at 280 nm. If the Yb fiber laser is used the port visible to the left is used as input for 1120 nm which is frequency-doubled resonantly to 560 nm in lithium borate (LBO). If the dye laser is used, the 560 nm are fed in via the port in the middle. A second resonant SHG stage frequency doubles the green light to 280 nm in a β−barium borate crystal (BBO). The 560 nm port is also used as output: If the fiber laser is used and not referenced to the frequency comb, a few milliwatt in the green are sampled and sent to an iodine spectrometer for frequency reference. The mode-matching lenses are labeled* **MM**, *the optics for the Hänsch-Couillaud locks* **HC**, **Diag.** *are photodiodes for intensity monitoring and* **AC** *is the astigmatism compensation of the UV beam.*

2.5.2. The dye laser

Photoionization of neutral magnesium atoms requires light at 285 nm, which cannot be provided by frequency-quadrupling an Yb fiber laser as described above. Also, the D1 $(3s_{1/2} - 3p_{1/2})$ transition at 280 nm is outside the tuning range. For these reasons and as backup system for the fiber laser a dye laser was set up by V. Batteiger and H. A. Schüssler.

The dye laser is a commercial Coherent 699/21, operating on Rhodamine 19 and pumped at 532 nm by a Coherent Verdi V10. For photoionization it is set to 570 nm, for laser cooling/ spectroscopy near 560 nm. The dye recipe we use is[11]: 1 g Rhodamine 19 solved in 250 ml benzyl alcohol and subsequently mixed with 1.75 l of ethylene glycol. The efficiency can be increased significantly by chemically tuning the dye mixture. Adding 8 g potassium hydroxide solved in 80 ml methanol nearly triples the output power at 560 nm. Pumped with 5 W we obtain up to 520 mW at 560 nm, at 7.2 W pump the output is about 1 W. A fresh dye mixture lasts under typical conditions about 8 weeks.

The free-running linewidth is rather large. A measurement of a beat note with a fiber laser yielded a full-width half maximum of 3.6 MHz.
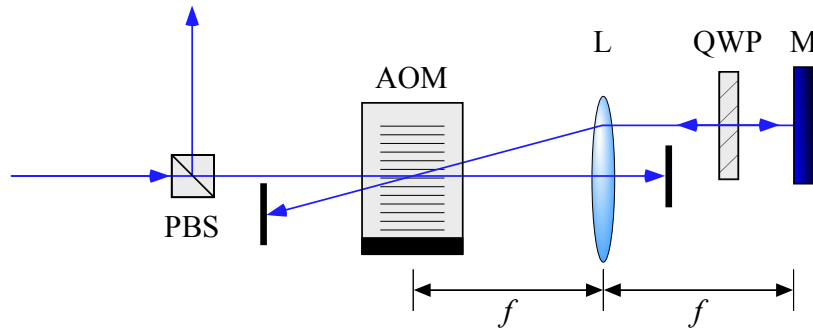
Figure 2.23.: *Schematic of a double-pass acousto-optic modulator. The linearly polarized input beam is partially deflected by the AOM. The first order beam is selected with an aperture and sent to a retro-reflector. A lens **L** placed one focal length f away from the AOM translates angular variations into parallel displacements, so that the reflected beam enters the AOM at the same angle as the original beam. The mirror **M** is also placed one focal length away from the lens, so it forms a telescope with magnification 1 and the beam stays collimated. To separate the input beam from the two times deflected beam a quarter wave plate is placed between the AOM and the mirror. After two passes it rotates the linear polarization by 90°, so the polarizing beam splitter (PBS) reflects only the desired light.*

2.5.3. The SHG stages

Both SHG stages are bow-tie cavities stabilized using the Hänsch-Couillaud method [37]. The first SHG stage utilizes a 15 mm long lithium borate (LBO) crystal as nonlinear medium and is phase-matched non-critically by heating it to $T \sim 86.5\,°\mathrm{C}$. Up to 900 mW at 560 nm are obtained. Thanks to temperature phase matching the output beam is nearly Gaussian, so no beam shaping is necessary. A biconvex lens focuses the light into the second cavity. In addition, a $\lambda/2$ wave plate together with a polarizing beam splitter allows to sample a variable amount of light for diagnostics and frequency stabilization. Alternatively, if the dye laser is used, this serves as a "port" to feed the green light into the system.

In the second stage, a 10 mm long β-barium borate (BBO) crystal converts the light into the UV near 280 nm. Phase matching is obtained critically, that is, by angle tuning. Up to 200 mW of UV light are generated. However, the output is strongly astigmatic and shows interference fringes. A telescope of two cylindrical lenses is used to obtain a symmetric beam profile, which is additionally filtered spatially by a 100 μm pinhole. Typical day-to-day power levels measured after the pinhole are between 10 mW and 20 mW. The setup is shown in Fig. 2.22.

The SHG stages worked very reliably. Once locked the system required no further attention, cleaning and alignment was necessary every 2-4 days only.

2.5.4. Double pass acousto-optic modulators

The experiments presented in the following chapters require two laser beams with independently controllable and stable intensities and frequencies. This is achieved using acousto-optic modulators (AOM). In these devices the incident light beam is diffracted by an acoustical wave in a crystal. The frequency of the first-order diffracted beam is shifted exactly by the acoustic frequency $\pm\nu_{\mathrm{aom}}$. In addition it is deflected by an angle that depends on ν_{aom}. To

---

[11]Courtesy of T. Schätz
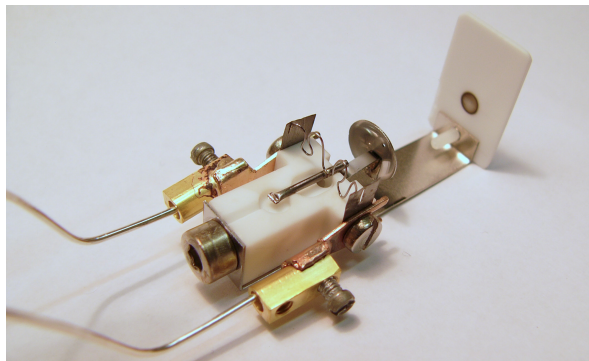
Figure 2.24.: *The atomic oven used in both the 6rod trap and the endcap trap experiments. The image shows a test set-up with a ceramic "target" attached to the oven in the same distance as the trap center will be. The tantalum tube is held in place by the heating wire which acts like a spring and pushes the tube into a milled guiding structure.*

compensate the angular deviations of the deflected beam and increase the scanning range, the AOMs were used in a double-pass (DP) configuration. A schematic of a DP-AOM is shown in Fig. 2.23.

Specifically, we used Brimrose QZF-150-100 shifters with a center frequency of 150 MHz and a specified tuning range of about 100 MHz. With 2 W of RF drive power a single pass diffraction efficiency of up to 70 % is achieved. Due to the rotation of the polarization the second pass is less efficient. In the double-pass configuration the total efficiency was up to 30 % but varied strongly as function of drive frequency. The usable frequency range was slightly below specification between 100 and 190 MHz, so in total the beam could be scanned across 180 MHz.

The DP-AOMs simultaneously served as "noise eaters", i.e. for intensity stabilization. For this purpose a $\lambda/2$ retarder and a polarization beam splitter was installed in the output beam path that allow to sample a variable amount of light which is directed onto a photodiode. This provides an error signal for feedback on the RF drive power.

The retro-reflector of the DP-AOM ensured good beam pointing stability. A CCD beam profiler located 3 m away from a DP-AOM could not detect any shifts of the center-of-gravity of the deflected beam. However, the beam profile was found to change slightly as the frequency of the beam is scanned. This turned out to be an important systematic uncertainty for the spectroscopy experiments described in the following chapter: Ions sample the intensity only at one point within the profile, so that even though the integrated intensity is stabilized, the ion will be subject to a systematically varying intensity as the frequency of the DP-AOM is scanned. This effect is removed by spatially filtering the output of the DP-AOM with a pinhole and sampling light for stabilization after it.

2.6. Ion creation

2.6.1. Atomic oven

Magnesium ions are loaded by directing an atomic beam at the trap center and ionizing the atoms within the trapping volume. The atomic beam is created by an oven which basically consists of a 1 mm diameter tantalum tube which is heated by running a current through
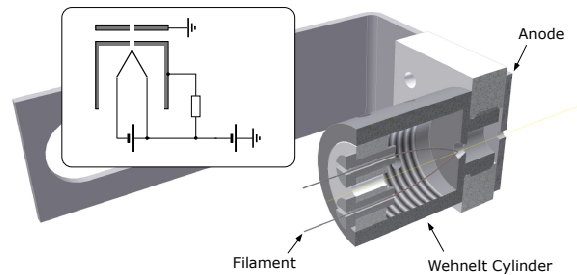
Figure 2.25.: *Cut-away view of the electron gun used in both the 6rod trap and the endcap trap experiments. The inset shows how the filament and Wehnelt cylinder are connected to the power supplies.*

a single winding of tantalum wire that is spot welded to it. The tube is held by a small Macor block milled in a way that it touches the tube only in two points, see Fig. 2.24. This improves the mechanical stability, facilitates aiming and minimizes thermal contact. A small 0.1 mm aperture collimates the beam, so that geometrically its diameter at the trap center is smaller than the electrode separation. Together with careful aiming this prevents coating the electrodes with Mg and the associated patch potentials. The oven is loaded with a 1 mm diameter Mg wire of natural isotopic composition. Prior to loading, the wire is cleaned and treated with citric acid, which replaces the magnesium oxide layer with a magnesium citrate layer. This prevents the wire to burst upon heating, an otherwise common problem: The MgO layer has a much higher boiling point than pure Mg. It therefore may happen that the inside of the wire melts while being held together by the still solid MgO. At some point the MgO layer will tear and the entire contents of the oven spills into the trap. Magnesium citrate has a *lower* boiling point than Mg, so this cannot happen anymore.

2.6.2. Electron gun

Electron impact ionization is a very simple and wide spread way of producing ions. As long as the electron energy exceeds the ionization energy any neutral species can be ionized. This is advantageous for systems where no lasers for photoionization are available, e.g. He. At the same time, this lack of selectivity is a great drawback, because the trap will be "polluted" with undesired species after loading. Further important disadvantages are the charging of insulated surfaces and the low efficiency. For these reasons the use of the electron gun was avoided whenever possible.

The design used in both traps is shown in Fig. 2.25. A 0.25 mm diameter thoriated tungsten wire (thorium reduces the brittleness of tungsten) is bent to form a tip and heated by running 1.4 A of current through it so it serves as thermal source of electrons. A potential difference of about 200 V between the filament and the cathode attracts and accelerates the emitted electrons.

2.6.3. Photoionization

Photoionization is very efficient, isotope selective and avoids the build-up of excess charges. Neutral magnesium atoms can be ionized in two steps: First, light at 285.2127 nm excites a transition from the ground state to the $3p_{3/2}$ state (linewidth $\Gamma = 2\pi \times 78.1$ MHz). In a
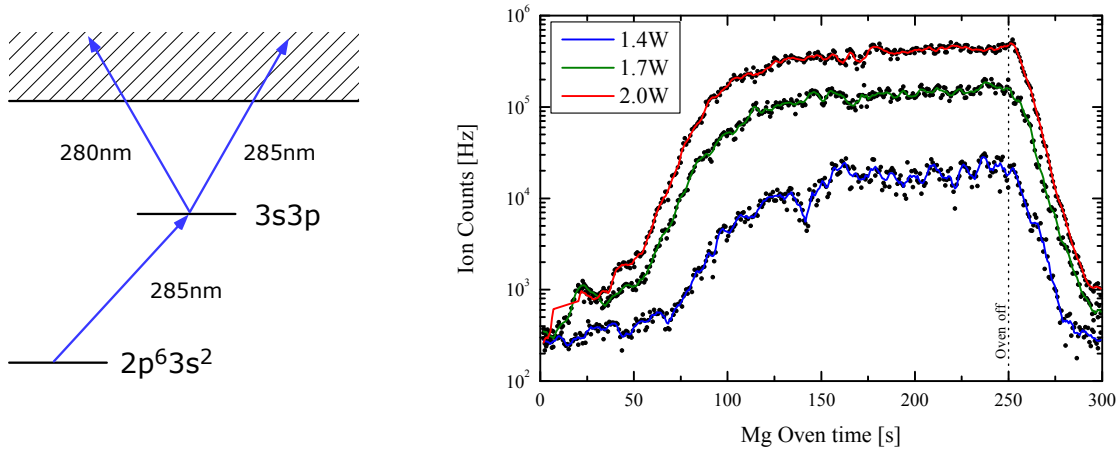
Figure 2.26.: *Energy levels of neutral magnesium relevant to our photoionization scheme (left image). The right plot shows the ion production rate using photoionization as a function of heating time of the oven for different heating powers.*

second step, a further 285 nm photon or a 280 nm photon from the cooling light reaches into the continuum. The saturation intensity for the first step is $4402\,\mathrm{W/m^2}$, which corresponds to 0.9 mW if the ionization beam is weakly focused to a diameter of 0.5 mm. The light at 285 nm is generated by frequency doubling the output of a dye laser operating at 570 nm. For second harmonic generation a copy of the 280 nm cavity was used (see section 2.5). Although it is used 10 nm off the design wavelength, the efficiency was sufficient for this purpose. With 200 mW input power about 1 mW at 285 nm is obtained. For loading the photoionization light is spatially overlapped with the cooling light at 280 nm and directed at the trap center. To quantify the loading process we measured the number of generated ions with a channeltron for different heating powers of the atomic oven. The result is shown in Fig. 2.26. The atomic oven takes about one and a half minutes to reach its equilibrium temperature and about one minute to cool down. Depending on the heating power up to a million ions are generated per second. In both the 6-rod and the endcap trap the neutral atom beam is not orthogonal to the photoionization laser. Therefore Doppler broadening causes the resonances of the stable isotopes to overlap that are otherwise well separated: The natural linewidth of less than 80 MHz is much smaller than the isotope splitting of about 1.5 GHz. However, the loading procedure is still partially isotope selective. By detuning the laser far below or above resonance predominantly $^{24}\mathrm{Mg^+}$ or $^{26}\mathrm{Mg^+}$ ions can be loaded. Chains of $^{25}\mathrm{Mg^+}$ can be loaded by subsequent purification using secular excitation, see Section 4.3.

3. Frequency metrology in the weak-binding limit: The Mg$^+$ D2 line

This chapter reports on a new spectroscopy method that allows to measure transitions in single trapped ions in the weak-binding limit with unprecedented accuracy. This regime is virtually unexplored for precision spectroscopy, so the technique, which is based on sympathetic cooling of a linear chain of ions and spatially resolved detection, may find numerous applications. Both a theory and experimental results are presented. As a demonstration we measured the absolute frequency of the astrophysically relevant $3s_{1/2} - 3p_{3/2}$ transition in single ^{24}Mg$^+$ ions.

3.1. Motivation

Ion traps are well known for having enabled the most precise spectroscopic measurements ever made. Recently, the NIST group [3] has performed a frequency comparison of the clock transition of a single aluminum ion with an accuracy of a few parts in 10^{17}, which is by far the most precise number ever obtained from an experiment. The tremendous accuracies achieved have several origins, notably the following:

TRAPS: RF traps enable long interaction times and provide excellent isolation from external perturbations. The operational principle implies that a single ion is trapped in a node of the confining field. Especially if laser-cooled it is well localized in an essentially field-free region. Further, ultra-high vacuum systems with pressures below 10^{-10} mbar have become standard so collisional or pressure shifts can be neglected.

TRANSITIONS: In addition to the already low level of external perturbations special transitions have been chosen that have both high quality factors and are particularly insensitive to the residual perturbations. Probed by well stabilized lasers this allows to observe extremely sharp resonances.

STRONG BINDING: The transitions were probed in the strong-binding limit where the secular frequency of the trapped ion is significantly larger than the transition linewidth. In this regime the absorption spectrum consists of a carrier with a number of motional sidebands of natural linewidth which are separated by the secular frequency (see Fig. 3.1). Choosing the carrier for spectroscopy decouples the interaction of the laser with the motional state and thus eliminates first order Doppler and recoil shifts. To illustrate how pivotal the strong-binding condition is, consider the aforementioned absolute frequency measurement on a single Al$^+$ ion. Neglecting other but statistical sources of error the line center of a transition can be determined with an uncertainty given by the transition linewidth divided by the signal-to-noise ratio of the data $\Delta\omega_0 \cong \Gamma/\text{SNR}$, provided the line profile is well understood. The observed linewidth was about 10 Hz and the transition frequency was determined to within 1 Hz. If the strong-binding condition could not have been achieved, the ion's temperature of about 2 mK would have led to a Doppler-broadened linewidth of 5 MHz, 5 order of magnitude
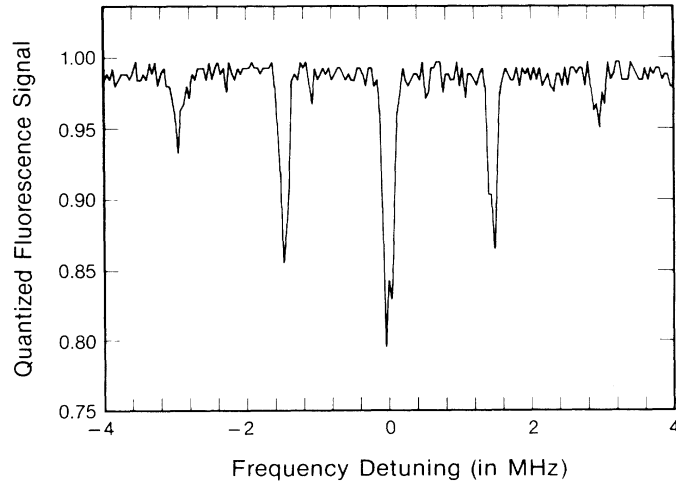
Figure 3.1.: *Absorption spectrum of a strongly bound single mercury ion cooled to 5.8 mK (taken from [38]). The linewidth of the individual components is limited by the linewidth of the "clock" laser to 160 kHz. The amplitudes of the sidebands lie under an envelope given by Doppler broadening ($\sim$4 MHz).*

larger than the actually observed width. Even worse, as will be detailed in the following sections, if no further measures are taken, the line shape is not Lorentzian anymore.

For strong dipole transitions it is very hard if not impossible to reach the strong-binding limit: Typical linewidths are larger than 20 MHz whereas practical secular frequencies are usually smaller than 5 MHz. In this regime, called weak-binding limit, a spectroscopy laser probing the resonance always drives transitions between electronic and motional states simultaneously. For many applications, such as Doppler cooling, this of course desirable. Aiming at precision spectroscopy though, this leads to a detuning dependent temperature and thus to an asymmetric, distorted line shape which limits the accuracy the line center or -width can be determined with. An example of a resonance recorded in the weak-binding limit is shown in Fig. 3.5, calculated spectra in Fig. 3.4.

Can one do better? How accurately can a transition in the weak-binding limit be measured? These questions are the starting point for the ideas and experiments presented in this chapter. The main result is a new spectroscopy method based on continuous sympathetic cooling of a chain of ions and spatially resolved detection. It allows to observe well understood line profiles with high signal-to-noise ratio, which we demonstrated on an astrophysically relevant transition in single Mg$^+$ ions. This measurement, which is the first absolute frequency measurement on a single ion in the weak-binding limit, yields a line center nearly 400 times more accurate than previous results. The pristine line shape further allowed us to determine the lifetime of the excited state in agreement with, but twice as accurate as previous values including beam-foil and Hanle-type measurements.

Why should one care about strong transitions? The following two sections discuss two fields where strong dipole transitions are of fundamental interest: The first is *astrophysics* where often metallic (i.e. heavier than helium) spectra of faint, distant objects are studied, e.g. for searches of possible drifts of fundamental constants. Only strong transitions show up in the weak stream of photons with good signal-to-noise ratio. The presented method

allows to provide accurate laboratory reference data for comparison. A second field is *nuclear physics*. Here, the study of exotic, i.e. either very neutron-rich or -deficient nuclei attracts considerable interest. One way of studying exotic nuclei is to measure isotope shifts relative to stable, well characterized isotopes very accurately. However, far off the valley of stability ions become rare and their lifetimes short. Strong dipole transitions allow to scatter many photons in a short time and thus allow to obtain a detectable signal from a very small number of ions quickly. These types of measurements have demanding requirements on the accuracy to be meaningful for studies of nuclear structure which could so far not be met [39]. The presented method is the first that has demonstrated the required accuracy.

Astrophysics: The many multiplet method

For decades theorists have been investing great efforts into finding a unified description of nature which includes all four fundamental forces. However, so far most of the candidates for such grand unified theories have limited predictive power, if any, and are therefore hard to challenge (falsify!) by an experiment. A notable exception is that most candidates allow or even require fundamental constants to vary with space and time, an idea that goes back to P. A. M. Dirac. Currently, several approaches are used to detect possible variations of fundamental constants, which all focus on the fine-structure constant α, since it is dimensionless and scales the best understood and tested of the basic field theories, quantum electrodynamics. One approach is laboratory based and relies on extremely precise laser spectroscopy of certain transitions, repeated on a time scale of years. Another approach is based on measuring transition energies in absorption spectra of intergalactic clouds that are (back-) illuminated by quasars (QSO, quasi stellar objects). The measured values are then compared to accurate laboratory reference data. The line shifts allow to determine changes of the fine-structure constant α as a function of the age of the cloud. Although the spectroscopic accuracy is far lower than in the laboratory based approach, here much longer timescales are considered so that the resulting sensitivity to variations is comparable (assuming a linear drift). While the laboratory based approach rules out present day variations of α on the level of 10^{-17}/year [40], astronomical observations indicate a variation of α in the early universe with a statistical significance of 5σ. This famous result by Webb et al. [41] is shown in Fig. 3.2.

Theorists have calculated the sensitivity of the transition energies of a great number of atomic and ionic species to variations of α. For example, the result for the $^{24}\mathrm{Mg}^+$ D1 and D2 transition reads in units of wavenumbers [43] (α_0 denotes the present day value):

$$\omega(3s_{1/2} - 3p_{1/2}) \quad = \quad 35\,669.298(2) + 119.6\left[\left(\frac{\alpha}{\alpha_0}\right)^2 - 1\right] \tag{3.1}$$

$$\omega(3s_{1/2} - 3p_{3/2}) \quad = \quad 35\,760.848(2) + 211.2\left[\left(\frac{\alpha}{\alpha_0}\right)^2 - 1\right]. \tag{3.2}$$

Depending on the particular transition the shift can have either sign. Further, the magnitude of the shift varies strongly and is larger for heavy (large Z) species. Due to the comparatively low sensitivity of the magnesium transitions (transitions in iron and chromium ions have a roughly 10 times larger sensitivity) they are called "anchor lines". Since the line center will also be shifted by the distance dependent red-shift z, the transition energy itself is not suitable to determine a variation of α. To discriminate between the two effects, the fine-structure splitting, which is proportional to $\propto \alpha^2$, is considered. The sensitivity and robustness is
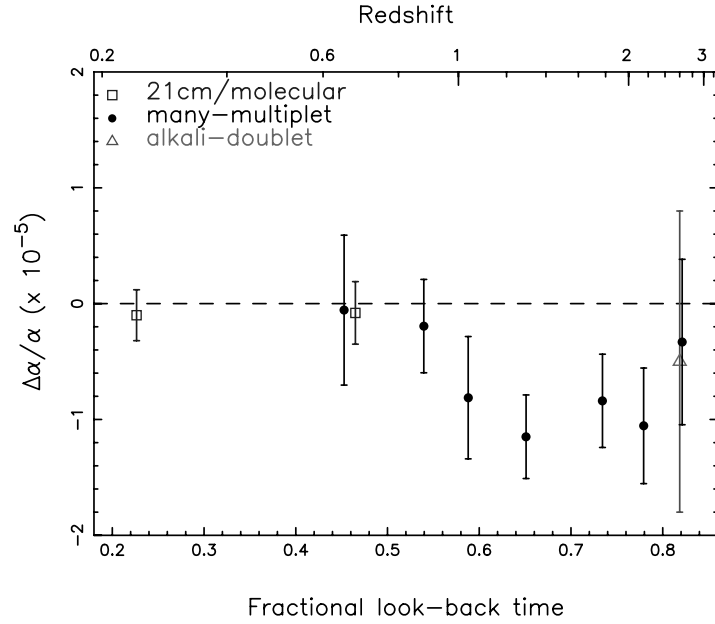
Figure 3.2.: *Relative deviation of the fine-structure constant from the present day value as function of the look-back time (0 corresponds to present day, 1 to the big bang; taken from [41]). The deviation of α in the early universe has a statistical significance of 4.7 σ [42].*

further enhanced by measuring not only one fine-structure doublet in one species but rather by considering a whole range of transitions in different atomic and ionic species relative to each other. The method is thus called "many multiplet method" [43] and naturally creates a demand for accurate laboratory reference data. Berengut et al. have compiled a wish list [44] for this purpose which also includes the Mg transitions measured as demonstration of our new method. Most transitions included in the wish list are strong dipole UV transitions in ions.

What level of accuracy do laboratory reference data have to achieve for this purpose? The data used for the evaluation of Fig. 3.2 was taken with the Keck 10 m telescope on Hawaii. The collected light was analyzed using the HIRES Echelle spectrometer with a resolution set to 43'000. The wavelength scale is calibrated by lines emitted from a Th-Ar hollow cathode lamp, which gives an accuracy of the wavelength calibration of about 0.002 cm^{-1} (= 60 MHz), limited mainly by the uncertainty of the reference lines in the Th-Ar atlas. High quality reference data should therefore at least exceed an accuracy of 60 MHz but the requirements might soon be more demanding: Currently, the application of frequency combs for the on-line calibration of spectrometers is being studied. Their dense grid of equidistant modes of known absolute frequency promises calibration uncertainties on the level of one part in 10^{10}. First experiments in this direction were quite promising [45].

Several possible causes of systematic errors have been discussed that could mimic a deviation of α. Among them the question of isotopic abundances is particularly important [46]. Depending on the age and the origin of the absorbing cloud the isotopic composition may be quite different from the one found on earth. Since the observed lines are not isotopically resolved, variations in the abundances can shift the observed, composite line. For this reason it is important to provide isotopically resolved reference data so that this effect can be modeled.
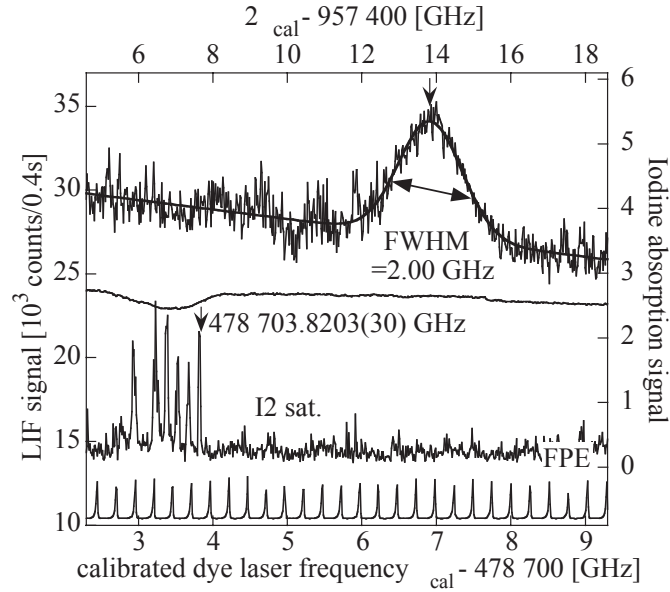
Figure 3.3.: *Measurement of the $2s_{1/2} - 2p_{3/2}$ transition in unstable $^{10}Be^+$ ions (taken from [47], natural linewidth 18 MHz, lifetime against β^- decay 1.5×10^6 years). The experiment was performed at the radioactive ion beam facility RIKEN, Japan. Ions from the accelerator were first slowed in a degrader and then trapped and buffer gas cooled with He in a cryogenic RF trap operating at 50 K. The linewidth of 2 GHz corresponds to a temperature of 84 K.*

Nuclear physics: Halo nuclei

Far off the valley of stability sometimes an unexpected and very interesting phenomenon can be observed in nuclei: Scattering experiments reveal an unusually large nuclear radius which deviates significantly from a simple drop model that predicts $r \sim r_0 \sqrt[3]{A}$. This is attributed to the formation of a proton or neutron "halo", i.e. a core with loosely bound protons or neutrons orbiting around it in a large distance. The halo can be formed from either one, two or four nucleons. Typical lifetimes are on the order of ms reaching up to nearly 14 s for ^{11}Be. An incomplete collection of examples for neutron halos reads: One neutron: ^{11}Be, lifetime 13.8 s and ^{19}C, 45 ms. Two neutrons (so-called "Borromean halos"): ^{6}He (806.7 ms), ^{11}Li (8.59 ms), ^{17}B (5.08 ms), ^{19}B (2.92 ms) and ^{22}C (6.1 ms). Four neutron halos are found in ^{8}He (119.1 ms) and ^{14}Be (4.35 ms). One approach to study these exotic objects is by precision laser spectroscopy. A measurement of the isotope shifts between stable and well characterized isotopes and a halo nucleus can together with extensive theoretical calculations provide valuable insight into its structure. However, this approach imposes demanding requirements on the spectroscopic accuracy. In the case of an envisioned experiment on trapped ^{11}Be$^+$ ions [39] it has been pointed out that the $2s_{1/2} - 2p_{1/2}$ dipole transition needs to be measured to within better than 200 kHz in order to obtain, quote, "meaningful values of the charge radius", which corresponds to an accuracy better than 1 % of the linewidth. So far, the experiments are orders of magnitude off this goal, see Fig. 3.3.

3.2. A new spectroscopy method for weakly bound ions

The basic challenge that needs to be addressed is the temperature variation of the ion as the spectroscopy laser is scanned across the transition, which leads to an asymmetric, distorted line shape: An ion in a thermal state characterized by a Maxwellian distribution of energies scatters photons according to a Voigt profile (resonance ω_0, detuning $\Delta\omega = \omega - \omega_0$)

$$V(\Gamma_L, \Gamma_G, \Delta\omega) = (L(\Gamma_L) * G(\Gamma_G))(\Delta\omega) \tag{3.3}$$

which is the convolution of the atomic Lorentzian (unity area, FWHM Γ_L, saturation parameter s)

$$L(\Gamma_L, \Delta\omega) = \frac{s}{2(1 + s + (\frac{2\Delta\omega}{\Gamma_L})^2)}, \tag{3.4}$$

and a Gaussian (unity area, FWHM Γ_G) due to Doppler broadening:

$$G(\Gamma_G, \Delta\omega) = \sqrt{\frac{4\ln 2}{\pi\Gamma_G^2}} \exp\left[-4\ln 2 \left(\frac{\Delta\omega}{\Gamma_G}\right)^2\right]. \tag{3.5}$$

If the spectroscopy laser is scanned adiabatically across the transition the temperature will vary as a function of detuning according to Eq. 1.16

$$T(\Delta\omega) = \frac{\hbar\Gamma_L}{8k_b}(1+\xi)\left((1+s)\frac{\Gamma_L}{2\Delta\omega} + \frac{2\Delta\omega}{\Gamma_L}\right), \tag{3.6}$$

so the amount of Doppler broadening and thus the width of the Gaussian Γ_G will vary, too:

$$\Gamma_G(T(\Delta\omega)) = \frac{\omega_0}{c}\sqrt{\frac{8\ln 2\, k_b T(\Delta\omega)}{m}}. \tag{3.7}$$

The resulting profile is not a Voigt profile anymore. Temperature profiles and the resulting line shapes calculated for magnesium and indium are shown in Fig. 3.4, a measurement in Fig. 3.5. The lines are not only asymmetric, but the exact shape depends on the particular species and the experimental conditions. The calculated line profile assumes no heating other than the heating due to spontaneous emission. In a real trap the trapping fields as well as the background pressure will lead to a heating rate that shifts the peak of the resonance to lower frequencies in a not well defined manner. Such resonances do not allow to determine the line center to within a small fraction of the linewidth and do not allow accurate measurements of the linewidth. The method presented in this section ensures a fairly constant temperature profile and allows to observe virtually unperturbed Voigt profiles with high signal-to-noise ratio.

This section is organized as follows: First, the principles of the new spectroscopy method and a simplified theoretical model are presented. Then, by comparison to molecular dynamics simulations the validity of this "toy model" is discussed. To assess the usefulness of the new approach for high precision spectroscopy systematic uncertainties inherent to the method are calculated which turn out to be exceedingly small. Finally, the new method is compared to established techniques.
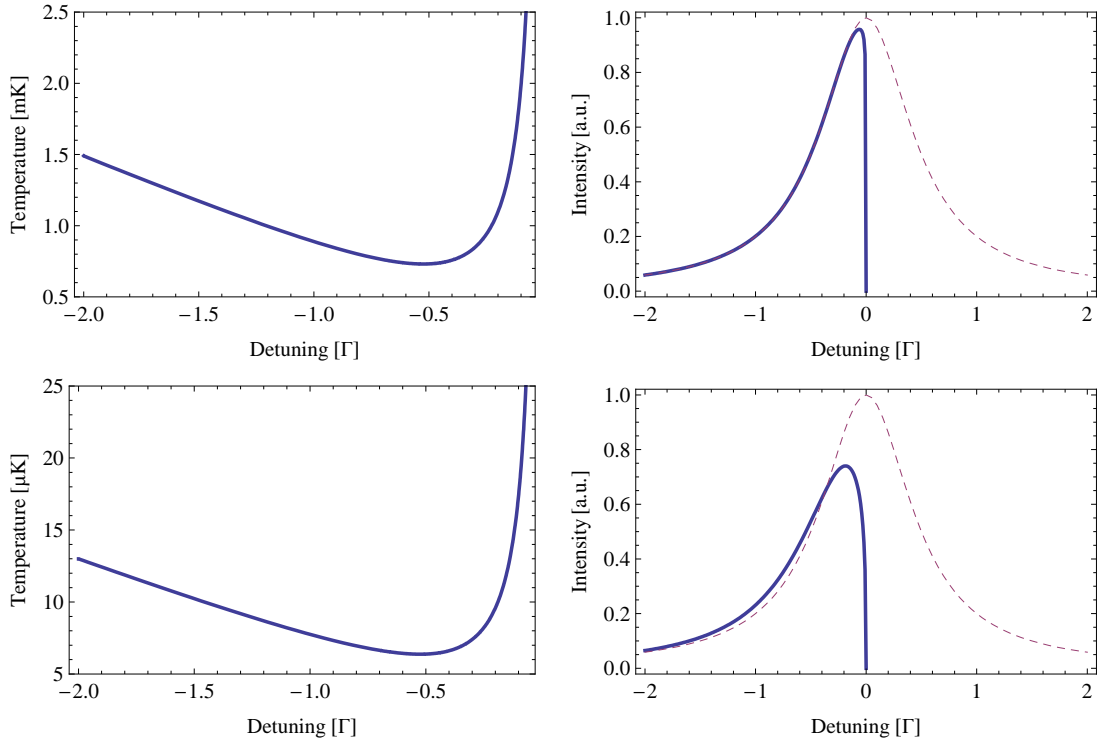
Figure 3.4.: *Calculated temperature and line shape of a $^{24}Mg^+$ and an $^{115}In^+$ ion if only one laser is scanned across their respective cooling transition from low to high frequencies. The dashed line indicates the natural Lorentzian. The upper two panels show magnesium, the lower two indium. The asymmetry of the line due to cooling and heating is clearly visible and, note, different for both ions. The peak of the observed resonance does not correspond to the true line center. The maximum of the calculated magnesium line is shifted about 6.5% of the natural linewidth to lower frequencies ($-2.7\,MHz$).*
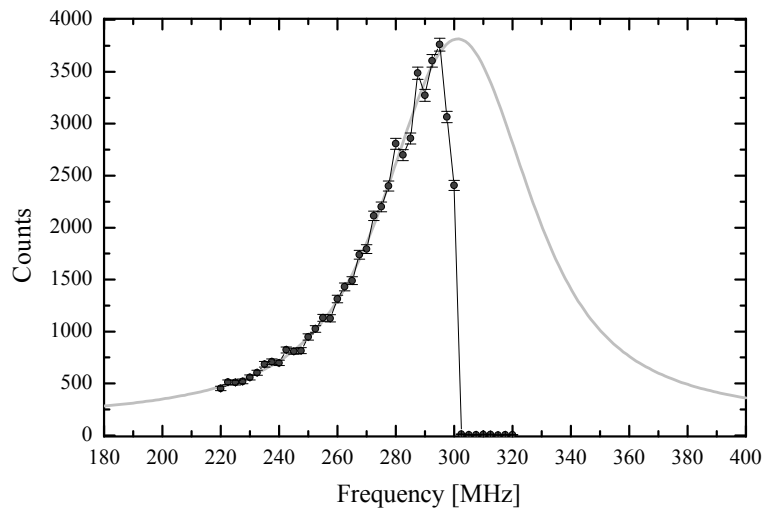
Figure 3.5.: *Fluorescence spectrum of a single, essentially uncooled $^{24}Mg^+$ ion obtained by scanning the spectroscopy laser across the resonance from low to high frequencies, see also Fig. 3.4. A 1000times weaker cooling beam was superimposed so that the ion would not be lost during the scan time of 2 min. The solid line is a Voigt fit to the first 31 data points (reduced $\chi^2 = 3.5$) and returns a line center 3.2 MHz below the true resonance with a statistical uncertainty of 5.3 MHz. The observed fluorescence peak is 9.4 MHz below the true line center. The calculations shown in Fig. 3.4 predict the maximum 2.7 MHz below the resonance which illustrates the sensitivity of this approach to the experimental conditions.*
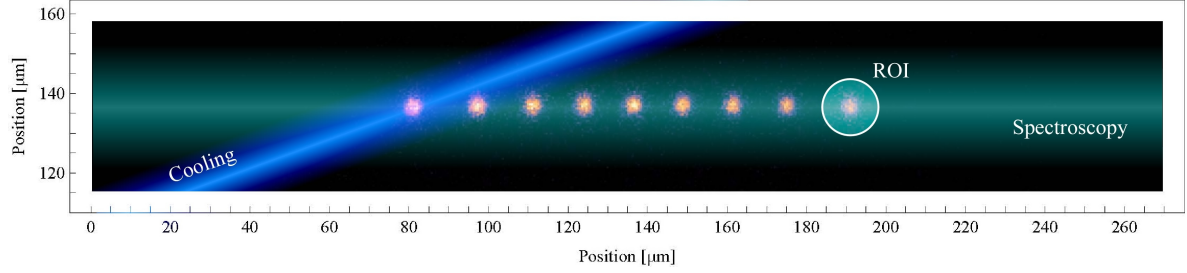
Figure 3.6.: *Schematic of the cooling and spectroscopy beam interacting with a chain of ions.*

3.2.1. Basic idea

The basic idea is to prepare a crystallized chain of ions stored in a linear radio frequency (RF) trap which is continuously laser cooled on one side only (see Fig. 3.6). Ions at the other end of the chain are sympathetically cooled but do not scatter photons from the cooling laser. A spectroscopy beam less intense than the cooling beam is then directed collinearly at the ion chain and an imaging photo detector records only photons from the sympathetically cooled ions. In this way temperature variations that lead to line shape distortions are strongly suppressed and adverse effects from the cooling laser (background, ac Stark shift) are eliminated, too. Directing the spectroscopy beam axially at the ion chain has two advantages: First, a larger number of ions is addressed, thus enhancing the signal-to-noise ratio. Second, the spectroscopy is insensitive to possible micromotion from the radial directions.

3.2.2. Two ions

To quantify how well this approach can suppress detuning-dependent temperature variations, let us first consider the simplified case of a crystallized pair of two ions. One ion is assumed to be cooled while spectroscopy is performed on the other. The motion of the ions can be described as a linear combination of its two eigenmodes, the center-of-mass and breathing mode. Since the motional sidebands are not resolved, the cooling laser will cool both modes simultaneously. For these conditions we calculate the equilibrium temperature in analogy to the derivation of the Doppler limit in Section 1.2. The (secular) cycle-averaged cooling or heating power $\langle P_l \rangle$ due to the interaction with one of the two laser beams, enumerated by i, reads [14]

$$\langle P_l^i \rangle = \langle \hbar k \, g(s_i, \Delta_i - k v_0 \cos(\omega_s t)) \, v_0 \cos(\omega_s t) \rangle. \tag{3.8}$$

Here, $\hbar$ denotes Planck's constant, k the wave vector, and g the scattering rate due to the natural Lorentzian line shape $g(s, \Delta) = \Gamma L(\Gamma, \Delta)$. Spontaneous emission heats the motion on average by

$$\langle P_h^i \rangle = \langle (1 + \xi) \frac{\hbar^2 k^2}{2m} g(s_i, \Delta_i - k v_0 \cos(\omega_s t)) \rangle, \tag{3.9}$$

where m is the ion's mass and $\xi = 2/5$ for non-isotropic dipole radiation. Since in both modes the ions move with the same velocity modulus at any instant of time we can solve the steady state condition $\sum_i (\langle P_l^i \rangle + \langle P_h^i \rangle) = 0$ for v_0 to obtain the ion's temperature $T = m \langle v^2 \rangle / 2k_b$, where $\langle v^2 \rangle = \frac{1}{2} v_0^2$ for a harmonic oscillation.
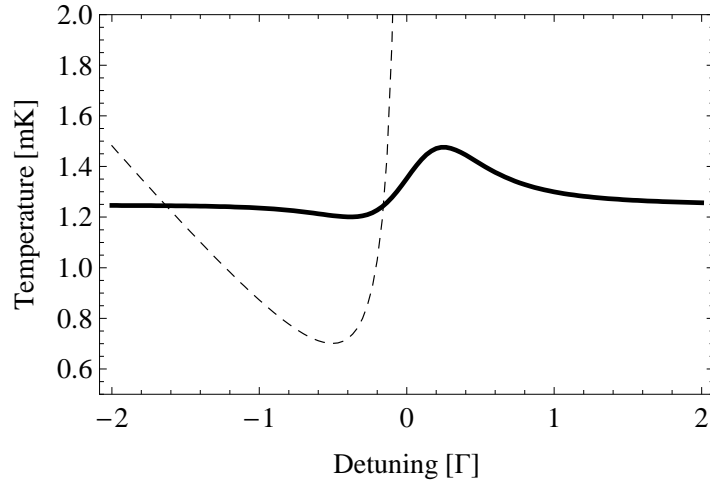
Figure 3.7.: *Calculated temperature profile of a "chain" of two Mg$^+$ ions (full line). The cooling laser is detuned to $\Delta = -2\pi\, 64\,MHz$, the saturation parameters are $s = 0.5$ and $s = 0.004$, respectively. The dashed line shows for comparison the temperature profile of the spectroscopy ion if the cooling laser is turned off.*

The result of such a calculation with parameters typical for the experimental demonstration presented in the next section is shown in Fig. 3.7. Temperature variations turn out to be suppressed remarkably well: The Doppler limit due to the cooling laser is 1.25 mK and the maximum temperature variation for a spectroscopy laser 125 times weaker than the cooling beam is 0.3 mK.

3.2.3. Long ion chains

This treatment of the cooling dynamics is straightforwardly generalized to strings of N ions by considering the chain mode by mode. An important difference is that the cooling laser will not cool all modes equally efficient if it interacts with a limited number of ions as illustrated in Fig. 3.8. For example, in an odd-numbered string of ions the stretch mode is not cooled at all if the cooling laser is focused on the center ion only because it does not oscillate and hence couple to the laser. An analysis of the normal modes shows that it is in general favorable to cool a group of ions at one end of the chain and perform spectroscopy on ions that lie symmetrically at the other end of the chain (Fig. 3.10). For such a configuration molecular dynamics simulations by Th. Udem including all forces (trapping fields, mutual Coulomb interaction, spontaneous emission) show that long ion chains are very well approximated by chains of two ions as described above if the saturation parameters are chosen such that the overall ratio of cooling to heating remains the same, see Fig. 3.9. In other words the ion chain makes essentially the entire cooling power available to the sympathetically cooled ions (Fig. 3.10). In what follows this is called "two-ion approximation". Note, that this discussion of the cooling dynamics equally applies to heterogeneous ion chains. If different ion species are present in the chain, this will change the eigenmodes and -frequencies. However, since the motional sidebands are not resolved they are still all cooled simultaneously by the cooling laser. Of course, similar limitations concerning the mode structure as in the homogenous case apply.
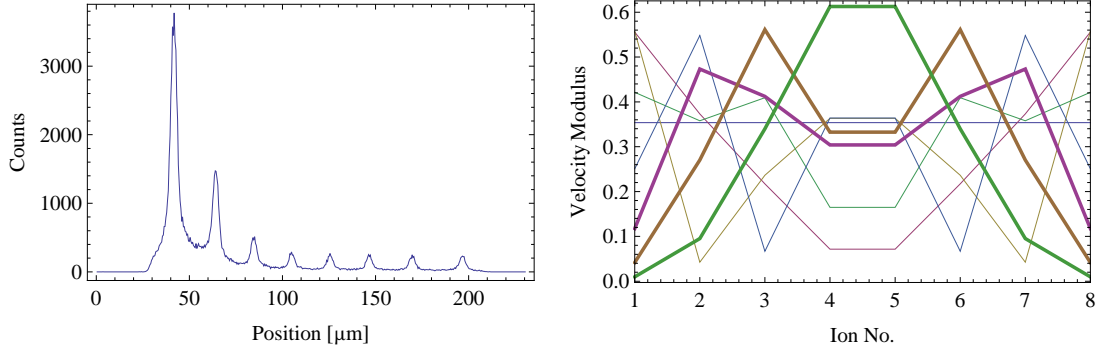
Figure 3.8.: *Validity of the two-ion approximation. The left plot shows a measured intensity profile of a chain of eight ions typical for a spectroscopy run (see also Fig. 3.6). The higher count rate to the left is due to the cooling laser. The right plot shows the relative velocity amplitudes of the ions for different eigenmodes of such a string. Since the ion/laser interaction is viscous this scales the cooling efficiency. In the cooling/spectroscopy geometry used in our experiments the cooling laser is confined to 1-2 ions to the left whereas the spectroscopy laser interacts with all ions. Therefore, the modes indicated with thick lines are cooled inefficiently since they couple well to the spectroscopy laser but only weakly to the cooling laser. Molecular dynamics simulations indeed show that the central ions are warmer than ions at either end of the chain (see temperature profiles marked gray in Fig. 3.9 and Fig. 3.10).*
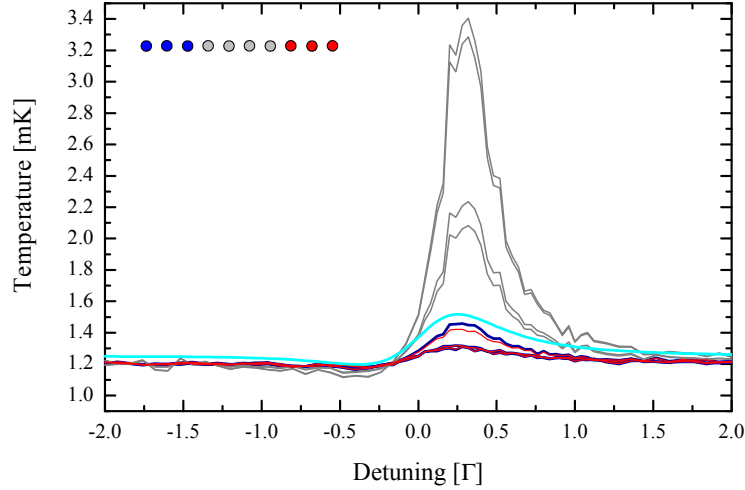
Figure 3.9.: *Detuning-dependent temperature profiles of sympathetically cooled ions in a chain, obtained from a molecular dynamics simulation. Three out of ten ions are cooled with $s = 0.5$ and $\Delta = -2\pi\,64\,MHz$ (blue curves). The spectroscopy laser is set to $s = 7 \times 10^{-4}$ and interacts will all ions. The temperature profiles of the ions used for spectroscopy are marked red, the other ions are shown in grey. As expected (see Fig. 3.8) the center ions show stronger temperature variations. The cyan line is the result of a calculation using the two-ion approximation and shows excellent agreement with the ions of interest. The systematic offset is most likely due to numerical errors in the MD simulation.*
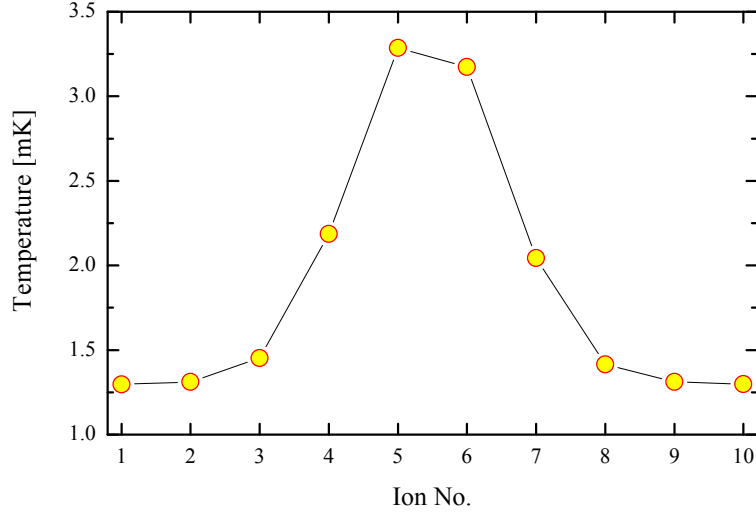
Figure 3.10.: *Spatial temperature profile obtained from a MD simulation (same calculation as in Fig. 3.9). The plot shows the individual temperatures of the ions when the detuning of the spectroscopy laser is set maximum heating (average temperature in the range $0.2\,\Gamma \ldots 0.36\,\Gamma$). The first three ions are cooled while the spectroscopy laser interacts with all ions. This plot illustrates that sympathetically cooled ions that lie symmetrically at the other end of the chain are cooled just as efficient as if they were cooled directly. Note the unusual shape of the temperature profile if compared to an analogous macroscopic system with finite heat conductivity such as a homogeneously heated rod cooled at one end. The shape of the temperature profile is well explained by the structure of the eigenmodes (Fig. 3.8).*

3.2.4. Method-inherent systematic uncertainties

The analysis so far has shown that sympathetic cooling can reduce temperature variations induced by the spectroscopy laser very effectively. However, albeit small, they are non-zero, so the expected line profile is not an exact Voigt profile. Therefore, an important question to address is how large the systematic uncertainties are if the deviations are ignored and Voigt profiles are fitted to the data. To quantify the residual deviations and their impact on high precision spectroscopy we performed simulations as follows: In a first step synthetic resonances were generated with temperature profiles $T(\Delta)$ calculated according to the two-ion approximation. In a second step Voigt profiles were fitted to the simulated data for a wide range of simulation parameters. In the limit of vanishing spectroscopy laser power there are of course no line shape distortions but there is also no signal. Therefore, the most interesting question to address is how intense the spectroscopy laser can be relative to the cooling laser for a given level of systematic uncertainty one is willing to tolerate.

The simulations were performed for Mg$^+$ ions excited on the D2 transition. The cooling laser is set to a detuning of $-\Gamma/2$ and an intensity of $s = 0.01$. Figure 3.11 shows as an example a data set simulated for an intensity ratio of 0.1 together with the fitted Voigt profile and the relative deviations between them.

The achievable accuracy as a function of the ratio of spectroscopy laser intensity to cooling laser intensity is shown in Fig. 3.12. Remarkably, the systematic line shift is never larger than $4\,\mathrm{kHz}$ or 10^{-4} of the linewidth. If, for example, the cooling laser is set to $s = 1$ and the spectroscopy beam's intensity is 10 times weaker the line center can be determined to within 10^{-5} of the linewidth while scattering photons at a *detected* rate exceeding $10\,\mathrm{kHz}$ from a single
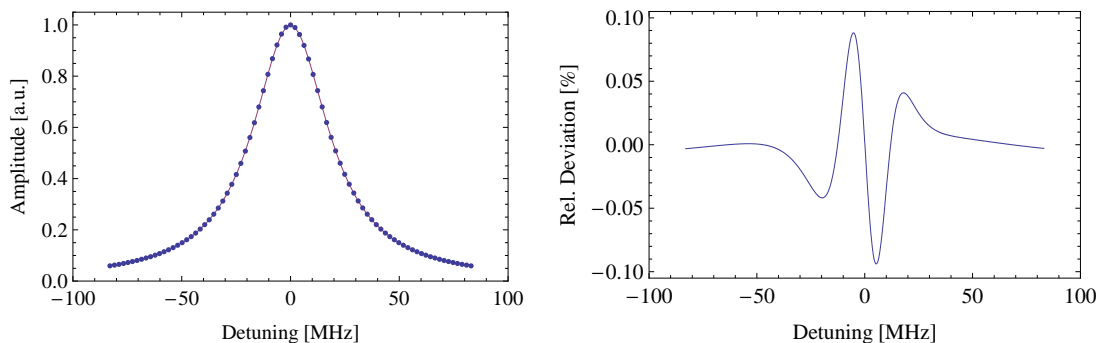
Figure 3.11.: *Simulated line profile for a sympathetically cooled Mg^+ ion probed with a spectroscopy laser 10times weaker than the cooling laser. The left panel shows the simulated data (dots) together with a fitted Voigt profile (solid line). The right panel shows the relative deviations between the data and the fit.*

ion (assuming a detection efficiency of 10^{-3}). The high scattering rate is pivotal to make use of the low systematic uncertainty: For a known line shape the statistical uncertainty in the line center reads $\Delta\omega_0 = \Gamma/\text{SNR}$. If we assume that the signal-to-noise ratio of the detected signal is limited by Poissonian (i.e. shot) noise then the accuracy relative to the linewidth reads $\Delta\omega_0/\Gamma = 1/\sqrt{n}$, where n is the number of detected photons. Therefore, in order to find the line center to within, say, 10^{-4} of the linewidth at least 10^8 signal photons need to be recorded. For reasonable measurement times on the order of hours ($\sim 10^4\,\text{s}$) this is only possible for a single ion if photons are detected at a rate of $10\,\text{kHz}$ or more.

We further studied the impact of residual distortions on the fitted linewidths. The result is shown in Fig. 3.12. The simulations show that the Lorentzian and Gaussian contribution to the linewidth respond quite differently to the deviations. While the relative error in the Lorentzian is always smaller than $0.25\,\%$ the Gaussian contribution is increased by $12\,\%$ at a ratio of 0.1 and even by $58\,\%$ at a ratio of 0.5. Therefore, if one wishes to measure the temperature of the ion very accurately very low intensity ratios smaller $1\,\%$ are in order. The different sensitivity can be understood as follows: Line profile distortions due to the method are limited to a region around $+\Gamma/2$ where heating is strongest (see Fig. 3.11). Since the Gaussian dominates the line profile in the central part of the resonance it responds sensitively to distortions while the Lorentzian has larger weight in the undistorted wings (at large detunings), so it is hardly affected.

Summarizing, the method enables to measure the line center of a single ion better than 10^{-4} of the linewidth by virtue of low systematic uncertainties and simultaneously excellent signal-to-noise ratio due to high scattering rates. The Gaussian and Lorentzian contributions to linewidth can be determined reliably, so the lifetime can be measured with an accuracy comparable or even exceeding established methods such as beam-foil or Hanle-type measurements.

3.2.5. Comparison to other schemes

How does the presented method compare to other schemes that have been used to measure strong dipole transitions in trapped ions?

ONE LASER: The simplest approach is to use one laser only and infer the line center from
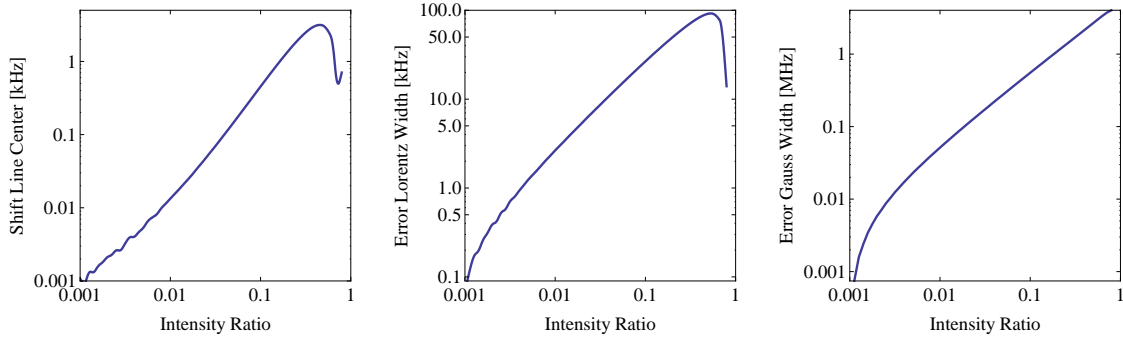
Figure 3.12.: *Simulated errors due to the spectroscopy method. In the calculations the two-ion approximation for Mg$^+$ was used and the cooling laser was detuned by $-\Gamma/2$. The left plot shows the impact on the determination of the line center, the middle and right plot on the Lorentzian and Gaussian width, respectively, all as a function of the intensity ratio of the spectroscopy to the cooling beam.*

the observed asymmetric line profile, as discussed in the introduction of this section. However, this approach has important disadvantages: i) Accuracy. The calculations suggest that the line center could be determined to within better than 10 % of the linewidth. In contrast, actual measurements show a great sensitivity to experimental conditions and poor agreement with the calculations. This is because the calculations exclude excess heating from the trapping conditions which are difficult to quantify. It appears hard to reliably extrapolate an observed rising fluorescence signal to the true peak to within a small fraction of the linewidth. ii) Linewidths. The asymmetric line is not suitable for accurate measurements of the linewidths. iii) Destructive. Finally, this approach is destructive, i.e. the ions are lost in each attempt.

BUFFER GAS COOLING: An easy approach to observe a symmetric line profile is to suppress the laser induced temperature variations by buffer gas cooling. However, this broadens the line significantly and introduces systematic uncertainties like pressure shifts. If ^{24}Mg$^+$ ions are cooled with room temperature helium buffer gas (300 K), then the natural linewidth of 41.5 MHz is Doppler broadened to 2.7 GHz. For 4 K buffer gas the linewidth still amounts to 313 MHz. Recall, that if the linewidth is increased by a factor p, the measurement time has to be increased by a factor p^2 to obtain the same statistical uncertainty of the line center. Since the linewidth is dominated by Doppler broadening this approach does not allow to measure the Lorentzian contribution and thus the lifetime of the excited state. Fig. 3.3 shows a measurement on ^{10}Be$^+$ ions which were buffer-gas cooled to 84 K.

TWO LASER/ CHOPPED SCHEMES: The "one laser" approach can be improved by super-imposing a cooling beam more intense than the spectroscopy beam to ensure a temperature constant to first order. This has been demonstrated on a cloud of Mg$^+$ ions stored in a Penning trap [48]. However, this method has two disadvantages: a) The cooling beam causes AC stark shifts and b) a weak signal has to be detected on a strong background. This can be circumvented by scattering cooling and spectroscopy photons sequentially. But then care must be taken that during the spectroscopy phase only a limited number of photons are scattered so that the temperature of the ion does not change significantly. The most unambiguous approach would be to set the intensity such that on average only one photon is scattered during a bright phase of the spectroscopy laser. However, this limits the scattering rate to one half of the chopping frequency. Fast mechanical choppers operate up to 4 kHz, so the

ion will scatter photons at less than $2\,\text{kHz}$. With typical photon detection efficiencies of 10^{-3} the detected signal rate will be on the order of Hz, four orders of magnitude lower than with the sympathetic cooling method. The use of an AOM to switch the cooling and spectroscopy beam would in principle allow chopping frequencies in the vicinity of $100\,\text{MHz}$, but this has to the best of my knowledge not been demonstrated yet.

A mechanically chopped scheme has been used to measure the cooling transition of a cloud of Ca^+ ions by Wolf et al. [49]. In this measurement a signal rate of $5\,\text{Hz}$ was detected per ion and an estimated 30 photons were scattered per ion during the spectroscopy phase. This allowed to determine the line center to within $7.6\,\%$ of the linewidth.

Summarizing, the requirement of constant temperature for precision spectroscopy of strong transitions has been recognized earlier and has previously been addressed using buffer gas cooling or by superimposing a cooling laser (continuously and chopped). However, the new approach presented in this thesis is the first that allows to observe virtually unperturbed and well-understood line profiles from single ions at the Doppler limit with simultaneously high signal-to-noise ratio. This allows not only to deduce the line center accurately, but also the Lorentzian and Gaussian contributions to the linewidth. This is a result of

- working with an ion chain in a linear rf trap with properly aligned laser beams, so the ions are not subject to perturbing trapping fields that shift energy levels and lead to excess motion (as opposed to, for example, a cloud of ions in a Paul trap or working in a Penning trap where a magnetic field is present in the entire trapping volume)

- the spatial separation of the cooling and spectroscopy regions together with spatially resolved detection. The spectroscopy ions are therefore not subject to the cooling light which shifts the energy levels (ac stark shift) and causes a strong fluorescence background.

- the surprisingly high efficiency of sympathetic cooling. Thanks to the symmetry of the eigenmode structure of a linear chain, the spectroscopy ions are cooled just as efficient as if they were cooled directly.

These three points together facilitate low systematic uncertainties. To take advantage of this, a high signal-to-noise-ratio is necessary, which is enabled by the latter two points: a high scattering rate is possible due to the efficiency of sympathetic cooling, a low background due to spatially resolved detection of ions that do not scatter cooling photons.

3.3. Experiment

To demonstrate the method we performed an absolute frequency measurement of the $3s_{1/2} - 3p_{3/2}$ (D2) transition in $^{24}\text{Mg}^+$. The natural linewidth of $41.5\,\text{MHz}$ is nearly three orders of magnitude larger than the secular frequency in our experiment of about $60\,\text{kHz}$, so the weak-binding condition is well fulfilled. Moreover, as pointed out in the introduction, the transition is of fundamental interest. It serves as an "anchor-line" in the many-multiplet method for searches of drifts of the fine-structure constant and has been requested for re-measurement [44].

3.3.1. Experimental setup

The experiment was performed using the endcap trap, described extensively in Section 2. A schematic of the setup is shown in Fig. 3.13. In brief, UV light near $280\,\text{nm}$ for spectroscopy
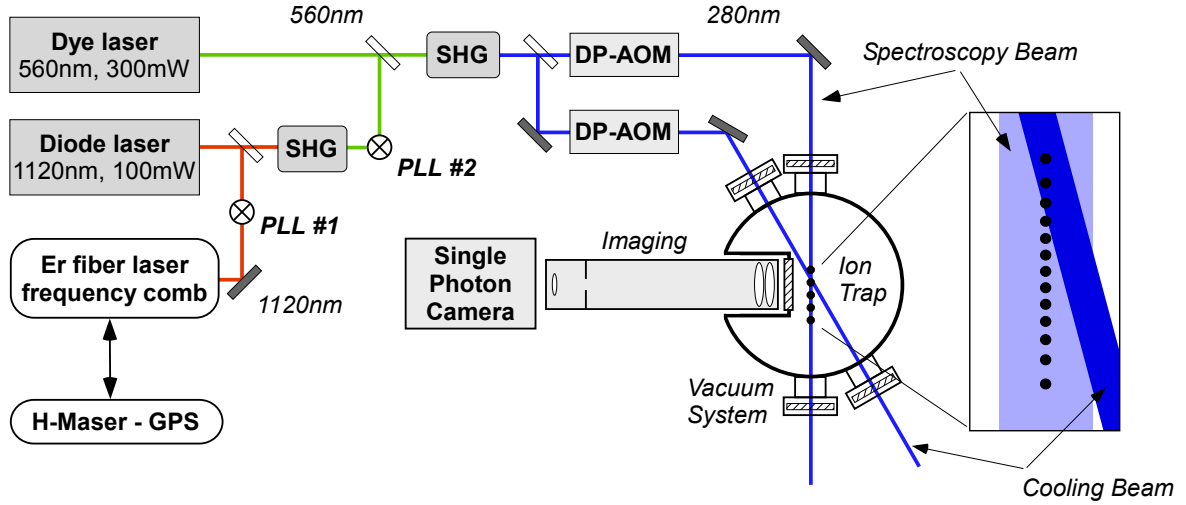
Figure 3.13.: *Schematic of the spectroscopy setup. The dye laser is phase-locked to a fiber laser frequency comb using a diode laser as transfer oscillator (phase-locked loops PLL #1 and #2, see also Fig. 3.14). The output of the dye laser is converted to 280 nm in a second harmonic generation (SHG) stage (Sec. 2.5). A spectroscopy and cooling beam with separately adjustable frequency and stabilized intensity is obtained by splitting the UV output and passing it through two double-pass AOM (DP-AOM, see Sec. 2.23) setups. The inset shows the geometry of the cooling and spectroscopy beam relative to the ion chain (to scale, see also Fig. 3.6).*

is generated either by frequency-quadrupling an Yb fiber laser or by frequency-doubling a dye laser. Due to the failure of the fiber laser most of the data were taken using the dye laser system. Two beams with independently controllable frequency and stabilized intensity required for cooling and spectroscopy are obtained by splitting the output and passing it through two double-pass acousto-optic modulators. The cooling beam enters the apparatus at an angle oblique to the trap's principal axes to ensure cooling along all directions. More precisely, it encloses an angle of 15° with the longitudinal trap axis and 4° with the vertical axis. The minimum achievable temperatures are therefore $0.7\,\text{mK}$ longitudinally, $3.5\,\text{mK}$ horizontally and $41.6\,\text{mK}$ vertically. The beam is tightly focused down to $w_0 \cong 20\,\mu\text{m}$ so it interacts with only about 1-3 ions in a chain. The spectroscopy beam on the other hand is aligned collinearly with the trap axis and is focused only weakly to $w_0 \cong 200\,\mu\text{m}$. An important part of the setup not described so far is the system for the stabilization and absolute frequency measurement of the spectroscopy laser.

Absolute frequency measurement

We measure the absolute frequency [50] of the spectroscopy laser using a frequency dissemination system developed by B. Bernhardt [51]. A GPS disciplined active hydrogen maser (Kvarz CH1-75A) in a separate "clock room" serves as primary frequency standard and provides a 10 MHz reference signal with a relative accuracy on the level of 7×10^{-15} and a stability of 2×10^{-13} in 1s. Its stability and accuracy is transferred to the optical domain by phase-locking a 100 MHz repetition rate Erbium fiber laser frequency comb (Menlo Systems) to it. The output is then distributed to four different experiments in the institute with up to 100 m long fibers.

For spectroscopy we phase-lock the dye laser to the frequency comb. This is not possible
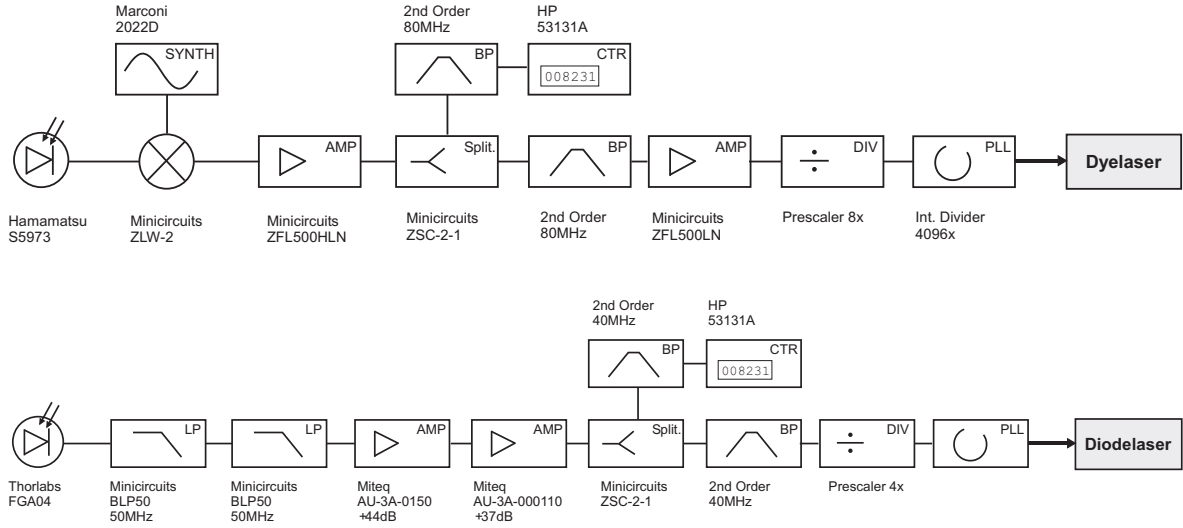
Figure 3.14.: *Electronics for the absolute frequency measurement. The phase lock of the dye laser to the diode laser at 560 nm is shown above (PLL #2). The phase of the dye laser is controlled by tuning the length of its built-in reference cavity. The lock of the diode laser to the fiber laser frequency comb at 1120 nm is shown below (PLL #1). The phase of the diode laser is controlled in two ways: A grating gives low bandwidth but large tuning range, modulating the current the opposite. Abbreviations:* **SYNTH** *synthesizer,* **AMP** *amplifier,* **Split** *power splitter,* **LP** *low-pass filter,* **BP** *band-pass filter,* **CTR** *counter,* **DIV** *prescaler,* **PLL** *phase-lock.*

directly since the dye laser has no spectral overlap with the super-continuum of the Er fiber comb. To bridge this gap we use a diode laser at 1120 nm as transfer oscillator. It is phase-locked to the comb in the IR and then frequency-doubled single-pass in LBO to provide a reference in the green. The lock of the dye laser to the transfer oscillator has been designed for low feedback bandwidth to a) match the low bandwidth of the frequency control of the dye laser and to b) prevent transferring the frequency comb's short term instability to the dye laser that has superior linewidth. However, in hindsight the data evaluation showed that our effort was not quite sufficient and the linewidth of the dye laser was increased by the lock from 3.6 MHz FWHM to 5 MHz. A schematic of the electronics set up by V. Batteiger is shown in Fig. 3.14. All the optical beat notes for the phase-locks exceed 30 dB signal-to-noise-ratio in 400 kHz bandwidth and are monitored by redundancy counters.

The optical frequency is then determined by a) the frequency of the comb mode $f_n = nf_r + f_{CEO}$ the transfer oscillator is locked to, b) the frequencies of the beat notes and local oscillators (LO) and c) the relative signs. With a scrupulous determination of the signs and the known beat and LO frequencies, the optical frequency is fixed modulo the repetition rate of 100 MHz. Finding the mode number n requires either a reference much more accurate than the mode spacing or measuring the transition frequency with different repetition rates. The latter is challenging using fiber laser frequency combs due to the limited tuning range of the repetition rate. The most accurate wavemeter available in the lab has a specified accuracy of 60 MHz, which is not sufficient for an unambiguous determination of n. The Mg^+ D2 transition itself is also unsuitable as a reference - previous measurements only achieved an accuracy of 60 MHz. For this reason the frequency of the Mg^+ resonance was measured with a second fiber laser frequency comb operating at a vastly different repetition rate of 250 MHz. The mode number

and absolute frequency determined this way is consistent with both the wave meter and the published wavelength of the transition.

Locking the Yb fiber laser at 1120 nm to the comb was quite similar but simpler, since it could be locked to the comb directly without a transfer oscillator.

3.3.2. Spectroscopy

To perform a measurement we load chains of 8-12 ions. The secular frequencies are about 1 MHz in the radial directions and 60 kHz axially, corresponding to stability parameters of $q_r = 0.18$ and $q_{ax} = 0.01$. One end is cooled by focusing the cooling beam onto 1-2 ions with an intensity of about $s = 0.5$ and detuned $\Delta = -2\pi\,64$ MHz below the transition (we did not chose $\Delta = -\Gamma/2$ for technical reasons). We determine the saturation parameter from the peak count rate r assuming the calculated detection efficiency of the imaging system $\eta = 6.2 \times 10^{-3}$ for isotropic emission

$$s = \frac{2r}{\Gamma\eta - 2r}. \tag{3.10}$$

The spectroscopy beam is aligned collinearly with the ion chain and is set to an intensity of $s = 7 \times 10^{-4}$. In the two-ion approximation this corresponds to one ion cooled with $s = 0.5$ and the spectroscopy beam set to $s = 0.004$ (six times the intensity acting on six times fewer ions). The intensity ratio is thus 8×10^{-3}.

To record a line we set the spectroscopy laser in random order to 31 different frequencies in a 180 MHz ($= 4.3\,\Gamma$) wide range roughly centered on resonance. Randomized data-taking makes a measurement insensitive to variety of possible drifts. At each point we integrate for 3 s. Including dead-times of the counters etc. a scan takes about 2 min. As signal we store the entire image recorded by the single-photon camera which is digitized in 512×512 px. For each run the raw data are thus a series of 31 images. The data acquisition and evaluation is performed with a software suite written by S. Knünz (for a screen shot see Fig. 3.15).

To evaluate the data in a first step resonances are extracted from the set of images using software that allows to define circular regions-of-interest (ROIs) around the ions (see Fig. 3.15). In a second step consistency checks of the phase locks and counters were performed and cycle-slips removed. Finally, Voigt profiles are fitted to each resonance using a non-linear least squares routine. Thereby, the following six parameters are varied: *offset, slope, amplitude, Gaussian FWHM, Lorentzian FWHM, center.* The fits were performed as weighted fits assuming shot-noise-limited detection, i.e. with Poissonian noise assigned ($\sqrt{N}$). The resulting parameters were then stored for each ion and run.
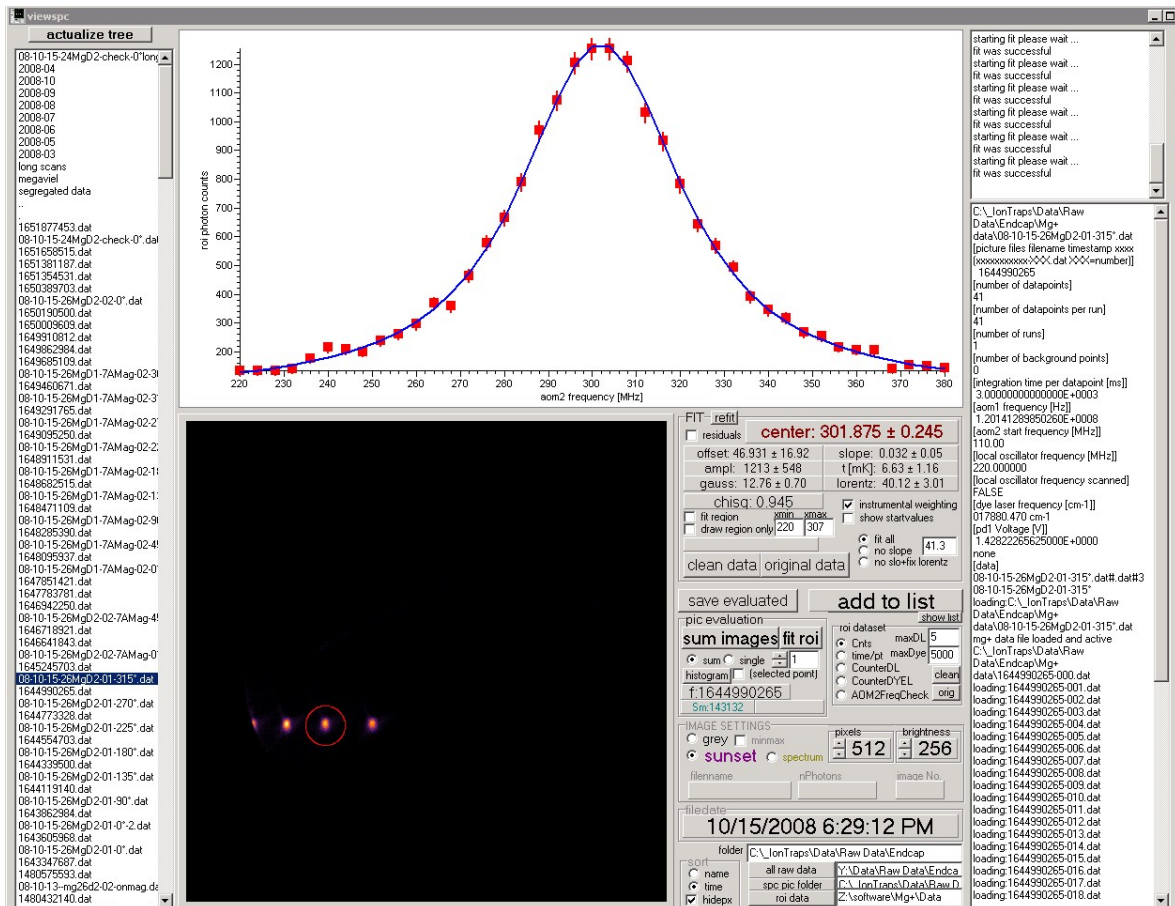
Figure 3.15.: *Screenshot of the software used for data evaluation. The large square panel shows the recorded images and allows to define regions-of-interest (ROI) around the ions (red circle). The top panel shows the resonance extracted from the ROI together with a weighted Voigt fit. Due to the limited dynamic range and poor linearity of the single-photon camera at high count rates we image only the sympathetically cooled ions and not the entire chain.*
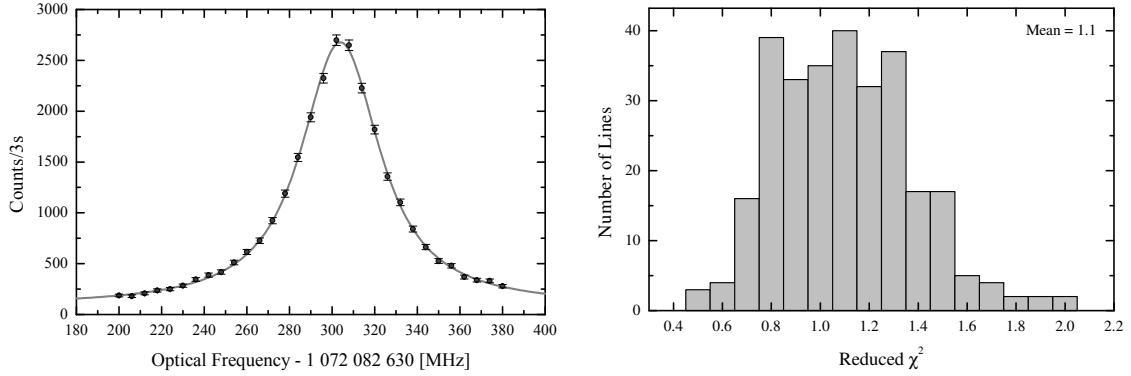
Figure 3.16.: *Typical measured $3s_{1/2} - 3p_{3/2}$ resonance from a single ^{24}Mg$^+$ ion (left). The error bars represent Poissonian noise as derived from the counts, the solid line is a Voigt fit. Note the peak detected count rate of about 1 kHz. The right plot is a histogram of the reduced χ^2 of the 264 lines included in the data evaluation. The average is 1.1, so no statistically significant deviation from a Voigt line shape could be detected, in agreement with both the theoretical model and the assumption of shot-noise-limited detection.*

3.4. Results

In total we recorded 264 lines from the outermost three ions in eleven measurement days.

3.4.1. Line profile

A typical measured resonance from a single ion together with a fitted Voigt profile is shown in Fig. 3.16.

Assuming Poissonian noise only the average reduced χ^2 of all lines is 1.1 (see Fig. 3.16). A value slightly higher than 1 is expected: A small amount of the cooling laser intensity "leaks" into the spectroscopy region and causes a background count rate of up to 100 Hz. Since we did not stabilize the intensity of the cooling laser, this background fluctuates and leads to excess noise. The fit residuals show no structure other than white noise. Therefore, no statistically significant deviation from a Voigt profile is found in a net integration time of close to 7 hours. This confirms both the theoretical model and the assumption of shot noise limited detection.

3.4.2. Linewidths

The fitted Lorentzian and Gaussian linewidths are shown in Fig. 3.17. The average Gaussian FWHM amounts to 11.5(3) MHz (statistical uncertainty), the average FWHM of the Lorentzian contribution is 41.5(2) MHz. The observed widths result from a convolution of the laser spectrum with the atomic lineshape plus systematic errors.

The spectrum of the dye laser available at the time of the experiment was measured to be approximately Gaussian with a width of about 5 MHz and a Lorentzian contribution smaller 40 kHz. We therefore estimate the linewidth in the UV to be 10(1) MHz. The rather large linewidth originates from the servo loops that transfer some of the frequency comb's short term instability to the laser despite low feedback bandwidth.
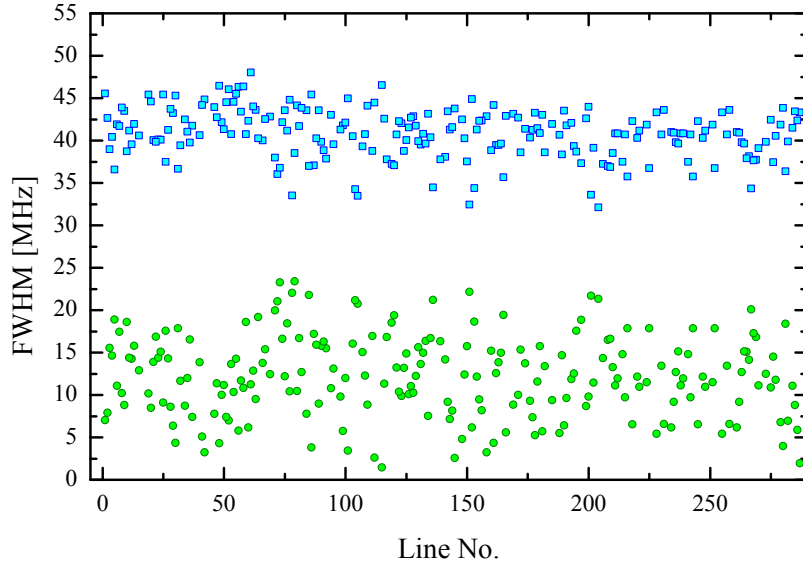
Figure 3.17.: *Measured linewidths. Blue squares show the Lorentzian FWHM, green circles the Gaussian FWHM.*

Due to the line shape model (discussed in Sec. 3.2.4) the Lorentzian contribution is underestimated by 14 kHz while the Gaussian width is increased by 250 kHz for our experimental parameters. A further important systematic uncertainty is due to micromotion. The ion chain is (weakly) confined axially by the RF fields. Ions not located in the node therefore perform a driven oscillation at the trap frequency Ω in the direction of the spectroscopy laser. This is equivalent to a phase-modulation of the laser which leads to sidebands separated by Ω and thus gives rise to a broadened spectrum. The intensity of the mth sideband is given by the Bessel function of first kind $J_m^2(\beta)$. The micromotion modulation index β [10] reads $\beta = kx_0q/2$, where k is the wave vector of the laser, x_0 is the oscillation amplitude and q is the stability parameter. From the imaged spot size of the ion an upper limit of the oscillation amplitude of $x_0 \leq 1\,\mu$m is found, so $\beta \leq 0.1$. Simulations (Fig. 3.18) show that this causes the Lorentzian and Gaussian widths to be increased by up to 54 kHz and 170 kHz, respectively. Here, it was assumed that the sidebands were modulated onto a Voigt profile with a Lorentzian and Gaussian width of 41.5 MHz and 5 MHz, respectively, and to a trap frequency of $2\pi\,15$ MHz.

Taking the spectrum of the dye laser into account, the measured average Gaussian linewidth of 11.5(3) MHz gives a residual Gaussian (Doppler) width of 6(2) MHz. This corresponds to a temperature of the ion string of 1.3(8) mK, in agreement with the expected single ion cooling limit of 1.3 mK. Averaging the Gaussian widths yielded a reduced χ^2 of 2. The excess scatter is attributed to the phase lock of the dye laser to the frequency comb, which, depending on the settings, can cause the linewidth of the laser to vary from day to day.

A detailed evaluation of the Lorentzian contributions revealed a correlation of the widths with the polarization of the spectroscopy laser. We therefore assume a systematic uncertainty of 1 MHz, likely due to magnetic fields, which dominates the error budget and requires further investigations. The final result reads:

$$\Gamma_L = 2\pi\,41.5(1.0)\,\text{MHz} \qquad \tau_{3\text{p}_{3/2}} = 3.84(10)\,\text{ns}. \tag{3.11}$$
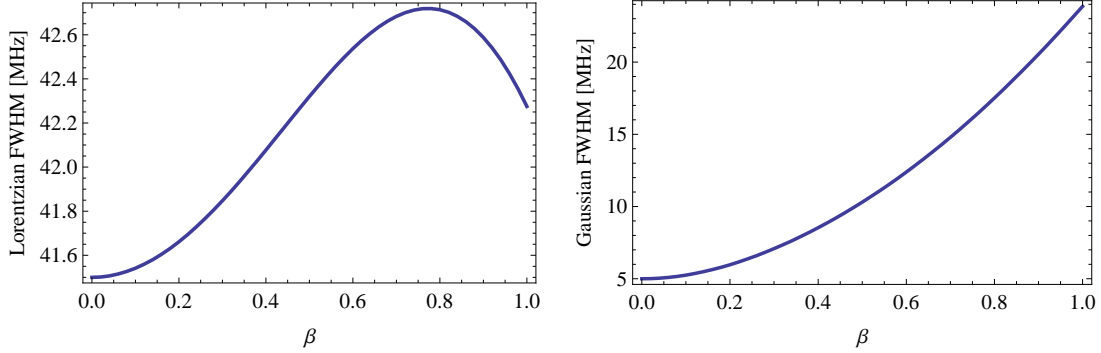
Figure 3.18.: *Influence of micromotion on the measured linewidths. Here, β denotes the micromotion modulation index.*

This value is in excellent agreement with the most accurate measured lifetime so far which corresponds to a linewidth of $41.8(4)\,\text{MHz}$ [52]. The low statistical uncertainty demonstrates the suitability of this approach for precision lifetime measurements, especially once the magnetic field related systematic uncertainty is resolved.

3.4.3. Line center

To obtain an accurate line center several systematic uncertainties need to be taken into account. Static **magnetic fields** pointing along the spectroscopy laser shift the line center due to the linear Zeeman effect if the polarization is not perfectly linear or optical pumping takes place for other reasons. The $s_{1/2}$ ground state and the $p_{3/2}$ excited state have two and four magnetic sub-levels, respectively, that are not resolved for the magnetic fields in our apparatus. For purely circularly polarized light the line is shifted by $14\,\text{kHz}/\mu\text{T}$, see Fig. 3.19.

For this reason we pass the spectroscopy beam through a quarter wave plate retarder (QWP) and measure the line center as function of polarization. If the polarization is expressed in terms of the rotation angle of the QWP, a sinusoidal modulation of the line center with a period of $180°$ is expected. Fig. 3.19 shows as an example the line centers of three ions at 9 different angles of the QWP. The amplitudes of the fitted sines correspond to a magnetic field of $19(3)\,\mu\text{T}$, in perfect agreement with an independent Hall probe measurement. Magnetic fields orthogonal to the spectroscopy laser should not shift the line center, which we confirmed by measuring the line center with an additional $400\,\mu\text{T}$ field applied perpendicularly.

The largest systematic uncertainty originates from the large linewidth of our spectroscopy laser and is not inherent to the method described here. By phase-locking the laser to the frequency comb we control the carrier phase. However, **correlated amplitude and phase modulation** can lead to asymmetries of the spectrum so its center-of-gravity does no longer coincide with the carrier frequency (see Fig. 3.20). Since the measured line profile is a convolution of the atomic response with the laser spectrum, this can lead to systematic shifts. To estimate the size of this effect we studied the in-loop spectrum of the heterodyne beat note between the dye laser and the diode laser locked to the frequency comb. By fitting a Gaussian to the spectrum we estimated its asymmetry by determining the difference between the peak of the Gaussian and the counted heterodyne beat signal. We found an average deviation of $80(60)\,\text{kHz}$ at $560\,\text{nm}$, so we assume an uncertainty of $160\,\text{kHz}$ in the UV. In addition we measured the transition on one day with a different laser system, that is with our Yb fiber
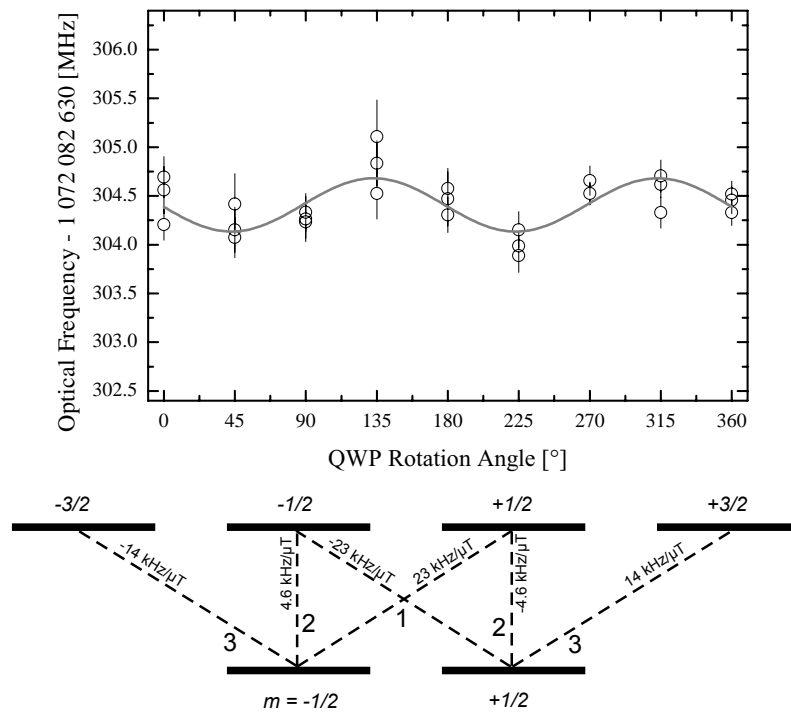
Figure 3.19.: *Compensation of magnetic field shifts. We measured the line center versus polarization, which in this plot is given as rotation angle of a quarter wave plate; before the retarder the beam is linearly polarized. For each polarization three ions are evaluated. Also shown is a Kastler diagram of the magnetic sub-levels of the $^{24}Mg^+$ D2 transition including the relative weights of the transitions and their sensitivity to magnetic fields.*
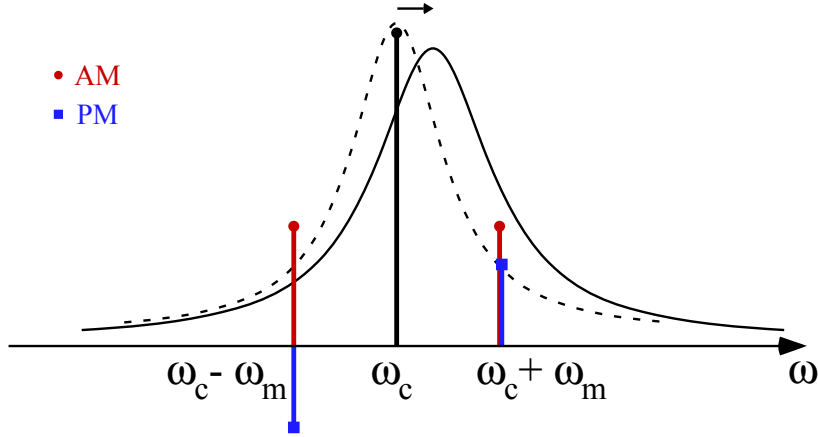
Figure 3.20.: *Influence of correlated amplitude and phase modulation on spectroscopy. The PLL stabilizes the carrier frequency ω_c of the laser. If both the amplitude and the phase are modulated at the same rate ω_m the net amplitudes of the sidebands and thus the spectrum of the laser can become asymmetric. Therefore, the center-of-gravity of the spectrum, as seen by the atom, does not necessarily coincide with the carrier frequency anymore. This behaviour is expected for many noise processes. If e.g. the pump of a laser fluctuates in intensity then not only the amplitude of the laser will be modulated but also the phase at the same rate, due to fluctuations of inversion and thus of the refractive index.*

laser. The measurement agreed with our previous measurements (see Fig. 3.21), confirming our estimated uncertainty.

The **DP-AOM**s used to scan the frequency are responsible for a further systematic uncertainty. We stabilize the total intensity of the spectroscopy beam but the ions sample the intensity at one point in space only. Therefore, if the beam profile changes when the frequency is scanned, the ions experience a detuning dependent intensity variation that distorts the line and thus leads to a shift. This also becomes apparent as an alignment sensitivity of the line center. To suppress this effect we ensure a stable beam profile by spatially filtering the spectroscopy beam with an additional small pinhole installed after the DP-AOM. Moreover, we evaluate the data by fitting a Voigt profile including a linearly varying background (fit parameter "*slope*") to account for residual intensity variations.

Other systematic uncertainties we considered are significantly smaller. The **ac Stark** effect shifts the line center due to the residual background from the cooling laser by [53]

$$\Delta\omega_{\mathrm{ac}} = \frac{s\Gamma^2}{4\Delta_c}, \tag{3.12}$$

where s, Δ_c are the saturation parameter and detuning of the cooling laser. The maximum background count rate was $120\,\mathrm{Hz}$ at a detuning of $\Delta_c = -2\pi\,64\,\mathrm{MHz}$ so the shift is smaller $10\,\mathrm{kHz}$. Even if micromotion is perfectly compensated a trapped ion samples an average quadratic electric field due to its motion caused by its finite temperature. This leads to a **quadratic dc Stark** shift from the trapping fields. The average quadratic electric field reads [10]

$$\langle E^2 \rangle = \frac{m\Omega^2 k_b T}{2e^2} \frac{a^2 + 2q^2}{2a^2 + q^2}. \tag{3.13}$$
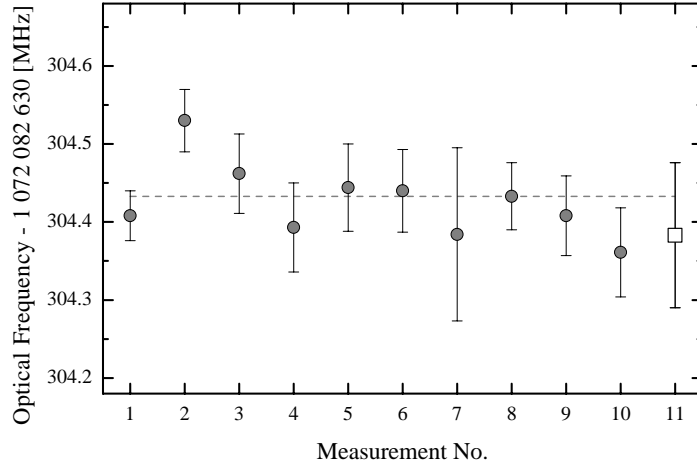
Figure 3.21.: *Reproducibility. We repeated the measurement on 11 days, the error bars represent statistical uncertainties. The first 10 data points were taken using the dye laser, the last data point (square) was measured with the fiber laser.*

This leads to a shift of [54]

$$\Delta\omega_{\rm dc} = -\frac{3e^2\hbar}{2m_e}\langle E^2\rangle \sum_{\gamma'J'} \frac{f_{\gamma J\gamma'J'}(2J+1)}{\hbar\Delta\omega_{\gamma J\gamma'J'}}, \tag{3.14}$$

where $|\gamma J\rangle$ are the quantum number of the ground and excited state and f are the oscillator strengths. With tabulated values of the transition energies and oscillator strengths [55] the D2 transition is calculated to be shifted by $-3.8 \times 10^{-6}\,{\rm Hz}/({\rm V/m})^2$. For our trapping conditions this is less than -33 mHz.

The **second order Doppler shift** of $\Delta\omega_{\rm dop} = 2\pi v^2/2c^2$ shifts the line by less than -0.3 Hz. The absolute frequency measurement is limited by the (in-)stability of the **maser** which leads to an error of 90 Hz. The **line shape model**, finally, contributes with an error of about 10 Hz, as detailed in the method section Sec. 3.2.4.

To test the reproducibility we repeated the measurements on eleven days within four weeks. The result is shown in Fig. 3.21. A weighted fit of the data gives a statistical uncertainty of 15 kHz, with a reduced χ^2 of 1. This is a resolution of 4×10^{-4} of the linewidth and clearly illustrates the potential of the method that can be achieved with straightforward improvements of the linewidth of the spectroscopy laser.

Including the correction due to the recoil shift (-106 kHz), the absolute frequency reads

$$\nu_{\rm D2} = 1\,072\,082\,934.33(16)\,{\rm MHz}.$$

This is in agreement with [56] but 375 times more accurate, and corresponds to a relative accuracy of 1.5×10^{-10}.

3.4.4. Comparison to literature

The $3s_{1/2}-3p_{3/2}$ transition has previously been measured three times. The first measurement was performed 1980 on a sample of about 100 laser cooled ions stored in a Penning trap [48]. The measurement was isotope resolved with an observed linewidth of 100 MHz (see Fig. 3.22).
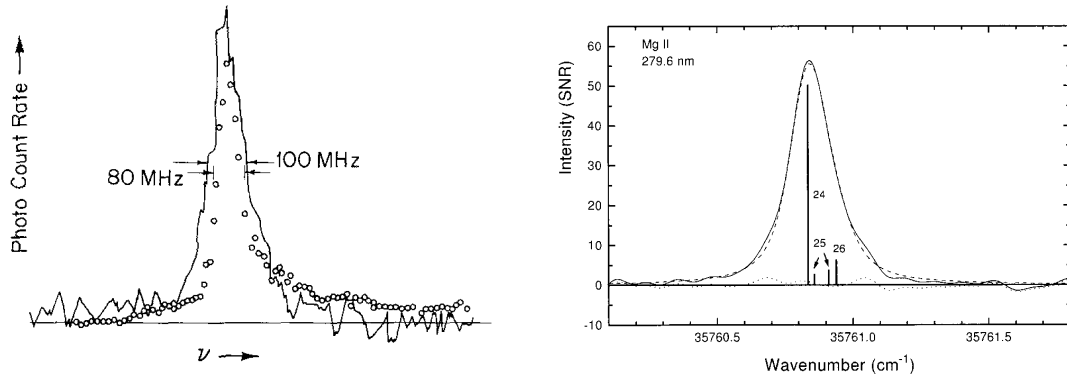
Figure 3.22.: *Previous measurements of the $3s_{1/2} - 3p_{3/2}$ resonance in Mg$^+$. The left plot shows a measurement on $\sim$ 100 ions stored in a Penning trap [48], the right plot was obtained from a hollow-cathode discharge lamp analyzed by a Fourier transform spectrometer [57].*

The wavelength of the transition was determined relative to an iodine line leading to an uncertainty of 120 MHz.

Two further measurements were performed 1998 and 2006 at Imperial College, London [57], [56]. In these measurements the transition was excited in a hollow cathode discharge lamp and analyzed by a Fourier transform spectrometer. The latter was calibrated with an uncertainty of 30 MHz against Ni$^+$ lines which are simultaneously emitted by the discharge lamp since the cathode is made of nickel. An observed line is shown in Fig. 3.22. They are not Doppler free and due to their width of 4.5 GHz they are also not isotopically resolved. The positions of the line centers of the individual isotopes are inferred indirectly using the isotope splitting measured in [48] which has an uncertainty of 100 MHz. In total, the error is specified to be 60 MHz, so [57] and [56] used to be the most accurate values.

A comparison of the result presented in this thesis with previous measurements is shown in Fig. 3.23.
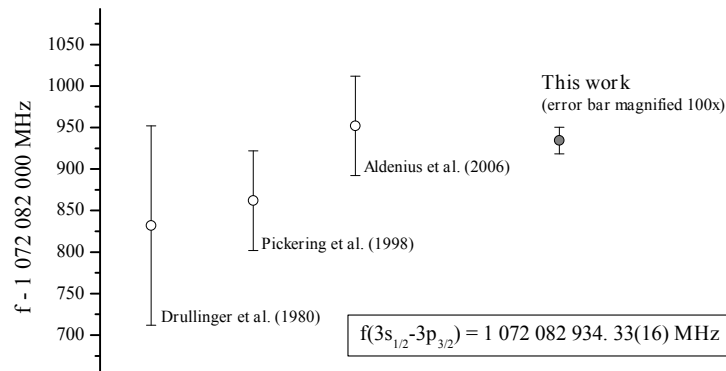
Figure 3.23.: *Comparison of the result presented in this thesis to previous measurements.*

3.4.5. Publication

The results of this chapter have been published in *Physical Review Letters*.

Frequency Metrology on Single Trapped Ions in the Weak Binding Limit: The $3s_{1/2} - 3p_{3/2}$ Transition in ^{24}Mg$^+$

M. Herrmann,[1] V. Batteiger,[1] S. Knünz,[1] G. Saathoff,[1] Th. Udem,[1] and T. W. Hänsch[1,2]

[1]*Max Planck Institut für Quantenoptik, Hans Kopfermann Strasse 1, 85748 Garching, Germany*
[2]*Ludwig-Maximilians-Universität München, 80333 München, Germany*
(Received 22 August 2008; published 9 January 2009)

We demonstrate a method for precision spectroscopy on trapped ions in the limit of unresolved motional sidebands. By sympathetic cooling of a chain of crystallized ions, we suppress adverse temperature variations induced by the spectroscopy laser that usually lead to a distorted line profile and obtain a Voigt profile with negligible distortions. We applied the method to measure the absolute frequency of the astrophysically relevant $D2$ transition in single ^{24}Mg$^+$ ions and find 1 072 082 934.33(16) MHz, a nearly 400-fold improvement over previous results. Further, we find the excited state lifetime to be 3.84(10) ns.

PACS numbers: 32.30.Jc, 32.70.Jz, 37.10.Ty, 37.10.Vz

Virtually all absolute frequency measurements on single trapped ions reported so far have been performed on narrow transitions in tightly confined ions so that the oscillation frequency ω_s of the ion around the trap center exceeded the transition linewidth $\omega_s \gg \Gamma$. In this regime, called strong-binding limit, the absorption spectrum consists of a "carrier" and a number of motional sidebands separated by ω_s. Spectroscopy of the carrier eliminates first-order Doppler and recoil shifts, an important prerequisite for the tremendous accuracies achieved. However, a variety of interesting transitions exists that can hardly be studied in this regime due to their large linewidths. In astrophysics, strong dipole transitions observed in quasar absorption spectra are studied to constrain possible variations of fundamental constants, which creates a demand for accurate laboratory reference data [1]. In nuclear physics, the structure of halo nuclei is being studied via isotope shift measurements on dipole transitions [2,3], with stringent requirements on the accuracy that so far could not be met. High precision spectroscopy outside the strong-binding limit is challenging since the spectroscopy laser induces detuning-dependent heating and cooling which distorts the line profile. In fact, all previous measurements in this regime were limited by the conventional spectroscopy techniques used to overcome the heating effects (e.g., [3,4]). In this Letter, we present both theory and an experimental demonstration of a new spectroscopy method that essentially removes the limitations due to the back action of the interrogating laser and allows us to observe a well understood line shape with high signal-to-noise ratio. The experimental demonstration yields a resonance statistically indistinguishable from a Voigt profile and thus allows us to determine the line center and linewidths with unprecedented accuracy.

The basic idea is to prepare a crystallized chain of ions stored in a linear radio frequency (rf) trap which is continuously laser-cooled on one side only. Ions at the other end of the chain are sympathetically cooled but do not

scatter photons from the cooling laser. A spectroscopy beam less intense than the cooling beam is then directed collinearly at the ion chain, and an imaging photo detector records only photons from the sympathetically cooled ions. Temperature variations that lead to line shape distortions are strongly suppressed, and adverse effects from the cooling laser (background, ac Stark shift) are eliminated, too. We demonstrate this method by measuring the 42 MHz wide $3s_{1/2} - 3p_{3/2}$ transition near 280 nm in single ^{24}Mg$^+$ ions. This line is an "anchor line" for the many-multiplet method used for the search for drifts of the fine-structure constant in quasar absorption spectra and has been requested for remeasurement [1]. Our new approach allows us to determine the line center to within 160 kHz, a 375-fold improvement over previous results [5]. Further, this is the first demonstration of an accuracy better than 1% of the linewidth in this regime, as required for the study of halo nuclei [2]. Thanks to the well understood line shape, we could determine the lifetime of the $3p_{3/2}$ state in excellent agreement with previously published values [6]. The presented measurement is the first absolute frequency measurement on a single, weakly bound ion.

To quantify how well our technique can suppress detuning-dependent temperature variations, consider two crystallized ions where one ion is cooled while spectroscopy is performed on the other. The motion can be described as a linear combination of their two eigenmodes, the center-of-mass and breathing mode. Since the motional sidebands are not resolved, the cooling laser will cool both modes simultaneously. For these conditions, we calculate the equilibrium temperature as follows: The secular cycle-averaged cooling or heating power $\langle P_l \rangle$ due to the interaction with one of the two laser beams, enumerated by i, reads [7]

$$\langle P_l^i \rangle = \langle \hbar k v_0 \cos(\omega_s t)\Gamma g(s_i, \Delta_i - k v_0 \cos(\omega_s t))\rangle. \quad (1)$$

Here, $\hbar$ denotes Planck's constant, k the wave vector, s_i is the dimensionless saturation parameter that measures the

intensity in units of the saturation intensity, Δ_i the detuning, v_0 the velocity amplitude, Γ the natural linewidth and g finally represents the Lorentzian line shape $g(s, \Delta) = s/2[1 + s + (\frac{2\Delta}{\Gamma})^2]$. Spontaneous emission heats the motion on average by

$$\langle P_h^i \rangle = \left\langle (1 + \xi) \frac{\hbar^2 k^2}{2m} \Gamma g(s_i, \Delta_i - kv_0 \cos(\omega_s t)) \right\rangle, \quad (2)$$

where m is the ion's mass and $\xi = 2/5$ for nonisotropic dipole radiation. Since in both modes the ions move with the same velocity modulus at any instant of time, we can solve the steady state condition $\sum_i (\langle P_l^i \rangle + \langle P_h^i \rangle) = 0$ for v_0 to obtain the ion's temperature $T = m\langle v^2 \rangle / 2k_b$, where $\langle v^2 \rangle = \frac{1}{2} v_0^2$. The result of such a calculation with parameters typical for our experiment is shown in Fig. 1.

This treatment of the cooling dynamics is straight forwardly generalized to strings of N ions by considering the chain mode by mode. An important difference is that the cooling laser will not cool all modes equally efficiently if it interacts with a limited number of ions. For example, the stretch mode of an odd-numbered string of ions is not cooled if the cooling laser is focused on the center ion only. An analysis of the normal modes shows that it is in general favorable to cool a group of ions at one end of the chain and perform spectroscopy on ions that lie symmetrically at the other end. For such a configuration, molecular dynamics simulations show that long ion chains are very well approximated by chains of two ions as described above if the intensities s_i are chosen such that the overall ratio of cooling to heating remains the same. The cooling dynamics remains unchanged for heterogeneous ion chains consisting of different species.

For a weakly bound ion $\omega_s \ll \Gamma$ in the classical limit $\hbar\omega_s \ll k_b T$, we expect the line shape to be a convolution of a power-broadened Lorentzian with a Gaussian due to the Maxwellian distribution of kinetic energies [8]. Thus, for constant temperature, a Voigt profile is expected [7]. However, the residual temperature variations calculated above cause the line shape to differ slightly from a Voigt
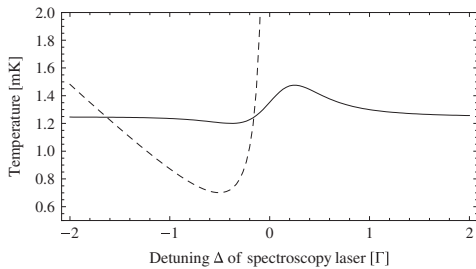
FIG. 1. Calculated temperature of the spectroscopy ion in a chain of two ions. The intensity of the cooling laser is set to a saturation parameter of $s = 0.5$ and tuned 64 MHz below resonance. The spectroscopy beam is set to $s = 0.004$. The dashed line shows for comparison the temperature profile if the cooling laser is turned off.

profile. To estimate size and impact of the deviations, we fitted Voigt profiles to synthetic data generated according to the calculations described above. For our experimental conditions, we find a systematic shift of the line center of less than 300 Hz corresponding to $< 10^{-5}$ of the linewidth. The extremely small deviations not only allow us to determine the line center with great accuracy but also allow us to extract information related to the linewidth precisely, e.g., the temperature of the ion and the lifetime of the excited state. The departure from a Voigt profile leads to an error determining the Lorentzian linewidth of less than 0.05%. These errors can be reduced even further by lowering the intensity ratio.

To demonstrate the method, we have measured the $3s_{1/2} - 3p_{3/2}$ transition near 280 nm in $^{24}\text{Mg}^+$. Ions are stored in a linear rf trap driven at 15.8 MHz with secular frequencies of 1 MHz radially and 60 kHz axially. The cooling beam encloses an angle of about 15° with the axis of the ion chain horizontally and 4° vertically, limited by the optical access of our vacuum vessel. The Doppler cooling limits for the trap's principal axes are thus $T_{\min} = (0.7, 3.5, 41.6)$ mK along the ion chain, horizontally and vertically, respectively. The pressure is below 5×10^{-11} mbar. We generate the cooling and spectroscopy beam with separately adjustable frequency and intensity at 280 nm as follows: The output of a dye laser (Coherent 699/21) near 560 nm is frequency doubled resonantly in β-barium-borate (BBO) [9] to produce about 15 mW at 280 nm. After spatially filtering the UV beam with a pinhole, it is split and passed through two double-pass acousto-optic modulators (DP-AOM) that can be tuned within $100 \ldots 190$ MHz, allowing us to scan the UV beam over 180 MHz. The spectroscopy beam is stabilized in intensity and spatially filtered with an additional 15 μm pinhole before it is focused onto the ions. The focused waist size in the trapping region is $w_0 \cong 200$ μm. For the cooling beam, we use the output of the DP-AOM directly (no intensity stabilization and spatial filtering) and focus the light on the ions tightly with a waist of $w_0 \cong 20$ μm. Both beams are polarized linearly. To determine the absolute frequency [10], we phase lock the dye laser to a 100 MHz repetition rate erbium fiber laser frequency comb which is referenced to a GPS-disciplined hydrogen maser (accuracy 10^{-14}). A diode laser serves as transfer oscillator and bridges the gap between the comb modes at 1120 nm and the dye laser at 560 nm. We determined the mode number of the comb mode by measuring the frequency of the dye laser simultaneously with an additional frequency comb operating at a different repetition rate of 250 MHz. The optical setup is sketched in Fig. 2.

To record a line, we load chains of 8–12 ions cooled at one end only by focusing the cooling laser onto 2–3 ions with an intensity of $s \cong 0.5$ and detuned 64 MHz below resonance (we did not chose $-\Gamma/2$ for technical reasons). We aligned the spectroscopy beam collinearly with the axis
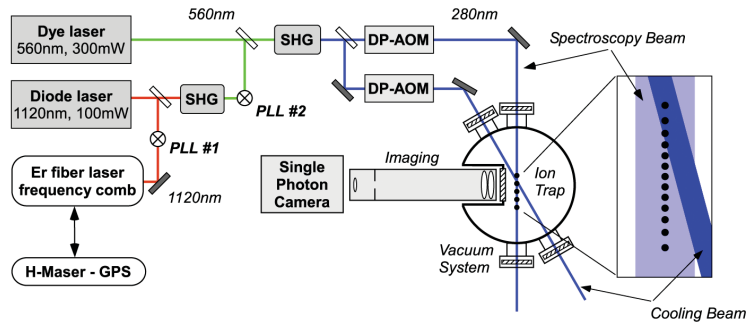
FIG. 2 (color). Schematic of the optical setup. The dye laser is phase locked to a fiber laser frequency comb using a diode laser as transfer oscillator (phase-locked loops PLL #1 and #2). The output of the dye laser is converted to 280 nm in a second harmonic generation (SHG) stage. Spectroscopy and cooling beams with separately adjustable frequency and stabilized intensity are obtained by splitting the UV output and passing them through two double-pass AOM (DP-AOM) setups. The inset shows the geometry of the cooling and spectroscopy beam relative to the ion chain (to scale).

of the ion chain to be insensitive to possible micromotion from the radial direction. Also, this is the direction where cooling is most effective. The spectroscopy laser is set to a saturation parameter of $s \cong 7 \times 10^{-4}$. This configuration corresponds to the parameters given in Fig. 1 with six times lower spectroscopy laser intensity acting on six times more ions. We collect the fluorescence with an $f/2$ imaging system capable of resolving single ions (Quantar Mepsicron II, background count rate 10^{-4} Hz/pixel, system resolution 2 μm, total detection efficiency 6×10^{-3}). In one spectroscopy run, we set the spectroscopy laser in random order to 31 different frequencies in a 180 MHz broad range centered on the transition. At each data point, we collect photons for 3 s. We record the entire image, digitized in 512×512 pixels, and evaluate the data by selecting circular regions-of-interest around the three outermost ions. A typical recorded line from a single ion together with a Voigt profile fitted to the data is shown in Fig. 3. In total, we recorded 264 lines from the outer three ions in 11 measurement days. The average reduced χ^2 of all lines assuming Poissonian noise only is 1.1. The fit residuals show no structure other than white noise. Thus, we cannot detect a statistically significant deviation from a Voigt profile, in agreement with both our theoretical analysis and the assumption of shot-noise limited detection.

The high signal-to-noise ratio allows us to separate the Lorentzian and Gaussian contributions to the width and thus to determine the lifetime of the excited state and the temperature of the ion. The average widths and statistical uncertainties of the Lorentzian and Gaussian contribution amount to 41.5(2) and 11.5(3) MHz, respectively. Residual line shape distortions due to our method lead to systematic uncertainties of 14 kHz (250 kHz) for the Lorentzian (Gaussian). The low statistical and method-inherent systematic uncertainties show the potential of our approach for precision lifetime measurements, corroborated by excellent agreement with previous measurements [6]. Other

systematic uncertainties not inherent to our method can be larger. With a measured upper bound on the micromotion modulation index, we find from simulations that the Lorentzian and Gaussian widths are overestimated by up to 54 and 170 kHz, respectively. Measurements of the polarization dependence of the linewidths indicate a systematic uncertainty due to magnetic fields of about 1 MHz. The spectrum of the dye laser available at the time of the experiment has been measured to be approximately Gaussian with a linewidth of 5 MHz and a Lorentzian contribution below 40 kHz. The width is limited by the servo loops that transfer some of the frequency comb's short term instability to the laser despite low feedback bandwidth. The resulting linewidth in the UV of 10(1) MHz gives a residual Doppler width of 6(2) MHz. This corresponds to a temperature of 1.3(8) mK, in agreement with the expected single-ion cooling limit of 1.3 mK.

To obtain an accurate line center, several systematic uncertainties need to be taken into account. Static magnetic fields pointing along the spectroscopy laser shift the line center due to the linear Zeeman effect if the polarization is
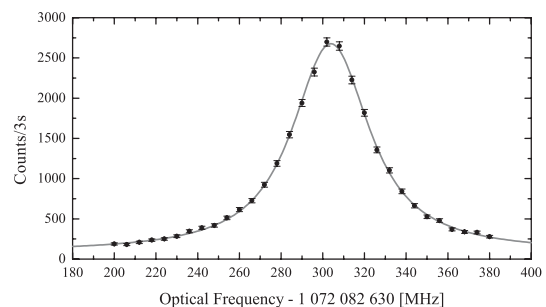
FIG. 3. Typical recorded resonance. The solid line is a Voigt fit to the data; the error bars represent Poissonian noise as derived from the counts.
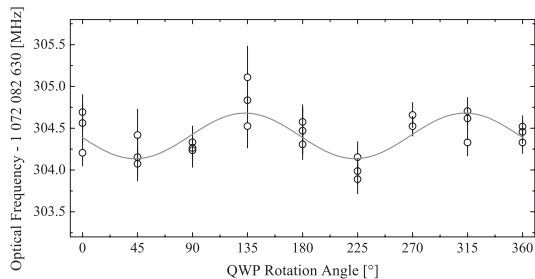
FIG. 4.   Compensation of magnetic field shifts. We measured the line center versus polarization. The polarization is given in terms of the rotation angle of the quarter wave plate used; before the retarder, the beam is linearly polarized. For each polarization, three ions were evaluated.

not perfectly linear or optical pumping takes place for other reasons. The $s_{1/2}$ ground state and the $p_{3/2}$ excited state have two and four magnetic sublevels, respectively, that are not resolved for the (laboratory) magnetic fields in our apparatus. For purely circularly polarized light, the line is shifted by 14 kHz/μT. For this reason, we pass the spectroscopy beam through a quarter wave plate retarder (QWP) and measure the line center as a function of polarization. If the polarization is expressed in terms of the rotation angle of the QWP, a sinusoidal modulation of the line center with a period of 180° is expected. Figure 4 shows as an example the line centers of three ions at nine different angles of the QWP. The amplitudes of the fitted sines correspond to a magnetic field of 19(3) μT, in agreement with a Hall probe measurement. Magnetic fields orthogonal to the spectroscopy laser should not shift the line center, which we confirmed by measuring the line center with a 200 μT field applied perpendicularly.

The DP-AOMs lead to small detuning-dependent irregular distortions of the initially Gaussian beam profile. We stabilize the total intensity, but the ions sample the intensity at one point in space only, so we observe a small alignment-dependent line center shift which we remove by spatially filtering the spectroscopy beam with a pinhole.
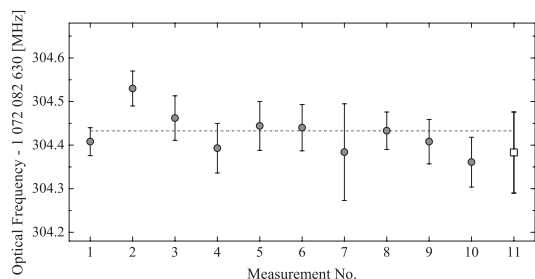
FIG. 5.   Measured line centers. We determined the line center as in Fig. 4 on 11 days within four weeks. The error bars represent the statistical uncertainty only. The last data point was measured with a different laser system (fiber laser).

In addition, we evaluate the data by fitting a Voigt profile including a linearly varying background to account for residual intensity variations. The largest systematic uncertainty originates from the large linewidth of our spectroscopy laser and is not inherent to the method described here. By phase locking the laser to the frequency comb, we control the carrier phase. However, correlated amplitude and phase modulation can lead to asymmetries of the spectrum so its center-of-gravity no longer coincides with the carrier frequency. Since the measured line profile is a convolution of the atomic response with the laser spectrum, this can lead to systematic shifts. To estimate the size of this effect, we studied the in-loop spectrum of the heterodyne beat note between the dye laser and the diode laser locked to the frequency comb. By fitting a Gaussian to the spectrum, we estimated its asymmetry by determining the difference between the peak of the Gaussian and the counted heterodyne beat signal. We found an average deviation of 80(60) kHz at 560 nm, so we assume an uncertainty of 160 kHz in the UV. In addition we measured the transition on one day with a different laser system (a frequency-quadrupled Yb fiber laser [9]). The measurement agreed with our previous measurements (see Fig. 5), confirming our estimated uncertainty. Other systematic uncertainties we considered are significantly smaller: ac Stark shift due to residual background from the cooling laser (30 kHz), dc Stark shift from the trapping fields (0.1 Hz) [11], line shape model (270 Hz), maser accuracy (10 Hz), and 2nd order Doppler shift (-0.3 Hz).

To test the reproducibility, we repeated the measurements on 11 days within four weeks. The result is shown in Fig. 5. A weighted fit of the data gives a statistical uncertainty of 15 kHz, with a reduced χ^2 of 1. Including the correction due to the recoil shift (-106 kHz), the absolute frequency reads $\nu = 1\,072\,082\,934.33(16)$ MHz, in agreement with [5] but 375 times more accurate.

[1]   J. C. Berengut *et al.*, arXiv:0408017.
[2]   M. Zakova *et al.*, Hyperfine Interact. **171**, 189 (2006).
[3]   T. Nakamura *et al.*, Phys. Rev. A **74**, 052503 (2006).
[4]   A. L. Wolf *et al.*, Phys. Rev. A **78**, 032511 (2008).
[5]   M. Aldenius *et al.*, Mon. Not. R. Astron. Soc. **370**, 444 (2006).
[6]   W. Ansbacher *et al.*, Phys. Lett. A **139**, 165 (1989).
[7]   D. J. Wineland *et al.*, Phys. Rev. A **20**, 1521 (1979).
[8]   S. Stenholm, Rev. Mod. Phys. **58**, 699 (1986).
[9]   A. Friedenauer *et al.*, Appl. Phys. B **84**, 371 (2006).
[10]   Th. Udem *et al.*, Nature (London) **416**, 233 (2002).
[11]   D. E. Kelleher *et al.*, J. Phys. Chem. Ref. Data **37**, 267 (2008).

4. A single ion regenerative oscillator

This section describes experiments with a particularly "clean" representation of a nonlinearly driven and damped harmonic oscillator: A single, harmonically bound ion interacting with two laser beams. Despite the conceptual simplicity a surprisingly rich variety of phenomena are observed experimentally and described theoretically. The analysis identifies four distinct dynamical regimes for the motional state of the ion: Thermal, coherent, bistable and unstable. In the coherent regime the ion constitutes a regenerative oscillator, most likely the smallest that can be realized. In close analogy to a laser it shows a threshold for oscillation that has striking parallels to a second-order phase transition and gain saturation. Moreover, bistability and hysteresis are predicted by the model and observed experimentally.

4.1. Theory

Our realization of a non-linearly driven and damped harmonic oscillator is shown schematically in Fig. 4.1. A single ion of mass m is harmonically confined in a linear Paul trap so it oscillates with a (secular) frequency of ω_s and amplitude x_0. The ion is assumed to be well approximated as a two-level system with a (cycling) transition of optical frequency ω_0 and linewidth Γ, so that the weak-binding condition is fulfilled $\Gamma \gg \omega_s$. Two collinear laser beams tuned close to resonance simultaneously damp and excite the motion, respectively. One laser beam of frequency ω_c, the cooling beam, is tuned below resonance ("red detuned") $\Delta_c = \omega_c - \omega_0 < 0$, so it damps and cools the center-of-mass motion. Likewise, a "blue detuned" beam set above resonance $\Delta_g > 0$ excites the motion. The intensity of both the cooling and the gain beam are described with the dimensionless saturation parameter s, which measures the intensity in units of the saturation intensity (Eq. 2.16).

In what follows we will study the center-of-mass motion as a function of the damping and excitation parameters. In particular we will consider the experimentally well accessible oscillation amplitude x_0 of the ion as a function of the intensity ratio of the gain laser to the cooling laser $r = s_g/s_c$ for different sets of detunings (Δ_c, Δ_g).

The theoretical model we develop is very similar to the model that describes the spectroscopy in the weak binding limit (Sec. 3.2). The major differences are that both beams act on the same ion and the parameters for which the equations are solved.

One laser beam

Let us first discuss the impact of a harmonic oscillation on the interaction of a *single* laser beam with the ion. The basic mechanism is that the detuning of the laser Δ is modulated by the first order Doppler shift $-kv$ due to the ion's oscillation

$$\Delta_i(t) = \Delta_i - kv(t) = \omega_i - \omega_0 - k\,x_0\omega_s\cos(\omega_s t), \tag{4.1}$$

where k is the wavenumber of the laser and i denotes either the cooling c or gain g beam. Including this modulation in the Lorentzian line shape and averaging over one secular cycle
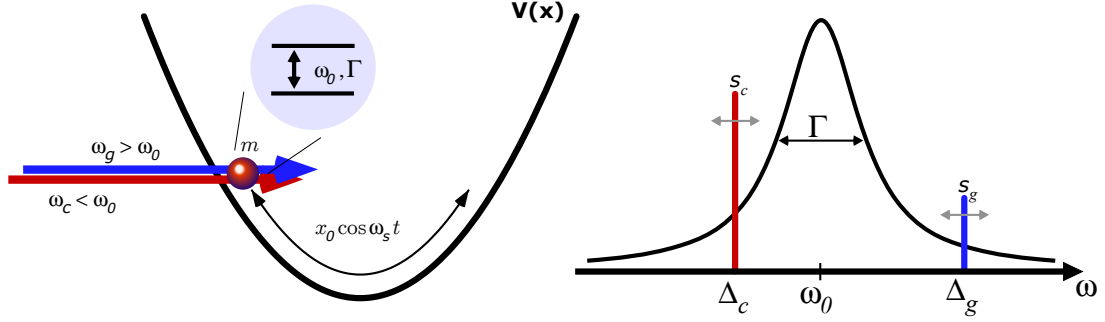
Figure 4.1.: *The model system. An ion of mass m is harmonically bound in a trap so it oscillates with a secular frequency ω_s and amplitude x_0. Two laser beams interact with the ion which is assumed to be a two-level system with resonance frequency ω_0 and linewidth Γ. Motional sidebands are not resolved $\Gamma \gg \omega_s$. A "red detuned" laser beam is set below resonance with an intensity s_c and detuning Δ_c so it damps the motion. Likewise, the "blue detuned" beam (s_g, Δ_g) excites the motion. The oscillatory motion modulates the detunings by the first-order Doppler effect $\Delta_i = \omega_i - \omega_0 - kv(t)$, illustrated by the grey arrows.*

gives the effective scattering rate $\langle g \rangle$

$$\langle g(s_i, \Delta_i(t)) \rangle_{\omega_s} = \frac{\omega_s}{2\pi} \int_0^{2\pi/\omega_s} dt \frac{\Gamma s_i}{2(1 + s_i + \frac{2(\omega_i - \omega_0 - kx_0 \cos(\omega_s t))^2}{\Gamma^2})}. \tag{4.2}$$

Depending on the detuning the scattering rate either decreases monotonically as the oscillation amplitude grows or initially increases before it eventually tends to zero. Fig. 4.2 illustrates this for a range of detunings between $\Delta = 0$ and $\Delta = \Gamma$. This of course also modifies the force the laser exerts on the ion. The cycle-averaged mechanical power reads (see Sec. 1.2 and [14])

$$\langle P_i^a \rangle = \langle \hbar k \, g(s_i, \Delta_i(t)) \, x_0 \omega_s \cos(\omega_s t) \rangle_{\omega_s}. \tag{4.3}$$

An analytical solution exists for this equation although it is rather complex and therefore does not provide additional insight. The resulting power calculated for a $^{24}\text{Mg}^+$ ion ($\Gamma = 2\pi \, 41.5 \, \text{MHz}$, $\lambda = 279.6 \, \text{nm}$) confined in a $\omega_s = 70 \, \text{kHz}$ trap and illuminated with an intensity of $s = 0.001$ is shown in Fig. 4.2. Due to the viscous nature of the interaction the power is at first zero before it rises to a maximum value and finally drops due to the decreasing scattering rate. The plots have been calculated for positive detunings; the power changes sign if the detuning changes sign. Spontaneous emission always excites (heats) the motion, regardless of the sign of the detuning

$$\langle P_i^e \rangle = \langle (1 + \xi) \frac{\hbar k^2}{2m} g(s_i, \Delta_i(t)) \rangle_{\omega_s}. \tag{4.4}$$

Two laser beams

If two laser beams interact with the ion, the net mechanical power exerted on the center-of-mass motion is found by simply adding the individual contributions

$$\langle P \rangle = \langle P_c^a \rangle + \langle P_c^e \rangle + \langle P_g^a \rangle + \langle P_g^e \rangle. \tag{4.5}$$
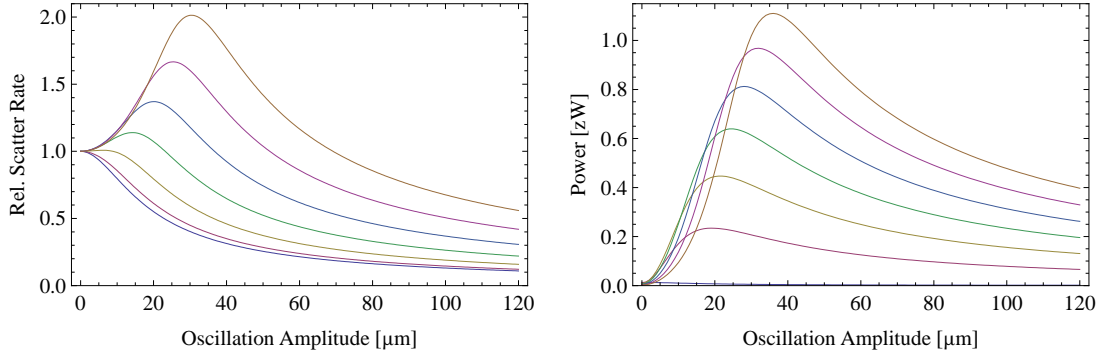
Figure 4.2.: *Relative scattering rate and power exerted on the ion as a function of the oscillation amplitude. The left plot shows the scattering rate normalized to the scattering rate for an ion at rest. The different curves correspond to six equally spaced detunings ranging from $\Delta = 0$ to $\Delta = +\Gamma$. In all cases the scattering rate tends towards zero as the oscillation amplitude grows towards infinity. For large detunings the scattering rate first increases before decreasing. The right plot shows the power exerted on the ion for the same set of detunings. Both plots were calculated for Mg^+ confined with $\omega_s = 70\,kHz$ and a saturation parameter of 10^{-3}.*

Stable solutions are located at the roots of this equation $\langle P(x_0') \rangle = 0$, but this is only a necessary but not a sufficient condition. In addition, the derivative $\partial_x \langle P(x) \rangle |_{x=x_0}$ must be negative, so that the solution is dynamically stable as well, that is, perturbations that increase the oscillation amplitude must be damped and vice versa. The absence of simple analytical solutions for $x_0(r)$ and the large parameter space $(s_c, r, \Delta_c, \Delta_g)$ makes the problem at first rather intangible. However, a systematic numerical study allows to classify the dynamical behaviour in four distinct regimes.

Dynamical regimes

For a given set of detunings there is an intensity ratio r that marks the point where the cooling power balances the entire power that excites the motion $\langle P_c^a \rangle = \langle P_c^e \rangle + \langle P_g^a \rangle + \langle P_g^e \rangle$. This critical intensity ratio r_t is called threshold. If we neglect saturation and spontaneous emission a simple analytical expression can be found for it

$$r_t = \frac{|\Delta_c|}{\Delta_g} \left(\frac{\Delta_g^2 + (\Gamma/2)^2}{\Delta_c^2 + (\Gamma/2)^2} \right)^2 . \tag{4.6}$$

Below the threshold $r < r_t$ the ion equilibriates in a **thermal distribution**. This is in close analogy to Doppler cooling, except that the motion is excited not only by spontaneous emission of the red-detuned beam but also by the blue-detuned laser, so the final temperature will be higher. Note, that this is the regime in which the spectroscopy based on sympathetic cooling has been performed, only that here single ions and not ion chains are considered.

Above threshold one might intuitively expect that the ion is simply driven out of the trap. However, the dynamics are richer and depend on a further distinction. If the detuning of the gain beam is larger or equal than the absolute detuning of the cooling beam $\Delta_g \geq |\Delta_c|$, in the following called **domain $\mathcal{B}$**, then the motion of the ion indeed becomes **unstable** above threshold. In the opposite case $\Delta_g < |\Delta_c|$ (**domain $\mathcal{A}$**) a stable oscillation can emerge for a certain range of intensity ratios r. In this oscillatory regime the center-of-mass motion
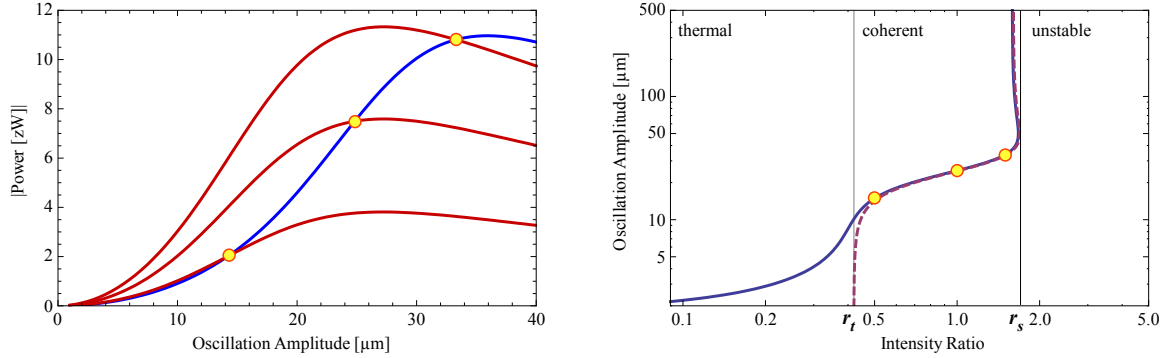
Figure 4.3.: *Regenerative oscillations and dynamical regimes in domain $\mathcal{A}$, calculated for (Mg^+, $\Delta_c=-\Gamma$, $\Delta_g=+5\Gamma/8$, $\omega_s=2\pi\,70\,kHz$, $s_c=0.01$). The left image illustrates how stable regenerative oscillations emerge. The blue line shows the absolute value of the cooling power $\langle P_c^a \rangle$, the red lines the mechanical power exciting the motion $\langle P_g^a \rangle + \langle P_g^e \rangle + \langle P_c^e \rangle$ for three different intensity ratios $r \in \{0.5, 1.0, 1.5\}$. The operational points where cooling balances amplification are indicated with yellow points. Note, that they are dynamically stable - perturbations that lead to larger amplitudes are damped and vice versa. The right plot shows oscillation amplitudes calculated this way for a wide range of intensity ratios. The solid line represents a full calculation, the dashed line excludes spontaneous emission and thus illustrates the role of fluctuations. The threshold is denoted r_t and the stability limit r_s. Dynamically stable points correspond to positive slopes and vice versa. The different dynamical regimes are clearly visible.*

of the ion is a sum of a thermal distribution due to spontaneous emission and a **coherent distribution** due to its oscillation, while the energy in the latter dominates. If the intensity ratio exceeds a second critical value r_s the cooling is not sufficient anymore to maintain a stable oscillation and the motion becomes unstable. **Bistability** between a thermal and a coherent state can occur in both domains but has quite different characteristics.

Domain $\mathcal{A}$

The most striking feature of domain $\mathcal{A}$ is the coherent regime with stable, classical oscillations above threshold. The underlying mechanism is illustrated in Fig. 4.3. Above threshold, gain exceeds damping so initially the oscillation amplitude grows. However, the cooling power grows as well and finally balances the mechanical gain. The oscillation is dynamically stable, that is, perturbations that increase the oscillation amplitude lead to damping and vice versa. The ion thus constitutes a regenerative oscillator, which is harmonically bound and both driven and damped by non-linear, stochastic forces.

A calculation of the oscillation amplitudes for a range of intensity ratios $x_0(r)$ is also shown in Fig. 4.3. The double-log plot clearly illustrates the different dynamical regimes. For low intensities of the gain laser $r \ll r_t$ the ion occupies a thermal state. In the vicinity of the threshold $r \sim r_t$ the oscillation amplitude grows continuously until it reaches the coherent regime $r_t < r < r_s$. Finally, the amplification is so large that the motion becomes unstable $r \geq r_s$. Unfortunately, no analytical expression for r_s has been found yet. The plot also shows for comparison a calculation excluding spontaneous emission. This illustrates the role of fluctuations: Spontaneous emission shifts and "softens" the threshold. The general structure of the oscillation amplitude vs. the intensity ratio shown in Fig. 4.3 is very similar for all possible parameter sets in domain $\mathcal{A}$. A numerical study of the parameter space reveals
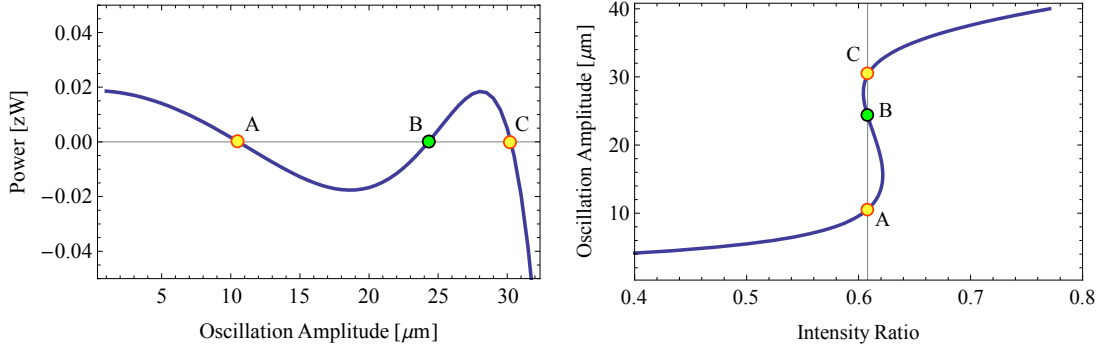
Figure 4.4.: *Origin of bistability in domain $\mathcal{A}$. The net power exerted on the ion, shown in the plot of $\langle P(x_0) \rangle$ to the left, has three roots. A zero crossing with a negative slope is dynamically stable since perturbations that lead to larger oscillation amplitude are damped and vice versa, while the opposite applies for positive slopes. Therefore, A and C are dynamically stable and B is dynamically unstable. The plot of $x_0(r)$ to the right shows the signature of bistability as an S-shaped threshold. Points with a positive slope correspond to stable oscillation and vice versa. The vertical grid line indicates the intensity ratio assumed in the left plot.*

following qualitative behaviour: The "width" of the coherent plateau r_s/r_t is proportional to $|\Delta_c|/\Delta_g$ and the threshold becomes steeper if both detunings get larger.

Remarkably, for "large" detunings of the cooling beam the dynamics can become bistable in the vicinity of the threshold. Again, no analytical expression could be found to quantify "large" yet, but numerical studies indicate that the absolute value of the cooling laser detuning must exceed $|\Delta_c| > 3\Gamma/2$. Fig. 4.4 illustrates the origin of bistability. For certain sets of parameters (r, Δ_c, Δ_g) the net mechanical power $\langle P(x_0) \rangle$ has three roots. Two of them, A and C have negative slopes and are thus dynamically stable, while B is unstable. In the bistable regime the ion can thus be either in a thermal or in a coherent state. The second graph shows how this translates into a plot of the oscillation amplitude vs. the intensity ratio.

Bistability entails hysteresis. This is illustrated in detail in Fig. 4.5 based on a discussion of $\langle P(x_0) \rangle$, but can also be understood from a plot of $x_0(r)$ as in Fig. 4.4: Assume, that the ion is initially in a thermal state and the intensity is steadily increased. At the point where the gradient becomes infinite the ion hops discontinuously to a coherent state. Likewise, if the intensity ratio is decreased again, it remains in the coherent state until the gradient becomes infinite again and the oscillation discontinuously collapses.

The surprising phenomenon of regenerative oscillation of a single ion allows to draw remarkable parallels to other systems. The mechanical oscillation of the ion behaves much like a laser if one identifies the output power with the oscillation amplitude x_0 and the pump power with the intensity ratio r: There is a threshold for oscillation which is started by fluctuations. Moreover, since the threshold for laser oscillation behaves analogous to a second-order phase transition [58], this suggests that this also applies to the oscillation of the ion. In this case the coherent part of the oscillation amplitude could be identified as order parameter, but this requires further investigations.
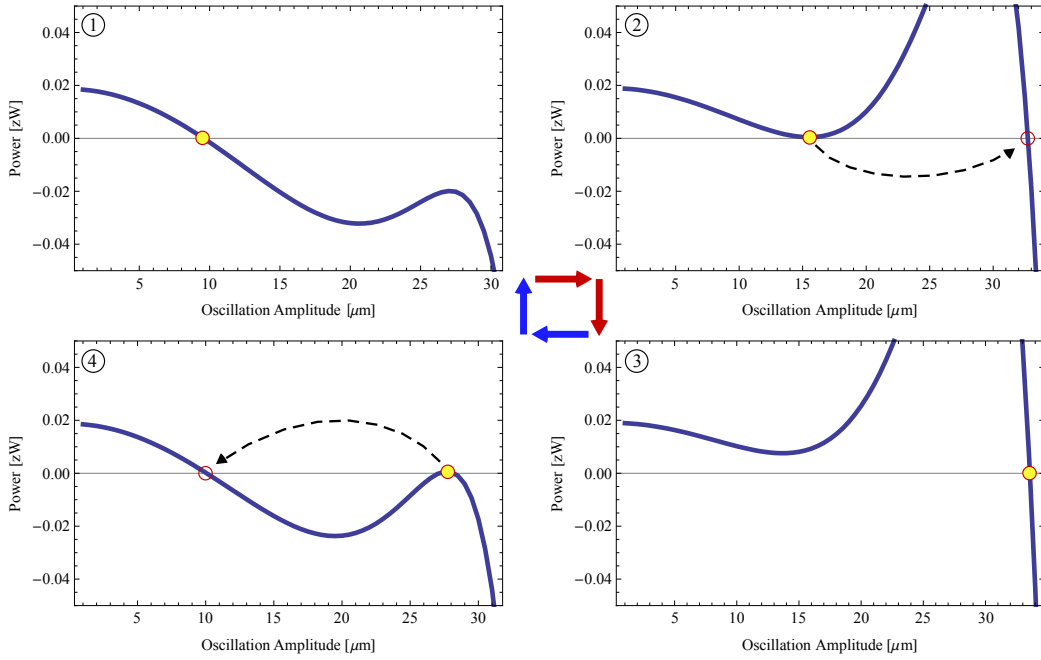
Figure 4.5.: *Origin of hysteresis in domain $\mathcal{A}$ (view clockwise, red arrows (blue arrows) indicate an increasing (decreasing) intensity ratio). The first plot shows the net mechanical power $\langle P \rangle$ versus oscillation amplitude x_0 for low gain laser intensity $r < r_t$, which gives one stable operating point. As the intensity is increased the first operating point vanishes and the ion hops discontinuously to the next. If the intensity is lowered again, as shown in panels 3 and 4, the ion remains at the operating point with larger oscillation amplitude until it disappears and the oscillation breaks down. See Fig. 4.10 for a measurement.*
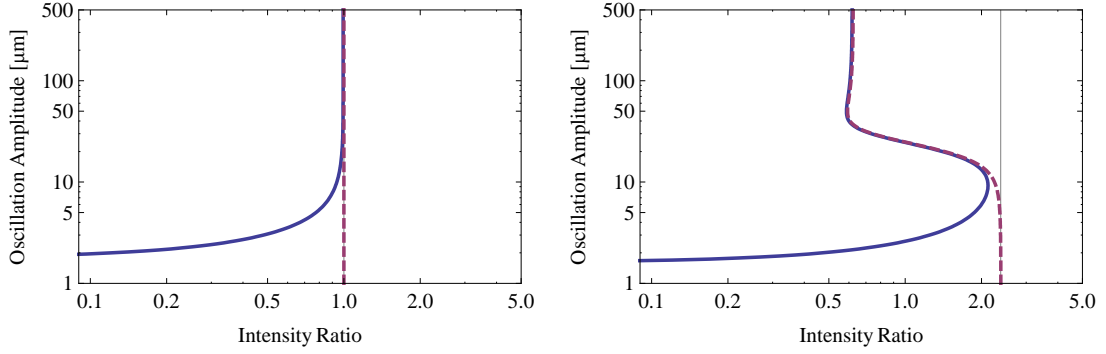
Figure 4.6.: *Domain $\mathcal{B}$. The left plot shows the transition between domains $\mathcal{A}$ and $\mathcal{B}$ for $|\Delta_c| = \Delta_g$. The right plot of $x_0(r)$ was calculated for the same conditions as in Fig. 4.3 but with exchanged detunings ($\Delta_c = -5\Gamma/8$, $\Delta_g = +\Gamma$). The vertical gridline indicates the threshold calculated from Eq. 4.6, which does not agree well with the full calculation because fluctuations are significant. In this domain the threshold r_t equals the stability limit r_s.*
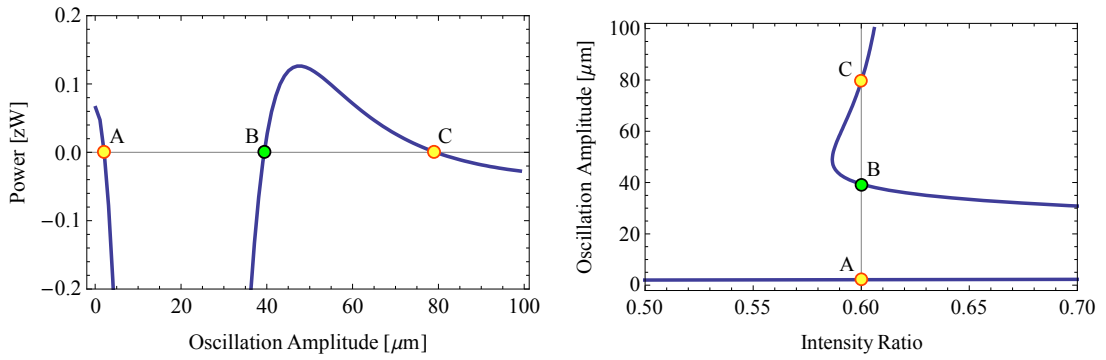
Figure 4.7.: *Bistability in domain $\mathcal{B}$. The net power $\langle P \rangle$ has, similar to domain $\mathcal{A}$ (Fig. 4.4) three roots. However, in contrast to domain $\mathcal{A}$, bistability does not occur in the vicinity of the threshold, but far below. The $x_0(r)$ plot to the right is a magnification of Fig. 4.6 around $r \sim 0.6$.*

.

Domain $\mathcal{B}$

Similar to domain $\mathcal{A}$ an ion in domain $\mathcal{B}$ also exhibits four dynamical regimes (thermal, coherent, bistable, unstable), but with two important differences: The threshold r_t marks the onset of unstable motion and the bistable regime is not located in the vicinity of the the threshold. A plot of the oscillation amplitude vs. intensity ratio typical for domain $\mathcal{B}$ is shown in Fig. 4.6. As in domain $\mathcal{A}$ the plot of $x_0(r)$ shown in Fig. 4.6 is a blueprint for other detunings, i.e. the general behaviour remains the same. The "prow" becomes more pronounced as the ratio of $\Delta_g/|\Delta_c|$ increases.

A further characteristic difference of bistability in domains $\mathcal{B}$ and $\mathcal{A}$ except the position is that in domain $\mathcal{B}$ the two dynamical states are not accessible by intensity variations of e.g. the gain laser. Thus, bistability does not lead to hysteresis with respect to r. Switching between the two states must rather be induced by an external perturbation. This can be seen in Fig. 4.7.
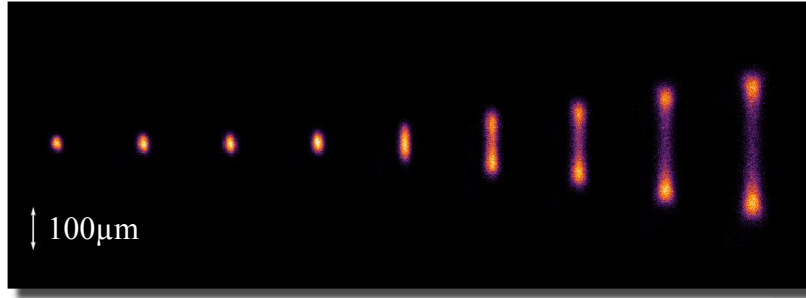
Figure 4.8.: *Series of images of a single regeneratively oscillating ion. For each image the ratio of gain to cooling laser intensity was increased in approx. equal steps. The threshold behaviour is clearly visible. Further, the images provide convincing evidence that the gain laser drives coherent motion rather than heating the ion incoherently. The bright lobes correspond to the turning points of the classical motion where the ions spends a comparatively long time.*

4.2. Observations

The experiments were performed in the endcap trap using an identical setup as for the spectroscopy experiments including the phase-lock to the frequency comb. An important difference is that here the cooling beam's intensity was stabilized, too. Both experiments benefited from each other thanks to a fruitful interplay. The metrology of the $^{24}Mg^+$ resonance together with the absolute frequency stabilization of the gain and cooling beam allowed to set the detunings extremely precisely. This is one of the origins of the remarkable agreement of experimental data with ab-initio calculations (no adjustable parameters!) presented in this section. On the other hand, the deeper understanding of the interaction of the gain (=spectroscopy!) laser with the motional state of the ion was very useful for the metrology experiments.

The experiments focused on the "non-trivial" regimes of regenerative oscillations and bistability, which we both studied in domain $\mathcal{A}$. A first, qualitative, set of measurements aimed at providing evidence for a threshold and that the ion actually oscillates classically in the coherent regime. To this end we recorded a set of images of a single ion where the intensity ratio r was increased in roughly equal steps. The compelling result is shown in Fig. 4.8. Not only is the threshold clearly visible, but also does the intensity profile clearly show an oscillation. The bright lobes correspond to the classical turning points of the motion where the ion spends more time. A thermal distribution would appear fundamentally different: Here the spatial probability density would be a Gaussian.

A second set of experiments studied the threshold and coherent regime quantitatively. Measurements of $x_0(r)$ for two different detunings together with a comparison with theoretical predictions are shown in Fig. 4.9. The astoundingly good agreement of ab-initio calculations with measured data is the result of a scrupulous determination of the experimental parameters. Prior to a measurement run the secular frequency is measured precisely by secular excitation, i.e. by applying an external perturbation and monitoring the fluorescence of the ion (see also Sec. 4.3). In a second step we use this result to calibrate the imaging system: We load two ions and relate the measured separation in pixels to the ion-ion distance predicted due to the measured secular frequency (Eq. 2.15). To conclude the preparations a spatially homogenous intensity profile of the cooling beam has to be ensured. This is because we use the beam that enters the apparatus at an angle oblique to the trap's principal axis for cooling
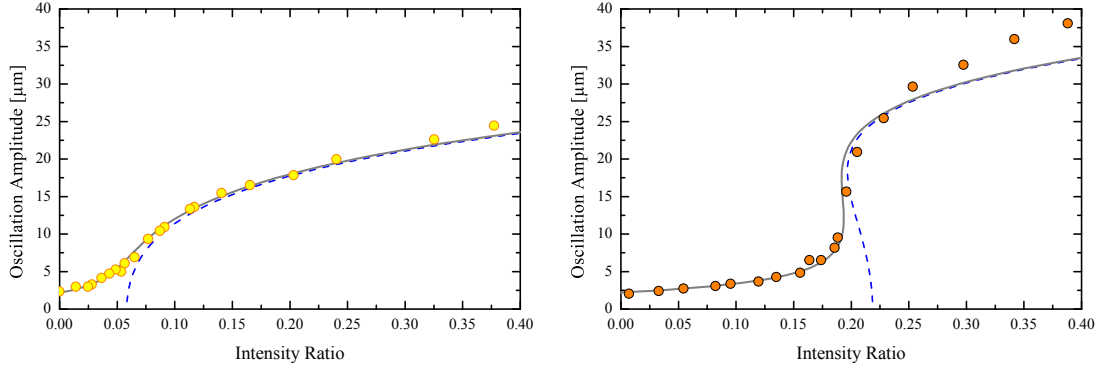
Figure 4.9.: *Measured oscillation amplitudes as a function of gain to cooling laser intensity ratio in domain A. In both cases the ion was bound with a secular frequency of 71 kHz and damped by a cooling laser detuned 74 MHz below resonance. The gain laser detuning is 12 MHz in the left plot and 40 MHz in the right plot. Solid and dashed lines are theoretical predictions that were calculated ab-initio with no adjustable parameters. The solid lines are the result of a full calculation, while the blue dashed lines were obtained excluding spontaneous emission.*

in order to cool the degrees of freedom orthogonal to the oscillation. On the other hand this leads to a Gaussian intensity profile of the cooling beam, so the ion experiences a spatially inhomogeneous cooling force. If both the cooling and gain beam were collinear to the linear trap axis, spontaneous emission would heat the radial directions and the ion would be lost quickly. Instead of including the spatially varying cooling power into the model, we try to minimize the intensity variations by alignment and focusing. To this end we load a very long ion chain to measure and match the brightness of the individual ions. The measurement run itself is carried out as follows. Each data point is a pair consisting of the intensity ratio r and the oscillation amplitude x_0. The raw data for the oscillation amplitude are a 40 s long exposure of the oscillating ion, as shown in Fig. 4.8. This we integrate along the direction perpendicular to the oscillation to obtain an intensity profile from which we determine the full-width at half maximum. The measurement of the intensity ratio is based on the detected fluorescence. First the intensity of the cooling beam is measured by tuning it slightly below resonance, blocking the gain beam and counting photons for 10 s. In a second step the gain beam is set to the same frequency, the cooling beam is blocked and again fluorescence is measured for 10 s. The ratio of detected counts gives the desired intensity ratio[1].

We also measured hysteresis, the result is shown in Fig. 4.10. Here, we only obtained qualitative agreement with ab-initio calculations. This is mainly because it is hard to ensure a sufficiently homogeneous intensity profile of the cooling laser for the large oscillation amplitudes in this regime. Fig. 4.9 shows that the model-data agreement becomes poorer above $35\,\mu$m while the coherent state oscillates with an amplitude of nearly $70\,\mu$m.

4.2.1. Outlook

The presented theoretical and experimental results are a snapshot of ongoing research and mark only the beginning. Much of the appeal of this system is its conceptual simplicity, so analytical solutions for r_t, r_s and the onset of bistability and its "coercivity" would certainly

---

[1]More elaborate calibration schemes involving several steps have been developed to overcome certain limitations due to our apparatus, but the general notion remains the same.
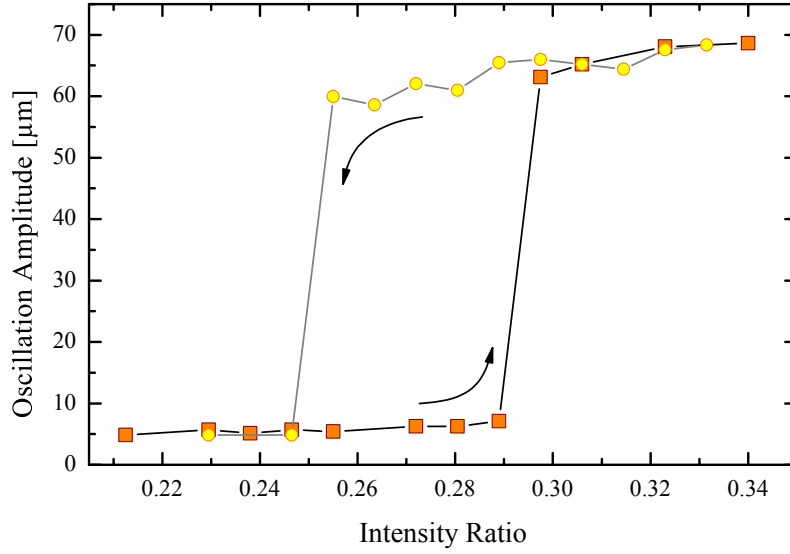
Figure 4.10.: *Hysteresis observed in domain $\mathcal{A}$. The orange data points show the oscillation amplitude as the intensity ratio is increased. At an intensity ratio of about 0.29 the oscillation starts discontinuously. As the intensity ratio is decreased (yellow data points) the gain laser intensity can be lowered below the point where the oscillation started, down to about 0.25. Then, the oscillation again collapses discontinuously. Here, the cooling laser detuning is -74 MHz, the gain laser is set to +50 MHz and the ion is confined with $\omega_s = 68$ kHz.*

valorize the theoretical framework. The conjectured analogy of the threshold for regenerative oscillations to a second-order phase transition should be studied in more detail. It would not be surprising if interesting phenomena related to phase transitions could be studied in this system that are otherwise not accessible, thanks to the exceptionally high degree of control a single trapped ion offers.

4.3. Secular scans

A standard technique to non-destructively perform mass spectroscopy of the contents of a trap are optical secular scans. The basic idea is to resonantly excite the secular motion of the trapped ions while simultaneously observing their laser fluorescence. Since the secular frequency ω_s is proportional to the charge-to-mass ratio Q/m this gives information on the mass of the trapped species, e.g. assuming they are only singly ionized. The theoretical framework developed in the previous sections allows to elucidate the mechanism and find optimum conditions.

The working principle is illustrated in Fig. 4.11. A single ion is cooled by a laser detuned below resonance. Then, a RF perturbation is applied to an external electrode in order to resonantly excite the motion of the ion with a certain power P_{sc}. On resonance energy is transferred to the oscillation and the amplitude x_0 grows. However, this also causes the cooling power to increase. If P_{sc} is sufficiently small the cooling power can balance P_{sc} and a stable oscillation emerges, similar to the oscillations excited by a blue-detuned laser in the previous section. Depending on the oscillation amplitude and detuning this causes the fluorescence level either to increase or to decrease, thus leading to a peak or to a dip in the
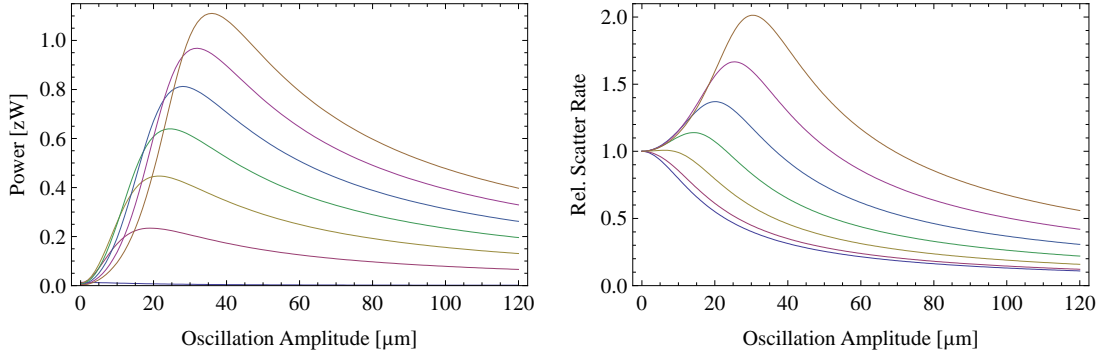
Figure 4.11.: *Working principle of secular scans. An external RF field excites the secular motion with a certain power P_{sc}. This causes the oscillation amplitude and thus cooling power to increase until it balances the excitation power and an equilibrium is reached (provided P_{sc} is small enough so that this condition can be met). The cooling power calculated for several detunings, ranging from 0 to $-\Gamma$ in steps of $\Gamma/6$ is shown in the left plot. The right plot illustrates for the same set of detunings how the scattering rate changes as the oscillation amplitude increases. Both plots were calculated for Mg^+ confined with $\omega_s = 70\,kHz$ and a saturation parameter of 10^{-3}. For small detunings the rate decreases, for large detunings the rate initially increases before it monotonically decreases. Thus, depending on the detuning, the signature can either be a dip or a peak in the fluorescent intensity.*

excitation spectrum.

The theory presented in the previous section allows to study this quantitatively and maximize the signal. The optimization procedure is as follows: In a first step for a given detuning the maximum possible stable oscillation amplitude was determined, which is at the maximum cooling power (Fig. 4.11, left). Then, the change of the scattering rate is calculated for this oscillation amplitude (Fig. 4.11, right). Finally, the resulting signal is weighted by the signal-to-noise ratio which is proportional to the square-root of the scattering rate. The result is shown in Fig. 4.12. The optimum detuning for a negative signal (dip) is about -0.05 Γ (-2 MHz for Mg^+) and about -Γ for a positive signal (peak). Note, that the contrast is minimal if the laser is set to a detuning optimal for cooling -$\Gamma/2$. The calculation shows that the secular signal is maximized for the "dip" case with a laser tuned very close to resonance. However, in practice it may be challenging to set the laser with high precision to the desired detuning and also this is close to the stability limit of a single ion cooled by one laser as discussed in the spectroscopy section, (Fig. 3.5). Including these considerations, a detuning of $\Delta = -\Gamma$ appears optimal.

An example of a secular resonance measured in the endcap trap for a large detuning of the cooling laser is shown in Fig. 4.13.
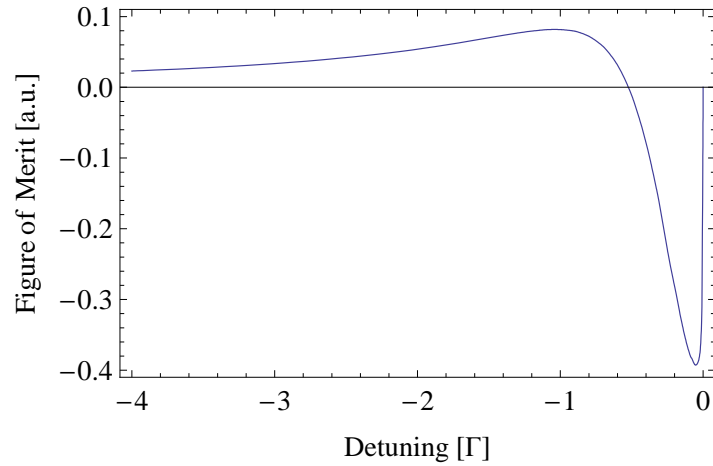
Figure 4.12.: *Optimum conditions for secular scans. See text for more details.*
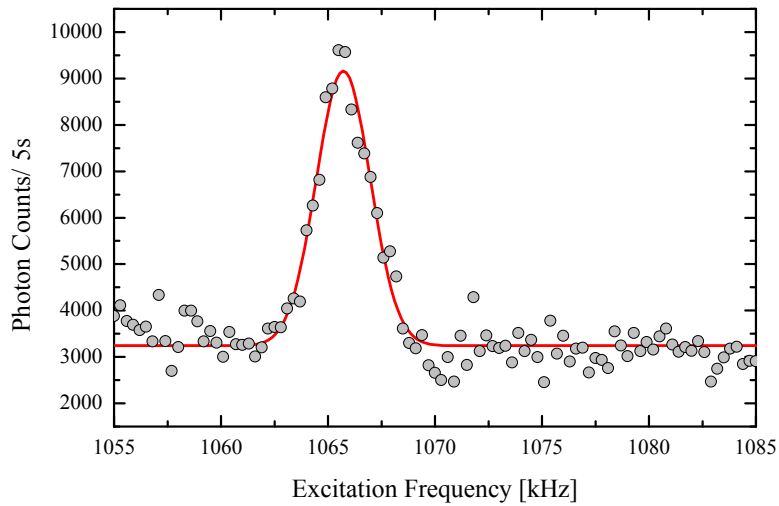
Figure 4.13.: *Radial motional resonance of a single Mg$^+$ ion in the endcap trap. The cooling laser detuning of $-1.5\,\Gamma$ is close to the optimum for positive signals. To test the robustness neither the intensity nor the frequency of the cooling laser were stabilized.*

5. The route towards 1S-2S in He$^+$

This chapter is a collection of coauthored manuscripts that summarizes progress towards 1S-2S frequency comb spectroscopy in He$^+$. A detailed theoretical study of the feasibility of the experiment and its impact on tests of bound state quantum electrodynamics is presented as well as important experimental milestones: The first demonstration of a suitable light source to excite the transition, a high-repetition rate XUV frequency comb, and a subsequent second generation system with orders of magnitude higher output power. In addition to the manuscripts so far unpublished proof-of-principle experiments that demonstrate the feasibility of the envisioned cooling and detection scheme are shown.

The theoretical considerations were done jointly with theorists from the Max-Planck-Institute of Nuclear Physics in Heidelberg and led to deeper insights into the role of ionization in the renowned hydrogen 1S-2S experiment. The resulting publication is also included in this chapter.

5.1. Feasibility and impact

The following manuscript is an in-depth study of the feasibility of high-precision spectroscopy on the 1S-2S transition in trapped He$^+$ ions using XUV frequency combs and analyzes its impact on tests of bound-state QED.

This is a tantalizing goal: Contributions of disputed higher-order QED corrections like e.g. B_{60} and B_{7i} could be tested for the first time. Moreover, a successful experiment would provide proof for the expectation that XUV frequency combs are quasi-cw sources suitable for high-precision spectroscopy of two-photon transitions far below 200 nm, where no other sources exist.

However, albeit possible, the experiment is shown to be challenging and unique compared to the vast majority of trapped ion metrology experiments for several reasons: All relevant wavelengths are deep in the XUV around 61 nm and below. CW lasers are not available and pulsed lasers typically have large bandwidth and low power. Even worse, light around 60 nm is absorbed by virtually everything, so the entire experiment has to be kept in vacuum conditions, no refractive optics are available and the best normal-incidence mirrors reflect only about 30 %. In addition, no suitable laser source exists that could drive a strong cycling transition, so standard cooling and detection schemes (i.e. "shelving") fail. Finally, the 1S-2S "clock" transition can be ionized by the spectroscopy laser, so frequent reloading will be necessary.

In brief, the analysis identifies following strategy as currently most promising: A high repetition rate XUV frequency comb is a suitable light source and can drive a two-photon transition much like a cw laser - the excitation rate is equivalent to a cw laser of the same average power (provided the pulses are not chirped) and the effective linewidth is given by a single comb mode and not the pulse bandwidth. However, power is scarce and about 1 μW average power focused to $w_0 \cong 0.5 \, \mu$m is required to obtain a rate of 1 Hz. Therefore, spectroscopy should be performed on single He$^+$ ions with tightly focused XUV beams. A second ion species introduced into the trap solves both the cooling and the detection issue. The He$^+$ ions are cooled sympathetically by the auxiliary ions which also serve as "detectors" as follows: Successful 2S excitations will be accompanied by ionization, so the production of He^{++} ions is a convenient signature. The trap can be operated such that He^{++} ions remain stored, which can then be detected by secular excitation (Sec. 4.3). The tight focusing necessary to obtain appreciable rates imposes stringent requirements on alignment precision. These can be relaxed by storing ions in a very steep trap and exciting 1S-2S collinearly. Finally, a suitable trap should provide multiple segments that serve as reservoirs for reloading. Summarizing, the envisioned procedure is as follows: i) Load one He$^+$ and one coolant ion into the trap ii) Sympathetically cool the He$^+$ ion iii) Excite the 1S-2S transition radially. If successful, a He^{++} will be produced iv) Detect presence of He^{++} ion by secular excitation v) Step XUV frequency and repeat.

Progress and status

Important progress has been made towards this goal, including the following milestones:

- Demonstration of a high-repetition rate XUV frequency comb by C. Gohle in 2005.

- Improvement of output power at 60.8 nm by five orders of magnitude over first demonstration by A. Ozawa in 2008. Now, close to a μW is available.
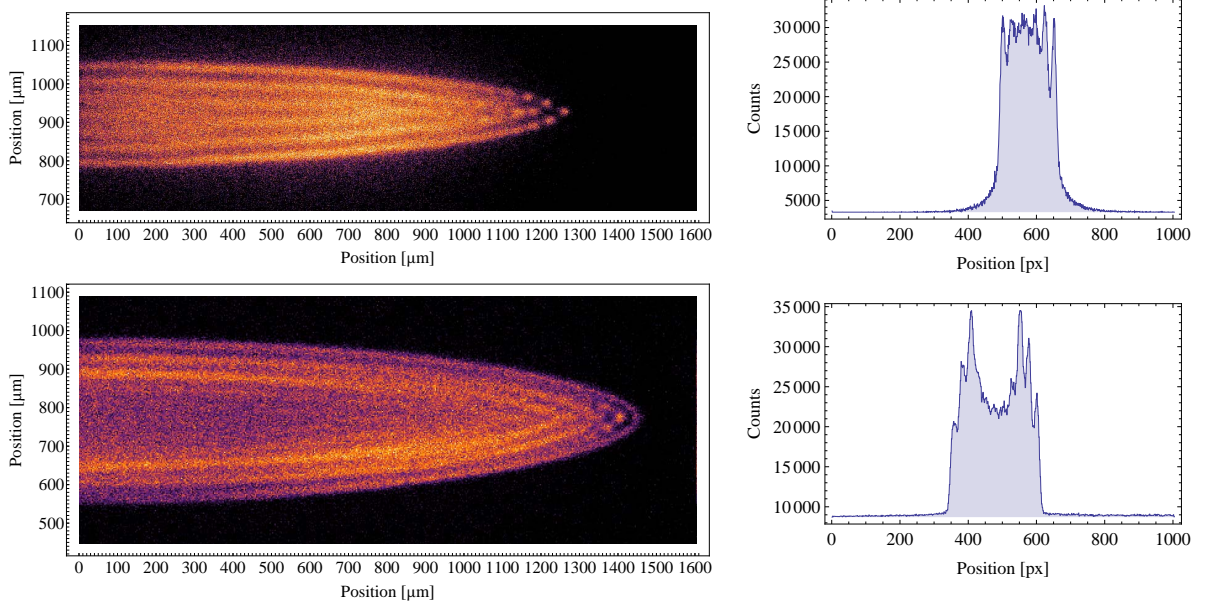
Figure 5.1.: *Images of large Mg^+ crystals stored in the 6-rod trap. The plots to the right show a vertical intensity profile integrated over 15 % of the images. The upper two figures show a pure Mg^+ crystal. For the lower two figures lighter ion species were loaded by operating the electron gun in a 10^{-6} mbar atmosphere of helium after loading Mg^+. The dark region of non-fluorescing ions in the center is due to lighter ions, most likely predominantly He^+.*

- Simultaneous storage and (most likely) sympathetic cooling of He^+ by Mg^+ (see Fig. 5.1).

- Detection via secular scans studied theoretically and demonstrated experimentally (see Sec. 4.3).

Next steps

The feasibility and complexity of the experiment scales very sensitively with the available XUV power. Therefore, first and foremost more powerful "third generation" XUV frequency combs need to be developed that can generate $\gg 10\,\mu W$ average power. Important open questions that need to be addressed concern the spatial beam quality (focusability) and spectral properties (coherence at $61\,nm$, mode linewidth and chirp) of the XUV frequency comb. An important practical problem that arises in view of the low reflectivity and low transmission of available materials is the efficient transport of the scarce XUV light from the source to the ion. Concerning the ion traps very steep ($\omega_s(He^+) \gg 10\,MHz$) traps with multiple segments need to be developed and the ion shuttling/ reloading process must be studied in detail.

Feasibility of coherent xuv spectroscopy on the 1*S*-2*S* transition in singly ionized helium

M. Herrmann,[1] M. Haas,[2] U. D. Jentschura,[3] F. Kottmann,[4] D. Leibfried,[5] G. Saathoff,[1] C. Gohle,[1] A. Ozawa,[1] V. Batteiger,[1] S. Knünz,[1] N. Kolachevsky,[1,*] H. A. Schüssler,[6] T. W. Hänsch,[1,7] and Th. Udem[1]

[1]*Max-Planck-Institut für Quantenoptik, 85748 Garching, Germany*
[2]*Department of Diagnostic Radiology, Medical Physics, University Hospital Freiburg, 79095 Freiburg, Germany*
[3]*Department of Physics, Missouri University of Science and Technology, Rolla, Missouri 65409-0640, USA*
[4]*Institut für Teilchenphysik, ETH Zürich, 8093 Zürich, Switzerland*
[5]*National Institute of Standards and Technology, Boulder, Colorado 80305-3328, USA*
[6]*Department of Physics, Texas A&M University, College Station, Texas 77843, USA*
[7]*Ludwig-Maximilians-Universität München, 80539 München, Germany*

The 1*S*-2*S* two-photon transition in singly ionized helium is a highly interesting candidate for precision tests of bound-state quantum electrodynamics (QED). With the recent advent of extreme ultraviolet frequency combs, highly coherent quasi-continuous-wave light sources at 61 nm have become available, and precision spectroscopy of this transition now comes into reach for the first time. We discuss quantitatively the feasibility of such an experiment by analyzing excitation and ionization rates, propose an experimental scheme, and explore the potential for QED tests.

I. OVERVIEW

The study of simple hydrogenic systems has played a central role in the development of physics. Theory is highly developed for such systems and can provide extremely accurate predictions to be compared with high-precision experimental data. Prominent tests of bound-state quantum electrodynamics (QED) include, e.g., two-photon spectroscopy on atomic hydrogen [1,2], *g* factor measurements on hydrogenlike carbon [3] and oxygen [4], or the study of exotic systems such as positronium [5] or muonium [6].

The 1*S*-2*S* two-photon transition in singly ionized helium (Fig. 1) is a sharp resonance in a hydrogenic system (linewidth $\Gamma = 84$ Hz [7]; quality factor $Q = 1.2 \times 10^{14}$) that extends the list of simple bound systems which have high potential to accurately test fundamental theories. Especially in comparison to the very successful QED tests in hydrogen 1*S*-2*S* spectroscopy, it reveals its strengths: QED corrections of higher order, which are currently of great interest, scale in hydrogenic systems with large powers of the nuclear charge *Z*. An example is given by higher-order two-loop self-energy corrections of order $\alpha^2(Z\alpha)^6$, where α denotes the fine-structure constant. The transition energy scales as Z^2; hence, the sensitivity to the interesting higher-order corrections is up to an order of magnitude larger. Further, since the ^{4}He nucleus carries no angular momentum, the centroid frequency is measured directly. Most importantly, He$^+$ is a charged particle and therefore may be trapped and (sympathetically) cooled in a radio-frequency or Penning trap. As demonstrated in Ref. [8], this allows one to prepare a cold ($T \lesssim 20$ mK) sample of helium ions, subject to low systematic uncertainties such as second-order Doppler shifts, collisional shifts, and time-of-flight broadening, and is thus ideally suited for high-precision spectroscopy.

Driving the 1*S*-2*S* transition in He$^+$ requires radiation at 61 nm. The recently demonstrated extensions of (near-infrared) frequency combs into the extreme ultraviolet (xuv) spectral region [9,10] represent the first coherent narrow-band sources for this wavelength. These first-generation sources, however, produced only 1 nW or less average power per harmonic in the xuv region. But we are witnessing rapid progress and current systems can now provide power levels approaching 1 μW [11,12]. In the second part of this paper (Sec. II), we therefore discuss available power levels at 61
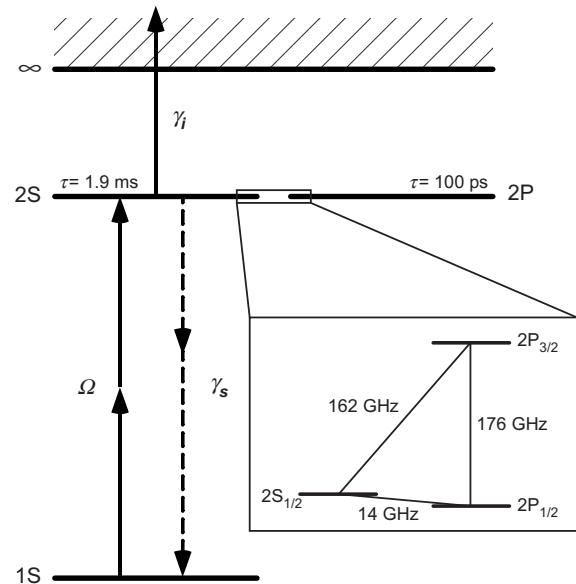
FIG. 1. Relevant energy levels of ^{4}He$^+$. The inset shows the fine structure and Lamb shift of the $n=2$ levels. After two-photon excitation from the ground state, the third ionizing photon reaches 6.8 eV into the continuum.

---

*Permanent address: P.N. Lebedev Physics Institute, Leninsky Prosp. 53, Moscow, 119991 Russia.

nm and analyze the excitation and ionization dynamics of He$^+$ for this regime. The analysis shows that spectroscopy of a small number of trapped ions with tightly focused xuv beams is currently the most promising approach. In Sec. III, we propose an experimental scheme for high-precision spectroscopy, and in Sec. IV, we explore its potential accuracy by analyzing expected systematic errors and, finally, in Sec. V, we quantitatively discuss the impact of such an experiment on QED tests.

II. EXCITATION DYNAMICS

A. xuv frequency combs

The $1S$-$2S$ two-photon resonance at 61 nm in He$^+$ (see Fig. 1) lies deep in the extreme ultraviolet about an octave beyond the LiF cutoff ($\sim$120 nm), which marks the shortest wavelength solid materials are transparent to. No continuous-wave (cw) lasers are available in this spectral region, so one has to resort to nonlinear conversion of powerful, typically pulsed, lasers or free-electron lasers. Four-wave mixing and high-harmonic generation (HHG) [13] in gaseous media are the most frequently chosen nonlinear processes. Among these approaches, HHG of a near-infrared femtosecond frequency comb is a particularly favorable approach for precision spectroscopy. Frequency combs excite two-photon transitions much like cw lasers and at the same time exhibit high peak intensities, which makes them well suitable for nonlinear conversion. This was recognized by Baklanov and Chebotaev [14] as early as 1976. They showed that the excitation of a two-photon transition with two counterpropagating frequency combs is equivalent to an excitation with a cw laser of the same average power, provided the pulses are transform limited and the comb mode spacing is at least twice as large as the linewidth of the transition [15]. This remarkable fact may be exemplified by considering a two-photon resonance ν_0 interacting with two anticollinearly propagating pulse trains, whose mode frequencies are given by the frequency-comb equation [16] $f_n = n f_r + f_c$, where f_n is the frequency of the nth mode of the comb, f_r is the repetition frequency, and f_c is the carrier-envelope offset frequency. If two photons from a mode f_{n_0} are in resonance $2(n_0 f_r + f_c) = \nu_0$ with the transition, then this is also the case for all other pairs of modes that lie symmetrically around $f_{n_0} = \nu_0/2$, for example, the sum of a red- and a blue-detuned mode, $(n_0 - 1) f_r + f_c + (n_0 + 1) f_r + f_c = \nu_0$. It can be shown [14] that for a transform-limited pulse all the modes add coherently and so the power of the entire comb contributes to the excitation of the transition. The effective linewidth is given by the linewidth of an individual comb mode, which can ultimately be as narrow as the best cw lasers [17], and not by the pulse bandwidth. Further, the ac Stark shift of the transition, an important systematic uncertainty, scales with the average power, not the peak power [18]. When the comb is scanned across the resonance, the spectrum repeats itself every half repetition rate, hence the requirement that the transition linewidth must be less than half the repetition rate. The main difference to the cw case is that the k vectors of the comb modes do not necessarily all cancel each other. For an atom excited by counterpropagating, but otherwise identical pulses, this does not cause a net shift but can lead to a broadening of the line. For unbound atoms this can be understood in the time domain as time-of-flight broadening because the duration of simultaneous interaction of moving atoms with the counterpropagating pulses is limited by the pulse-collision volume, which in turn is inversely proportional to the pulse bandwidth. Trapped atoms or ions can be localized within the pulse-collision volume so this effect does not occur. Thus, with respect to two-photon transitions, frequency combs can be regarded as quasi-cw sources allowing for high-resolution spectroscopy [18,19].

Owing to the high peak intensities of femtosecond frequency combs, it is possible to shift the comb from the ir to the xuv spectral region by HHG. This process occurs when atoms interact with a laser field whose peak intensity exceeds 10^{13} W/cm^2 so that the electric field of the laser becomes comparable to the Coulomb field that binds the electron to the nucleus. In this case a small fraction of the electron's wave function can be liberated by tunnel ionization, whereupon it is accelerated in the electric field and finally recombines emitting odd harmonics collinear with the driving laser field. In order to enable direct frequency-comb spectroscopy with these high harmonics, the following conflicting requirements have to be addressed: efficient generation of HHG requires large pulse energies and thus low repetition rates. Spectroscopy on the other hand favors well-separated modes, that is, high repetition rates.

Prior 2005 methods such as chirped-pulse amplification have been used to effectively concentrate a given average power of a laser in fewer pulses per second, thus sacrificing repetition rate for pulse energy. Typical repetition rates that allow for HHG with Ti:sapphire laser systems are in the kilohertz regime and represent a very dense frequency comb which may be considered a continuum unless the modes are stabilized to a linewidth much narrower than 1 kHz and are used to probe very narrow transitions. So far HHG with the highest repetition rate obtained by pulse selection and reamplification made use of regenerative amplifiers and reached 100 kHz [20]. In addition, high harmonics have been produced directly with a Ti:sapphire oscillator at 75 MHz, by exploiting the local field enhancement induced by resonant plasmons within a metallic nanostructure [21]. While the mode spacing would be suitable for high-resolution spectroscopy in both cases, the generated xuv power levels are currently too low for our application.

Currently the most promising route to push the repetition rates for HHG into the megahertz regime while maintaining high efficiency makes use of an enhancement resonator [9,10]. This method is similar to resonantly enhanced second-harmonic generation (SHG) that has been used for many years. However, there are extra requirements that need to be fulfilled in order to resonantly enhance all modes of the frequency comb simultaneously. First, the length of the cavity has to match the repetition rate of the laser and second, the group-velocity dispersion needs to be minimized so that the pulse retains its shape when circulating in the cavity. The collinearly generated high harmonics were extracted by total external reflection from an intracavity sapphire plate oriented at Brewster's angle for the fundamental laser. The frequency-

comb structure is expected to be preserved, which could be confirmed by heterodyne beats with the third harmonic.

We also wish to highlight the dramatic progress that is being made with high-power Yb-fiber lasers. Recent demonstrations achieved up to 68 W average power at a repetition rate of close to 1 MHz [22]. When combined with an enhancement resonator such a system can generate close to 1 μW of xuv power [12]. In fact it may even be conceivable that future systems could be used for high-harmonic generation directly from such a laser oscillator.

Finally, one could use amplified *finite* pulse trains. This approach has been used successfully for xuv spectroscopy on krypton [23,24] and xenon [25]. However, the observed linewidth is limited by the length of the pulse train, and it is challenging to control pulse-to-pulse phase shifts with an accuracy suitable for high-resolution spectroscopy. For this reason an "infinite" pulse train, i.e., a frequency comb, appears advantageous. We therefore limit the discussion in the following to spectroscopy with frequency combs.

B. Power at 61 nm

We assume that the xuv frequency comb is produced by high-harmonic generation in an external enhancement cavity for femtosecond pulses. For our discussion we write the output power as

$$P_{\text{xuv}} = P_{\text{ir}} G \epsilon r. \tag{1}$$

The incident power of the frequency comb, denoted by P_{ir}, is enhanced in an external cavity by a factor G, and converted into the xuv with a single-pass conversion efficiency of ϵ. The latter depends strongly on peak intensity and focusing, so in total P_{xuv} scales highly nonlinearly with P_{ir}. The generated radiation is extracted from the cavity by means of an output coupler of efficiency r. The first-generation setup described in Ref. [9] enhanced $P_{\text{ir}} = 700$ mW in the infrared, provided by an oscillator with a repetition rate of $f_r = 112$ MHz and a pulse length of $t_p = 20$ fs, by a factor $G = 54$, resulting in 38 W circulating in the cavity. The stored pulses were converted into the xuv with a single-pass conversion efficiency of $\epsilon = 2 \times 10^{-12}$ for the 13th harmonic at 61 nm. The xuv output coupler had an efficiency of 14% at that wavelength, resulting in roughly 10 pW of power extracted. As we will show in Sec. II D this is orders of magnitude short of obtaining a reasonable transition rate. In this experiment, though, the 13th harmonic was in the cutoff region and far from saturation.

Recently, two "second-generation" systems were reported that are capable of producing xuv power levels approaching 1 μW. In [12] a high-power (10 W) 136 MHz repetition rate Yb-fiber laser source together with a new low-dispersion outcoupling method allowed storage of 2.6 kW of 100 fs pulses. Here, the power in the 17th harmonic at 63 nm was measured to be 54 nW, a 5000-fold improvement over the power at 61 nm reported in [9]. We followed a different strategy [11] and reduced the repetition rate to 10.8 MHz. Together with careful dispersion management [26] this allowed us to observe even higher power levels near 61 nm, namely, 840 nW at the 13th harmonic. When comparing these two

results the different wavelengths of the driver pulses need to be taken into account. Although longer wavelengths allow one to push the cutoff to higher energies, the harmonic yield decreases $\propto \lambda^{-x}$, where exponents in the range of $x = 3, \ldots, 6$ are being discussed [27].

It is clear that more powerful femtosecond oscillators and improved enhancement cavities will lead to higher stored pulse energies and thus to higher xuv power levels. The details of the scaling of the output power as a function of the experimental parameters are quite involved, but as a general guideline we note the following:

(i) The output power of the harmonics scales with a large exponent of the peak intensity. The value of the exponent depends on the experimental parameters and has been measured to be about ~ 9 for the 11th harmonic in [9].

(ii) Looser focusing increases the interaction volume $\propto w_0^4$ and reduces the adverse Guoy phase shift $\propto w_0^2$, where w_0 is the Gaussian beam waist. In fact, it has been shown that the conversion efficiency scales as $\epsilon \propto b^3 \propto w_0^6$ [28], where b is the confocal parameter of the focused ir beam.

(iii) Single-pass conversion efficiencies on the order of 10^{-7} are reported to be typical for HHG in a gas jet using chirped-pulse amplifier (CPA) systems [13], with records reaching up to $\epsilon \sim 3 \times 10^{-4}$ [29] for the 13th harmonic. This shows that even slight improvements can lead to orders of magnitude higher output, owing to the nonlinearity of the process. Generally speaking, the xuv output is maximized by optimizing the system such that an intensity in the range $5 \times 10^{13} - 10^{14}$ W/cm^2 is obtained with the largest possible focus.

For spectroscopy the focused average intensity is the relevant parameter, not the power. Previous experiments have shown that HHG radiation is typically emitted in a (near-)diffraction-limited beam [13]. The high beam quality and the short wavelengths therefore allow tight focusing in principle, but will probably be limited by the surface accuracy of the mirrors used. Typical manufacturer specifications are around $\lambda/10$ at 633 nm [30], which corresponds to only $\sim \lambda$ at 61 nm. Nonetheless, in Ref. [31] the 27th harmonic of a Ti:sapphire femtosecond laser at 29.6 nm was focused down to 1 μm spot size using an off-axis paraboloid with a surface accuracy of $\lambda/8$ at 633 nm. The spot size exceeded the diffraction limit in this case only by less than a factor of 2.

Since virtually all materials absorb significantly around 60 nm, delivering the xuv beam from the source to the He$^+$ ion with low loss presents a challenging task. First, the diverging xuv beam has to be directed at and focused on the ions. To our knowledge, the highest reflectivity normal-incidence mirrors for 61 nm reported so far are B$_4$C-Ir multilayers that reflect only about 33% [32]. The use of grazing incidence mirrors reduces losses significantly and also allows tight focusing, but is experimentally more demanding. With arrangements of two orthogonal grazing incidence elliptical mirrors such as the Kirkpatrick-Baez design [33], diffraction-limited focusing of x rays at the 100 nm level has been achieved [34]. Second, from the xuv spectrum generated, one might want to isolate the desired wavelength to suppress ionization and ac Stark shifts from the strong ir and other harmonics. This could be done, e.g., by replacing a beam steering or collimation mirror with a toroidal grating. An

elegant alternative is to place the grating inside the HHG cavity as a replacement for a Brewster window as described above [12]. A thin aluminum foil is an interesting alternative to diffractive optics, which acts as a bandpass in the region of 17–83 nm, although the transmission is very low, only about 10% at 60 nm for 150 nm thickness [35]. Finally we note that if the experiment is performed on trapped ions, as our analysis in Secs. II D and III suggests, two vacuum chambers at unequal pressures need to be connected: An ultrahigh vacuum chamber housing the ion trap ($\leq 10^{-10}$ mbar) and the xuv generation chamber which is at much higher pressure due to the gas jet ($\geq 10^{-6}$ mbar).

Depending on the available xuv power, very simple to highly complex "beam lines" can be thought of. In a simple approach two normal-incidence off-axis paraboloids collimate, direct, and focus the xuv light on the He$^+$ ions, and a thin aluminum foil provides coarse wavelength selectivity and acts as a physical barrier between the vacuum systems. However, this way only about 1% of the power is delivered to the ion. Sophisticated grazing incidence focusing elements with a windowless connection by differential pumping can improve the efficiency by more than an order of magnitude.

In our calculations we assume transform-limited pulses. However, the xuv pulses may posses a temporally varying carrier phase due to the HHG process itself. The largest contribution is expected to be a negative linear chirp [36]. The impact on the excitation rate depends on the details of the spectral phase and is therefore difficult to predict. In case the effect will turn out to significantly reduce the excitation rate, it is possible to precompensate the spectral phase, e.g., by shaping the ir driver pulse accordingly [37], although this will reduce the achievable peak power in the ir and thus the xuv power.

The 10^4-fold improvement from the first- to second-generation cavity-assisted HHG sources and the highly non-linear response to the stored power raise hope that further significant improvements can be expected. In total, it does not seem unrealistic to expect time-averaged intensities exceeding 10^7 W/m^2=10 μW/μm^2. For example, $P=10$ μW focused down to $w_0=0.5$ μm yields $I=2P/\pi w_0^2=25$ μW/μm^2 on axis.

C. Excitation dynamics

We model the He$^+$ ion as an open two-level system including spontaneous decay and ionization. The latter is important since any hydrogenic system excited from the ground state to a nS or nD state with two photons may be ionized by a third photon of the same laser field. As explained in Sec. II A we treat the xuv comb as a cw laser with the same time-averaged power [14].

From a master equation for the two-level density matrix ρ, we derive, after applying the rotating wave approximation, the following set of equations for the ground- (ρ_{11}) and excited-state (ρ_{22}) populations and coherences ($\rho_{12}=\rho_{21}^*$; for a detailed discussion, see Ref. [38]):

$$\dot{\rho}_{11} = -\Omega \, \text{Im}(\rho_{12}) + \gamma_s \rho_{22}, \quad (2a)$$

TABLE I. Various physical quantities (two-photon Rabi frequency coefficients, ionization width coefficients, ac Stark coefficients, and spontaneous decay constants), which are related to atomic structure used in the calculations [38] for He$^+$ 1S-2S spectroscopy. We follow the conventions of Ref. [38].

β_{12}	2.30164×10^{-6} Hz W^{-1} m^2
β_{ioni}	7.51609×10^{-6} Hz W^{-1} m^2
β_{ac}	1.04236×10^{-5} Hz W^{-1} m^2
γ_s	526.72 rad s^{-1}

$$\dot{\rho}_{12} = -i\Delta\omega\rho_{12} + \frac{i\Omega}{2}(\rho_{11}-\rho_{22}) - \frac{\gamma_i + \gamma_s}{2}\rho_{12}, \quad (2b)$$

$$\dot{\rho}_{22} = \Omega \, \text{Im}(\rho_{12}) - (\gamma_i + \gamma_s)\rho_{22}. \quad (2c)$$

Here, Ω is the two-photon Rabi frequency defined as

$$\Omega = 2(2\pi\beta_{12})I, \quad (3)$$

where β_{12} denotes the squared transition matrix element and I is the total (time-averaged) intensity sampled by the ion (we follow the notational conventions and the normalization of the matrix elements as used in Ref. [38]). The coefficients γ_s and γ_i describe the dampings due to spontaneous decay and ionization losses from the 2S state, respectively. We assume that the transition is driven by two laser fields of equal frequency, so the ionization rate reads

$$\gamma_i = 2\pi\beta_{\text{ioni}}I. \quad (4)$$

Here, we once again treat the comb like a cw laser. This is justified by the fact that the ionization cross section varies only slightly over the bandwidth of a typical pulse whose duration is on the order of 10 fs. The detuning $\Delta\omega$ finally is defined as

$$\Delta\omega = 2\omega_L - \omega_{12}, \quad (5)$$

where ω_L is the frequency of the laser field. For a more comprehensive study of the line shape and systematic effects, one can include other contributions from, e.g., the ac Stark shift or the second-order Doppler shift in the detuning. The numerical values related to atomic structure used in the calculations are collected in Table I.

D. Rates

The optical Bloch equations [Eqs. (2a)–(2c)] were solved numerically [39] for zero detuning (neglecting the ac Stark shift) for an average intensity of 10 μW/μm^2 at 61 nm. The excitation and ionization probabilities as a function of inter-action time are plotted double logarithmically in Fig. 2. The graph shows a few notable features. First, no Rabi oscillations can be seen, since the system is strongly damped by spontaneous decay and ionization. For sufficiently long interaction times, the He$^+$ ion will be ionized with unity probability. For short interaction times the curves show a slope of 2 for excitation and 3 for ionization, as expected for a two-photon and a three-photon process, respectively. In view of a
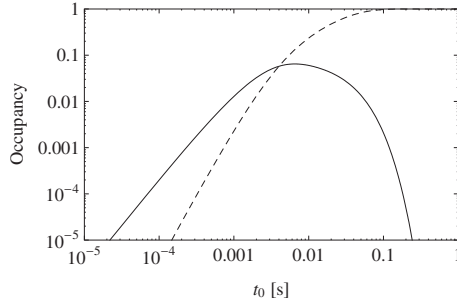
FIG. 2. Excited- (solid line) and ionized-state (dashed line) populations as functions of interaction time t_0 for an He$^+$ ion illuminated by an average intensity of 10 μW/μm^2 at 61 nm. We describe the 1S-2S two-photon transition including the ionization channel, as given by Eq. (2), and employ a three-level scheme consisting of the 1S ground state, the 2S excited state, and a continuum state.

spectroscopy experiment, an important result is that excitation is always accompanied by ionization.

It may be more convenient to express this in terms of "rates." However, this is a poorly defined quantity when dealing with high intensities and/or long interaction times. We therefore define a rate with the following experimental procedure in mind: a single ion interacts with the exciting laser field for a given time t_0. Then, the ions' state is analyzed whereupon the ion is reinitialized and a new cycle begins. In general, there will be a dead time t_d per cycle, e.g., because the excited state needs to be quenched or, in the case of a trapped ion, it needs to be recooled. In total, $f = 1/(t_0 + t_d)$ experiments may be performed per second. Multiplying f with the excited- or ionized-state occupancy at t_0 given by $[\rho_{22}(t_0)]$ or $[1 - \rho_{11}(t_0) - \rho_{22}(t_0)]$, respectively, gives the experimental rates in hertz. For each intensity I and dead time t_d, there is an optimum interaction time $t_0'(t_d, I)$ that maximizes either the excitation or the ionization rate. To give an example, such an optimization is depicted in Fig. 3 for an intensity of 10 μW/μm^2. We use the idealized assumption that there is no dead time; that is, we set $t_d = 0$. Therefore, the resulting rates are upper limits on rates that actually may be observed.
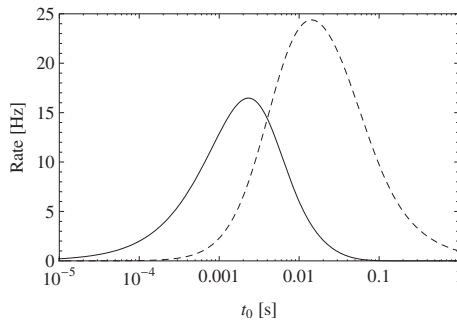
FIG. 3. Optimization of the interaction time t_0 with the exciting laser field to maximize either the excitation rate (solid line) or the resonant three-photon ionization rate (dashed line). The dead time is set to zero and the laser intensity is assumed to be 10 μW/μm^2.
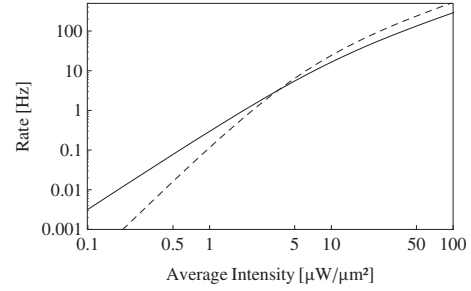
FIG. 4. Excitation (solid line) and resonant ionization rates (dashed line) for a single anticollinearly excited He$^+$ ion.

To determine the maximum excitation and (resonant) ionization rates as functions of available average intensity, we numerically calculate $t_0'(t_d = 0, I)$ and the corresponding rates for a range of intensities as discussed above. The result is shown in Fig. 4. Because we set $t_d = 0$, the excitation rate does not saturate at the maximum fluorescence rate given by the lifetime of the 2S state in He$^+$ ($\frac{1}{2}\Gamma = 42$ Hz). This limit can indeed be overcome in practice by, e.g., reducing the lifetime of the excited state by a perturbing dc electric field (quenching). In order to put the data plotted in Fig. 4 into perspective, we note that an ionization rate of 1 Hz requires an intensity of 2.3 μW/μm^2, which may be obtained, e.g., by focusing 0.9 μW average power at 61 nm down to $w_0 = 0.5$ μm.

III. EXPERIMENT

In this section we discuss possible realizations of a precision spectroscopy experiment on the 1S-2S transition in He$^+$. The results from Sec. II show that the currently available xuv power levels make tight focusing down to <10 μm and long interaction times necessary to achieve signal rates in the range of ~1 Hz. Furthermore, typical xuv pulses have a duration of roughly 100 fs or shorter, which corresponds to a spatial pulse length of (only) ~30 μm. If the He$^+$ ion is excited with anticollinearly propagating pulse trains, the interaction volume (given by the pulse collision-volume) will be very small. These requirements on localization and long interaction times are most conveniently fulfilled by a sample of cold trapped He$^+$ ions. Therefore, we restrict our discussion for the remainder of this paper to the spectroscopy of a small number of He$^+$ ions trapped in a linear rf trap.

A. Cooling

Cooling He$^+$ ions directly is not straightforward. Laser (Doppler) cooling requires a fairly strong (preferably dipole) cycling transition. In He$^+$, the longest wavelength cycling transition is the 1S-2P transition at 30 nm. However, no narrow-band (cw) source suitable for cooling is available or in sight for this wavelength [40]. This problem can be solved by introducing a second, easy to cool, ion species into the trap, which sympathetically cools the He$^+$ ions. The mass of the cooling ions should be as close as possible to the mass of the He$^+$ ions, (i) to ensure efficient motional coupling and (ii)

to be able to operate the rf trap with convenient parameters. By convenient we mean that the (Mathieu) q parameter of the rf trap is in the range of $0.05 < q < 0.6$. This dimensionless parameter determines the dynamics of the trapped particle and reads $q = \frac{2QU_{rf}}{mr_0^2\Omega^2}$, where Q and m are the charge and mass of the ion, U_{rf} and Ω are the rf amplitude and angular frequency and r_0 is the size of the trap, defined as half the distance between (hyperbolic) electrodes. Since q is inversely proportional to the mass, this implies that the cooling ion's mass should be smaller than 48 amu. Therefore, Be^+, Mg^+, and Ca^+ appear to be good choices. Especially Mg^+ is an interesting candidate, since light for the cooling transition near 280 nm can be provided by quadrupling an Yb-fiber laser at 1120 nm in two SHG stages [41].

B. Detection

The vast majority of absolute frequency measurements on single ions utilize shelving (as a "quantum amplifier") [42] in order to detect transitions on narrow lines. Spectroscopy on the $^1S_0$-$^3P_0$ clock transition of Al^+ is a notable exception [43], and methods adopted from quantum computing were used for readout in this case. The He^+ ion also lacks a suitable shelving transition, again because no appropriate 30 nm source is available to date. Direct detection of fluorescence from the 2S-1S two-photon decay appears not to be viable. The natural fluorescence rate of $\frac{1}{2}\Gamma = 42$ Hz is very low in conjunction with typical detection efficiencies of 10^{-3} (including the limited solid angle covered by a typical detector) and photomultiplier dark count rates exceeding 10 Hz. In addition, the two photons emitted by the 2S state are in general of unequal wavelength and are, furthermore, not emitted back to back [44]. The situation could be improved by quenching the excited state. This leads to a higher rate and to a well-defined photon energy but on the other hand increases the linewidth and introduces systematic uncertainties. Applying a quantum logic readout scheme similar to the Al^+ experiment would be possible in principle too. But this presents a significant experimental effort (including ground-state cooling) and ionization complicates this approach further. However, the significant ionization probability itself can be utilized to our advantage, that is, for detection. Using the production of He^{2+} ions as signature has the advantageous property that unlike an emitted photon the ion can be stored and detected with an efficiency approaching unity and very low background. Furthermore, it is possible to enhance the expected ionization rate beyond the results discussed in Sec. II D by an additional laser.

In a condensed form, the main steps of our proposed experimental procedure read as follows: (i) trap a cold mixed ion crystal, composed of He^+ and coolant ions; (ii) attempt to excite 1S-2S with the xuv comb; (iii) if successful, He^{2+} will be produced; (iv) detect He^{2+} by excitation of its unique secular frequency; and (v) step frequency of xuv comb and repeat.

In particular, consider a crystal of two trapped ions, one He^+ and one cooling ion. The ion trap is operated at a (Mathieu) q parameter chosen such that all three involved species, the coolant ion and He^+ and He^{2+}, are within the stability range of the trap. If Mg^+ is used as a coolant ion, this could be realized by choosing, e.g., $q_{Mg^+} = 0.05$ and therefore $q_{He^+} = 0.3$ and $q_{He^{2+}} = 0.6$. The trapped ions oscillate around the trap center with two frequencies: a fast quiver with the trap frequency Ω and a slow charge-to-mass ratio–dependent oscillation, called secular frequency $\omega_s \sim q\Omega/\sqrt{8}$. A successful 2S excitation will produce a He^{2+} ion with a certain probability which will (radially) oscillate at twice the secular frequency at which the singly charged He^+ ion did. When we apply an additional perturbing dipolar electric field, we can excite this motion and thus heat the crystal, which in turn will change the fluorescence of the cooling ion. This method, called secular excitation, is routinely used in diagnostics of trapped ions [45]. It might also be sufficient to simply observe a change in the position of the cooling ion due to the He^{2+} ion. A further alternative is to operate the ion trap such that both He^+ and the coolant ion are confined, but He^{2+} will be expelled and can be detected immediately by, e.g., a channeltron.

We would like to emphasize that the proposed detection scheme is essentially background free. If the detection via secular excitation is error free, only very unlikely events can create a false positive. A true positive event, that is, a $Q/m = \frac{1}{4}\frac{e}{u}$ ion disappears and a $Q/m = \frac{1}{2}\frac{e}{u}$ ion appears instead, may be mimicked only by such rare events as the collision of an He^+ ion with an H_2^+ ion from the background gas, where the He^+ ion is ejected and in exchange the hydrogen molecular ion is trapped. This is important in view of the feasibility of the experiment since the expected signal (ionization) rates are in the hertz range or below, and sensitivity is generally limited by the background.

In the proposed spectroscopy scheme, the clock ions are lost due to ionization, so frequent reloading will be necessary. This could be realized by using a linear trap with multiple segments. Two segments serve as reservoirs and store a large number of He^+ and coolant ions, respectively. Specially designed electrodes transport the ions to a further segment where the two species are merged and the spectroscopy is performed [46], possibly automated by a computer. Alternatively, the He^{2+} ions can be "recycled" to He^+ by purging the trap chamber with a short burst of neutral helium gas. Then, charge exchange collisions of the following type can take place:

$$He^{2+} + He \rightarrow 2He^+. \tag{6}$$
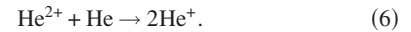
The rate of this type of reaction has been determined to be 4.4×10^{-14} cm^3/s for low-energy collisions at 300 K [47]. A charge-exchange rate of 1 Hz thus requires a He pressure of 10^{-3} mbar.

C. Excitation geometry

Due to the low expected transition rate per ion, the question arises as to whether one can take advantage of the large particle numbers ($N \sim 10^6$) ion traps can store. Aiming at precision spectroscopy though, only ions in field-free regions of the trap are useful. In a spherical Paul trap this is only one point in space, in a linear trap the axis with no rf confinement. Outside these regions, ions are subject to oscillating

electric quadrupole fields which cause several adverse effects, including ac Stark shifts, second-order Doppler shifts, and a reduction of the lifetime of the excited state by quenching [48]. In the following, we will therefore discuss whether one can benefit from exciting a string of ions in a linear Paul trap rather than working with single ions.

In general, a two-photon transition can be excited either anticollinearly by two counterpropagating photons or collinearly by two copropagating photons. Both processes are described by the same matrix elements, although in the first case the line is free of first-order Doppler and recoil shift, whereas in the second case the line will be broadened and shifted. For unbound atoms excited by counterpropagating beams, this implies that the absorption spectrum consists of a Doppler-broadened pedestal from collinear excitation and a sharp Doppler-free peak in the center. For trapped ions this picture is modified. We will discuss the two contributions separately and also address differences that arise from the orientation of the xuv beams relative to the trap axis, axial or radial.

1. Anticollinear excitation

a. Radial anticollinear excitation. In a radial anticollinear excitation geometry, the xuv beams are oriented antiparallel and perpendicular to the (linear) trap axis. For both collinear and anticollinear radial excitation, simple scaling arguments show that the ionization rate is maximized by focusing down to a single ion. For a three-photon process, the rate scales as $\propto I^3 \propto w_0^{-6}$, where w_0 is the waist size, but the number of interacting ions is proportional to w_0. In total, the rate is thus proportional to w_0^{-5}. Numerical studies outside the regime where this scaling is valid support this statement. The resulting rates are therefore given by the rates for a single ion as shown in Fig. 4.

b. Axial anticollinear excitation. In an axial anticollinear excitation geometry, the xuv beams point along the direction of the axis of dc confinement of the Paul trap, which is parallel to the ion chain. In this case the total rate is enhanced over the radial case simply by the number of He$^+$ ions in the pulse-collision volume, which is limited by the spatial pulse length and reads $\ell \simeq 2c\tau$, where ℓ is the length of the collision volume and τ is the pulse duration. The number of He$^+$ ions that can be located in this volume depends on the trapping parameters and cannot be determined analytically. In practice, one considers a given trap with a maximum radial confinement strength described by the radial secular frequency ω_r. To maintain a linear string of ions and prevent breakup into more complicated (e.g., zigzag) structures, the axial confinement ω_{ax} needs to be weaker than the radial by a factor that depends on the number of ions N. This factor has been determined by several authors with different methods, including numerical studies, experimental determinations, and thermodynamical considerations. A recent theoretical result of the latter type which is in good agreement with experimental data reads $\omega_{ax} = \frac{4}{3}\omega_r N^{-1}\sqrt{\ln N}$ [49]. For a given number of ions N and corresponding axial confinement ω_{ax}, the equilibrium positions are then determined numerically by minimizing the potential energy [50]. Figure 5 shows
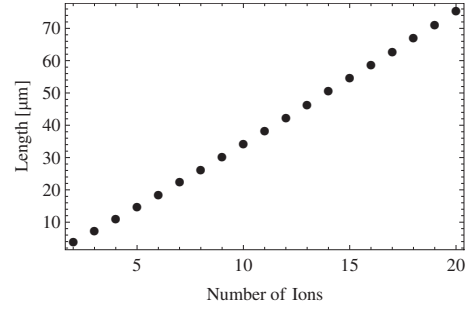
FIG. 5. Numerically determined length l_i of an He$^+$ ion chain with constant radial confinement of $\omega_r = 2\pi \times 10$ MHz and variable axial confinement to maintain a linear string. The length is well approximated linearly by $l_i \sim N\, 4\ \mu m - 5\ \mu m$.

the length of an ion chain as a function of ion number in a rather steep trap with a radial secular frequency of $\omega_r = 2\pi \times 10$ MHz for He$^+$.

In this case, 30 fs xuv pulses can interact with up to 6 He$^+$ ions. The length of the chain may of course be reduced by tighter confinement, although one gains only proportional to $\omega_{ax}^{-2/3}$.

From a practical point of view, both radial and axial anticollinear excitations bear great challenges. The signal rate is maximized by tight focusing, so two beams of ~ 1-μm-sized pulses need to be overlapped (i) spatially, (ii) temporally, and (iii) with the He$^+$ ions. Recall that a repetition rate of, e.g., 100 MHz corresponds to a 3 m pulse-to-pulse separation, so each of the two focusing mirrors may have to be placed 1.5 m away from the ion as low reflective optics inhibit folding the beam.

2. Collinear excitation

For an unbound atom or ion a Doppler-broadened spectrum would be observed, which would limit the spectroscopic accuracy. In the resolved-sideband limit of a trapped ion, the situation is quite different, that is, if the secular frequency of the ion exceeds the linewidth of the transition. In this case, the absorption spectrum consists of a Doppler- and recoil-free carrier with sidebands separated by the secular frequency. All sidebands are of natural linewidth and, for average motional quantum numbers $\bar{n} \gg 1$, lie under an envelope given by Doppler broadening. The center of gravity of the envelope will be shifted by the angular recoil frequency of $\omega_{rec} = \hbar(2k)^2/2m_{He} = 2\pi \times 54$ MHz to the high-frequency side of the spectrum. Note that here as well as in the following, the angular wave number k is multiplied by an extra factor of 2 because two photons are absorbed. The resulting recoil frequency is 2 orders of magnitude larger than in typical spectroscopy experiments on trapped ions, which is the reason why the resulting spectra may appear unfamiliar. Precise spectroscopy can therefore be performed either on the carrier or, if the secular frequency and the order of the sideband are well known, on one of the sidebands. This allows circumvention of the intricate alignment of the xuv beams in anticollinear excitation by simply exciting the He$^+$ ion with

one xuv beam only. Further, the interaction volume will not be limited by the xuv pulse length anymore, but roughly by the confocal parameter of the focused beam. If, for example, the xuv beam is focused to $w_0 = 1$ μm the Rayleigh length is $2\pi w_0^2/\lambda = 103$ μm. For pulses shorter than 172 fs, this allows one to address more ions simultaneously. The downside is an overall reduction of the rates and an absorption spectrum featuring a larger number of motional sidebands. In the following we will quantify these statements.

The spectrum is calculated as follows. The interaction between the light field and the motional state is characterized by the dimensionless Lamb-Dicke parameter η, which measures the extent of the ion's ground-state wave packet relative to the wavelength

$$\eta = 2kx_0 = 2k\sqrt{\frac{\hbar}{2m\omega_s}} = \sqrt{\frac{\omega_{\mathrm{rec}}}{\omega_s}}. \qquad (7)$$

The extent of the ground-state wave packet is denoted by x_0, m is the ion's mass, and ω_s is the secular frequency of the ion. Unlike the usual definition, an extra factor of 2 accommodates the fact that two photons are absorbed. The matrix element for transitions between motional Fock states $|n\rangle$ due to the interaction with the laser reads [51]

$$|\langle n'|e^{i2k\hat{x}}|n\rangle| = |\langle n'|e^{i\eta(\hat{a}+\hat{a}^\dagger)}|n\rangle|$$
$$= e^{-\eta^2/2}\eta^{|n'-n|}\sqrt{\frac{n_<!}{n_>!}}L_{n_<}^{|n'-n|}(\eta^2), \qquad (8)$$

with the common creation and annihilation operators for the ions' vibration. Further, $n_< = \min(n,n')$, $n_> = \max(n,n')$, and L denotes the generalized Laguerre polynomial. The sideband spectrum is then obtained by summing the squared matrix elements over all possible initial and final states, where the initial states are weighted according to their population [52],

$$\kappa(\Delta\omega) = \sum_{E_n - E_{n'} = \hbar\Delta\omega} |\langle n'|e^{i\eta(\hat{a}+\hat{a}^\dagger)}|n\rangle|^2 P(n). \qquad (9)$$

The sum over all sideband strengths κ equals 1. The effect on the excitation dynamics is to reduce Rabi frequency equation (3) to

$$\Omega = \kappa 2(2\pi\beta_{12})I. \qquad (10)$$

The ionization rate remains unchanged. If the ion is in a thermal state, e.g., after cooling, the distribution $P(n)$ reads

$$P(n) = \exp\left(-\frac{n\hbar\omega_s}{k_B T}\right)\left[1 - \exp\left(-\frac{\hbar\omega_s}{k_B T}\right)\right], \qquad (11)$$

where k_B is the Boltzmann constant.

It is straightforward to generalize this treatment to strings of N ions (closely following Ref. [52]). In a first step, a particular ion string is specified, which can also include cooling ions (e.g., a string consisting of He$^+$, He$^+$, Mg$^+$, He$^+$). Then, for a given confinement strength, which is specified by the secular frequency of a single ion [which equals the frequency of the center-of-mass (c.m.) mode for an arbitrary number of ions], the positions, eigenmodes β^α, and corresponding eigenfrequencies (secular frequencies) ω_s^α are de-
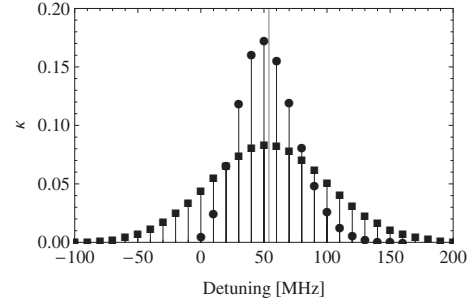
FIG. 6. Sideband spectrum of a collinearly excited He$^+$ ion with a secular frequency of $\omega_s = 2\pi \times 10$ MHz. The vertical line indicates the recoil frequency of 54 MHz. Circles and squares indicate whether the ion is assumed to be cooled to the ground state of motion or to 1 mK, respectively.

termined [50]. Here, α enumerates the N eigenmodes. The vector β^α of length N contains the oscillation amplitudes and relative phases of ion j and mode α. Next, the Lamb-Dicke parameter is generalized, so it reads for the jth ion and mode α as

$$\eta_j^\alpha = 2k\beta_j^\alpha\sqrt{\frac{\hbar}{2m_j\omega_s^\alpha}}. \qquad (12)$$

This takes not only the different secular frequencies of the modes into account, but also the various oscillation amplitudes β_j^α, which depend on the mode α and the ion number j. Consider, e.g., the "stretch" mode of a string of three ions of equal mass. In this case, the center ion will be at rest, so its motion will not couple to the light field, as opposed to the outer ions. The motional state vector $|n\rangle$ is replaced by $|\mathbf{n}\rangle = |n_1, n_\alpha, \ldots, n_N\rangle$. With these generalizations, absorption spectra are calculated in close analogy to the single-ion case:

$$\kappa(\Delta\omega) = \sum_{E_n - E_{n'} = \hbar\Delta\omega} |\langle \mathbf{n}'|e^{i\eta_j^\alpha(\hat{a}+\hat{a}^\dagger)}|\mathbf{n}\rangle|^2 P(\mathbf{n}). \qquad (13)$$

The argument of the sum is a product over all eigenmodes α. The sum itself extends over all ions j and combinations of $|n\rangle$ and $|n'\rangle$. For a given trap storing a string of ions one can choose between radial or axial collinear excitation, where "radial" means that the laser propagation direction is perpendicular to the trap axis. It is not immediately clear which orientation yields higher rates.

a. Radial collinear excitation. Figure 6 shows a calculated sideband spectrum of a radially excited tightly confined He$^+$ ion with a secular frequency of $\omega_s = 2\pi \times 10$ MHz. In one case it is assumed to be cooled to $T = 1$ mK, which corresponds to the Doppler cooling limit of Mg$^+$. In the other case it is assumed to be cooled to the ground state of motion. As expected, the spectrum of the ion cooled to the ground state is narrower and exhibits stronger individual components. Remarkably, the carrier is stronger for the warmer ion. This is due to the fact that the entire spectrum is shifted by the recoil frequency of $\omega_{\mathrm{rec}} = 2\pi \times 54$ MHz, because the ion's confinement is weak in comparison to the recoil energy ($\omega_s < \omega_{\mathrm{rec}}$). For very low temperatures, the distribution of
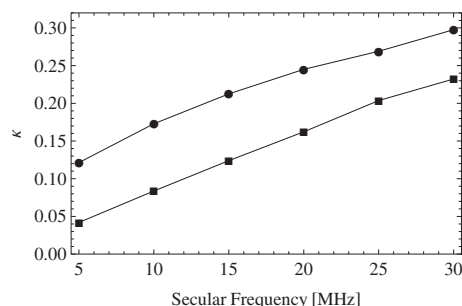
FIG. 7. Relative magnitude of the strongest sideband as a function of secular frequency for He$^+$ ions cooled to 1 mK (squares) or to the ground state (circles).

sidebands becomes so narrow that the carrier diminishes. For increasing temperatures, the distribution will broaden and flatten so the carrier will become weaker, too. Incidentally, the chosen temperature of 1 mK is near the optimum temperature for which the carrier is maximal ($T_{\text{opt}}=1.3$ mK) for these parameters. In a steeper trap, the absorption spectrum will consist of less and stronger sidebands. In the trap with the highest secular frequencies reported so far [45], ^{9}Be$^+$ ions were confined with secular frequencies of up to 50 MHz. The magnitude of the strongest sideband as a function of the secular frequency is shown for an ion cooled to 1 mK and cooled to the ground state in Fig. 7. We chose the strongest component and not the carrier, since the expected rates are already rather low, and assuming that the secular frequency can be determined sufficiently precise so it will not limit the overall accuracy.

This shows that collinear excitation reduces the Rabi frequency in this example by a factor of 5–10, which has to be compensated for by either five to ten times more xuv power or two to three times tighter focusing to achieve the same rate as in anticollinear excitation.

b. Axial collinear excitation. In this orientation, despite tight focusing, a number of ions can be addressed simultaneously, whose number is in principle only limited by the confocal parameter of the focused xuv beam. On the other hand, as pointed out in Sec. III C 1, the secular frequency is
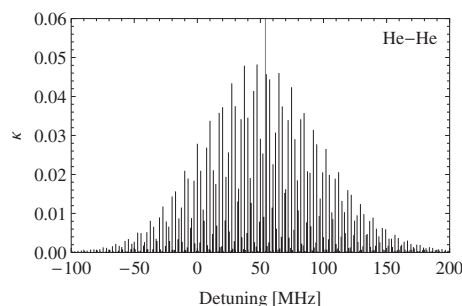
FIG. 8. Sideband spectrum of a string of two axially excited He$^+$ ions confined with a secular c.m. frequency of 10 MHz and cooled to 1 mK. The vertical line indicates the recoil frequency.
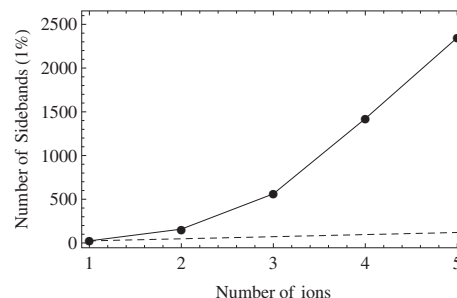
FIG. 9. Calculated number of sidebands that exceed 1% of the strongest component as a function of the number of ions. The secular frequency is 10 MHz; the temperature is 1 mK. The dashed line shows for comparison a hypothetical linear increase in the number of sidebands.

weaker in this direction. For clarity, however, we have studied absorption spectra of ion chains with constant axial trap stiffness, to be able to discriminate the effect of the greater number of ions and the reduced secular frequencies.

Figure 8 shows an absorption spectrum of two He$^+$ ions cooled to 1 mK with a center-of-mass frequency of 10 MHz. It consists of a rather dense collection of sidebands, none of which is more intense than the strongest component in the spectrum of a single He$^+$ ion (Fig. 6). This rather counterintuitive result (two ions exhibit no stronger component than a single ion) can be understood as follows: the sum of all sideband strengths in relative units equals the number of ions [53]. But it turns out that if the number of ions is increased, the number of sidebands increases much more rapidly. This is because sidebands are not limited to integer multiples of the N different mode frequencies of the string, as one may tend to expect, but can also occur at sums and differences of integer multiples of the frequencies, as long as energy conservation is fulfilled. In a string of two ions, for example, not only the c.m. *or* the stretch mode can be excited individually, but also any combination. Since the frequencies of the eigenmodes are incommensurate, this results in a dense grid where sidebands can occur in principle. The number of sidebands depends on the definition of how intense a component needs to be to be included. If, for example, all sidebands are counted that exceed 1% of the strongest component, a string of five He$^+$ ions confined in a $\omega_{\text{c.m.}}=2\pi\times 10$ MHz trap and cooled to 1 mK exhibits 2348 sidebands. This is illustrated in Fig. 9.

We also studied the influence of cooling ions in the string. It turns out that this does not improve the spectrum: the additional cooling ions cause more sidebands without contributing to the signal. An example is shown in Fig. 10 for an ion string consisting of two He$^+$ and one Mg$^+$ ion, cooled to 1 mK. As mentioned before, all these spectra have been calculated for constant axial confinement. In a real experiment with given radial confinement, the axial secular frequency needs to be reduced as the number of ions increases to maintain a linear string. The resulting spectra will therefore be even denser with weaker individual components.
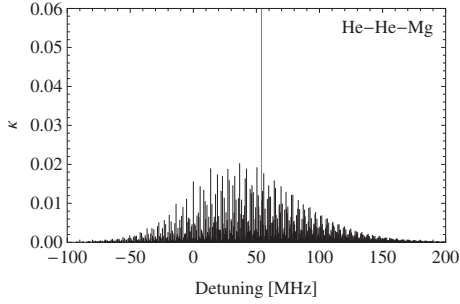
FIG. 10. Same as Fig. 8 except one Mg+ cooling ion was added.

3. Comparison excitation geometries

From the geometries discussed, axial anticollinear and radial collinear excitations turn out to be the most promising approaches. The anticollinear arrangement yields the highest rates, and if excited axially, on the order of 10 He+ ions can be addressed simultaneously. The drawback is the possibly intricate alignment of the xuv beams required. Collinear excitation facilitates the alignment significantly, although the Rabi frequency is strongly reduced, and roughly an order of magnitude more xuv power is required to obtain the same rate. Radial collinear excitation of a single ion in a steep trap yields higher rates and clearer spectra than axial collinear excitation of a chain of ions. In all cases, the ionization rate is maximized by tight focusing. In Fig. 11, the scaling of the maximum excitation and ionization rate is shown, recalculated for the case where the Rabi frequency is reduced to 10% by the selection of a particular sideband. The dynamics is slightly different, because the 1S-2S Rabi frequency is reduced, but the ionization cross section remains unchanged.

For clarity the sideband spectra shown do not take the comb structure of the laser into account. The experimentally observable spectrum is obtained by convolving the spectrum of the xuv comb with the spectrum of the ion. If the width of the absorption spectrum is not significantly narrower than the repetition rate of the comb, this will lead to an even denser spectrum and make it quite challenging to identify the car-
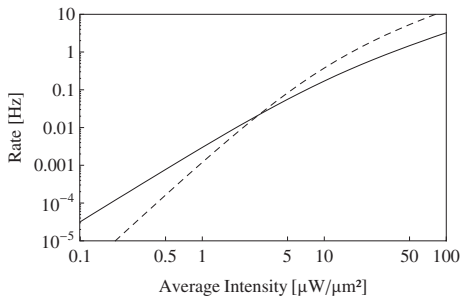
FIG. 11. Maximum excitation (solid line) and ionization rates (dashed line) for one collinearly excited He+ ion. The Rabi frequency has been reduced to 10%. Since the ionization cross section remains unchanged, the dynamics is slightly different from that in Fig. 4.

rier. On the other hand, under certain circumstances, the comb structure of the xuv source can be used to increase the excitation rate. The sidebands of a single collinearly excited He+ ion form a regular grid with a line spacing given by the secular frequency. If the ratio of the repetition rate of the comb to the secular frequency is rational, it will drive several sidebands simultaneously (all if the ratio is 2).

IV. SYSTEMATIC UNCERTAINTIES

In order to illustrate the potential accuracy of a high-precision spectroscopy experiment on He+, we estimate some typical systematic uncertainties. In particular, we assume He+ ions stored in a rf trap driven with $\Omega = 2\pi \times 60$ MHz and cooled to $T = 1$ mK. The ionic motion due to the finite temperature will cause the line center of the carrier to be shifted by the second-order Doppler effect by

$$\Delta\nu = -\frac{\omega_{12}}{4\pi}\left(\frac{v}{c}\right)^2 = -0.2 \text{ Hz}, \qquad (14)$$

where ω_{12} is the 1S-2S transition frequency. The corresponding fractional frequency shift is 2×10^{-17}.

The secular oscillation of the ion around the trap center causes it to sample an average quadratic electric field, which is calculated by integrating the square of the electric field of the potential up to the classical turning points of the oscillation [48]:

$$\langle E^2 \rangle = \frac{m\Omega^2 k_B T}{e^2} = 51 \times 10^{-3} \text{ V}^2/\text{cm}^2. \qquad (15)$$

This leads to a dc Stark shift of [54]

$$\Delta\nu_{dc} = (3610 \text{ Hz cm}^2/\text{V}^2)\langle E^2 \rangle Z^{-6} = 3 \text{ Hz}, \qquad (16)$$

which corresponds to a relative uncertainty of 3×10^{-16} for the electric field given above. The average quadratic electric field will also cause a broadening of the line by reducing the lifetime of the $2S_{1/2}$ state through admixture of the fast-decaying $2P_{1/2}$ state. The lifetime against quenching can easily be calculated by considering the admixture received by the 2S state from the 2P state, and relating the mixture coefficient to the well-known lifetime of the 2P state which decays via a one-photon electric dipole transition to the ground state. The result is

$$\tau' = \frac{0.0158}{\langle E^2 \rangle} \text{ V}^2 \text{ s/cm}^2 = 0.3 \text{ s}. \qquad (17)$$

The broadening is only about 0.6% in units of the natural linewidth so that the dynamics calculated above is hardly affected.

The effects discussed so far (second-order Doppler shift, dc Stark shift, and quenching) have been calculated for an ideal trap. Even small stray fields and phase differences between rf electrodes can cause excess micromotion which can increase the uncertainties by orders of magnitude. Great care must therefore be taken to measure and compensate for excess micromotion [48].

The shift due to blackbody radiation (BBR) has recently been calculated to be 0.12 Hz at 300 K [55].

If we assume a time-averaged laser intensity of $10 \ \mu\text{W}/\mu\text{m}^2$, the ac Stark effect shifts the observed line center by

$$\Delta\nu_{\text{ac}} = \beta_{\text{ac}}I = 100 \ \text{Hz}. \tag{18}$$

This contribution is, however, no fundamental limitation, since the measured frequency of the line center can be extrapolated to zero laser intensity after having been recorded for a range of intensities.

Shifts due to external magnetic fields cancel to first order if a $\Delta m = 0$ component is measured because the Landé g factors of all S states are identical. However, if we include higher-order corrections we find that the g factors of the ground and excited S states differ slightly. The dominant contribution to the dependence of the g factor on the principal quantum number is given by the following well-known leading term in the $Z\alpha$ expansion of the Breit formula for the bound-electron g factor for S states. This leads to a magnetic-projection-dependent Zeeman energy shift of [56]

$$\Delta E = 2\mu_B B m_J \left[1 - \frac{1}{3}\left(\frac{Z\alpha}{n}\right)^2 \right], \tag{19}$$

where μ_B is the Bohr magneton, and $m_J = -\frac{1}{2}, \frac{1}{2}$ is the spin projection on the axis of the magnetic field B. This residual Zeeman effect shifts the magnetic field–insensitive components by 0.7 Hz in a field of 10 G, leading to a relative uncertainty of 8×10^{-17}.

It should be pointed out that the $1S$-$2S$ transition is not affected by quadrupole shifts, because neither the ground nor the excited state possesses a quadrupole moment.

With the assumptions made we find the largest systematic line shift to be on the order of 10^{-16} (dc Stark shift). The statistical uncertainty for a known line shape reads

$$\Delta\nu_{1S\text{-}2S} = \frac{\Gamma}{S/N} = \frac{\Gamma}{\sqrt{N_{\text{He}^{2+}}}}. \tag{20}$$

The ionization-based detection method proposed above is virtually background free, so the signal-to-noise ratio S/N is limited by the total number of counts $N_{\text{He}^{2+}}$, which justifies the last equal sign. The linewidth of the comb modes in the infrared can be stabilized down to 1 Hz [17]. The corresponding linewidth in the xuv region has not been measured yet and depends on the noise processes involved in the HHG process. We assumed in the calculation of the excitation and ionization rates a linewidth of the comb modes narrower than the natural linewidth. Otherwise the rate would be reduced due to poor spectral overlap. For the calculation of the statistical uncertainty we are more pessimistic and conservatively assume a linewidth of 10 kHz. If we further assume an event rate of 0.1 Hz and a measurement time of 10^5 s, then the line center could be determined to within less than 50 Hz, which corresponds to a measurement on the 2×10^{-14} level.

V. IMPACT ON QED

Testing a physical theory means to compare its predictions to experimental findings. The best tests therefore demand a system that can be both measured and calculated

with very high accuracy. For a long time the confrontation of transition frequencies in atomic hydrogen with theoretical calculations has allowed for one of the best tests of bound-state QED [1,57]. The $1S$-$2S$ transition plays a prominent role because it possesses a particularly large line quality factor and can be excited in a Doppler-free arrangement with two photons. In hydrogen, theoretical predictions have been limited for many years by inconsistencies of the published values for the proton charge radius that is used as input to these calculations. Even though the nuclear-size-dependent term enters only with 4 parts in 10^{10} to the transition frequency, it contributes by far the largest uncertainty. Even worse, the various values for the proton charge radii discussed in the literature disagree by several standard uncertainties.

In comparison, absolute frequency measurements in He$^+$ are more promising because the contributions of higher-order QED effects are larger than the uncertainty due to the nuclear charge radius. In hydrogen, the B_{60} and B_{7i} terms contribute with -8 kHz, while the uncertainty of the proton charge radius amounts to 44 kHz. In contrast, in He$^+$ B_{60} and B_{7i} are significantly larger and amount to -543 kHz, which is twice as large as the uncertainty due to the nucleus of 295 kHz. The corresponding values are shown in Table II. $\Delta E_{2S\text{-}1S} = E_{2S} - E_{1S}$ is the measured transition energy. We define the Lamb shifts $\mathcal{L}_{1S}$ and $\mathcal{L}_{2S}$ according to the generally adopted convention that recoil corrections, which are beyond the Dirac energy value but do not lift the $2S_{1/2}$-$2P_{1/2}$ degeneracy, as well as hyperfine effects, are *excluded* from the definition of the Lamb shift $\mathcal{L}$. Essentially, the Lamb shift is the sum of radiative corrections, effects due to the finite nuclear size and nuclear polarizability, and higher-order recoil (two-body effects) and radiative-recoil corrections. The following implicit definition [63] is the commonly adopted one, and reads

$$E = c^2 m_r[f(n,j) - 1] - \frac{c^2 m_r^2}{2(m_e + M)}[f(n,j)-1]^2 + \mathcal{L} + E_{\text{hfs}}. \tag{21}$$

Here, E is the energy level of the bound two-body system (electron+nucleus), and $f(n,j)$ is the dimensionless Dirac energy. For example, we have $f(1,\frac{1}{2}) = f(1S) = \sqrt{1 - (Z\alpha)^2}$ and $f(2,\frac{1}{2}) = f(2S) = \sqrt{\frac{1}{2}[1 + \sqrt{1-(Z\alpha)^2}]}$ for the $1S$ and $2S$ states, respectively. The other symbols are as follows: $m_r(M)$ is the reduced mass of the system, and E_{hfs} is the energy shift due to hyperfine effects. The latter is absent for a spinless nucleus.

The difference in the Dirac energies, $\Delta E_{2S\text{-}1S}^{\text{Dirac}}$, can be calculated for the $1S$-$2S$ transition with an uncertainty $(\delta R_\infty/R_\infty)\Delta E_{2S\text{-}1S}^{\text{Dirac}} \approx (\delta R_\infty/R_\infty)\Delta E_{2S\text{-}1S}$ (see Table II), which is proportional to the relative uncertainty of the Rydberg constant, $\delta R_\infty/R_\infty = 6.6 \times 10^{-12}$ [61]. The Lamb shift difference $\mathcal{L}_{1S} - \mathcal{L}_{2S}$ can be determined to the same absolute precision in frequency units from H spectroscopy because $\Delta E_{2S\text{-}1S}$ has been measured [1] to an accuracy of 1.4×10^{-14}, much better than R_∞. Present knowledge of R_∞ comes mainly from precision spectroscopy of H($1S$-$2S$), H($2S$-$8D$), H($2S$-$12D$), and similar transitions [2]. A more elaborate version of this approach is based on the method of least squares [2,64], and

TABLE II. Comparison of H and ^{4}He$^+$. This listing includes the transition frequency and critical contributions to the energy levels such as the Lamb shift $\mathcal{L}$, some higher-order QED terms, and the energy shifts due to the nuclear size and polarizability. Uncertainties are given in parentheses. The nuclear-size corrections are calculated with the rms charge radii $R_p = 0.897(18)$ fm [58,59] for the proton and $R_\alpha = 1.681(4)$ fm for the α particle [60]. The nuclear polarizability corrections are the results of calculations; see Eq. (A11) of Ref. [61] and Ref. [62] for the proton and the α particle, respectively. With regard to the potential improvement of the nuclear-size uncertainty due to the ongoing muonic hydrogen and muonic helium experiments, we note that the value in the last row for He$^+$(1S-2S) is obtained under the additional assumption that the nuclear polarizability correction of the μ^4He 2S state can be calculated to 5% uncertainty.

	H(1S-2S) (kHz)	He$^+$(1S-2S) (kHz)	Z dependence
Frequencies			
$\Delta E_{2S\text{-}1S}$	2.466×10^{12}	9.869×10^{12}	Z^2
1S-2S natural linewidth	0.0013	0.084	Z^6
Selected individual contributions and theoretical Lamb shift values			
Nuclear polarizability	−0.06(2)	−28(3)	
B_{60} and B_{7i} terms	−8(3)	−543(185)	$Z^{6\cdots}$
Nuclear size (for the proton and the ^{4}He nucleus)	1102(44)	62079(295)	$Z^4 R^2$
$\mathcal{L}_{1S} - \mathcal{L}_{2S}$	7127887(44)	93856127(348)	$\approx Z^{3.7}$
Some relevant uncertainties and projected improvements			
Uncertainty due to uncalculated higher-order terms (C_{50}, recoil, etc.)	±2	±100	$Z^{5\text{-}7}$
Conceivable reduced uncertainty of the nuclear-size correction assuming the availability of μH and μ^4He$^+$ Lamb shift measurements	±2	±40	

on the assumption that all currently measured accurate transitions can be described with a single coherent theory described by quantum electrodynamics, which covers all transitions among the hydrogenic bound states.

Deriving the Rydberg constant in this way, the main relevant input parameters are the H(1S-2S), H(2S-8D), and H(2S-12D) transitions. A measurement of the H(1S-3S) transition with increased accuracy (a realistic goal is on the level of 1 kHz precision) is currently being pursued at the Max-Planck-Institute of Quantum Optics (Garching) and at the Laboratoire Kastler-Brossel in Paris. If successful, these ongoing experiments would reduce the uncertainty in R_∞ by a factor of 2, with a corresponding reduction in the contribution to the theoretical uncertainty of the He$^+$ frequencies due to the Rydberg constant.

Concerning the entry for $\mathcal{L}_{1S} - \mathcal{L}_{2S}$ in Table II, we note that the Lamb shift does not scale exactly as Z^4 because the leading term has an additional $\ln[(Z\alpha)^{-2}]$ dependence. Both at $Z=1$ and at $Z=2$, the dependence on Z can be approximated by a noninteger power $\approx Z^{3.7}$. For the determination of the fractional power, it is crucial to take into account the dependence of the argument of the logarithm on the fine-structure constant, and the approximate value of the exponent slightly depends on the nuclear charge number. For $Z=1,2$ the exponent is well approximated as 3.7.

The quoted theoretical uncertainties for the Lamb shift differences $\mathcal{L}_{1S} - \mathcal{L}_{2S}$ in H and He$^+$ take into account the recent investigations reported in Refs. [65–67] for H and in

Ref. [68] for He$^+$. The theoretical uncertainties of these calculated Lamb shift differences result from quadratically adding the uncertainties of the nuclear-size term and computational uncertainties, where we note the reduction in the uncertainty of the nuclear-size correction for the Lamb shift difference $\mathcal{L}_{1S} - \mathcal{L}_{2S}$ by a factor of 7/8 in comparison to $\mathcal{L}_{1S}$ as taken from Table 3 of Ref. [68]. The resulting relative uncertainty in He$^+$ of 3.7 ppm (±348 kHz) is roughly half the size of the corresponding value in hydrogen (6.3 ppm or ±44 kHz) and is composed in almost equal parts of uncertainties in the nuclear size and computational uncertainties. This is in sharp contrast to the situation in hydrogen where no immediate progress is possible by improved calculations. The total theoretical uncertainties of the Lamb shift differences are presently a lot larger than their uncertainties due to the Rydberg constant alone (16 and 65 kHz, or 2.2 and 0.7 ppm, respectively, due to R_∞).

We now turn to a brief discussion regarding the evaluation of the theoretical Lamb shift values from QED theory. In general, the long tradition of bound-state QED computations has led to precise values for many of the higher-order terms for the one-loop and two-loop self-energies, vacuum polarization, etc., as tabulated in Ref. [57] for H and in Ref. [68] for He$^+$. Many of these terms were calculated to such high numerical precision that we can disregard their uncertainty in the present context, as is evident, e.g., from Table 3 of Ref. [68]. In recent years, intensive studies of the higher-order two-loop corrections to the Lamb shift (with self-energy,

vacuum polarization, and mixed graphs) have been performed with two different methods. The first of these is based on an expansion in powers of $Z\alpha$ and $\ln[(Z\alpha)^{-2}]$, with coefficients labeled as B_{40}, B_{50}, and B_{6i} with $i \in \{0,1,2,3\}$, and B_{7i} with $i \in \{0,1,2\}$, where the first index of the B coefficients labels the power of $Z\alpha$ and the second index labels the power of the logarithm $\ln[(Z\alpha)^{-2}]$ (see Ref. [66]). The second method is based on a nonperturbative (in $Z\alpha$) numerical approach [67]. The B_{6i} coefficients have turned out to be surprisingly large, with a remaining contribution to B_{60} due to high-energy virtual photons still being investigated. The convergence of this expansion is rather modest, and non-negligible contributions from unknown B_{7i} terms cannot be excluded.

Nonperturbative all-order calculations were performed first at high Z and recently down to $Z=10$, and then extrapolated to $Z=1$. The result differs from the perturbative approach by nearly 7 kHz for the H(1S) two-loop shift. Moreover, following common practice (see also the discussion in Ref. [66]), we take half of this discrepancy as uncertainty, resulting in the 3 kHz theoretical uncertainty quoted in Table II for the B_{60} and B_{7i} terms. Obviously, these terms become quite large for He$^+$ because they scale as Z^6 and higher powers. Other uncalculated effects included in the two-loop uncertainty estimate are the three-loop C_{50} term of order $\alpha^3(Z\alpha)^5$ in units of the electron mass and uncalculated higher-order recoil corrections.

The uncertainties of the nuclear radii could be reduced by a factor of 10–20 via a measurement of the 2S-2P energy difference in muonic hydrogen (denoted in the literature as μp or μH; here we use μH) and muonic helium ions (μ^4He$^+$), where the nuclear-size shift is an important part of the Lamb shift and can therefore be deduced with high accuracy. For μH, such a Lamb shift experiment is presently being performed at the Paul Scherrer Institute [69] using a pulsed infrared laser system ($\lambda=6$ μm, corresponding to $\Delta E_{2P\text{-}2S}=0.2$ eV). The μH experiment is very challenging for several reasons but appears to be simpler in μHe$^+$. The cross sections for collisional 2S quenching are much smaller in the case of helium as compared to muonic hydrogen, and the muon experiment can thus be performed at significantly higher gas densities. In addition there are better detectors available for 8 keV photons from μHe$^+$(2P-1S) transitions than for 2 keV photons.

In order to provide a historical perspective, we note that for μHe$^+$ red laser light (812 nm) is needed, and a 2S-2P resonance line was measured at CERN already in the 1970s [70]. The experiment [70] was based on a lifetime of the metastable μHe$^+_{2S}$ state of at least 1 μs, but much shorter lifetimes were found by other groups at high He gas pressures [71,72]. A new laser experiment [73] was therefore initiated at low pressures, where collisional 2S quenching becomes negligibly small. No μHe$^+$(2S-2P) resonance line was found at the wavelength claimed by the previous experiment [70], which means that the search for this 2S-2P resonance is still an open task [73]. With the progress in laser technology and muon-beam intensities, such muonic Lamb shift experiments are feasible today.

A summary of transition frequencies, interesting contributions to the Lamb shift, and other data relevant to the current

project is given in Table II. We note that the nuclear polarizability correction for ^{4}He$^+$ has been computed very recently for the first time [62]. The correction is numerically significant on the precision level which may be reached in the not-too-distant future.

To conclude the discussion, we note the current theoretical prediction for the 1S-2S transition frequency in ^{4}He$^+$, which reads

$$\nu_{1S\text{-}2S}(^4\text{He}^+) = 9\,868\,561\,006.74(35)\ \text{MHz}, \qquad (22)$$

where the uncertainty is obtained by quadratically adding the Lamb shift uncertainty of ± 348 kHz and the uncertainty due to the Rydberg constant of ± 65 kHz. A measurement of the 1S-3S transition in hydrogen on the level of 1 kHz would halve the uncertainty due to R_∞. It is obvious for both H and He$^+$ that higher-order QED contributions can be tested on a sensitive level only when better values for the nuclear radii become available from muonic Lamb shift measurements. If we assume, furthermore, that a moderate improvement of the R_∞ uncertainty can be achieved (e.g., via a 1S-3S measurement), this will open the field for a very sensitive test of bound-state QED in the case of He$^+$, on the level of 50 kHz (0.5 ppm of the Lamb shift) or better. Due to the scaling of the interesting QED corrections with high powers of Z, we believe that He$^+$ offers promising opportunities in comparison to H. The number of theoretical digits that can be compared with experiments is currently about the same in hydrogen and He$^+$, but the scaling of the limiting contributions with $Z^6/Z^2=16$ means that the same higher-order QED effects are tested already with more than one digit less experimental accuracy in He$^+$.

VI. SUMMARY AND OUTLOOK

We have discussed the feasibility of two-photon spectroscopy of the 1S-2S transition in He$^+$ using xuv frequency combs generated in external enhancement cavities and the impact of such a measurement on QED tests. The spectroscopy is shown to have a number of unique features in comparison to the vast majority of precision spectroscopy experiments on trapped ions. Most importantly, we note the ionization of the "clock" transition and the lack of a narrow-band laser to drive a strong cycling transition so that standard cooling and detection schemes fail.

Our analysis of the excitation and ionization dynamics shows that the power levels at 61 nm we expect ($P_{\text{xuv}} \sim 10$–100 μW) will be sufficient for spectroscopy, although tight focusing down to <10 μm and long interaction times are necessary to attain appreciable rates. This can conveniently be fulfilled by a sample of cold trapped He$^+$ ions. We propose to use the production of He^{2+} ions as a signature for successful excitations. Auxiliary ions are introduced into the trap that sympathetically cool the He$^+$ ions and also serve as "detectors" for successful excitations via secular excitation. This detection scheme is virtually background free. Anticollinear axial excitation yields the highest rates but presents a significant experimental challenge, because of the need for temporal and spatial overlap of the short light pulses with the ions. Collinear radial excitation simplifies the ex-

periment considerably but requires up to an order of magnitude more power and/or tighter focusing.

A measurement of the He$^+$ 1S-2S transition frequency can provide valuable input for tests of bound-state QED. Higher-order corrections which currently cannot be tested in other hydrogenic systems would be accessible, especially if more precise nuclear radii from measurements on muonic helium and an improved Rydberg constant become available. The transition frequency can currently be predicted to within 350 kHz, corresponding to a relative uncertainty of 3.5 $\times 10^{-11}$, equally limited by the accuracy of the charge radius

and the B_{60} and B_{7i} terms. An analysis of typical systematic errors promises uncertainties far below that level, on the order of 10^{-16}.

[1] M. Niering, R. Holzwarth, J. Reichert, P. Pokasov, Th. Udem, M. Weitz, T. W. Hänsch, P. Lemonde, G. Santarelli, M. Abgrall, P. Laurent, C. Salomon, and A. Clairon, Phys. Rev. Lett. **84**, 5496 (2000).

[2] B. de Beauvoir, C. Schwob, O. Acef, L. Jozefowski, L. Hilico, F. Nez, L. Julien, A. Clairon, and F. Biraben, Eur. Phys. J. D **12**, 61 (2000).

[3] H. Häffner, T. Beier, N. Hermanspahn, H. J. Kluge, W. Quint, S. Stahl, J. Verdú, and G. Werth, Phys. Rev. Lett. **85**, 5308 (2000).

[4] J. Verdu, S. Djekic, H. Haffner, S. Stahl, T. Valenzuela, M. Vogel, G. Werth, H. J. Kluge, and W. Quint, Phys. Rev. Lett. **92**, 093002 (2004).

[5] M. W. Ritter, P. O. Egan, V. W. Hughes, and K. A. Woodle, Phys. Rev. A **30**, 1331 (1984).

[6] W. Liu, M. G. Boshier, S. Dhawan, O. van Dyck, P. Egan, X. Fei, M. Grosse Perdekamp, V. W. Hughes, M. Janousch, K. Jungmann, D. Kawall, F. G. Mariam, C. Pillai, R. Prigl, G. zu Putlitz, I. Reinhard, W. Schwarz, P. A. Thompson, and K. A. Woodle, Phys. Rev. Lett. **82**, 711 (1999).

[7] U. D. Jentschura, Phys. Rev. A **69**, 052118 (2004).

[8] B. Roth, U. Fröhlich, and S. Schiller, Phys. Rev. Lett. **94**, 053001 (2005).

[9] C. Gohle, Th. Udem, M. Herrmann, J. Rauschenberger, R. Holzwarth, H. A. Schuessler, F. Krausz, and T. W. Hänsch, Nature (London) **436**, 234 (2005).

[10] R. J. Jones, K. D. Moll, M. J. Thorpe, and J. Ye, Phys. Rev. Lett. **94**, 193201 (2005).

[11] A. Ozawa, J. Rauschenberger, C. Gohle, M. Herrmann, D. R. Walker, V. Pervak, A. Fernandez, R. Graf, A. Apolonski, R. Holzwarth, F. Krausz, T. W. Hänsch, and Th. Udem, Phys. Rev. Lett. **100**, 253901 (2008).

[12] D. C. Yost, T. R. Schibli, and J. Ye, Opt. Lett. **33**, 1099 (2008).

[13] J. G. Eden, Prog. Quantum Electron. **28**, 197 (2004).

[14] Y. V. Baklanov and V. P. Chebotayev, Appl. Phys. (Berlin) **12**, 97 (1977).

[15] J. N. Eckstein, A. I. Ferguson, and T. W. Hänsch, Phys. Rev. Lett. **40**, 847 (1978).

[16] Th. Udem, R. Holzwarth, and T. W. Hänsch, Nature (London) **416**, 233 (2002).

[17] A. Bartels, C. W. Oates, L. Hollberg, and S. A. Diddams, Opt. Lett. **29**, 1081 (2004).

[18] P. Fendel, S. D. Bergeson, Th. Udem, and T. W. Hänsch, Opt. Lett. **32**, 701 (2007).

[19] M. J. Snadden, A. S. Bell, E. Riis, and A. I. Ferguson, Opt. Commun. **125**, 70 (1996).

[20] F. Lindner, W. Stremme, M. G. Schatzel, F. Grasbon, G. G. Paulus, H. Walther, R. Hartmann, and L. Struder, Phys. Rev. A **68**, 013814 (2003).

[21] S. Kim, J. Jin, Y.-J. Kim, I.-Y. Park, Y. Kim, and S.-W. Kim, Nature (London) **453**, 757 (2008).

[22] A. Ancona, F. Roesser, K. Rademaker, J. Limpert, S. Nolte, and A. Tuennermann, Opt. Express **16**, 8958 (2008).

[23] S. Witte, R. Th. Zinkstok, W. Ubachs, W. Hogervorst, and K. S. E. Eikema, Science **307**, 400 (2005).

[24] S. Cavalieri, R. Eramo, M. Materazzi, C. Corsi, and M. Bellini, Phys. Rev. Lett. **89**, 133002 (2002).

[25] R. Th. Zinkstok, S. Witte, W. Ubachs, W. Hogervorst, and K. S. E. Eikema, Phys. Rev. A **73**, 061801(R) (2006).

[26] A. Schliesser, C. Gohle, Th. Udem, and T. W. Hänsch, Opt. Express **14**, 5975 (2006).

[27] J. Tate, T. Auguste, H. G. Muller, P. Salieres, P. Agostini, and L. F. DiMauro, Phys. Rev. Lett. **98**, 013901 (2007).

[28] L. A. Lompre, A. L'Huillier, M. Ferray, P. Monot, G. Mainfray, and C. Manus, J. Opt. Soc. Am. B **7**, 754 (1990).

[29] E. J. Takahashi, Y. Nabekawa, H. Mashiko, H. Hasegawa, A. Suda, and K. Midorikawa, IEEE J. Sel. Top. Quantum Electron. **10**, 1315 (2004).

[30] U. Birnbaum and R. Schreiner, Proc. SPIE **5965**, 59650T (2005).

[31] H. Mashiko, A. Suda, and K. Midorikawa, Opt. Lett. **29**, 1927 (2004).

[32] J. I. Larruquert and R. A. M. Keski-Kuha, Appl. Opt. **41**, 5398 (2002).

[33] P. Kirkpatrick and A. V. Baez, J. Opt. Soc. Am. **38**, 766 (1948).

[34] S. Matsuyama, H. Mimura, H. Yumoto, K. Yamamura, Y. Sano, Y. Endo, Y. Mori, Y. Nishino, K. Tamasaku, T. Ishikawa, M. Yabashi, and K. Yamauchi, Rev. Sci. Instrum. **76**, 083114 (2005).

[35] The tabulated transmission is higher, but in practice oxide layers reduce the transmission significantly.

[36] K. Varjú, Y. Mairesse, B. Carré, M. B. Gaarde, P. Johnsson, S. Kazamias, R. López-Martens, J. Mauritsson, K. J. Schafer, P. Balcou, A. L'huillier, and P. Salières, J. Mod. Opt. **52**, 379 (2005).

[37] M. Murakami, J. Mauritsson, A. L'Huillier, K. J. Schafer, and M. B. Gaarde, Phys. Rev. A **71**, 013410 (2005).

[38] M. Haas, U. D. Jentschura, C. H. Keitel, N. Kolachevsky, M. Herrmann, P. Fendel, M. Fischer, Th. Udem, R. Holzwarth, T. W. Hänsch, M. O. Scully, and G. S. Agarwal, Phys. Rev. A **73**, 052501 (2006).

[39] S. Wolfram, *Mathematica—A System for Doing Mathematics by Computer* (Addison-Wesley, Reading, MA, 1988).

[40] A xuv comb at 30 nm is no appropriate source, since 1*S*-2*P* is a one-photon transition, so the quasi-cw argument of a two-photon transition does not hold.

[41] A. Friedenauer, F. Markert, H. Schmitz, L. Petersen, S. Kahra, M. Herrmann, Th. Udem, T. W. Hänsch, and T. Schätz, Appl. Phys. B: Lasers Opt. **84**, 371 (2006).

[42] H. Dehmelt, Bull. Am. Phys. Soc. **20**, 60 (1975).

[43] T. Rosenband, P. O. Schmidt, D. B. Hume, W. M. Itano, T. M. Fortier, J. E. Stalnaker, K. Kim, S. A. Diddams, J. C. J. Koelemeij, J. C. Bergquist, and D. J. Wineland, Phys. Rev. Lett. **98**, 220801 (2007).

[44] S. Klarsfeld, Phys. Lett. **30A**, 382 (1969).

[45] S. R. Jefferts, C. Monroe, E. W. Bell, and D. J. Wineland, Phys. Rev. A **51**, 3112 (1995).

[46] M. A. Rowe, A. Ben-Kish, B. DeMarco, D. Leibfried, V. Meyer, J. Beall, J. Britton, J. Hughes, W. M. Itano, B. Jelenkovic, C. Langer, T. Rosenband, and D. J. Wineland, Quantum Inf. Comput. **2**, 257 (2002).

[47] J. S. Cohen and J. N. Bardsley, Phys. Rev. A **18**, 1004 (1978).

[48] D. J. Berkeland, J. D. Miller, J. C. Bergquist, W. M. Itano, and D. J. Wineland, J. Appl. Phys. **83**, 5025 (1998).

[49] G. Morigi and S. Fishman, Phys. Rev. Lett. **93**, 170602 (2004).

[50] H. Goldstein, *Classical Mechanics*, 2nd ed. (Addison-Wesley, Reading, MA, 1980), p. 672.

[51] D. J. Wineland and W. M. Itano, Phys. Rev. A **20**, 1521 (1979).

[52] G. Morigi and H. Walther, Eur. Phys. J. D **13**, 261 (2001).

[53] This was part of the consistency checks in the calculation of the spectra.

[54] H. A. Bethe and E. E. Salpeter, *Quantum Mechanics of One-and Two-Electron Atoms* (Springer, Berlin, 1977).

[55] U. D. Jentschura and M. Haas, Phys. Rev. A **78**, 042504 (2008).

[56] G. Breit, Nature (London) **122**, 649 (1928).

[57] M. I. Eides, H. Grotch, and V. A. Shelyuto, Phys. Rep. **342**, 63 (2001).

[58] P. G. Blunden and I. Sick, Phys. Rev. C **72**, 057601 (2005).

[59] I. Sick, Phys. Lett. B **576**, 62 (2003).

[60] I. Sick, Phys. Rev. C **77**, 041302(R) (2008).

[61] P. J. Mohr and B. N. Taylor, Rev. Mod. Phys. **77**, 1 (2005).

[62] K. Pachucki and A. M. Moro, Phys. Rev. A **75**, 032521 (2007).

[63] J. Sapirstein and D. R. Yennie, in *Quantum Electrodynamics*, edited by T. Kinoshita, Advanced Series on Directions in High Energy Physics Vol. 7 (World Scientific, Singapore, 1990), pp. 560–672.

[64] U. D. Jentschura, S. Kotochigova, E.-O. Le Bigot, P. J. Mohr, and B. N. Taylor, Phys. Rev. Lett. **95**, 163003 (2005).

[65] K. Pachucki and U. D. Jentschura, Phys. Rev. Lett. **91**, 113005 (2003).

[66] U. D. Jentschura, A. Czarnecki, and K. Pachucki, Phys. Rev. A **72**, 062102 (2005).

[67] V. A. Yerokhin, P. Indelicato, and V. M. Shabaev, Phys. Rev. A **71**, 040101(R) (2005).

[68] U. D. Jentschura and M. Haas, Can. J. Phys. **85**, 531 (2007).

[69] T. Nebel, F. D. Amaro, A. Antognini, F. Biraben, J. M. R. Cardoso, C. A. N. Conde, A. Dax, S. Dhawan, L. M. P. Fernandes, A. Giesen, T. W. Hänsch, P. Indelicato, L. Julien, P. E. Knowles, F. Kottmann, E. Le Bigot, Y.-W. Liu, J. A. M. Lopes, L. Ludhova, C. M. B. Monteiro, F. Mulhauser, F. Nez, R. Pohl, P. Rabinowitz, J. M. F. dos Santos, L. A. Schaller, K. Schuhmann, C. Schwob, D. Taqqu, and J. F. C. A. Veloso, Can. J. Phys. **85**, 469 (2007).

[70] G. Carboni, G. Gorini, G. Torelli, L. Palffy, F. Palmonari, and E. Zavattini, Nucl. Phys. A **278**, 381 (1977).

[71] H. von Arb, F. Dittus, H. Heeb, H. Hofer, F. Kottmann, S. Niggli, R. Schaeren, D. Taqqu, and J. Unternährer, Phys. Lett. **136B**, 232 (1984).

[72] M. Eckhause, P. Guss, D. Joyce, J. R. Kane, R. T. Siegel, W. Vulcan, R. E. Welsh, R. Whyley, R. Dietlicher, and A. Zehnder, Phys. Rev. A **33**, 1743 (1986).

[73] P. Hauser, H. P. von Arb, A. Biancchetti, H. Hofer, F. Kottmann, C. Luchinger, R. Schaeren, F. Studer, and J. Unternährer, Phys. Rev. A **46**, 2363 (1992).

5.2. Dynamics of 1S-2S

The feasibility study of 1S-2S in He$^+$ triggered a collaboration with two theorists from Heidelberg, M. Haas and U. D. Jentschura on the dynamics of the 1S-2S transition in hydrogenic systems in general. The following manuscript is a result of this collaboration and offers a detailed discussion of the damped optical Bloch equations (to which the author mainly contributed to) and a re-derivation of relevant matrix elements in SI units which resolves some inconsistencies found in the literature.

Two-photon excitation dynamics in bound two-body Coulomb systems including ac Stark shift and ionization

M. Haas, U. D. Jentschura, and C. H. Keitel

Max-Planck-Institut für Kernphysik, Saupfercheckweg 1, 69117 Heidelberg, Germany

N. Kolachevsky,* M. Herrmann, P. Fendel, M. Fischer, Th. Udem, R. Holzwarth, and T. W. Hänsch

Max-Planck-Institute of Quantum Optics, Hans-Kopfermann-Straße 1, 85748 Garching, Germany

M. O. Scully

Institute for Quantum Studies and Department of Physics, Texas A&M University, College Station, Texas 77843-4242, USA
and Princeton Institute for Materials Research, Princeton University, Princeton, New Jersey 08544-1009, USA

G. S. Agarwal

Physics Research Laboratory, Nevrangpura, Ahmedabad-380 009, India
and Department of Physics, Oklahoma State University, Stillwater, Oklahoma 74078, USA
(Received 19 January 2006; published 3 May 2006)

One of the dominant systematic effects that shift resonance lines in high-precision measurements of two-photon transitions is the dynamic (ac) Stark shift. For suitable laser frequencies, the ac Stark shift acquires an imaginary part which corresponds to the rate of resonant one-photon ionization of electrons into a continuum state. At the current level of spectroscopic accuracy, the underlying time-dependent quantum dynamics governing the atomic two-photon excitation process must be well understood, and related considerations are the subject of the present paper. In order to illustrate the basic mechanisms in the transient regime, we investigate an analytically solvable model scenario for the population dynamics in the density matrix formalism and describe in detail how to generalize the corresponding equations of motion for individual experimental use. We also calculate the dynamic Stark shift for two-photon *S-S* and *S-D* transitions in bound two-body Coulomb systems and the corresponding two-photon transition matrix elements. In particular, we investigate transitions for which the 1*S* ground state or alternatively the metastable 2*S* state acts as the lower-energy state, and for which states with $n \leqslant 20$ represent the upper states. Relativistic and radiative corrections to the excitation dynamics, and the corresponding limitations to the accuracy of the measurements, are briefly discussed. Our considerations suggest the general feasibility of a detection mechanism, offering high quantum efficiency, based on two-step three-photon resonant ionization spectroscopy, for large classes of experimentally relevant two-photon transitions in two-body Coulomb systems.

I. INTRODUCTION

Like the electron gyromagnetic ratio, two-photon transitions in hydrogenlike systems belong to the few cases where experimental values can be compared with quantum electrodynamic (QED) calculations with very high precision. These comparisons are the basis for verification or falsification of this fundamental theory. In view of the increasing accuracy of two-photon spectroscopic experiments, it is necessary to understand in detail the excitation dynamics and the line profile of the relevant resonances, as they can be observed under realistic experimental conditions. Experiments investigating the hydrogen *S-S* and *S-D* transitions are also important for the determination of fundamental constants and their possible time variation [1–3].

Concurrent with the experimental progress in this field, there has been a wealth of theoretical studies addressing systematic effects, predicting the spectral line profile and calculating atomic properties connected to these problems [4–13]. Ionization cross sections of atoms in excited states of typical two-photon transitions have been obtained in [4] as early as 1930. Very detailed studies of dynamic Stark shifts and broadening effects on the spectral line shape of two-photon transitions in hydrogen have been carried out, e.g., in [5–9]. In these investigations, a large set of values for the dynamic polarizability for transitions to highly excited states is given. For hydrogen, the emphasis has been on the metastable 2*S* state acting as the ground state. A detailed review of two-photon transition line shapes and experiments aimed at the determination of the Rydberg constant can be found in [10].

Experiments investigating the 1*S*-2*S* transition in muonium and positronium for the first time [11,12], and accurate measurements of the transition frequency [13] have been reported, extending high-precision spectroscopy to bound two-body Coulomb systems beyond atomic hydrogen. A detection scheme for muonium, based on ionization, has been both described experimentally [13,14] and analyzed theoretically [8]. For the future, measurements on antihydrogen and hy-

drogenlike ions are planned, and coherent light sources in the extreme ultraviolet, which are needed for some of these experiments, have been demonstrated recently [15].

In this paper, we reconsider the derivation of the dynamic polarizabilities and transition matrix elements for *S*-*S* and *S*-*D* two-photon transitions in hydrogenlike systems in a unified treatment, compiling the results in SI units for convenient experimental use. We include the dependence on the nuclear charge number *Z*, where the two-photon resonance condition for the laser frequency is maintained for different *Z*, and the dependence on the nuclear mass, so that our results are applicable to general two-body Coulomb systems, such as hydrogen, positronium, muonium, antiprotonic helium, etc. Considering the excited state *nS* of a bound two-body Coulomb system, driven by a laser field on two-photon resonance with the 1*S*-*nS* transition, absorption of one additional photon is sufficient to ionize the system. The same applies to all but *n*=3 of the 2*S*-*nS* transitions and to the corresponding *S*-*D* transitions. The excitation of many two-photon transitions must therefore necessarily take place in the transient regime, because the driving laser would otherwise ionize all atoms in the excited state, in the limit of infinite interaction time (neglecting recombination). Thus we consider the time-dependent quantum dynamics for *S*-*S* and *S*-*D* transitions, including both photoionization and spontaneous decay of the system. We obtain an analytic solution of the master equation for finite times in the special case of constant intensity, and observe some interesting features in the line shape of the transition. Straightforward generalizations of the formalism to specific setups are given, which are accessible to a numerical treatment. For different nuclear charges, the relative importance of spontaneous decay versus ionization is discussed.

Even though this work aims to facilitate experimental tests of QED, it should be stressed that calculations in the framework of nonrelativistic Schrödinger theory are currently sufficient to describe the experimental line shape for low *Z* accurately. However, relativistic and radiative corrections to the matrix elements that enter into the line shape constitute small but interesting effects. We give explicit relativistic results for selected transitions, to indicate the orders of magnitude, and we clarify some minor inconsistencies in the literature, in particular with respect to the ionization cross section and a few numerical differences.

As a concrete case, we consider the 1*S*-2*S* hydrogen measurement [16], where the natural linewidth of the metastable 2*S* level is 1.31 Hz and yet the observed spectral width of the resonance line is about a few hundred hertz. The contributions due to the time-of-flight broadening, and the ionization broadening are intertwined with the quantum dynamics of the excitation process, so that they cannot simply be added in quadrature or in any other simple algebraic way.

In short, the purpose of this paper is twofold. Our first aim is to indicate the importance of ionization in the quantum dynamics and to describe the absorption spectrum in two-photon resonance spectroscopy. The second aim is to compile results for the two-photon transition matrix elements, dynamic polarizabilities and ionization cross sections that enter into the equations of motion, keeping all factors of $\hbar$, c, and ϵ_0 in the derivation. In combination, these ingredients

provide a toolkit to readily model a large variety of experimental situations in the proper SI units.

The paper is organized as follows: In Sec. II, the quantum dynamics in terms of the optical Bloch equations is discussed. Section III is dedicated to the two-photon transition matrix elements of a variety of two-photon transitions in two-body Coulomb systems. In Sec. IV, we present the dynamic Stark shift and ionization coefficients for the same set of transitions, including a brief outline of radiative and relativistic corrections in Sec. IV D. Finally, conclusions are drawn in Sec. V.

II. QUANTUM DYNAMICS

A. Introduction

Two-photon transitions in hydrogen and hydrogenlike ions are of special interest to high-precision spectroscopy [16,17], because they allow for a suitable elimination of the first-order Doppler shift via absorption of two counterpropagating photons. In order to calculate the absorption line shape, taking into account the remaining systematic effects, it is necessary to study the time-dependent interaction process, which is the subject of this section, including the dynamic Stark effect, the ionization of the excited state, and the second-order Doppler shift. The resulting equations of motion for the atom-laser interaction can be adapted to suit different experimental setups and different two-body Coulomb systems. For the special case of constant light intensity, they are solvable analytically.

In the mentioned experiment [16], a beam of hydrogen atoms is excited by laser radiation in a linear cavity which serves to produce an amplified standing wave. The injected atoms (initially in the 1*S* ground state) can be excited to the 2*S* state by two-photon absorption, and the number of excited 2*S* atoms is measured as a function of laser frequency after a certain interaction time. This signal, referred to as "the line shape" below, is generated by an ensemble of atoms, characterized by the experimental setup. Decisive parameters include (i) the spatial light intensity profile, (ii) the second-order Doppler shift, (iii) the finite light-atom interaction time, i.e., temporal intensity profile, and (iv) the varying ionization probability during the interaction. The resulting contributions of the atomic ensemble, specific to the experiment, can be taken into account in a numerical integration of the equations of motion presented in the following. For the hydrogen 1*S*-2*S* experiment, this has been carried out in a Monte Carlo approach [18].

B. Basic quantum dynamics

In this section, the basic model which we use for the excitation and ionization of two-body Coulomb systems is described. The main approximations we will make is to consider the driving laser field to be monochromatic, and to neglect the direct three-photon ionization of the ground state.

The appropriate description of excitation with a finite-bandwidth laser field necessitates a treatment involving stochastic differential equations [19,20] and is out of the scope of this paper. However, we would like to stress that in most

systems, the monochromatic approximation is a good approximation, because the ionization of the excited state limits the total interaction time of the bound system with the laser field. As long as the finite bandwidth of the laser is small compared to the transient width of the excited state, which for reasons of principle can never be smaller than the inverse interaction time, a monochromatic laser is a good approximation. Note that for spectroscopic experiments probing a steady state, with an infinite interaction time, we would have to compare the laser linewidth to the natural linewidth instead.

Although the current paper is exclusively concerned with a laser whose linewidth is so small that it can be regarded as monochromatic for the purposes of the current investigation (see the discussion above), we would like to comment briefly on the issues regarding a finite laser linewidth. For short-time evolution of the density matrix in the regime where the excited state population $\rho_{ee} \propto \Omega^2 t^2$ (Ω is the two-photon Rabi frequency on two-photon resonance), a simple averaging of ρ_{ee} over the power spectrum of the laser can be applied [see Eq. (2.74) of [21]], but this averaging is not applicable for longer excitation times. In the latter case, one has to take into account the fact that the phase fluctuations of a laser typically constitute a stochastic process which necessitates a modification of the coherence terms in the optical Bloch equations, in the sense discussed in [22], resulting in further damping terms entering the right-hand side of Eq. (10b) below.

As an example for the monochromatic excitation, one may consider the hydrogen 1S-2S experiment, where the excitation typically takes place on a submillisecond time scale. The spectral line width of the laser is on the order of 200 Hz at 121 nm, which is small compared to the typical inverse interaction time of some kilohertz, while the natural linewidth of the 2S state is only 1.31 Hz.

The standard approach [23,24] is to solve the density matrix equations for a two-level system. We can restrict the Hilbert space of the atom to only two relevant states, an excited state $|e\rangle$ and a ground state $|g\rangle$, because near resonance, only that two-photon transition will be driven significantly by the laser field. We will assume that the atoms are initially in $|g\rangle$ and are irradiated with the intensity $I(t)$, as observed by the atom, starting from time $t = 0$. For specific considerations concerning the intensity in a standing wave, see Sec. II E below. The straightforward treatment of this interacting two-level system is extended by including decay channels due to spontaneous decay and ionization into the density matrix equations, which will turn out to be crucial ingredients.

Our starting point is the von Neumann equation [23] for the density operator ρ,

$$i\hbar \frac{\partial}{\partial t}\rho = [\widetilde{H},\rho], \qquad (1)$$

with

$$\widetilde{H} = E_g|g\rangle\langle g| + E_e|e\rangle\langle e| + \frac{\hbar\Omega}{2}[\exp(i\omega_L t) + \exp(-i\omega_L t)]^2$$
$$\times(|e\rangle\langle g| + |g\rangle\langle e|), \qquad (2)$$

$$E_g = h\nu_g + h\Delta\nu_{ac}(g), \qquad (3)$$

$$E_e = h\nu_e + h\Delta\nu_{ac}(e). \qquad (4)$$

The tilde on $\widetilde{H}$ signifies that the Hamiltonian is restricted to the two atomic states under consideration, as opposed to the following sections. The angular frequency of the laser is denoted by ω_L. Generally, throughout the paper, we will use both the symbols ω and Ω for angular frequencies (measured in rad/s) appearing in the argument of exponential functions of the form $\exp(i\omega t)$, and ν for frequencies as measured in hertz (compatible with the international unit system SI).

The energies of the excited state E_e and ground state E_g already include the dynamic Stark effect, expressed by the respective frequency shift $\Delta\nu_{ac}$. As will be presented in detail in Sec. IV, these frequency shifts are proportional to the intensity $I(t)$ of the exciting laser field, and in accordance with [6], the ac Stark coefficient β_{ac} is defined as

$$\Delta\nu_{ac}(g) = \beta_{ac}(g)I(t), \qquad (5)$$

and likewise for the excited state. The ac Stark coefficients are calculated in Sec. IV and listed in SI units in Tables IV–VII below. Further, we define the two-photon Rabi frequency Ω as

$$\Omega = 2(2\pi\beta_{ge})I(t), \qquad (6)$$

and due to the two-photon nature of the excitation process, Ω is also proportional to the light intensity, rather than to the electric field amplitude, as is the case for one-photon dipole-allowed transitions. Section III treats the calculation of the two-photon transition matrix elements β_{ge} and lists the results for a set of transitions in Tables II and III below.

For the description of the population dynamics of the system, it is useful to factor out a fast-oscillating term of the off-diagonal elements of the density matrix in the equations of motion (1). We denote the transformed density matrix elements by a prime and define

$$\rho'_{gg} := \rho_{gg}, \quad \rho'_{ge} := \rho_{ge}\exp(-i2\omega_L t), \qquad (7a)$$

$$\rho'_{ee} := \rho_{ee}, \quad \rho'_{eg} := \rho_{eg}\exp(i2\omega_L t). \qquad (7b)$$

This corresponds to a transformation into the interaction picture, but with a phase factor of $\exp(-i2\omega_L t)$ instead of $\exp(-i\omega_{eg}t)$ for the coherence ρ_{ge}. Note that the diagonal elements of the density matrix, representing the population, are invariant under this transformation. The resulting equations of motion (EOMs) for the matrix elements of the transformed density operator ρ' then contain both slowly varying terms, which determine the time scale of the population dynamics, and terms oscillating with $\pm 2\omega_L$ and $\pm 4\omega_L$. We can now employ the rotating-wave approximation, dropping the terms oscillating at these optical frequencies, thereby neglecting the Bloch-Siegert shifts [25]. Relative to the ac Stark shift, the Bloch-Siegert shift in a two-photon transition is suppressed by a factor of Ω/ω_L, which is on the order of 10^{-10} for realistic intensities considered here. This is a small effect, compared with the relativistic, radiative, and field configuration corrections discussed below.

The spontaneous decay and the ionization of the excited state can now be taken into account by adding

$$\rho'_{\text{relax}} = -(\gamma_i + \gamma_s)\rho'_{ee}|e\rangle\langle e| + \gamma_s\rho'_{ee}|g\rangle\langle g|$$
$$-\frac{\gamma_i + \gamma_s}{2}(\rho'_{ge}|g\rangle\langle e| + \rho'_{eg}|e\rangle\langle g|) \quad (8)$$

to the right-hand side of Eq. (1), after performing the transformation (7). The spontaneous decay rate is denoted by γ_s, while γ_i represents the rate with which the excited state is depopulated due to one-photon resonant ionization:

$$\gamma_i = 2\pi\beta_{\text{ioni}}(e)I(t). \quad (9)$$

All transition rates in this paper, denoted by γ with an appropriate index, are given in angular frequency units rad/s. In cases where the decay γ is the governing broadening mechanism this translates into a linewidth (Lorentzian full width at half maximum) of $\Delta\nu_\gamma = \gamma/2\pi$. The ionization coefficient β_{ioni} is closely connected to the dynamic Stark effect which is discussed in Sec. IV. Essentially, the dynamic Stark coefficient is a complex quantity, the real part yielding β_{ac}, and the imaginary part determining β_{ioni}. The ionization rate (9) is included into the equations of motion in analogy with the spontaneous decay rate, with one important difference. In the particular case of the 1S-2S experiment, the atomic density is very low, in order to avoid collisional effects on the transition frequency. Therefore, the recombination probability for protons and electrons to form again a hydrogen atom in the ground state is extremely small. Consequently, we do not include a recombination term into ρ'_{relax}. In cases where recombination by radiative or three-body processes cannot be neglected, the respective rates are described by the principle of detailed balance (see, e.g., pp. 102 and 151 of [26]).

In the cases where the lower level $|g\rangle$ is the 2S state, the excited state nS or nD can decay spontaneously into several levels, which in turn cascade (i) to the metastable 2S state, dominantly with an effective rate γ_s^{2S} and (ii) to the 1S ground state, with an effective rate γ_s^{1S}. If the decay cascade ends in $|1S\rangle$, the population is lost for the dynamics of the considered two-level system, and can therefore be treated as an additional intensity-independent ionization rate: $\gamma_i \rightarrow 2\pi\beta_{\text{ioni}}(e)I + \gamma_s^{1S}$.

We arrive at the following set of equations, which are equivalent to, e.g., Eq. (8) of Ref. [8], in the case where $\gamma_s = 0$:

$$\frac{\partial}{\partial t}\rho'_{gg} = -\Omega\,\text{Im}(\rho'_{ge}) + \gamma_s\rho'_{ee}, \quad (10a)$$

$$\frac{\partial}{\partial t}\rho'_{ge} = -i\Delta\omega\rho'_{ge} + i\frac{\Omega}{2}(\rho'_{gg} - \rho'_{ee}) - \frac{\gamma_i + \gamma_s}{2}\rho'_{ge}, \quad (10b)$$

$$\frac{\partial}{\partial t}\rho'_{ee} = \Omega\,\text{Im}(\rho'_{ge}) - (\gamma_i + \gamma_s)\rho'_{ee}, \quad (10c)$$

with the definition for the excitation detuning

$$\Delta\omega = 2\pi\Delta\nu = 2\omega_L - 2\pi\nu_{eg} - 2\pi[\Delta\nu_{\text{ac}}(e) - \Delta\nu_{\text{ac}}(g)]. \quad (11)$$

Here, the absolute frequency of the unperturbed transition is ν_{eg}. Whereas the first-order Doppler shift is often canceled by the use of two counterpropagating beams, the second-order Doppler shift of an atom moving with velocity v, like any other single-particle frequency shift, can be included into the excitation detuning by adding

$$\Delta\omega_{\text{D2}} = (2\pi\nu_{eg})\frac{1}{2}\frac{v^2}{c^2} \quad (12)$$

to the right-hand side of Eq. (11). At this point, we would like to remark that the EOMs (10) are similar to the case of a two-level system, coupled by a laser field driving a dipole-allowed one-photon transition. In fact, the main conceptual difference lies in the calculation of the transition matrix elements entering into the Rabi frequency and the dynamic Stark coefficients. In particular, the dynamic Stark effect is fundamentally different for the two-photon case, where the harmonic electric field is an off-resonant perturbation of second order, as opposed to the resonant one-photon case, where the level shift is linear in the electric field amplitude. Note also that, in contrast to one-photon transitions, the spontaneous decay rate is modified slightly in the presence of the laser field due to virtual intermediate P states, even for the 1S-2S transition, as detailed in Appendix D.

C. Analytic solution for constant intensity

In the above form (10), for constant intensity $I(t) = I$, the EOMs are a coupled set of first-order differential equations with constant coefficients and hence are solvable analytically for all times. The somewhat lengthy expression for the full solution is given in Appendix B.

An analytic solution to Eqs. (10) without ionization ($\gamma_i = 0$), taken in the limit of infinite interaction time, leads to the well-known steady state of the system with a Lorentzian line shape for the excited-state population [23]. In this case, it is assumed that the population that decays out of the excited state reappears in full at the ground state. When discussing two-photon S-S and S-D transitions, this hardly ever happens. Even the 2S-3S transition, for which indeed $\gamma_i = 0$, does not satisfy this condition, because the population in the 3S state also spontaneously decays to the 1S state, mainly via 2P, and does not reappear in the 2S state.

In this section, we will first focus on the case of vanishing spontaneous decay, $\gamma_s = 0$. This is often a good approximation when atoms or ions are excited in beams or gas cells, as opposed to trapped particles. In particular, it is a very good approximation for the hydrogen 1S-2S transition, because for typical intensities, the ionization rate dominates over the two-photon spontaneous decay rate. Later in this section, we will come back to the general solution, for cases where the spontaneous decay rate is no longer negligible (e.g., for systems with nuclear charge number $Z > 1$).

We recall that the EOMs describe an atom at rest or moving with a constant velocity, for which the Doppler shift can be included into the detuning $\Delta\omega$. The initial state is the

ground state, so $\rho_{gg}(t=0)=1$ and $\rho_{ee}(0)=\rho_{ge}(0)=\rho_{eg}(0)=0$. Starting from time $t=0$, the system is interacting with a monochromatic laser field of constant intensity I. The transient line shape, which is defined as the population in the excited $2S$ state as a function of detuning and time, $\rho'_{ee}(\Delta\omega,t)$, can then be expressed as

$$\rho'_{ee}(\Delta\omega,t) = \frac{4\Omega^2}{G} \exp\left(-\frac{\gamma_i}{2}t\right)[\sin^2(\Omega_1 t) + \sinh^2(\Omega_2 t)], \quad (13a)$$

$$\rho'_{gg}(\Delta\omega,t) = \rho'_{ee}(\Delta\omega,t) + \frac{1}{G\Omega_1\Omega_2} \exp\left(-\frac{\gamma_i}{2}t\right)$$
$$\times \{\Omega_2(4\Omega_1^2 - \Delta\omega^2)[4\Omega_1\cos(2\Omega_1 t)$$
$$+ \gamma_i \sin(2\Omega_1 t)] + \Omega_1(4\Omega_2^2 + \Delta\omega^2)$$
$$\times[4\Omega_2\cosh(2\Omega_2 t) + \gamma_i \sinh(2\Omega_2 t)]\}, \quad (13b)$$

where

$$G = \sqrt{16\Delta\omega^2\gamma_i^2 + (4\Delta\omega^2 + 4\Omega^2 - \gamma_i^2)^2}, \quad (14a)$$

$$\Omega_1 = \frac{1}{4\sqrt{2}}\sqrt{G + 4\Delta\omega^2 + 4\Omega^2 - \gamma_i^2}, \quad (14b)$$

$$\Omega_2 = \frac{1}{4\sqrt{2}}\sqrt{G - 4\Delta\omega^2 - 4\Omega^2 + \gamma_i^2}. \quad (14c)$$

The angular frequencies Ω_1 and Ω_2 are always real. Reassuringly, we have found that this solution has been obtained in a rather different form in [20,27], but agrees with our result. These works focus on resonant multiphoton ionization and it is not surprising that the same master equations are relevant for these studies.

For the case of vanishing ionization $\beta_{ioni}=0$, we have $\Omega_2=0$ and we obtain the familiar Rabi oscillations with generalized Rabi frequency $\sqrt{\Delta\omega^2+\Omega^2}$:

$$\rho'_{ee}(\Delta\omega,t) = \frac{1}{2}\frac{\Omega^2}{\Delta\omega^2 + \Omega^2}[1 - \cos(\sqrt{\Delta\omega^2 + \Omega^2}t)], \quad (15)$$

as we should. Note that the exponential decay of the excited-state population seems to take place with only half the expected rate in Eq. (13). However, as the result describes excitation starting from the ground state and subsequent decay, the population decay rate is not simply γ_i for this particular solution. In comparison, the solution obtained with the same method, but with the excited state as the initial state and vanishing laser excitation ($\Omega=0$) does in fact decay with the rate γ_i, independent of the detuning.

In Figs. 1–4, the analytic solution for the transient line shape of the $2S$ population in the vicinity of the hydrogen $1S$-$2S$ two-photon resonance is illustrated, where an intensity of 2.3 MW/m^2 is used, which is a typical magnitude in the experiment of [16]. Specifically, in Figs. 1 and 2, we investigate the influence of the ionization channel on the transient line shape for a typical interaction time of the $1S$-$2S$ experiment [16]. Observe that the inclusion of the ionization channel mainly changes the excitation efficiency while having only little effect on the spectral linewidth or on coherence
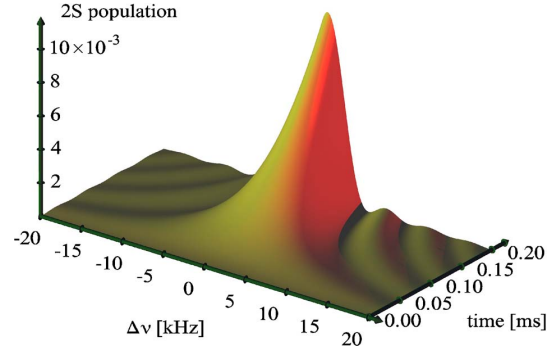
FIG. 1. (Color online) Atomic population in the $2S$ state of hydrogen ($Z=1$) as a function of interaction time t with the laser, and of detuning $\Delta\nu$ from the $1S$-$2S$ transition frequency, as defined in Eq. (11) with $\nu_{eg}\approx 2466$ THz. The laser intensity is $I=2.3$ MW/m^2, corresponding to $\Omega=2\pi\times 169$ Hz. The initial state at $t=0$ is the $1S$ state. In the time evolution of the system, ionization from the $2S$ state into the continuum and spontaneous decay of the $2S$ state have been neglected, i.e., ρ'_{ee} from Eq. (15) is plotted.

features. This is plausible, because on this time scale, which is much shorter than the Rabi oscillation time, the $2S$ state is only populated very little.

In Figs. 3 and 4, one can observe the strong influence of the ionization on the line shape for interaction times on the order of one Rabi oscillation and longer. With ionization taken into account (Fig. 4), the excitation of the $2S$ level is much less efficient, the coherence features (fringes) are washed out and spectral hole burning occurs, because close to zero detuning, excitation, and subsequent ionization is enhanced.

As the EOMs suggest, we obtain a symmetric line shape around $\Delta\omega=0$. However, it should be pointed out that this is no longer true for a collective signal from a thermal atomic beam. In that case, different second-order Doppler shifts according to Eq. (12), which all have the same sign, asym-
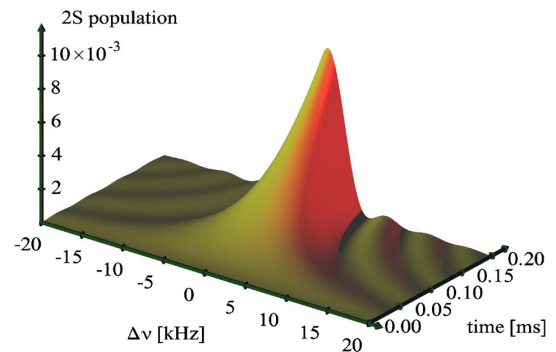
FIG. 2. (Color online) Same situation as in Fig. 1, except that in this plot, the effect of ionization was included, as in Eqs. (13) and (14). The ionization rate $\gamma_i=2\pi\times 276$ Hz. For the short times considered here, there is only a small difference to Fig. 1 in the total excitation efficiency, which is due to the ionization loss from the excited state.
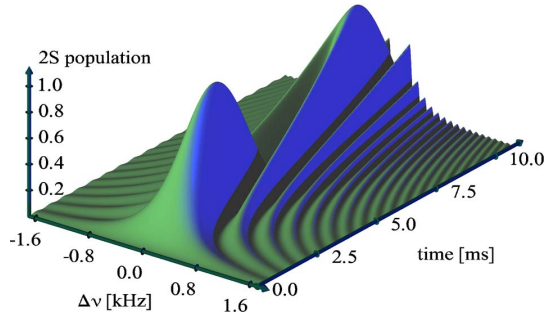
FIG. 3. (Color online) Same as Fig. 1, but for interaction times that are comparable with the Rabi oscillation time. Ionization from the 2S state is not taken into account. At zero detuning, the $\sin^2$-shaped Rabi oscillations with full amplitude can be observed. All the other sections with constant detuning can also be understood as the well-known Rabi oscillations with diminished amplitude and generalized Rabi frequency $\Omega_R = \sqrt{\Delta\omega^2 + \Omega^2}$ in complete analogy with one-photon transitions except that the two-photon Rabi frequency Ω as defined in Eq. (6) is proportional to the intensity, instead of the electric field amplitude.

metrically distort the line shape, depending on the atomic beam parameters. However, the discussion here also applies to a monoenergetic beam of atoms. In this case the line symmetry point is simply shifted by the second-order Doppler effect and the dynamic Stark effect. The discussion of the linewidth is more involved, because for each point in time, the line shape is different and therefore the width is not defined unambiguously in the transient regime. Nevertheless, we want to discuss qualitatively the influence of ionization, excitation intensity, and interaction time on the $\Delta\omega$ dependence of the line shape.

Consider the two $\Delta\omega$-dependent factors in the expression for the line shape (13a). The factor $1/G$ is time independent
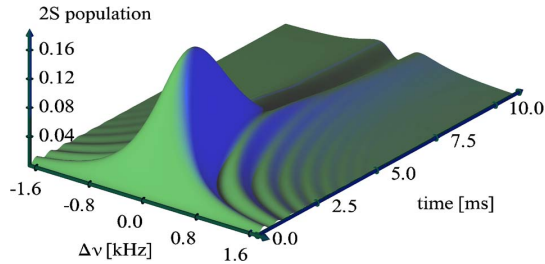
FIG. 4. (Color online) Same situation as in Fig. 3, except that here the ionization from the 2S state has been properly included. The presence of the ionization channel now makes a big difference as compared to Fig. 3, because at times comparable to the Rabi oscillation time, the 2S state is significantly populated and consequently the ionization probability is not negligible. The decay of the 2S population, spectral hole burning, and loss of coherence can be observed in this image. The maximum population of the 2S state is 0.175 [see Eq. (16)], whereas without ionization the 2S population repeatedly reaches 100% for $\Delta\nu = 0$. Including the 2S spontaneous two-photon decay of $\gamma_s = 2\pi \times 1.31$ Hz does not change the plot discernibly.

and indicates two contributions to the width. For increasing detuning, $1/G$ decreases more slowly if the intensity-dependent Rabi frequency Ω is large. This results in a time-independent power-broadening contribution. Likewise, the presence of an ionization channel, quantified by the ionization rate γ_i adds to this width, constituting an ionization broadening.

For the time-dependent factor $\sin^2(\Omega_1 t) + \sinh^2(\Omega_2 t)$, first consider the case of vanishing ionization, $\Omega_2 = 0$ (see also Fig. 3). The remaining term $\sin^2(\Omega_1 t)$ produces fringes within the line shape that become arbitrarily narrow with increasing interaction time t in the absence of any damping. However, the envelope of these fringes as well as any un-fringed line shape always increase in width [28] if ionization is introduced by virtue of the $\sinh^2$ term. The same holds true for power broadening described by the line shape (13). In Figs. 1 and 2, the $\sin^2(\Delta\omega)/\Delta\omega^2$ type of line shape, which is characteristic for the sudden turn-on of the excitation, can be recognized.

Comparing the detuning ranges of Figs. 1 and 2 with Figs. 3 and 4, one also observes that the width of the central peak decreases for increasing interaction time. This is observable in the experiment as a time-of-flight-dependent broadening. On two-photon resonance ($\Delta\nu = 0$) and for short interaction times, the 2S population initially grows proportionally to t^2. The maximum excited-state population $\rho'^{(max)}_{ee}$, which occurs at zero detuning $\Delta\omega = 0$, reads

$$\rho'^{(max)}_{ee} = \exp\left(-\frac{\beta_{ioni}\arccos\left(\frac{\beta_{ioni}^2}{8\beta_{ge}^2} - 1\right)}{\sqrt{16\beta_{ge}^2 - \beta_{ioni}^2}}\right), \qquad (16)$$

and is independent of the intensity of the laser field. Note that for the strongly damped case where $\beta_{ioni} > 4\beta_{ge}$, both the arccos and the square root are complex valued, but the result remains real. If spontaneous decay is included into the dynamics, as described below, the peak excited state population $\rho'^{(peak)}_{ee}$ is always less than given in Eq. (16). Expression (16) then gives the high-intensity limit for $\rho'^{(peak)}_{ee}$, where ionization dominates over the spontaneous decay.

One can hardly overemphasize that the steady state of the density matrix equation (10) is the one where the entire atomic population is in the ionized state. For a two-level system without ionization, in the steady state the population depends on the driving laser frequency in the form of a Lorentz curve [23]. Obviously, the ionization term changes this property drastically.

D. Quantum dynamics with spontaneous decay

In the following, we will focus on systems, in which the spontaneous decay channel is no longer negligible. As concrete examples, we will treat the 1S-2S and the 1S-3S transitions in systems where the nuclear charge number is not restricted to $Z=1$. Consider the Z scaling of the spontaneous decay rates, listed in Table I (see, e.g., [29–31] and pp. 266–267 in [32]). One-photon spontaneous decay rates of dipole-allowed transitions are denoted by $\gamma_s^{1\gamma}$; for two-photon spontaneous decay rates, we write $\gamma_s^{2\gamma}$. The ionization rate

TABLE I. Spontaneous decay rates (angular frequency) relevant to the description of the quantum dynamics of the 1S-2S and 1S-3S transition in hydrogenlike systems with nuclear charge number Z.

$\gamma_s^{1\gamma}(3S \to 2P)$	6.32×10^6 s^{-1} Z^4
$\gamma_s^{1\gamma}(2P \to 1S)$	6.25×10^8 s^{-1} Z^4
$\gamma_s^{2\gamma}(3S \to 1S)$	2.08 s^{-1} Z^6
$\gamma_s^{2\gamma}(3S \to 2S)$	6.45×10^{-2} s^{-1} Z^6
$\gamma_s^{2\gamma}(2S \to 1S)$	8.23 s^{-1} Z^6

coefficient β_{ioni} scales with Z^{-4} [see Eq. (43) below]; therefore the ratio R of the spontaneous decay rate and the ionization rate γ_i, as defined in (9), scales as

$$R^{1\gamma} = \frac{\gamma_s^{1\gamma}}{\gamma_i} \propto Z^8, \quad R^{2\gamma} = \frac{\gamma_s^{2\gamma}}{\gamma_i} \propto Z^{10}, \quad (17)$$

for a given laser intensity. Recall that in hydrogen, for typical intensities, the spontaneous decay rate is small compared to the ionization rate, i.e., $R^{2\gamma} \ll 1$. In contrast, for the 1S-2S transition in hydrogenlike helium ($Z=2$) and the same intensity of 2.3 MW/m^2, both rates are of comparable magnitude, with $R^{2\gamma} \approx 1.6$. The simplified form of the analytic solution (13) is therefore no longer valid, and even qualitative discussions of the analytic form of the full solution for the line shape (see Appendix B) are complicated. Nevertheless, one can plot the full solution (B1), and Figs. 5 and 6 show the transient line shape of the excited He$^+$ ion, irradiated with a cw laser of intensity 2.3 MW/m^2. This intensity is chosen to simplify the comparison with the hydrogen plots, although a cw-laser source at 61 nm does not yet exist.

In Fig. 5 one can observe that on a time scale comparable to the inverse spontaneous decay rate, the line shape evolves into a "quasi-steady-state" of approximate Lorentzian profile. Only on a longer time scale does ionization become impor-

FIG. 6. (Color online) 2S population dynamics including two-photon spontaneous decay in a He$^+$ ion as in Fig. 5, but on a much longer time scale. Here the decay of the population due to ionization is visible. Note that the effective population loss is by far smaller than the ionization rate $\gamma_i = 2\pi \times 17.3$ Hz (corresponding to a characteristic ionization time of 58 ms), because the quasi-steady-state population of the excited state is small. The peak population in the excited state is 10.6×10^{-3} for the considered intensity of 2.3 MW/m^2. The steep rise before $t=20$ ms is shown in more detail in Fig. 5.

tant, and the excited state is significantly depopulated (see Fig. 6).

The characteristic decay time of the excited 2S population is by far longer than the inverse ionization rate $2\pi/\gamma_i$. The reason for this seemingly unintuitive behavior is that the laser field continuously drives the system toward the steady state, which it would reach for $\gamma_i=0$. When the excited state is depopulated by ionization, population is again transferred into the excited state from the ground state, which is much more populated than the excited state for the intensity considered.

For $\gamma_s \neq 0$, the peak population of the excited state, $\rho_{ee}'^{(\text{peak})}$, occurring in the transient dynamics, is a function of the intensity of the driving laser, when spontaneous decay is included in the EOMs. For He$^+$, this dependence is shown in Fig. 7. For large intensities, the peak population approaches the maximum value given in Eq. (16).

By calculating the population in the continuum P state, $1 - \rho_{gg}'(\Delta\omega, t) - \rho_{ee}'(\Delta\omega, t)$, one obtains the probability of ionization via the two-photon resonant excited state as a func-

FIG. 5. (Color online) 2S population in a He$^+$ ion, as a function of detuning [defined in Eq. (11)] and interaction time with the laser driving the 1S-2S transition. Ionization and spontaneous two-photon decay of the 2S state are taken into account. A constant intensity of 2.3 MW/m^2 is assumed and the ion is in the 1S ground state at time $t=0$. On the time scale considered, the system evolves into a quasi-steady-state with approximate Lorentzian line shape.

FIG. 7. Peak 2S population in He$^+$, as a function of intensity, including spontaneous decay (solid line) and without spontaneous decay (dashed line), which is equal to $\rho_{ee}'^{(\text{max})}$ in Eq. (16), evaluated for the 1S-2S transition. For increasing intensity, the ionization rate eventually becomes large compared to the spontaneous decay rate, and the peak population increases, approaching the maximum $\rho_{ee}'^{(\text{max})}$.
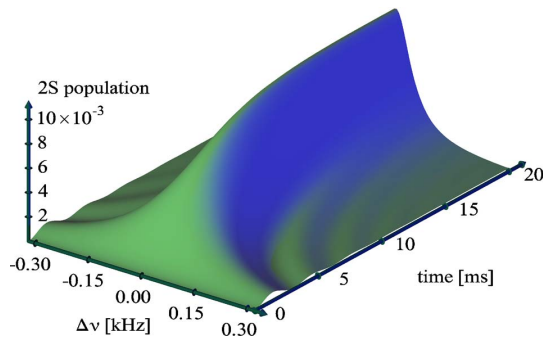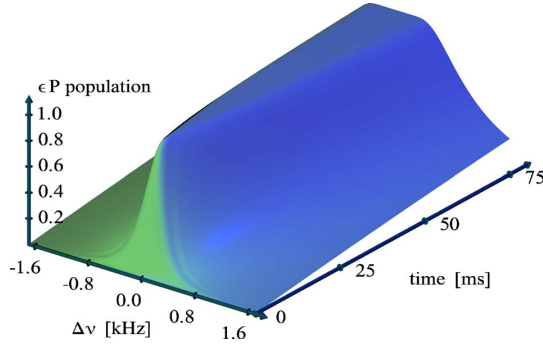
FIG. 8. (Color online) Population in the continuum P state as a function of detuning [defined in Eq. (11)] and interaction time with the laser, driving the hydrogen 1S-2S transition, including spontaneous two-photon decay of the intermediate 2S state with $\gamma_s = 2\pi \times 1.31$ Hz. A constant intensity of 2.3 MW/m^2 is assumed and the atom is in the 1S ground state at $t=0$.

tion of detuning and time, if $|g\rangle$ is the 1S state. In Fig. 8, we plot this εP population from the full solution (B1) of the EOMs (10) for the 1S-2S transition in hydrogen, and an intensity of 2.3 MW/m^2, as before. Note that in this case of nonvanishing laser intensity and ionization $\gamma_i \neq 0$, the steady state can be defined as the completely ionized atom, while for $\gamma_i = 0$, a regular steady state with a certain population distribution between the excited and ground states exists. The limit $\gamma_i \rightarrow 0$ is therefore nonuniform, in the sense that the steady state for $\gamma_i \neq 0$ does not tend to the steady state of the case $\gamma_i = 0$. As a result, for increasing interaction time, the detuning range in which the atomic population is completely ionized is increasing in width, as can be observed in Fig. 8. For a precision experiment relying on the detection of the free electrons, or alternatively the ionic cores, this means that the interaction time has to be chosen carefully in order to obtain a signal of minimal width. Using a detection scheme for charged particles instead of excited atoms has the advantage of a much higher detection efficiency.

For the 1S-2S transition, the direct two-photon spontaneous decay rate γ_s is the only spontaneous decay channel (see also Appendix D). For the 1S-3S transition the dominating decay takes place via the real intermediate 2P state, because the one-photon rates are orders of magnitude larger than the two-photon rates (see Table I and Fig. 9).

Strictly speaking, it would be necessary to introduce a new set of EOMs including the real intermediate 2P level. However, the 2P state is not resonantly coupled to some other state by the laser field and is populated only by incoherent decay. In addition, the decay rate out of 2P is 100 times larger than the decay rate into it. We can therefore approximate the quantum dynamics of a 1S-3S transition by the EOMs (10), if we use an effective decay rate from 3S to 1S which equals $\gamma_{eff} = \gamma_s^{1\gamma}(3S \rightarrow 2P)$. The direct two-photon decay and the two-step process of two-photon decays via the 2S level are completely negligible in comparison.

E. Generalizations of the EOMs

Now we will turn to more general cases, accommodating points (i)–(iv) from Sec. II A for a more realistic description of the interaction process.
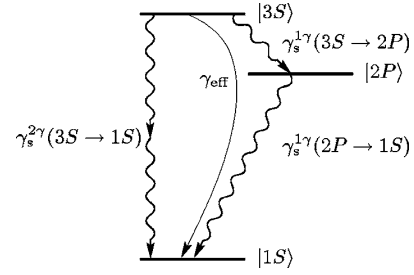
FIG. 9. Level scheme of the 3S-1S spontaneous decay. The two-step one-photon channel with the rates $\gamma_s^{1\gamma}$ dominates over the direct two-photon decay, and can be expressed by a direct effective rate γ_{eff}. The two-step two-photon channel via the 2S state is omitted.

The light intensity in most experiments is not constant, e.g., the atom under consideration may move through an inhomogeneous laser profile. In this case, the laser intensity can be described in terms of the trajectory as $I(\mathbf{r}(t))$. The atom may also be excited with a pulsed laser field, where the time-dependent intensity $I(t)$ is known explicitly. In general, an analytic solution including the varying ac Stark effect and Rabi frequency is then either extremely convoluted or impossible to find. Nonetheless, the EOMs can then be readily integrated numerically, for example by using the Runge-Kutta routines from Ref. [33], if we include a time-dependent intensity $I(t)$, specific to the experimental setup, into Eq. (10).

When we use the intensity in the context of two-photon spectroscopy, we must be aware of the resonator nature of most of these experiments. Typically the light is coupled into an enhancement cavity, mainly serving two purposes. First, the two photons necessary to drive the transition can be absorbed from opposite directions, leading to a cancellation of the first-order Doppler shift. Second, the total power circulating inside the interaction region is much larger than the in-coupling laser power, increasing the excitation probability.

If we consider a standing plane wave in the resonator on resonance, the intensity profile in the longitudinal direction is spatially modulated as

$$I_s(x) = 2I \cos^2(kx), \quad (18)$$

where I is the mean intensity, and where we take the cavity axis as the x axis with k being the modulus of the wave vector. If the atoms are fixed in space they simply observe the intensity at their respective position which ranges from 0 to 2I. In this case one faces the experimental problem of figuring out precisely where the atoms are, which could probably only be done for trapped ions.

For moving atoms in a standing wave, the description of a harmonic electric field with one frequency ω_L is no longer appropriate, since in the frame of the atom, the electric field can only be described by a superposition of two oppositely running wave fields which are Doppler shifted with opposite signs, corresponding to the atomic velocity v with respect to the laboratory frame. However, this superposition of electric fields, if inserted into the Hamiltonian (2), leads to the same

set of equations (10), where I is again the mean intensity, if the Doppler shift frequency is large compared to the characteristic frequencies occurring in the master equation (10):

$$\omega_{\mathrm{L}}\left(\frac{1+\beta}{\sqrt{1-\beta^2}}-1\right) \gg \max\{\Omega, \gamma_{\mathrm{i}}, \gamma_{\mathrm{s}}\}, \qquad (19)$$

where $\beta = v/c$. This is, in analogy with the rotating-wave approximation, a time-scale argument and it is not a strong restriction of the model presented here as the required minimum velocity to satisfy condition (19) for a thermal beam typically is quite low. For a Rabi frequency that occurs at some MW/m^2 in the hydrogen 1S-2S transition, this minimum velocity corresponds to a temperature on the order of 10^{-14} K. From a laboratory frame point of view, condition (19) simply means that an atom passes through the intensity profile (18) quickly enough, such that it effectively averages over the nodes and antinodes of the field and can be treated as if it was driven by a homogeneous intensity I. An intensity averaging very similar to the movement of a single atom takes place when many atoms sample different fixed positions of the standing laser wave. Any slower variation of the intensity, in the sense that (19) is not satisfied, cannot be eliminated from the EOMs and has to be taken into account explicitly, such as the radial intensity variation of a Gaussian beam.

Consider a situation where the total electric field is a superposition of waves running in opposite directions and with different time-dependent intensities $I_l(t)$ and $I_r(t)$, as observed at the location of the atom, e.g., for excitation with counterpropagating pulses. For the description of the dynamics of the first-order Doppler free transition component, the following replacements have to be made in Eq. (10):

$$\Omega = 2(2\pi\beta_{ge})I(t) \rightarrow \Omega = 2(2\pi\beta_{ge})2\sqrt{I_l(t)I_r(t)}, \quad (20)$$

$$\Delta\nu_{\mathrm{ac}} = \beta_{\mathrm{ac}}I(t) \rightarrow \Delta\nu_{\mathrm{ac}} = \beta_{\mathrm{ac}}[I_l(t) + I_r(t)], \qquad (21)$$

$$\gamma_{\mathrm{i}} = (2\pi\beta_{\mathrm{ioni}})I(t) \rightarrow \gamma_{\mathrm{i}} = (2\pi\beta_{\mathrm{ioni}})[I_l(t) + I_r(t)], \quad (22)$$

again assuming that effective averaging over the maxima and minima of the standing field takes place, either because the atom is moving or by having many spatially distributed atoms contributing to the signal. The Rabi frequency in Eq. (20) scales with the product of the field amplitudes (i.e., field envelopes). To calculate the contribution of the Doppler-shifted components, where the atom absorbs both photons from one beam only, the Rabi frequency becomes

$$\Omega = 2(2\pi\beta_{ge})I_r(t) \qquad (23)$$

for absorption of photons from the "right" beam, whereas the expressions for the ac Stark shift and the ionization rate are unaffected, since these processes are nonresonant. For these components, the first-order Doppler shift, including recoil effects, must be added to the laser detuning as given by Eq. (11).

Any additional spontaneous decay channels can also be fully included in a numerical integration algorithm. In addition to the intensity-dependent frequency shifts $\Delta\nu_{\mathrm{ac}}$, any other frequency-shifting effect can be easily included into the

numerical approach by adapting Eq. (11), as described already for the velocity-dependent second-order Doppler shift in Eq. (12).

Finally, in most cases, instead of a single atom one considers an ensemble of atoms, all of which may experience different intensities, Doppler shifts, and interaction times along different trajectories. The contribution of each single atom to the line shape can be calculated exactly like described above, and the line shape produced by the atomic ensemble is then the sum of all single-atom contributions, given that the single atoms interact independently with the laser. In a dilute beam experiment this condition is very well satisfied.

Together with the atomic constants presented in the following sections, the set of equations (10) are thus a tool for a wide range of problems in spectroscopy. For a specific implementation using a Monte Carlo method for the atomic ensemble in the case of the 1S-2S experiment, see [18].

Note that the transition matrix elements and Stark coefficients that enter into Eq. (10) vary slightly with the laser frequency. However, the detuning $\Delta\nu$ is typically a few kilohertz, whereas the optical resonance frequencies are on the order of 10^{15} Hz. For the 1S-2S transition, the resulting relative variation of β_{ac} is on the order of 10^{-12}, which is negligibly small. The question of different gauges, for two-photon excitation off resonance, has been discussed, e.g., in [34].

III. CALCULATION OF TWO-PHOTON TRANSITION MATRIX ELEMENTS

A. Calculation

In this and the next section, we will present the calculation of the two-photon transition matrix elements and the dynamic Stark coefficients, which are used in the quantum dynamics of the two-level system of Sec. II B.

In that section, the interacting system of atom and laser field has been described by an effective two-level Hamiltonian, focusing on the time-dependent atomic population of these levels. In order to describe transition matrix elements and dynamic Stark coefficients, involving virtual intermediate states, we have to consider the full, time-dependent Hamiltonian

$$H(t) = H_0 + V(t), \qquad (24)$$

where

$$H_0 = \frac{\mathbf{p}^2}{2m_{\mathrm{e}}} - \frac{Ze^2}{4\pi\epsilon_0 r}, \qquad (25\mathrm{a})$$

$$V(t) = V\frac{1}{2}[\exp(i\omega_{\mathrm{L}}t) + \exp(-i\omega_{\mathrm{L}}t)], \qquad (25\mathrm{b})$$

$$V = -ez\mathcal{E}_{\mathrm{L}}, \qquad (25\mathrm{c})$$

describing a one-electron system with nuclear charge number Z in a harmonic laser field of angular frequency ω_{L} and classical electric field amplitude $\mathcal{E}_{\mathrm{L}}$, linearly polarized in the z direction. The electron mass is denoted by m_{e}. The inter-

action potential $V(t)$ is chosen to be in the length gauge, which has some advantages in the description of time-dependent problems (for a detailed discussion see for example [35]), and the dipole approximation is made. The time-dependent two-photon transition matrix element connecting the ground state $|g\rangle$ and excited state $|e\rangle$ then reads

$$\left\langle e \left| V(t) \frac{1}{(E_g + \hbar\omega_L) - H_0} V(t) \right| g \right\rangle, \tag{26}$$

where E_ϕ is the Schrödinger energy of any eigenstate $|\phi\rangle$ of H_0, depending only on its principal quantum number n and is defined by

$$E_\phi = -\frac{(Z\alpha)^2 m_e c^2}{2n^2}, \tag{27}$$

with α being the fine-structure constant. Now we can establish the connection with the off-diagonal element of the two-level Hamiltonian $\tilde{H}$ from Sec. II B, Eq. (2), by equating

$$-\left\langle e \left| V(t) \frac{1}{H_0 - (E_g + \hbar\omega_L)} V(t) \right| g \right\rangle$$
$$= \frac{\hbar\Omega}{2} [\exp(i\omega_L t) + \exp(-i\omega_L t)]^2. \tag{28}$$

Observe that a minus sign is explicitly pulled out with respect to Eq. (26) in order to write the Green's function in the familiar form $1/[H_0 - E]$, with intermediate state energy E. With the definition of the two-photon Rabi-frequency from Eq. (6)

$$\Omega = 2(2\pi\beta_{ge})I, \tag{29}$$

and the intensity of an electromagnetic plane wave

$$I = \frac{1}{2}\epsilon_0 c \mathcal{E}_L^2, \tag{30}$$

we obtain for the time-independent two-photon transition matrix element

$$\beta_{ge} = -\frac{e^2}{2hc\epsilon_0} \left\langle e \left| z \frac{1}{H_0 - (E_g + \hbar\omega_L)} z \right| g \right\rangle. \tag{31}$$

Note that the prefactor does not contain a factor Z, because it originates in the interaction part of the Hamiltonian (25c), describing the singly charged electron in the laser field.

In the literature, two common notations are used in expressing the transition matrix elements, and for completeness we will state that they are connected via the simple relation

$$\left\langle e \left| z \underbrace{\frac{1}{(E_g + \hbar\omega_L) - H_0} z}_{\propto |\delta g\rangle} \right| g \right\rangle$$
$$= \left\langle e \left| z \frac{1}{(E_g + \hbar\omega_L) - H_0} \mathbb{1} z \right| g \right\rangle = \sum_r \frac{\langle e|z|r\rangle\langle r|z|g\rangle}{(E_g + \hbar\omega_L) - E_r}, \tag{32}$$

with a complete set of H_0 eigenstates $|r\rangle$ denoted by

$$\mathbb{1} = \sum_r |r\rangle\langle r|. \tag{33}$$

The explicit sum over intermediate states at the bottom of Eq. (32) is widely used throughout the experimental laser spectroscopy literature, while the notation in the first line, involving the two-photon transition operator, is used mainly in publications inspired by a field-theoretic formalism (e.g., Refs. [36,37]). We will stick to the latter form in this paper, because it allows for an intuitive perturbation theoretic interpretation of (31) as the usual one-photon transition matrix element between the excited state $|e\rangle$ and the virtual intermediate state $|\delta g\rangle$ with energy $E_g + \hbar\omega_L$. The intermediate state $|\delta g\rangle$ is apparently the first-order perturbation to the ground state $|g\rangle$, generated by the potential V, such that the matrix element itself is of second order in the perturbation potential.

At least three algorithms exist for the evaluation of matrix elements involving the nonrelativistic hydrogen Green's function as in Eq. (31). These are (i) a fully analytic evaluation based on the Sturmian representation of the radial Green's function for the hydrogen atom, in terms of Laguerre polynomials, (ii) a discretization of real space (of the radial variable) according to [38], and (iii) the solution of differential equations as, e.g., in [39]. We have used the first of these possibilities, the basic formalism of which has been laid out in [40–42], with the nonrelativistic hydrogen Green's function reading

$$\left\langle \mathbf{r}_1 \left| \frac{1}{H_0 - E(\eta)} \right| \mathbf{r}_2 \right\rangle = \sum_{l,m} g_l(r_1, r_2; \eta) Y_{lm}(\theta_1, \varphi_1) Y_{lm}^*(\theta_2, \varphi_2), \tag{34}$$

with

$$g_l(r_1, r_2; \eta) = \frac{2m_e}{\hbar^2} \left(\frac{2}{a_0\eta}\right)^{2l+1} (r_1 r_2)^l e^{-(r_1+r_2)/a_0\eta}$$
$$\times \sum_{k=0}^{\infty} \frac{L_k^{2l+1}\left(\frac{2r_1}{a_0\eta}\right) L_k^{2l+1}\left(\frac{2r_2}{a_0\eta}\right)}{(k+1)_{2l+1}(l+1+k-\eta)}, \tag{35}$$

where the usual spherical coordinates $\mathbf{r}_i = \{r_i, \theta_i, \phi_i\}$ are used, and $(a)_n \equiv \Gamma(a+n)/\Gamma(a)$ is the Pochhammer symbol. The Bohr radius is denoted by a_0, the symbols L_k^{2l+1} designate the associated Laguerre polynomials, and we employ the invertible energy parametrization

$$\eta \equiv \eta(E) = \frac{Z\hbar}{a_0}\sqrt{-\frac{1}{2m_e E}} \tag{36}$$

for conciseness of notation, converting any energy E into the dimensionless parameter η, chosen such that for eigenstates $|\phi\rangle$ of H_0 with main quantum number n we have $\eta(E_\phi) = n$. For the calculation of the transition matrix elements, we have to consider a virtual intermediate P state in the propagator, with energy $E_g + \hbar\omega_L$, and ω_L is fixed by the two-photon resonance condition. Because the intermediate state is between two bound states, its energy is always negative, and therefore η and the transition matrix elements are real. When we will come to the calculation of the dynamic Stark coeffi-

cients in the next section, there will also be intermediate states in the continuum involved, and consequently the Stark coefficients will acquire an imaginary part.

Up to now, the states $|g\rangle$ and $|e\rangle$ have been characterized by the principal quantum number n and orbital angular momentum quantum number l only. Evaluated for any S-S transition, the two-photon transition operator

$$T^{ij} = r^i \frac{1}{H_0 - (E_g + \hbar\omega_L)} r^j \qquad (37)$$

has isotropic symmetry, $\langle e|T^{xx}|g\rangle = \langle e|T^{yy}|g\rangle = \langle e|T^{zz}|g\rangle$, $\langle e|T^{ij}|g\rangle = 0$ for $i \neq j$ and therefore transforms like a scalar under rotation. As a consequence, the two-photon transition matrix element for each individual allowed transition between fine structure (FS) and hyperfine structure (HFS) substrates can be obtained from β_{ge} of the gross structure transition without any angular prefactors. We refer to transitions among states with different principal quantum number as the "gross structure" of the atom. For S-D transitions, the rotational symmetry is broken by the D state, and $\Sigma_i \langle e|T^{ii}|g\rangle = 0$. We therefore calculate the reduced matrix elements of the rank-2 component $\beta_{ge}^{(2)}$ for orbital angular momentum eigenstates

$$\beta_{ge}^{(2)} = -\frac{e^2}{2hc\epsilon_0} \langle n'D\|\mathbf{T}(2)\|nS\rangle, \qquad (38)$$

from which the transition matrix elements for specific magnetic sublevels can be obtained via the Wigner-Eckhart theorem. For the gross structure S-D transition the only transition which can be driven by linearly polarized light is the $m_l = 0 \rightarrow m_l' = 0$ transition. For transitions between FS sublevels of angular momentum $J = L + S$ and $J' = L' + S$, where S is the spin of the orbiting particle, the angular momenta have to be recoupled via the $6j$ symbols [43]

$$\langle n'(L'S)J'\|\mathbf{T}(2)\|n(LS)J\rangle$$
$$= \sqrt{(2J+1)(2J'+1)} \times (-1)^{L'+S+J+2} \begin{Bmatrix} L' & J' & S \\ J & L & 2 \end{Bmatrix}$$
$$\times \langle n'L'\|\mathbf{T}(2)\|nL\rangle, \qquad (39)$$

because the two-photon transition operator only acts on the orbital angular momentum part of the wave function. If HFS sublevels are resolved, also the nuclear spin I has to be taken into account in the same way. Denoting the total angular momenta by $F = J + I$ and $F' = J' + I$, one obtains

$$\langle n'(J'I)F'\|\mathbf{T}(2)\|n(JI)F\rangle$$
$$= \sqrt{(2F+1)(2F'+1)} \times (-1)^{J'+I+F+2} \begin{Bmatrix} J' & F' & I \\ F & J & 2 \end{Bmatrix}$$
$$\times \langle n'(L'S)J'\|\mathbf{T}(2)\|n(LS)J\rangle. \qquad (40)$$

Finally, via the Wigner-Eckhart theorem, the transition matrix element between hyperfine magnetic sublevels $|g\rangle = |nS, (JI)Fm_F\rangle$ and $|e\rangle = |n'D, (J'I)F'm_F'\rangle$ in a linearly z-polarized laser reads

TABLE II. Two-photon transition matrix elements β_{ge} in units of Hz (W/m^2)$^{-1}$ for $1S \Leftrightarrow nS$ and $2S \Leftrightarrow nS$ transitions, as defined in Eq. (31), evaluated for atomic hydrogen ($Z = 1$), in the nonrelativistic dipole approximation. The electron mass is employed in the calculation; reduced-mass effects and the dependence of the results on the nuclear charge number Z are given in Eq. (43). For transitions between $F = F' = 0$ and $F = F' = 1$ HFS sublevels, these values are valid with a unit angular prefactor and directly give the coefficient β_{ge} defined in Eq. (41).

n	$1S \Leftrightarrow nS$ β_{ge} [Hz (W/m^2)$^{-1}$]	$2S \Leftrightarrow nS$ β_{ge} [Hz (W/m^2)$^{-1}$]
2	3.68111×10^{-5}	
3	1.00333×10^{-5}	1.23306×10^{-3}
4	5.13409×10^{-6}	7.79393×10^{-5}
5	3.28555×10^{-6}	-4.39666×10^{-5}
6	2.35088×10^{-6}	-6.89568×10^{-5}
7	1.79744×10^{-6}	-7.26216×10^{-5}
8	1.43591×10^{-6}	-6.99362×10^{-5}
9	1.18344×10^{-6}	-6.52683×10^{-5}
10	9.98415×10^{-7}	-6.01620×10^{-5}
11	8.57763×10^{-7}	-5.52069×10^{-5}
12	7.47736×10^{-7}	-5.06214×10^{-5}
13	6.59655×10^{-7}	-4.64686×10^{-5}
14	5.87791×10^{-7}	-4.27450×10^{-5}
15	5.28215×10^{-7}	-3.94201×10^{-5}
16	4.78153×10^{-7}	-3.64542×10^{-5}
17	4.35589×10^{-7}	-3.38061×10^{-5}
18	3.99031×10^{-7}	-3.14375×10^{-5}
19	3.67348×10^{-7}	-2.93136×10^{-5}
20	3.39672×10^{-7}	-2.74039×10^{-5}

$$\beta_{ge} = (-1)^{F'-m_F'} \begin{pmatrix} F' & 2 & F \\ -m_F' & 0 & m_F \end{pmatrix}$$
$$\times \left(-\frac{e^2}{2hc\epsilon_0} \langle n'(J'I)F'\|\mathbf{T}(2)\|n(JI)F\rangle \right), \qquad (41)$$

where the $3j$ symbol is defined as in Ref. [43]. In summary, to arrive at β_{ge} for a specific HFS transition, one starts with the value for $\beta_{ge}^{(2)}$ of the gross structure transition from Table III, solves Eq. (38) for the reduced matrix element, and sequentially inserts the results into Eqs. (39)–(41). For FS transitions, the step implied by Eq. (40) is skipped and in Eq. (41), one substitutes $F \rightarrow J$, $m_F \rightarrow m_J$ and $F' \rightarrow J'$, $m_F' \rightarrow m_J'$.

B. Results for two-photon transitions

Results for the two-photon transition matrix elements β_{ge} for the transitions $1S \Leftrightarrow nS$ ($2 \leq n \leq 20$) and $2S \Leftrightarrow nS$ ($3 \leq n \leq 20$) are given in Table II. For the transitions $1S \Leftrightarrow nD$ and $2S \Leftrightarrow nD$ ($3 \leq n \leq 20$), the reduced matrix elements for orbital angular momentum eigenstates are given in Table III. We have devoted Appendix E to the comparison with other

TABLE III. Two-photon reduced transition matrix elements $\beta_{ge}^{(2)}$ in units of Hz (W/m²)⁻¹ for $1S \Leftrightarrow nS$ and $2S \Leftrightarrow nS$ transitions, as defined in Eq. (38), evaluated for atomic hydrogen ($Z=1$), in the nonrelativistic dipole approximation. The electron mass is employed in the calculation; reduced-mass effects and the dependence of the results on the nuclear charge number Z is given in Eq. (43). For specific transitions in FS and HFS sublevels, the angular prefactors in Eqs. (39)–(41) must be taken into account, as applicable.

n	$1S \Leftrightarrow nD$ $\beta_{ge}^{(2)}$ [Hz (W/m²)⁻¹]	$2S \Leftrightarrow nD$ $\beta_{ge}^{(2)}$ [Hz (W/m²)⁻¹]
3	-6.16579×10^{-5}	4.23147×10^{-4}
4	-3.89301×10^{-5}	-2.23806×10^{-3}
5	-2.72644×10^{-5}	-1.75124×10^{-3}
6	-2.04728×10^{-5}	-1.39563×10^{-3}
7	-1.61138×10^{-5}	-1.15144×10^{-3}
8	-1.31174×10^{-5}	-9.74048×10^{-4}
9	-1.09516×10^{-5}	-8.39046×10^{-4}
10	-9.32523×10^{-6}	-7.32816×10^{-4}
11	-8.06659×10^{-6}	-6.47159×10^{-4}
12	-7.06862×10^{-6}	-5.76793×10^{-4}
13	-6.26133×10^{-6}	-5.18119×10^{-4}
14	-5.59721×10^{-6}	-4.68586×10^{-4}
15	-5.04300×10^{-6}	-4.26327×10^{-4}
16	-4.57477×10^{-6}	-3.89943×10^{-4}
17	-4.17491×10^{-6}	-3.58362×10^{-4}
18	-3.83018×10^{-6}	-3.30751×10^{-4}
19	-3.53048×10^{-6}	-3.06453×10^{-4}
20	-3.26799×10^{-6}	-2.84944×10^{-4}

literature sources, where some of these results are also obtained, clarifying the prefactors and discussing some occasional inconsistencies, which we encountered in our literature search related to the problem. These nonrelativistic results are relevant for the given transitions in any bound two-body Coulomb system with nuclear charge number Z, where $1 \leqslant Z \leqslant 10$. Generally, we will refer to one of the particles involved as "the nucleus," although it need not be made up of baryons. Because the values, as listed in Tables II and III, have been obtained for $Z=1$ and infinite nuclear mass, the scaling with Z and the dependence on the reduced mass of the system remain to be clarified. We use the scaling relations for the position operator as a function of Z [32], and for the propagator denominators in (31). Note that the relevant laser frequency $\omega_L(Z) = Z^2 \omega_L(Z=1)$ has to be scaled by a factor of Z^2 as compared to the corresponding frequency in hydrogen. Thus, we find that

$$\beta_{ge}(Z) = \frac{1}{Z^4} \beta_{ge}(Z=1). \qquad (42)$$

Consider a bound two-body system, consisting of particles with respective masses m_N for the nucleus and m_S for the other particle. This system is equivalent to a system with infinite nuclear mass and an orbiting particle with reduced

mass μ. It is therefore sufficient to replace the electron mass with the reduced mass in our calculations, bearing in mind that also the Bohr radius $a_0 = 4\pi\epsilon_0 \hbar^2 / m_e e^2$ needs to be replaced. Therefore, to obtain the transition matrix elements β_{ge} for a two-body Coulomb system of nuclear charge number Z and reduced mass μ (even for hydrogen itself), the values from Tables II and III must be multiplied by a factor

$$\frac{1}{Z^4}\left(\frac{m_e}{\mu}\right)^3 = \frac{1}{Z^4}\left(\frac{m_e(m_N + m_S)}{m_N m_S}\right)^3. \qquad (43)$$

This scaling law equally applies for the Stark coefficients β_{ac} and β_{ioni} discussed below. Note that for atomic nuclei, we also obtain isotope shifts to the transition matrix elements via the dependence on the nuclear mass m_N. In the next section, we will obtain nonrelativistic results for the dynamic Stark coefficients and consider radiative, relativistic, and field configuration corrections. We would like to mention here that these corrections, calculated for the transition matrix elements, are on the same order of magnitude as for the dynamic Stark coefficients.

IV. CALCULATION OF THE AC STARK SHIFT

A. Introduction

This section treats the dynamic Stark shift of atomic energy levels, which is a consequence of the interaction with the laser field used to probe an atomic transition. This systematic shift cannot be suppressed experimentally and constitutes one major systematic effect in many precision spectroscopic experiments.

As opposed to one-photon resonant transitions, where the system of atom and laser field must be described in a nonperturbative dressed-state picture, in two-photon transitions involving the $1S$ or $2S$ states as ground states and an excited S or D state, the perturbation is always off resonant with respect to any one-photon transition. In contrast, a laser field driving the $3S$-$5S$ two-photon transition, is also one-photon resonant with the $5S$-$15P$ transition, according to Schrödinger theory [see Eq. (27)]. As a consequence, for our case of $1S$ or $2S$ states as ground states, the effect of the harmonic laser field as defined in Eq. (25) can be described in a perturbation theory approach for the present investigation. In the classical picture used for the electric field in this paper, the dynamic Stark shift falls into the domain of time-dependent perturbation theory. However, in the more general theory, where the electromagnetic field is quantized, the same effect may be described in a time-independent framework with a static expression of the light field as a photon field with one macroscopically populated mode. The ac Stark shift has also been characterized as a stimulated radiative correction, because it results from a self-energy-like formalism when restricting the sum over virtual modes of the photon field to one single mode, the laser mode [44].

Both the classical time-dependent theory, and the time-independent fully quantized treatment, in the limit of macroscopic photon number, yield the same physical result as presented in [45], where also the connection to the to the Gell-Mann-Low-Sucher theorem has been reemphasized. In the

notation of the previous section for the Hamiltonian [see Eqs. (24) and (25)] we can therefore express the dynamic Stark shift of the state $|\phi\rangle$ as [see Eq. (18) of [45]]

$$\Delta E_{ac}(\phi) = \frac{e^2 \mathcal{E}_L^2}{4} \sum_{\pm} \left\langle \phi \left| z \frac{1}{E_\phi - H_0 \pm \hbar\omega_L} z \right| \phi \right\rangle. \quad (44)$$

This form of $\Delta E_{ac}(\phi)$ can be divided into a product, with one factor being the dynamic polarizability of the atom

$$P_{\omega_L}(\phi) = \sum_{\pm} \left\langle \phi \left| z \frac{1}{H_0 - E_\phi \pm \hbar\omega_L} z \right| \phi \right\rangle, \quad (45)$$

for an angular frequency ω_L, and a prefactor containing the laser intensity (30), such that we have

$$\Delta E_{ac}(\phi) = -\frac{e^2}{2\epsilon_0 c} I P_{\omega_L}(\phi). \quad (46)$$

B. Matrix elements

The calculation of the dynamic Stark shift of any reference state $|\phi\rangle$ now reduces to calculating the matrix element of the dynamic polarizability (45), where we use the same analytic technique as for the two-photon transition matrix elements [see Eqs. (34)–(36)]. Note that the contributions of two intermediate states, with energies $E_\phi + \hbar\omega_L$ and $E_\phi - \hbar\omega_L$, have to be summed. These energies are determined by the choice of angular frequency of the laser field $\omega_L = (E_e - E_g)/2\hbar$ in the two-photon resonant spectroscopy of the transition $g \Leftrightarrow e$. For laser detunings which drive the transition appreciably, the matrix elements are constant to a good approximation (see also end of Sec. II E). If the upper intermediate state is a continuum state, the energy parameter $\eta(E_\phi + \hbar\omega_L > 0)$ [see Eq. (36)] is complex, and the dynamic polarizability acquires an imaginary part, describing the population loss rate due to ionization. The real part of the ac Stark shift determines the frequency shift of the atomic level $|\phi\rangle$ in hertz via the relation

$$\Delta\nu_{ac}(\phi) = \frac{1}{h} \mathrm{Re}[\Delta E_{ac}(\phi)] = \beta_{ac}(\phi)I; \quad (47)$$

see also Eq. (5). The imaginary part of the ac Stark shift, if present, yields the decay constant of the probability amplitude of the atom to be in the reference state $|\phi\rangle$. The atomic-state population, as described by the diagonal elements of the density matrix in (10), is equal to the modulus squared of this probability amplitude, therefore the ionization rate of the population in $|\phi\rangle$ reads

$$\gamma_i = -\frac{2}{\hbar} \mathrm{Im}[\Delta E_{ac}(\phi)] = 2\pi\beta_{ioni}(\phi)I, \quad (48)$$

proportional to twice the imaginary part of the ac Stark shift. Note that we have given the ionization rate in units of angular frequency.

Standard selection rules for dipole transitions apply in determining the virtual intermediate states. In particular, as the laser is assumed to be linearly polarized in the z direction,

we can restrict the sum over m of the intermediate states in the propagator (34) to the $m=0$ term. This choice of polarization does not restrict the generality of our discussion, because the initial S states of the investigated transitions are spherically symmetric.

In Appendix A, one explicit polarizability matrix element $\langle 3S | z(H_0 - E)^{-1} z | 3S \rangle$ is given. It involves the hypergeometric function ${}_2F_1$, which originates from the infinite sum over Laguerre polynomials. In general, after the radial integrations we obtain a sum involving several hypergeometric functions, which can be reduced to a single one, using the contiguous relations for the hypergeometric functions (see, e.g., [46]). In Appendix C, the connection of β_{ioni} to the usual ionization cross section is discussed.

To calculate the Stark shift coefficient β_{ac} and ionization coefficient β_{ioni} for FS and HFS states, the same considerations as for the transition operator apply. For S states, the coefficients for the Schrödinger states are also applicable to each individual FS and HFS sublevel without modification. For an nD state, the light shift operator

$$Q^{ij} = \sum_{\pm} r^i \frac{1}{H_0 - E_n \pm \hbar\omega_L} r^j \quad (49)$$

consists of both a nonzero scalar component $\mathbf{Q}(0)$ and a rank-2 traceless component $\mathbf{Q}(2)$. To obtain the dynamic Stark shift coefficient $\beta_{ac}(nD)$ in a linearly z-polarized laser field, the reduced matrix elements $\beta_{ac}^{(0)}$ and $\beta_{ac}^{(2)}$ have to be added after applying the appropriate angular prefactors.

In particular, the reduced matrix element $\beta_{ac}^{(0)}$ needs no modification for FS and HFS sublevels, while $\beta_{ac}^{(2)}$ must be multiplied by

$$(-1)^{L+S+J}(2J+1) \begin{Bmatrix} L & J & S \\ J & L & 2 \end{Bmatrix} \quad (50)$$

for a FS level with angular momentum $J = L+S$, where $L=2$, and additionally by

$$(-1)^{J+I+F}(2F+1) \begin{Bmatrix} J & F & I \\ F & J & 2 \end{Bmatrix} \quad (51)$$

if the state under consideration is a HFS level with angular momentum $F = J+I$. The Wigner-Eckhart theorem yields the dependence on the magnetic quantum number, such that, e.g., for a HFS state $|\phi\rangle = |nD, (JI)Fm_F\rangle$ in a linearly z-polarized laser field, we obtain

$$\beta_{ac}(\phi) = \frac{1}{\sqrt{2L+1}}\beta_{ac}^{(0)}(nD) + (-1)^{L+S+2J+I+2F-m_F}(2J+1)$$

$$\times (2F+1) \times \begin{pmatrix} F & 2 & F \\ -m_F & 0 & m_F \end{pmatrix} \begin{Bmatrix} L & J & S \\ J & L & 2 \end{Bmatrix}$$

$$\times \begin{Bmatrix} J & F & I \\ F & J & 2 \end{Bmatrix} \beta_{ac}^{(2)}(nD), \quad (52)$$

where $L=2$ for D states. The ionization coefficient β_{ioni} of an nD state is calculated in exactly the same way.

TABLE IV. Dynamic Stark shift coefficients β_{ac} and ionization coefficients β_{ioni} for $1S \Leftrightarrow nS$ transitions (on two-photon resonance), as defined in Eqs. (5), (9), (47), and (48), in the nonrelativistic dipole approximation, evaluated for nuclear charge number $Z=1$ and infinite nuclear mass. Reduced-mass effects and the dependence of the results on Z can be included by multiplication with the scaling factor (43). For all S states, the values are also applicable to all FS and HFS sublevels. The nonrelativistic treatment implies that the physical accuracy of the results given here is limited by corrections of relative order $(Z\alpha)^2$. Thus, about three decimals of the results in this table are relevant for a comparison of theory and experiment. Nevertheless, we indicate the data with a larger numerical accuracy, in order to facilitate the independent verification of the results.

$1S \Leftrightarrow nS$	$\beta_{ac}(1S)$ [Hz $(W/m^2)^{-1}$]	$\beta_{ac}(nS)$ [Hz $(W/m^2)^{-1}$]	$\beta_{ioni}(nS)$ [Hz $(W/m^2)^{-1}$]
$1S$-$2S$	-2.67827×10^{-5}	1.39927×10^{-4}	1.20208×10^{-4}
$1S$-$3S$	-3.02104×10^{-5}	9.80847×10^{-5}	2.02241×10^{-5}
$1S$-$4S$	-3.18301×10^{-5}	8.66487×10^{-5}	7.10785×10^{-6}
$1S$-$5S$	-3.26801×10^{-5}	8.20398×10^{-5}	3.35245×10^{-6}
$1S$-$6S$	-3.31724×10^{-5}	7.97219×10^{-5}	1.85663×10^{-6}
$1S$-$7S$	-3.34805×10^{-5}	7.83897×10^{-5}	1.13885×10^{-6}
$1S$-$8S$	-3.36851×10^{-5}	7.75526×10^{-5}	7.50088×10^{-7}
$1S$-$9S$	-3.38277×10^{-5}	7.69918×10^{-5}	5.20731×10^{-7}
$1S$-$10S$	-3.39307×10^{-5}	7.65976×10^{-5}	3.76481×10^{-7}
$1S$-$11S$	-3.40076×10^{-5}	7.63098×10^{-5}	2.81130×10^{-7}
$1S$-$12S$	-3.40664×10^{-5}	7.60932×10^{-5}	2.15538×10^{-7}
$1S$-$13S$	-3.41124×10^{-5}	7.59261×10^{-5}	1.68914×10^{-7}
$1S$-$14S$	-3.41490×10^{-5}	7.57945×10^{-5}	1.34855×10^{-7}
$1S$-$15S$	-3.41786×10^{-5}	7.56889×10^{-5}	1.09389×10^{-7}
$1S$-$16S$	-3.42029×10^{-5}	7.56030×10^{-5}	8.99638×10^{-8}
$1S$-$17S$	-3.42231×10^{-5}	7.55321×10^{-5}	7.48861×10^{-8}
$1S$-$18S$	-3.42400×10^{-5}	7.54729×10^{-5}	6.30029×10^{-8}
$1S$-$19S$	-3.42544×10^{-5}	7.54229×10^{-5}	5.35100×10^{-8}
$1S$-$20S$	-3.42667×10^{-5}	7.53804×10^{-5}	4.58347×10^{-8}

C. Results for *S-S* transitions

We have investigated the nonrelativistic dynamic Stark coefficients β_{ac} and β_{ioni} as defined in Eqs. (47) and (48), for laser frequencies on two-photon resonance with *S-S* and *S-D* transitions. In particular, we give an overview of the values for transitions within the manifolds $1S \Leftrightarrow nS$ in Table IV, $2S \Leftrightarrow nS$ in Table V, $1S \Leftrightarrow nD$ in Table VI, and $2S \Leftrightarrow nD$ in Table VII up to $n=20$. The analytic results evaluated in the tables are obtained in the dipole approximation and with the approximation of retaining only the second-order in perturbation theory [see Eq. (44)]. In this case, both the frequency shift $\Delta\nu_{ac}$ and the angular ionization rate γ_i are proportional to the light intensity. Corrections beyond the nonrelativistic dipole approach are discussed in the following Secs. IV D and IV E.

Some of the results listed in the tables have appeared in the literature before (e.g., Ref. [6]). Diverse unit systems and prefactors are encountered. Here, we present all results in SI units. An overview of the previous results is provided in Appendix E. Our results are in full agreement with those given in Refs. [5–7,10] and we add some more transitions to the analysis. In the comparison with results given in atomic units, as in [6], the conversion

$$\beta_{ac}(\phi) \text{ (a.u.)} = \beta_{ac}(\phi) \text{ (SI)} \times \frac{\hbar^2}{m_e a_0^4 \alpha} \qquad (53)$$

has to be used, and analogously for β_{ioni} [see also Eq. (E2) in Appendix E]. At this point we would like to reemphasize that in this section, the intensity is assumed to be constant at the location of the atom. For a discussion of the implications atoms moving in an inhomogeneous laser profile, see Sec. II B.

Concerning the dependence of the results on the nuclear charge number Z and the reduced mass μ of the system, the same considerations apply as for the transition matrix elements in Sec. III. In particular, the values from Tables IV–VII must be multiplied by the scaling factor (43), for a specific two-body Coulomb system.

The $1/Z^4$ dependence of the dynamic Stark coefficients, and especially the 16-fold reduction of the ionization coefficient, might be important in the context of planned measurements on trapped hydrogenlike helium. For spectroscopic experiments on systems with $Z > 1$, the required light sources with ultrastable frequencies and sufficient intensity have recently been demonstrated to be within reach in the near future [15].

TABLE V. Dynamic Stark shift coefficients and ionization coefficients (on two-photon resonance) as in Table IV, but for $2S \Leftrightarrow nS$ transitions.

$2S \Leftrightarrow nS$	$\beta_{ac}(2S)$ [Hz (W/m^2)$^{-1}$]	$\beta_{ac}(nS)$ [Hz (W/m^2)$^{-1}$]	$\beta_{ioni}(nS)$ [Hz (W/m^2)$^{-1}$]
$2S$-$3S$	-7.18795×10^{-4}	-6.99895×10^{-3}	0
$2S$-$4S$	-9.47799×10^{-4}	2.11716×10^{-3}	1.25626×10^{-3}
$2S$-$5S$	-1.16885×10^{-3}	1.70310×10^{-3}	4.65485×10^{-4}
$2S$-$6S$	-1.36379×10^{-3}	1.52064×10^{-3}	2.28478×10^{-4}
$2S$-$7S$	-1.52869×10^{-3}	1.42368×10^{-3}	1.30721×10^{-4}
$2S$-$8S$	-1.66537×10^{-3}	1.36562×10^{-3}	8.23925×10^{-5}
$2S$-$9S$	-1.77773×10^{-3}	1.32791×10^{-3}	5.55288×10^{-5}
$2S$-$10S$	-1.86994×10^{-3}	1.30194×10^{-3}	3.93145×10^{-5}
$2S$-$11S$	-1.94583×10^{-3}	1.28325×10^{-3}	2.89099×10^{-5}
$2S$-$12S$	-2.00858×10^{-3}	1.26932×10^{-3}	2.19090×10^{-5}
$2S$-$13S$	-2.06078×10^{-3}	1.25865×10^{-3}	1.70162×10^{-5}
$2S$-$14S$	-2.10451×10^{-3}	1.25029×10^{-3}	1.34890×10^{-5}
$2S$-$15S$	-2.14138×10^{-3}	1.24361×10^{-3}	1.08794×10^{-5}
$2S$-$16S$	-2.17269×10^{-3}	1.23819×10^{-3}	8.90578×10^{-6}
$2S$-$17S$	-2.19945×10^{-3}	1.23372×10^{-3}	7.38465×10^{-6}
$2S$-$18S$	-2.22247×10^{-3}	1.23000×10^{-3}	6.19281×10^{-6}
$2S$-$19S$	-2.24238×10^{-3}	1.22687×10^{-3}	5.24540×10^{-6}
$2S$-$20S$	-2.25971×10^{-3}	1.22420×10^{-3}	4.48258×10^{-6}

The analytic calculation of the matrix elements for the highly excited states would be a formidable task without the use of computer algebra software [47]. The reason that the calculations are carried out up to rather high quantum numbers is that the availability of a large number of results permits the evaluation of the asymptotic limit of the light shifts

TABLE VI. Dynamic Stark coefficients as in Table IV, but for $1S \Leftrightarrow nD$ transitions. The respective coefficients for the $1S$ state, $\beta_{ac}(1S)$, are identical with those from Table IV, and are therefore not listed again. For FS and HFS sublevels of an nD state, the appropriate angular prefactors from Eqs. (50)–(52) must be taken into account.

$1S \Leftrightarrow nD$	$\beta_{ac}^{(0)}(nD)$ [Hz (W/m^2)$^{-1}$]	$\beta_{ac}^{(2)}(nD)$ [Hz (W/m^2)$^{-1}$]	$\beta_{ioni}^{(0)}(nD)$ [Hz (W/m^2)$^{-1}$]	$\beta_{ioni}^{(2)}(nD)$ [Hz (W/m^2)$^{-1}$]
$1S$-$3D$	2.11378×10^{-4}	1.30662×10^{-5}	3.67432×10^{-6}	-2.11508×10^{-6}
$1S$-$4D$	1.90315×10^{-4}	4.70825×10^{-6}	1.39210×10^{-6}	-8.11183×10^{-7}
$1S$-$5D$	1.81694×10^{-4}	2.24738×10^{-6}	6.70000×10^{-7}	-3.92504×10^{-7}
$1S$-$6D$	1.77255×10^{-4}	1.25298×10^{-6}	3.74221×10^{-7}	-2.19848×10^{-7}
$1S$-$7D$	1.74652×10^{-4}	7.71734×10^{-7}	2.30562×10^{-7}	-1.35678×10^{-7}
$1S$-$8D$	1.72990×10^{-4}	5.09668×10^{-7}	1.52256×10^{-7}	-8.96938×10^{-8}
$1S$-$9D$	1.71863×10^{-4}	3.54487×10^{-7}	1.05879×10^{-7}	-6.24189×10^{-8}
$1S$-$10D$	1.71062×10^{-4}	2.56634×10^{-7}	7.66377×10^{-8}	-4.52039×10^{-8}
$1S$-$11D$	1.70472×10^{-4}	1.91828×10^{-7}	5.72754×10^{-8}	-3.37962×10^{-8}
$1S$-$12D$	1.70025×10^{-4}	1.47183×10^{-7}	4.39391×10^{-8}	-2.59345×10^{-8}
$1S$-$13D$	1.69678×10^{-4}	1.15414×10^{-7}	3.44509×10^{-8}	-2.03388×10^{-8}
$1S$-$14D$	1.69403×10^{-4}	9.21865×10^{-8}	2.75145×10^{-8}	-1.62467×10^{-8}
$1S$-$15D$	1.69182×10^{-4}	7.48066×10^{-8}	2.23252×10^{-8}	-1.31844×10^{-8}
$1S$-$16D$	1.69001×10^{-4}	6.15416×10^{-8}	1.83651×10^{-8}	-1.08470×10^{-8}
$1S$-$17D$	1.68851×10^{-4}	5.12407×10^{-8}	1.52901×10^{-8}	-9.03172×10^{-9}
$1S$-$18D$	1.68726×10^{-4}	4.31191×10^{-8}	1.28659×10^{-8}	-7.60040×10^{-9}
$1S$-$19D$	1.68620×10^{-4}	3.66289×10^{-8}	1.09289×10^{-8}	-6.45656×10^{-9}
$1S$-$20D$	1.68529×10^{-4}	3.13799×10^{-8}	9.36238×10^{-9}	-5.53143×10^{-9}

TABLE VII. Dynamic Stark coefficients as in Table VI, but for $2S \Leftrightarrow nD$ transitions. The respective coefficients for the $2S$ state, $\beta_{ac}(2S)$, are identical with those from Table V.

$2S \Leftrightarrow nD$	$\beta_{ac}^{(0)}(nD)$ [Hz (W/m²)⁻¹]	$\beta_{ac}^{(2)}(nD)$ [Hz (W/m²)⁻¹]	$\beta_{ioni}^{(0)}(nD)$ [Hz (W/m²)⁻¹]	$\beta_{ioni}^{(2)}(nD)$ [Hz (W/m²)⁻¹]
$2S$-$3D$	-1.17698×10^{-2}	4.99866×10^{-3}	0	0
$2S$-$4D$	5.47527×10^{-3}	-1.64045×10^{-4}	1.91609×10^{-3}	-1.10511×10^{-3}
$2S$-$5D$	3.91342×10^{-3}	1.89977×10^{-4}	5.84726×10^{-4}	-3.43343×10^{-4}
$2S$-$6D$	3.40856×10^{-3}	1.64090×10^{-4}	2.62740×10^{-4}	-1.55670×10^{-4}
$2S$-$7D$	3.17241×10^{-3}	1.21898×10^{-4}	1.43176×10^{-4}	-8.52682×10^{-5}
$2S$-$8D$	3.03968×10^{-3}	8.99553×10^{-5}	8.75750×10^{-5}	-5.23245×10^{-5}
$2S$-$9D$	2.95642×10^{-3}	6.74381×10^{-5}	5.78591×10^{-5}	-3.46451×10^{-5}
$2S$-$10D$	2.90022×10^{-3}	5.15428×10^{-5}	4.03987×10^{-5}	-2.42271×10^{-5}
$2S$-$11D$	2.86026×10^{-3}	4.01348×10^{-5}	2.94079×10^{-5}	-1.76557×10^{-5}
$2S$-$12D$	2.83068×10^{-3}	3.17867×10^{-5}	2.21175×10^{-5}	-1.32900×10^{-5}
$2S$-$13D$	2.80812×10^{-3}	2.55609×10^{-5}	1.70777×10^{-5}	-1.02684×10^{-5}
$2S$-$14D$	2.79046×10^{-3}	2.08355×10^{-5}	1.34753×10^{-5}	-8.10656×10^{-6}
$2S$-$15D$	2.77637×10^{-3}	1.71910×10^{-5}	1.08282×10^{-5}	-6.51678×10^{-6}
$2S$-$16D$	2.76493×10^{-3}	1.43390×10^{-5}	8.83715×10^{-6}	-5.32030×10^{-6}
$2S$-$17D$	2.75549×10^{-3}	1.20777×10^{-5}	7.30950×10^{-6}	-4.40183×10^{-6}
$2S$-$18D$	2.74762×10^{-3}	1.02634×10^{-5}	6.11704×10^{-6}	-3.68459×10^{-6}
$2S$-$19D$	2.74098×10^{-3}	8.79168×10^{-6}	5.17212×10^{-6}	-3.11603×10^{-6}
$2S$-$20D$	2.73533×10^{-3}	7.58614×10^{-6}	4.41334×10^{-6}	-2.65934×10^{-6}

for $n \to \infty$. Thus, if theoretical predictions are sought for higher n than those included in the tables, these can be obtained by fits involving inverse powers of the principal quantum number to the real and to the imaginary parts of the data in Tables IV and V; see also Table Ic in [6]. The limit as $n \to \infty$ might be interesting especially in view of the long lifetime of highly excited S states, which allows for a high spectral resolution [48].

D. Relativistic and radiative corrections

The transition matrix elements and dynamic Stark coefficients involved in the quantum dynamics (10) have been calculated nonrelativistically, which is a good approximation for low-Z systems. For use in high-precision measurements, however, one should at least consider leading-order relativistic and radiative corrections to ensure the validity of the approximation.

For an estimation of magnitude, it is helpful to remark that the leading relativistic corrections are of relative order $(Z\alpha)^2$, whereas the leading radiative corrections are of order $\alpha(Z\alpha)^2\ln[(Z\alpha)^{-2}]$. It follows that for atomic hydrogen, they do not exceed a relative magnitude of 10^{-4}, and therefore at least three digits in the Tables IV and V are significant regarding a comparison of theory and experiment in hydrogen and low-Z hydrogenlike systems.

In the electric dipole approximation, the relativistic corrections to the dynamic polarizability of $1S$ and $2S$ have recently been calculated to all orders in $Z\alpha$ in the form of generalized hypergeometric series [39], employing the fully relativistic Dirac-Coulomb propagator. Regarding an experimental verification of the relativistic, multipole, and retarda-

tion corrections, as well as the radiative contributions, we only mention that the required accurate measurement of the laser intensity would be the most difficult task.

In this section, we only give results for the mentioned corrections to the dynamic polarizability for selected states, which are of interest in the spectroscopic analysis at hand. The purpose is to demonstrate that these corrections are below the currently accessible experimental precision.

We compare the radiative corrections to the dynamic polarizability $\delta P_{\omega_L}(\phi)$ in leading logarithmic order to the uncorrected matrix element $P_{\omega_L}(\phi)$ defined in Eq. (45), where the real and imaginary parts are treated separately to reflect the correction to the dynamic Stark coefficient $\delta\beta_{ac}(\phi)$ and the correction to the ionization coefficient $\delta\beta_{ioni}(\phi)$:

$$\eta_{rad}R_{rad}(\phi) = \frac{\text{Re}[\delta P_{\omega_L}(\phi)]}{\text{Re}[P_{\omega_L}(\phi)]} = \frac{\delta\beta_{ac}(\phi)}{\beta_{ac}(\phi)}, \quad (54)$$

$$\eta_{rad}I_{rad}(\phi) = \frac{\text{Im}[\delta P_{\omega_L}(\phi)]}{\text{Im}[P_{\omega_L}(\phi)]} = \frac{\delta\beta_{ioni}(\phi)}{\beta_{ioni}(\phi)}, \quad (55)$$

with $\eta_{rad} = \alpha(Z\alpha)^2\ln[(Z\alpha)^{-2}]$. For the relativistic corrections, the definitions of $R_{rel}(\phi)$ and $I_{rel}(\phi)$ are completely analogous, but with $\eta_{rel} = (Z\alpha)^2$.

For the transitions $1S$-$2S$, $1S$-$3S$, and $2S$-$3S$ the relative magnitude of the radiative corrections is given in Table VIII.

The relativistic corrections are not defined unambiguously, because of the existence of field-configuration-dependent corrections which enter at the same order of magnitude $(Z\alpha)^2$ (see Sec. IV E). In addition, we have neglected

TABLE VIII. Radiative corrections to the dynamic polarizability in leading logarithmic order as defined in Eqs. (54) and (55).

Transition $\lvert g\rangle \Leftrightarrow \lvert e\rangle$	$R_{\mathrm{rad}}(g)$	$R_{\mathrm{rad}}(e)$	$I_{\mathrm{rad}}(e)$
1S-2S	3.617	5.281×10^{-1}	-8.077×10^{-1}
1S-3S	4.045	1.042×10^{-1}	-1.103
2S-3S	8.861	$2.937 \times 10^{+1}$	

corrections due to the interaction of the magnetic field with the electron. In contrast, the leading radiative correction is well defined because it entails the electric-dipole approximation. The relativistic corrections considered include the contributions from the zitterbewegung of the electron, the spin-orbit coupling, and the leading-order relativistic momentum correction, and are given in Table IX, again for the transitions 1S-2S, 1S-3S, and 2S-3S.

E. Field-configuration-dependent corrections

In this section we will consider the leading field configuration correction to the dynamic polarizability, which is due to the fact that the laser field, interacting with an atom of finite extension, is not strictly a dipole field, but also varies in space for a fixed time t. We will consider the case of a plane standing wave, which approximates the situation in the hydrogen 1S-2S experiment [16] well enough for the discussion of this correction. For other field configurations like, e.g., tight foci, the results of this section (see Table X) are not applicable, but must be reevaluated to suit the corresponding geometry. For this reason we give a rather detailed description of the calculation of the corrections here.

Up to now, all results were obtained in the electric dipole approximation, where the interaction part of the Hamiltonian was expressed as

$$V_{\mathrm{dip}}(t) = -e\mathbf{r} \cdot \mathbf{E}(t). \tag{56}$$

In long-wavelength QED (see [37] and Eq. (3.59) of [49]), the interaction with an electric field varying in both space and time can be written as

TABLE IX. Relativistic corrections to the dynamic polarizability as defined in analogy to Eqs. (54) and (55).

Transition $\lvert g\rangle \Leftrightarrow \lvert e\rangle$	$R_{\mathrm{rel}}(g)$	$R_{\mathrm{rel}}(e)$	$I_{\mathrm{rel}}(e)$
1S-2S	-1.185	-1.903×10^{-1}	2.047×10^{-1}
1S-3S	-1.280	-7.410×10^{-2}	1.199×10^{-1}
2S-3S	-3.831	$-2.134 \times 10^{+1}$	

TABLE X. Field configuration corrections to the dynamic polarizability occurring in a plane standing wave, as defined in Eqs. (64) and (65).

Transition $\lvert g\rangle \Leftrightarrow \lvert e\rangle$	$R_{\mathrm{fc}}(g)$	$R_{\mathrm{fc}}(e)$	$I_{\mathrm{fc}}(e)$
1S-2S	-2.256×10^{-2}	-1.988×10^{-1}	3.750×10^{-2}
1S-3S	-3.244×10^{-2}	-1.105	1.185×10^{-1}
2S-3S	-1.008×10^{-2}	3.771×10^{-3}	

$$V_{\mathrm{LW}}(t,\mathbf{r}) = -e\mathbf{r} \cdot \mathbf{E}(t,\mathbf{0}) - \frac{e}{2} r^i r^j \left. \frac{\partial E^i(t,\mathbf{r})}{\partial r^j} \right|_{\mathbf{r}=0}$$
$$- \frac{e}{6} r^i r^j r^k \left. \frac{\partial^2 E^i(t,\mathbf{r})}{\partial r^j \, \partial r^k} \right|_{\mathbf{r}=0}. \tag{57}$$

For a plane standing wave of linearly z-polarized light with wave vector $\mathbf{k}$, aligned along the x direction, the electric field is

$$\mathbf{E}(t,x) = \hat{e}_z \mathcal{E}_{\mathrm{L}} \cos(\omega t)\cos(kx), \tag{58}$$

and consequently for the last term in (57) we obtain simply

$$V_{\mathrm{LW}}^{(2)} = \frac{e}{6} z k^2 x^2 \mathcal{E}_{\mathrm{L}} \cos(\omega t). \tag{59}$$

The leading-order correction to the dynamic polarizability of state $\lvert \phi\rangle$ therefore reads

$$\delta P_{\omega_{\mathrm{L}}}(\phi) = -\frac{k^2}{3} \sum_{\pm} \left\langle \phi \left| z \frac{1}{H_0 - E_\phi \pm \hbar\omega_{\mathrm{L}}} x^2 z \right| \phi \right\rangle, \tag{60}$$

because the lower-order contributions vanish for symmetry reasons:

$$-\frac{k}{2} \left\langle \phi \left| z \frac{1}{H_0 - E} xz \right| \phi \right\rangle = 0, \tag{61}$$

$$\frac{k^2}{4} \left\langle \phi \left| zx \frac{1}{H_0 - E} xz \right| \phi \right\rangle = 0. \tag{62}$$

The modulus of the wave vector k of the standing wave is determined by the two-photon resonance condition

$$k = \frac{3}{16}(Z\alpha)^2 \frac{cm_{\mathrm{e}}}{\hbar} = \frac{\omega_{\mathrm{L}}}{c} \tag{63}$$

for the 1S-2S transition, which also yields the frequency ω_{L} at which the polarizability itself is evaluated. With these parameters fixed, we obtain the leading-order correction, relative to the polarizability in dipole approximation

$$\eta_{\mathrm{fc}} R_{\mathrm{fc}}(\phi) = \frac{\mathrm{Re}[\delta P_{\omega_{\mathrm{L}}}(\phi)]}{\mathrm{Re}[P_{\omega_{\mathrm{L}}}(\phi)]}, \tag{64}$$

$$\eta_{\text{fc}} I_{\text{fc}}(\phi) = \frac{\text{Im}[\delta P_{\omega_L}(\phi)]}{\text{Im}[P_{\omega_L}(\phi)]}, \qquad (65)$$

where again the corrections to the real part R_{fc} and to the imaginary part I_{fc} are considered separately, and the factor

$$\eta_{\text{fc}} = (Z\alpha)^2 \qquad (66)$$

is used. We see that the field-configuration-dependent corrections are of the same order in $Z\alpha$ as the relativistic corrections. Note that the correction $\delta P_{\omega_L}(\phi)$ is of the order $(Z\alpha)^{-2}$, while the polarizability $P_{\omega_L}(\phi)$ is of the order $(Z\alpha)^{-4}$. The results, evaluated for the same transitions as in the previous subsection, are listed in Table X.

V. CONCLUSIONS

In this paper, we have presented in a unified treatment the quantum dynamics and atomic constants describing the two-photon excitation process in ongoing and planned precision experiments on bound two-body Coulomb systems, including the dependence on Z and the reduced mass of the system.

The influence on the linewidth by ionization from the excited atomic state has been studied in the density matrix formalism, and an analytic solution to the corresponding equations of motion has been discussed, in which features like spectral hole burning due to the ionization have been observed (see Figs. 1–4). Ionization is therefore a decisive feature of the quantum dynamics and cannot be ignored in high-precision two-photon spectroscopy experiments.

In particular, we have focused on the 1S-2S transition in hydrogen and hydrogenlike helium. In the latter case, we observed that the effective loss rate of the atomic population is significantly smaller than expected, if one considers the ionization coefficient of the excited state without taking into account the excitation dynamics.

Potential applications include detection schemes in planned experiments on hydrogen and He$^+$.

In this paper we have restricted the discussion to the case of monochromatic cw excitation of a single atom, initially in the ground state. In realistic cases, the effect of an inhomogeneous laser intensity profile and the velocity distributions of an atomic ensemble can be taken into account with a numerical integration of the equations of motion presented here. Two such applications can be found in [18], on the analysis of the hydrogen 1S-2S transition, and in [50], discussing high-precision spectroscopy in hydrogenlike helium.

Finally, results of relativistic, radiative, and field-configuration-dependent corrections to the dynamic polarizability have been briefly discussed for the most interesting transitions in the context of this paper. These corrections, which have some theoretical interest of their own, are found to be small, as expected, but might become relevant in the future.

APPENDIX A: 3S DYNAMIC POLARIZABILITY

Below, we give as an example the exact analytic solution for a matrix element $\langle\phi|z\{1/[H_0-E(\eta)]\}z|\phi\rangle$, the reference state being the $|3S\rangle$ state. The energy parametrization $E(\eta)$ is defined in Eq. (36). The Bohr radius is denoted by a_0, m_e is the electron mass, and H_0 is the unperturbed hydrogen Hamiltonian (25a):

$$\left\langle 3S \left| z \frac{1}{H_0-E(\eta)} z \right| 3S \right\rangle = \frac{m_e a_0^4}{Z^4\hbar^2} \times \frac{54\eta^2}{(9-\eta^2)^8} \Bigg[110\,008\,287 - 87\,156\,324\,\eta^2 + 29\,819\,745\,\eta^4 - 6\,022\,998\,\eta^6 - 1\,259\,712\,\eta^7$$
$$+ 2\,106\,081\,\eta^8 + 1\,912\,896\,\eta^9 - 504\,792\,\eta^{10} - 737\,856\,\eta^{11} - 31\,041\,\eta^{12} + 84\,672\,\eta^{13} + 15\,538\,\eta^{14}$$
$$+ 3456\,\eta^7(27-7\eta^2)^2(1-\eta^2)\,_2F_1\left(1,-\eta,1-\eta,\left(\frac{3-\eta}{3+\eta}\right)^2\right) \Bigg]. \qquad (A1)$$

For higher excited states, the analytic results have a more complex analytic structure, which necessitates the use of computer algebra systems [47]. In Ref. [36], the authors have observed that the $_2F_1$ hypergeometric function occurs in the result for integrals containing the Schrödinger-Coulomb Green's function in the above form.

APPENDIX B: ANALYTIC SOLUTION FOR THE POPULATION

In this section, we give the explicit expression for the time-dependent line shape of excited atoms $\rho'_{ee}(\Delta\omega,t)$ and the ground-state population $\rho'_{gg}(\Delta\omega,t)$, satisfying the master

equation (10). The ionization probability can be obtained by evaluating $1-\rho'_{ee}(\Delta\omega,t)-\rho'_{gg}(\Delta\omega,t)$, which is needed to model the line shape in an experiment using the detection of ionized particles instead of intact atoms in the excited state. We obtain

$$\rho'_{ee}(\Delta\omega,t) = C\Omega^2\{e^{-\Omega_c t}\Omega_b[\Omega_a(\Omega_a^2-\Omega_b^2)\cosh(\Omega_a t)+\Omega_c(3\Omega_a^2+\Omega_b^2-4\Omega_c^2)\sinh(\Omega_a t)]+e^{\Omega_c t}\Omega_a[\Omega_b(\Omega_b^2-\Omega_a^2)\cosh(\Omega_b t)$$
$$-\Omega_c(\Omega_a^2+3\Omega_b^2-4\Omega_c^2)\sinh(\Omega_b t)]\}, \tag{B1}$$

$$\rho'_{gg}(\Delta\omega,t) = \rho'_{ee}(\Delta\omega,t)+C\times\left[2e^{-\Omega_c t}\Omega_b\left(\Omega_a[8\Omega_c^4+(\Omega_a^2-\Omega_b^2)(\Delta\omega^2+\Omega_a^2)+\Omega_c(\gamma_i+\gamma_s)(2\Delta\omega^2+\Omega_a^2+\Omega_b^2-2\Omega_c^2)\right.\right.$$
$$-\Omega_c^2(5\Omega_a^2+3\Omega_b^2)]\cosh(\Omega_a t)+\left\{\Omega_c[\Omega_a^2(\Omega_a^2+3\Omega_b^2)+\Omega_c^2(\Omega_b^2-\Omega_a^2-4\Omega_c^2)+\Delta\omega^2(3\Omega_a^2+\Omega_b^2-4\Omega_c^2)]+\frac{\gamma_i+\gamma_s}{2}\right.$$
$$\left.\times[(\Omega_a^2-\Omega_b^2+4\Omega_c^2)(\Delta\omega^2+\Omega_a^2+\Omega_c^2)-8\Omega_a^2\Omega_c^2]\right\}\sinh(\Omega_a t)\right)+2e^{\Omega_c t}\Omega_a\left(\Omega_b[8\Omega_c^4+(\Omega_b^2-\Omega_a^2)(\Delta\omega^2+\Omega_b^2)\right.$$
$$-\Omega_c(\gamma_i+\gamma_s)(2\Delta\omega^2+\Omega_a^2+\Omega_b^2-2\Omega_c^2)-\Omega_c^2(3\Omega_a^2+5\Omega_b^2)]\cosh(\Omega_b t)-\left\{\Omega_c[\Omega_b^2(\Omega_b^2+3\Omega_a^2)+\Omega_c^2(\Omega_a^2-\Omega_b^2-4\Omega_c^2)\right.$$
$$\left.\left.+\Delta\omega^2(\Omega_a^2+3\Omega_b^2-4\Omega_c^2)]-\frac{\gamma_i+\gamma_s}{2}[(\Omega_b^2-\Omega_a^2+4\Omega_c^2)(\Delta\omega^2+\Omega_b^2+\Omega_c^2)-8\Omega_b^2\Omega_c^2]\right\}\sinh(\Omega_b t)\right)\right], \tag{B2}$$

with

$$C = \frac{e^{-(\gamma_i+\gamma_s)t/2}}{2\Omega_a\Omega_b[(\Omega_a-\Omega_b)^2-4\Omega_c^2][(\Omega_a+\Omega_b)^2-4\Omega_c^2]}, \tag{B3}$$

$$\Omega_a = \frac{\sqrt{2(\gamma_i+\gamma_s)^2-8\Delta\omega^2-8\Omega^2-3\gamma_s\Omega^2/\Omega_c-D-K}}{2\sqrt{6}}, \tag{B4}$$

$$\Omega_b = \frac{\sqrt{2(\gamma_i+\gamma_s)^2-8\Delta\omega^2-8\Omega^2+3\gamma_s\Omega^2/\Omega_c-D-K}}{2\sqrt{6}}, \tag{B5}$$

$$\Omega_c = \frac{\sqrt{(\gamma_i+\gamma_s)^2-4\Delta\omega^2-4\Omega^2+D+K}}{2\sqrt{6}}, \tag{B6}$$

$$K = \frac{16\Delta\omega^4+[(\gamma_i+\gamma_s)^2-4\Omega^2]^2+8\Delta\omega^2[4\Omega^2-7(\gamma_i+\gamma_s)^2]}{4D}, \tag{B7}$$

$$D = 2^{2/3}\left\{27\gamma_i\Omega^2(\gamma_i+\gamma_s)^3+2\left(\frac{5}{4}(\gamma_i+\gamma_s)^2+\Delta\omega^2+\Omega^2\right)^3-\frac{9}{2}\gamma_i\Omega^2(\gamma_i+\gamma_s)[5(\gamma_i+\gamma_s)^2+4\Delta\omega^2+4\Omega^2]-\frac{9}{8}(\gamma_i+\gamma_s)\right.$$
$$\times[4\Delta\omega^2+5(\gamma_i+\gamma_s)^2+4\Omega^2][4\Delta\omega^2(\gamma_i+\gamma_s)+(\gamma_i+\gamma_s)^3+2(2\gamma_i+\gamma_s)\Omega^2]+\frac{27}{16}[4\Delta\omega^2(\gamma_i+\gamma_s)+(\gamma_i+\gamma_s)^3$$
$$+2\Omega^2(2\gamma_i+\gamma_s)]^2+\left[-4\left(\Delta\omega^4+\frac{1}{16}[(\gamma_i+\gamma_s)^2-4\Omega^2]^2+\frac{1}{2}\Delta\omega^2[-7(\gamma_i+\gamma_s)^2+4\Omega^2]\right)^3+\frac{1}{1024}\{(\gamma_i+\gamma_s)^6-64\Delta\omega^6-64\Omega^6$$
$$-12\Omega^2(\gamma_i+\gamma_s)^4+24\Omega^4(2\gamma_i^2+4\gamma_i\gamma_s-7\gamma_s^2)-48\Delta\omega^4[11(\gamma_i+\gamma_s)^2+4\Omega^2]+12\Delta\omega^2[11(\gamma_i+\gamma_s)^4-40\Omega^2(\gamma_i+\gamma_s)^2$$
$$\left.-16\Omega^4]\}^2\right]^{1/2}\right\}^{1/3}.$$

In this form, the auxiliary variables Ω_a, Ω_b, Ω_c, K, and D are not necessarily real, depending on the relative magnitude of the spontaneous decay rate γ_s, the ionization rate γ_i, and the two-photon Rabi frequency Ω. Nevertheless, the resulting populations ρ_{ee} and ρ_{gg} are real quantities.

In earlier works dealing with multiphoton ionization (see, e.g., [51,52]), where the above solution is contained in the limiting case $\gamma_s = 0$ [see Eqs. (13)], the emphasis is on efficient ionization, and in strong fields, either the spontaneous decay of the intermediate state is neglected in comparison with the ionization rate or, if present in the master equations, it is treated numerically.

However, in experiments that detect the excited-state line shape, and are therefore carried out in a relatively weak field, the spontaneous decay rate and the ionization rate can be of comparable magnitude; therefore only the above solution (B1) describes the constant-intensity case appropriately, as detailed in Sec. II D. Of course, a more compact expression would be highly desirable; however, we were not able to simplify it further. Quite generally, spontaneous decay channels complicate the exact solution of the dynamics, because it reduces the symmetry of the EOMs, as has been shown for a different set of master equations, considering autoionizing states in a laser field [53,54].

APPENDIX C: CALCULATION OF THE PHOTOIONIZATION CROSS SECTION

The photoionization cross sections obtained in this section are generally applicable to the regime of ionization by low-intensity laser radiation with a minimum photon energy of $Z^2 \times 13.6$ eV$/n^2$, where $n = 1, 2$ is the principal quantum number of the initial atomic state and Z is the nuclear charge. The theory for this process has been very well understood since the 1930s [4], including the Z scaling, and a comparison of the results constitutes an independent verification of the ionization rate coefficients β_{ioni} obtained in Sec. IV.

In analogy to bound states (27), one can assign to the continuum state a generalized principal quantum number n', which is real and positive, such that the energy of the electron in the continuum can be written as

$$E_{n'} = -\frac{(Z\alpha)^2 m_e c^2}{2(in')^2} > 0. \qquad (C1)$$

Here, the continuum threshold is taken as the zero point of the energy scale, such that bound states extend into the negative energy region (this is different from the conventions used in an early article [4] on this subject).

If we consider a dipole transition from the bound $2S$ state to the continuum εP state, the one-photon ionization cross section of a single atom for linearly polarized light is proportional to the square of the transition matrix element and reads

$$\sigma_{2S} = \frac{\pi e^2 \omega_L}{\epsilon_0 c} |\langle 2S|z|\varepsilon P\rangle|^2, \qquad (C2)$$

where ω_L is the angular frequency of the incident laser radiation, and e is the electron charge. The radial integrals encountered can be calculated in at least two ways: (i) direct

integration of terms generated by the series representation of the ${}_1F_1$ hypergeometric function occurring in the εP wave function, and (ii) contour integration using an integral representation of the hypergeometric function (see, e.g., [32]) and evaluation of the residues. Both (i) and (ii) lead to the same result

$$|\langle 2S|z|\varepsilon P\rangle|^2 = \frac{2^{17} a_0^4 m_e}{3Z^4 \hbar^2} \frac{\exp[-4n'\operatorname{arccot}(n'/2)]}{1 - \exp(-2\pi n')} \frac{n'^{10}(1 + n'^2)}{(4 + n'^2)^6}. \qquad (C3)$$

Observe that the left-hand side is proportional to $1/Z^4$ because the matrix element contains one continuum state. For two bound states, the transition matrix element squared would scale as $1/Z^2$. In [55], one can find a result differing by a factor of $\frac{3}{2}$ from Eq. (C3).

For the case of an incident laser angular frequency of one-half of the $1S$-$2S$ transition frequency, the generalized quantum number of the continuum state is $n' = 2\sqrt{2}$, and we obtain the nonrelativistic result

$$\sigma_{2S} = \frac{1}{Z^2} 6.174 \times 10^{-18} \text{ cm}^2. \qquad (C4)$$

We can compare the ionization rate coefficient β_{ioni} from Sec. IV directly with the $2S$ cross section calculated above using the relation

$$\sigma_{\text{ioni}} = 2\pi\beta_{\text{ioni}}\hbar\omega_L = \frac{1}{Z^2} 6.174 \times 10^{-18} \text{ cm}^2, \qquad (C5)$$

which agrees with (C4). Here, the Z scaling of the ionization cross section is the result of a factor Z^{-4} for the ionization coefficient β_{ioni} and the Z^2 scaling of the photon energy $\hbar\omega_L$, required for maintaining two-photon resonance with a given transition. In Table XI the ionization cross sections in cm^2 for a set of excited nS levels is given, as obtained from the imaginary part of the dynamic Stark coefficient β_{ioni}. All considerations concerning the relativistic and radiative corrections to β_{ioni} given in Sec. IV D also apply to the ionization cross section through relation (C5). Their magnitude is small and below the current precision of measurement, decreasing even for larger nuclear charge. This behavior is different than in most radiative corrections of nondynamic processes [56].

APPENDIX D: COMBINED INDUCED-SPONTANEOUS TWO-PHOTON DECAY

In the context of laser driven two-photon S-S transitions and two-photon spontaneous emission, one also has to consider the two-step process of combined induced-spontaneous two-photon decay of the excited level. In this process, the interaction of the excited atom with the laser field and the vacuum modes leads to a final state of the system, where the atom is in the ground state, the laser mode photon number is increased or decreased by 1, and one photon is spontaneously emitted into an empty mode of the electromagnetic field. One contribution is depicted Fig. 10, where the interaction with the laser field takes place before the spontaneous emission.

TABLE XI. Ionization cross sections for hydrogen atoms ($Z=1$) in the excited state nS, at an incident laser frequency on two-photon resonance with the respective $1S \Leftrightarrow nS$ or $2S \Leftrightarrow nS$ transition, as obtained via Eq. (C5) from the dynamic Stark coefficient β_{ioni}. This table is provided for convenient comparison with other cross section calculations. Therefore, the values are here given in the usual units cm^2 instead of SI units.

n	$1S \Leftrightarrow nS$ $\sigma_{ioni}(nS)$ (cm^2)	$2S \Leftrightarrow nS$ $\sigma_{ioni}(nS)$ (cm^2)
2	6.174×10^{-18}	
3	1.231×10^{-18}	0
4	4.563×10^{-19}	1.613×10^{-17}
5	2.204×10^{-19}	6.694×10^{-18}
6	1.236×10^{-19}	3.477×10^{-18}
7	7.640×10^{-20}	2.055×10^{-18}
8	5.057×10^{-20}	1.322×10^{-18}
9	3.522×10^{-20}	9.037×10^{-19}
10	2.552×10^{-20}	6.462×10^{-19}
11	1.909×10^{-20}	4.786×10^{-19}
12	1.466×10^{-20}	3.647×10^{-19}
13	1.150×10^{-20}	2.844×10^{-19}
14	9.188×10^{-21}	2.262×10^{-19}
15	7.458×10^{-21}	1.830×10^{-19}
16	6.137×10^{-21}	1.501×10^{-19}
17	5.111×10^{-21}	1.247×10^{-19}
18	4.301×10^{-21}	1.047×10^{-19}
19	3.654×10^{-21}	8.881×10^{-20}
20	3.131×10^{-21}	7.598×10^{-20}

We describe the interaction of the atom with the laser mode with the second-quantized interaction Hamiltonian

$$H_L = -ez \sqrt{\frac{\hbar \omega_L}{2\epsilon_0 \mathcal{V}}} (a_L^\dagger + a_L), \qquad (D1)$$

where the dipole approximation is used and a_L and $a_L^\dagger$ are the annihilation and creation operators for a photon of energy
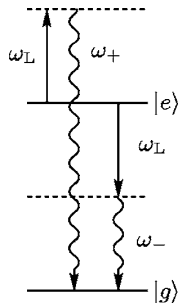

FIG. 10. Combined induced-spontaneous decay process leading to a depopulation of the excited state $|e\rangle$. Absorption or stimulated emission of one laser photon with energy $\hbar \omega_L$ and subsequent spontaneous decay of the virtual intermediate states (dashed) to the ground state can take place, via emission of a photon of energy $\hbar \omega_+$ or $\hbar \omega_-$, respectively.

TABLE XII. Combined induced-spontaneous two-photon decay coefficients β_{is} between two S states interacting with a laser field on two-photon resonance, as defined in Eq. (D6).

Transition	β_{is} [Hz/(W/m^2)]
$1S$-$2S$	$8.05160 \times 10^{-11} Z^{-2}$
$1S$-$3S$	$1.11235 \times 10^{-11} Z^{-2}$
$2S$-$3S$	$1.00370 \times 10^{-8} Z^{-2}$

$\hbar \omega_L$ in the laser mode, given the quantization volume $\mathcal{V}$. The interaction with the vacuum modes is described by the interaction Hamiltonian

$$H_V = -e \sum_{\{\mathbf{k},\lambda\} \neq L} \mathbf{r} \cdot \boldsymbol{\epsilon}_\lambda(\mathbf{k}) \sqrt{\frac{\hbar \omega_k}{2\epsilon_0 \mathcal{V}}} [a_\lambda^\dagger(\mathbf{k}) + a_\lambda(\mathbf{k})]. \quad (D2)$$

Here, $\mathbf{k}$ is the wave vector of any mode of the electromagnetic field except the laser mode, with polarization vector $\boldsymbol{\epsilon}_\lambda(\mathbf{k})$. We denote the initial state by $|\phi_0\rangle = |e, n_L, 0\rangle$, with n_L photons in the laser mode and no photons in any other mode. To evaluate the transition rate of the combined induced-spontaneous decay, one needs to evaluate the imaginary part of the principal term of the fourth-order energy perturbation

$$\begin{aligned} &\Delta E_{LV}^{(4)}(\phi_0) \\ &= \left\langle \phi_0 \left| H_{LV} \frac{1}{E_0 - H_0} H_{LV} \frac{1}{E_0 - H_0} H_{LV} \frac{1}{E_0 - H_0} H_{LV} \right| \phi_0 \right\rangle, \end{aligned}$$
$$(D3)$$

where $H_{LV} = H_L + H_V$, taking into account only those terms that contain both the laser interaction and the vacuum interaction in second order. Here, the unperturbed Hamiltonian H_0 includes the atomic spectrum as well as the field modes:

$$H_0 = \sum_n E_n |n\rangle\langle n| + \hbar \omega_L a_L^\dagger a_L + \sum_{\{\mathbf{k},\lambda\} \neq L} \hbar \omega_k a_\lambda^\dagger(\mathbf{k}) a_\lambda(\mathbf{k}).$$
$$(D4)$$

From the resonances caused by the possible final states $|g, n_L+1, 1_z(\mathbf{k}_-)\rangle$ and $|g, n_L-1, 1_z(\mathbf{k}_+)\rangle$, we obtain the induced-spontaneous decay rate γ_{is} as

$$\gamma_{is} = (2\pi \beta_{is}) I, \qquad (D5)$$

$$\begin{aligned} \beta_{is} = \frac{4e^4}{6\pi c^4 \epsilon_0^2 h} \bigg(&\omega_-^3 \left| \left\langle e \left| z \frac{1}{H_A - (E_e - \hbar \omega_L)} z \right| g \right\rangle \right|^2 \\ &+ \omega_+^3 \left| \left\langle e \left| z \frac{1}{H_A - (E_e + \hbar \omega_L)} z \right| g \right\rangle \right|^2 \bigg), \end{aligned}$$
$$(D6)$$

where $H_A = \sum_n E_n |n\rangle\langle n|$ is the atomic part of the unperturbed Hamiltonian, and $\omega_\pm = c|\mathbf{k}_\pm| = \omega_{eg} \pm \omega_L$. For a small set of transitions, we list the results in Table XII. It is obvious that for typical intensities of several MW/m^2, as considered in Sec. II, the contribution of this process to the width of the excited state is small, when compared to ionization and spontaneous decay.

APPENDIX E: OTHER LITERATURE SOURCES

1. 1S-2S transition

This section is dedicated to a comparison of the results given in this paper with previous work. For the convenience of the reader, we try to describe all the prefactors in detail, where different conventions and different units are used. The collection of articles covered in the following is not claimed to be comprehensive.

For the 1S-2S transition matrix element, we obtain $\beta_{ge}=3.68111\times10^{-5}$ Hz/(W/m^2) (see Table II), with

$$\beta_{ge}=-\frac{e^2}{2hc\epsilon_0}\left\langle 2S\left| z\frac{1}{H_0-(E_{1S}+\hbar\omega_\mathrm{L})}z\right|1S\right\rangle$$
$$=-\frac{e^2}{2hc\epsilon_0}\sum_n\frac{\langle 2S|z|n\rangle\langle n|z|1S\rangle}{E_n-E_{1S}-\hbar\omega_\mathrm{L}}, \tag{E1}$$

with intermediate states $|n\rangle$. To relate our result in SI units to atomic units, where $\hbar=a_0=e=m_\mathrm{e}=1$, one has to apply the conversion

$$\beta_{ge}\ (\mathrm{a.u.})=\beta_{ge}\ (\mathrm{SI})\times\frac{\hbar^2}{m_\mathrm{e}a_0^4\alpha}, \tag{E2}$$

in which these constants are reinstated, resulting in a value of $\beta_{ge}=7.85366$ atomic units. In Ref. [57], the authors define

$$D[J_0]=\frac{3}{2}\sum(1+P_{12})\frac{\hat{\mathbf{e}}_1\cdot\langle 2S|\mathbf{r}/a_0|n\rangle\langle n|\mathbf{r}/a_0|1S\rangle\cdot\hat{\mathbf{e}}_2}{\nu(n)-\nu(1s)-\nu_2} \tag{E3}$$

as the two-photon transition probability amplitude and obtain a value of -11.7805 atomic units, which differs precisely by a factor of $-\frac{3}{2}$ from our result. The opposite sign is obviously just a consequence of a different definition of the Green's function. The operator P_{12} interchanges the polarization vectors $\hat{\mathbf{e}}_1$ and $\hat{\mathbf{e}}_2$ and the frequencies of the two photons. In that work, the light fields are treated more generally to have different frequencies. For distinguishable photons, there are two different ways to excite the atom, one path with first low-frequency and then high-frequency photon absorption and another with first high-frequency and then low-frequency photon absorption.

To reduce definition (E3) to the case of equal polarizations and equal frequencies, as considered in this paper, we

TABLE XIII. Comparison of squared transition matrix elements M, as defined in Ref. [59].

Literature source	Transition	M
Tung *et al.* [59]	1S-3S	4.2812
This work	1S-3S	4.5822
Tung *et al.* [59]	2S-6S	261.44
This work	2S-6S	216.4420

have to set the polarization vectors $\hat{\mathbf{e}}_1=\hat{\mathbf{e}}_2=\hat{\mathbf{e}}_z$ and we have to omit the part where the polarizations and frequencies are interchanged, because the photons are indistinguishable. Then the manifest prefactor of $\frac{3}{2}$ in Eq. (E3) explains the numerical difference as being only a matter of definition, while the physical results agree. This value of $D[J_0]$ is cited and used by Ref. [58]; therefore the same considerations apply there.

2. 1S-3S transition

The result of this work for the 1S-3S transition matrix element, reads $\beta_{ge}=1.00333\times10^{-5}$ Hz/(W/m^2) (see Table II), or $\beta_{ge}=2.14061$ when converted to atomic units. This equals the value given in Ref. [3]. Also the other S-S transition matrix elements calculated there, namely, for the 2S-6S and 2S-8S transitions, are equal to the results presented here, if converted according to Eq. (E2).

In Ref. [59], Table 20, the squares of the transition matrix elements, called M, for the transitions 1S-nS, 1S-nD, 2S-nS, and 2S-nD with n up to 6 are given. Out of these 18 squared matrix elements (given in atomic units), our results are in agreement with 16 values. The cases in which differences occur are the values for the 1S-3S and the 2S-6S transitions (see Table XIII). The value for $M(1S$-$3S)$ given by Tung *et al.* is equal to twice the transition matrix element from this work (2.14061), not the square, so it is likely that Tung *et al.* inadvertently doubled their correct result for the transition matrix element instead of squaring it. The second inconsistency might be explained by a twist of digits.

In an even older study [60], the authors work in the velocity gauge, as opposed to the length gauge used in all articles considered previously. Tung *et al.* [59] agree with their results for the absorption cross section, which is related to the transition matrix element. This supports the assumption that Tung *et al.* have obtained matrix elements in agreement with the results presented here, while the numerical differences originated in the compilation process.

3. Light shifts

The complete set of results for the light shifts of S states, for transitions where the 2S state acts as the ground state (see

Table V), agree with Table Ic of Ref. [6]. In that work, where atomic units are used, only the real parts of the dynamic Stark shifts are presented; the light shift of 20S in the 2S-20S transition, for example, is 261.18 atomic units in Ref. [6], which can be converted via relation (E2) into

$\beta_{ac}(20S) = 1.224\,20 \times 10^{-3}$ Hz/(W/m^2) in agreement with the value given in Table V. The light shifts of the D states given in the same table in Ref. [6] agree with the values obtained in this paper, when the atomic FS and HFS are unresolved.

[1] F. Biraben *et al.*, in *The Hydrogen Atom: Precision Physics of Simple Atomic Systems*, edited by S. G. Karshenboim, F. S. Pavone, G. F. Bassani, M. Inguscio, and T. W. Hänsch (Springer, Berlin, 2001), pp. 18–41.

[2] M. Fischer *et al.*, Phys. Rev. Lett. **92**, 230802 (2004).

[3] B. de Beauvoir, C. Schwob, O. Acef, L. Jozefowski, L. Hilico, F. Nez, L. Julien, A. Clairon, and F. Biraben, Eur. Phys. J. D **12**, 61 (2000).

[4] M. Stobbe, Ann. Phys. **7**, 661 (1930).

[5] J. C. Garreau, M. Allegrini, L. Julien, and F. Biraben, J. Phys. (France) **51**, 2263 (1990).

[6] J. C. Garreau, M. Allegrini, L. Julien, and F. Biraben, J. Phys. (France) **51**, 2275 (1990).

[7] J. C. Garreau, M. Allegrini, L. Julien, and F. Biraben, J. Phys. (France) **51**, 2293 (1990).

[8] V. Yakhontov, R. Santra, and K. Jungmann, J. Phys. B **32**, 1615 (1999).

[9] V. Yakhontov and K. Jungmann, Z. Phys. D: At., Mol. Clusters **38**, 141 (1996).

[10] B. de Beauvoir, C. Schwob, O. Acef, L. Jozefowski, L. Hilico, F. Nez, L. Julien, A. Clairon, and F. Biraben, Eur. Phys. J. D **12**, 61 (2000).

[11] S. Chu, A. P. Mills, A. G. Yodh, K. Nagamine, Y. Miyake, and T. Kuga, Phys. Rev. Lett. **60**, 101 (1988).

[12] K. Danzmann, M. S. Fee, and S. Chu, Phys. Rev. A **39**, R6072 (1989).

[13] K. Jungmann *et al.*, Z. Phys. D: At., Mol. Clusters **21**, 241 (1991).

[14] V. Meyer *et al.*, Phys. Rev. Lett. **84**, 1136 (2000).

[15] Ch. Gohle, Th. Udem, M. Herrmann, J. Rauschenberger, R. Holzwarth, H. A. Schuessler, F. Krausz, and T. W. Hänsch, Nature (London) **436**, 234 (2005).

[16] M. Niering *et al.*, Phys. Rev. Lett. **84**, 5496 (2000).

[17] C. Schwob, L. Jozefowski, B. de Beauvoir, L. Hilico, F. Nez, L. Julien, F. Biraben, O. Acef, J. J. Zondy, and A. Clairon, Phys. Rev. Lett. **82**, 4960 (1999).

[18] N. Kolachevsky, M. Haas, U. D. Jentschura, M. Herrmann, M. Fischer, R. Holzwarth, Th. Udem, C. H. Keitel, and T. W. Hänsch (unpublished).

[19] B. J. Shortt, P. J. M. van der Burgt, and F. Giammanco, Laser Phys. **12**, 1402 (2002).

[20] P. Zoller, Phys. Rev. A **19**, 1151 (1979).

[21] W. Demtröder, *Laser Spectroscopy*, 3rd ed. (Springer, Berlin, 2003).

[22] G. S. Agarwal, Phys. Rev. Lett. **37**, 1383 (1976).

[23] M. Scully and M. Zubairy, *Quantum Optics* (Cambridge University Press, Cambridge, U.K., 1999).

[24] W. Vogel, D.-G. Welsch, and S. Wallentowitz, *Quantum Optics: An Introduction* (Wiley-VCH, Berlin, 2001).

[25] F. Bloch and A. Siegert, Phys. Rev. **57**, 522 (1940).

[26] H. F. Beyer, H.-J. Kluge, and V. P. Shevelko, *X-Ray Radiation of Highly Charged Ions* (Springer, Berlin, 1997).

[27] B. L. Beers and L. Armstrong, Phys. Rev. A **12**, 2447 (1975).

[28] For the lines inverted in the center (see, e.g., Fig. 4 for long interaction times) we use the distance of the outermost half values as the linewidth.

[29] U. D. Jentschura, Phys. Rev. A **69**, 052118 (2004).

[30] J. D. Cresser, A. Z. Tang, G. J. Salamo, and F. T. Chan, Phys. Rev. A **33**, 1677 (1986).

[31] V. Florescu, I. Schneider, and I. N. Mihailescu, Phys. Rev. A **38**, 2189 (1988).

[32] H. A. Bethe and E. E. Salpeter, *Quantum Mechanics of One- and Two-Electron Atoms* (Springer, Berlin, 1957).

[33] W. H. Press, B. P. Flannery, S. A. Teukolsky, and W. T. Vetterling, *Numerical Recipes in C: The Art of Scientific Computing*, 2nd ed. (Cambridge University Press, Cambridge, U.K., 1993).

[34] P. M. Koch, Phys. Rev. Lett. **41**, 99 (1978).

[35] D. H. Kobe, J. Phys. B **16**, 1159 (1983).

[36] M. Gavrila and A. Costescu, Phys. Rev. A **2**, 1752 (1970).

[37] K. Pachucki, Ann. Phys. (N.Y.) **226**, 1 (1993).

[38] S. Salomonson and P. Öster, Phys. Rev. A **40**, 5559 (1989).

[39] V. Yakhontov, Phys. Rev. Lett. **91**, 093001 (2003).

[40] R. A. Swainson and G. W. F. Drake, J. Phys. A **24**, 79 (1991).

[41] R. A. Swainson and G. W. F. Drake, J. Phys. A **24**, 95 (1991).

[42] R. A. Swainson and G. W. F. Drake, J. Phys. A **24**, 1801 (1991).

[43] A. R. Edmonds, *Angular Momentum in Quantum Mechanics* (Princeton University Press, Princeton, NJ, 1957).

[44] C. Cohen-Tannoudji, J. Dupont-Roc, and G. Grynberg, *Atom-Photon Interactions* (Wiley, New York, 1992).

[45] M. Haas, U. D. Jentschura, and C. H. Keitel, Am. J. Phys. **74**, 77 (2006).

[46] H. Bateman, *Higher Transcendental Functions* (McGraw-Hill, New York, 1953), Vol. 1.

[47] S. Wolfram, *Mathematica—A System for Doing Mathematics by Computer* (Addison-Wesley, Reading, MA, 1988).

[48] J. C. de Vries, Ph.D. thesis, MIT Report No. 658, 2002 (unpublished).

[49] J. Evers, U. D. Jentschura, and C. H. Keitel, Phys. Rev. A **70**, 062111 (2004).

[50] M. Herrmann, Th. Udem, C. Gohle, N. Kolachevsky, T. W. Hänsch, D. Leibfried, D. Wineland, M. Haas, U. D. Jentschura, and C. H. Keitel (unpublished).

[51] C. E. Theodosiou, L. Armstrong, M. Crance, and S. Feneuille, Phys. Rev. A **19**, 766 (1979).

[52] J. L. F. de Meijere and J. H. Eberly, Phys. Rev. A **17**, 1416 (1978).

[53] G. S. Agarwal, S. L. Haan, K. Burnett, and J. Cooper, Phys. Rev. Lett. **48**, 1164 (1982).

[54] G. S. Agarwal, S. L. Haan, and J. Cooper, Phys. Rev. A **29**, 2552 (1984).

[55] S. A. Lee, Ph.D. thesis, Stanford University, M. L. Report No. 2460, 1975 (unpublished).

[56] U. D. Jentschura and C. H. Keitel, Ann. Phys. (N.Y.) **310**, 1 (2004).

[57] F. Bassani, J. J. Forney, and A. Quattropani, Phys. Rev. Lett.

39, 1070 (1977).

[58] M. G. Boshier, P. E. G. Baird, C. J. Foot, E. A. Hinds, M. D. Plimmer, D. N. Stacey, J. B. Swan, D. A. Tate, D. M. Warrington, and G. K. Woodgate, Phys. Rev. A **40**, 6169 (1989).

[59] J. H. Tung, A. Z. Tang, G. J. Salomo, and F. T. Chan, J. Opt. Soc. Am. B **3**, 837 (1986).

[60] Y. Gontier and M. Trahin, Phys. Lett. **36A**, 463 (1971).

The detailed study of the excitation and ionization dynamics of 1S-2S in hydrogenic systems led to a deeper understanding of the role of ionization in hydrogen 1S-2S spectroscopy. The result of Monte-Carlo simulations performed by N. Kolachevsky, M. Haas and the author are summarized in the following manuscript. An important insight gained from these studies is that the detection of protons rather than photons might significantly improve the accuracy of the experiment.

Photoionization broadening of the 1*S*-2*S* transition in a beam of atomic hydrogen

N. Kolachevsky,[1,2] M. Haas,[3] U. D. Jentschura,[3] M. Herrmann,[1] P. Fendel,[1] M. Fischer,[4] R. Holzwarth,[1,4] Th. Udem,[1] C. H. Keitel,[3] and T. W. Hänsch[1,5]

[1]*Max-Planck-Institut für Quantenoptik, Hans-Kopfermann-Strasse 1, 85748 Garching, Germany*
[2]*P.N. Lebedev Physics Institute, Leninsky prosp. 53, 119991 Moscow, Russia*
[3]*Max-Planck-Institut für Kernphysik, Saupfercheckweg 1, 69117 Heidelberg, Germany*
[4]*MenloSystems GmbH, Am Klopferspitz 19, 82152 Martinsried, Germany*
[5]*Ludwig-Maximilians-University, Munich, Germany*
(Received 19 June 2006; published 15 November 2006)

We consider the excitation dynamics of the two-photon 1*S*-2*S* transition in a beam of atomic hydrogen by 243 nm laser radiation. Specifically, we study the impact of ionization damping on the transition line shape, caused by the possibility of ionization of the 2*S* level by the same laser field. Using a Monte Carlo simulation, we calculate the line shape of the 1*S*-2*S* transition for the experimental geometry used in the two latest absolute frequency measurements [M. Niering *et al.*, Phys. Rev. Lett. **84**, 5496 (2000) and M. Fischer *et al.*, Phys. Rev. Lett. **92**, 230802 (2004)]. The calculated line shift and linewidth are in excellent agreement with the experimentally observed values. From this comparison we can verify the values of the dynamic Stark shift coefficient for the 1*S*-2*S* transition for the first time on a level of 15%. We show that the ionization modifies the velocity distribution of the metastable atoms, the line shape of the 1*S*-2*S* transition, and has an influence on the derivation of its absolute frequency.

I. INTRODUCTION

High-precision spectroscopy of the 1*S*-2*S* transition in atomic hydrogen and deuterium provides an essential contribution to the determination of the Rydberg constant, the Lamb shift [1], the 2*S* hyperfine interval [2] as well as allowing one to study nuclear properties of the proton [3] and the deuteron [4]. Recently it has been shown that monitoring the absolute frequencies of narrow clock transitions (like the 1*S*-2*S* transition in hydrogen and quadrupole transitions in the Hg$^+$ and Yb$^+$ ions) over a prolonged time interval, opens an opportunity to set a stringent restriction on the possible slow variation of the fine structure constant [5,6], testing very fundamental aspects of physics. This laboratory approach relies on the accuracy of the 1*S*-2*S* frequency measurement, which has now reached the level of 1.4×10^{-14}, but in principle still has room for improvement, since the Q factor of this transition is about 2×10^{15}. The accuracy which is achievable experimentally is restricted by a number of systematic effects which shift the frequency and change the line shape. So a further increase of accuracy requires not only an upgrade of the experimental setup and an improvement of the signal-to-noise ratio, but also a tighter control of the systematic effects. Among these, the dynamic Stark shift, the second-order Doppler effect and the time-of-flight (TOF) broadening have been considered as the most important issues until recently.

In this paper, we analyze how the presence of ionization losses of the 2*S* state via the absorption of 243 nm photons contributes to the line shape of the 1*S*-2*S* transition in the experimental configuration used for recent absolute frequency measurement [5,7]. Comparing the experimentally obtained intensity-dependent linewidth and frequency shift of the 1*S*-2*S* transition with results of a numerical simulation, we can also indirectly validate a number of atomic parameters like the two-photon transition matrix element, the ac Stark shift coefficient, and the ionization coefficient, which were recently rederived in a unified formalism [8]. In addition, Monte Carlo simulations allow one to study systematic effects which are difficult to quantify experimentally. From this we gain insights on the origin of the scatter in the 1*S*-2*S* absolute frequency data observed in the experiments of 1999 and 2003 [5,7].

The paper is organized as follows: In Sec. II, we describe in brief the experimental apparatus emphasizing points important for the current analysis, while the numerical model is given in Sec. III. We analyze the results in Sec. IV, followed by the conclusions.

II. EXPERIMENTAL SETUP

The basic experimental setup used for the spectroscopy of the 1*S*-2*S* transition in a cold beam of atomic hydrogen is described in detail in [9]. In this section we will focus on a description of the apparatus depicting the main features necessary for the current analysis and will present the relevant experimental results.

The dipole-forbidden 1*S*-2*S* transition is excited by means of a Doppler-free two-photon driving scheme in counter-propagating waves of equal frequencies. The necessary 243 nm radiation is produced by doubling the cw light emitted by a 486 nm dye laser in a β-barium borate crystal. The laser is stabilized to an external ultrastable cavity and has a spectral linewidth of about 60 Hz while the drift of the laser frequency is less than 0.5 Hz/s [5]. The frequency of the 486 nm laser is measured using the frequency comb technique [5,10] which is described in detail in [11].

To efficiently excite the 1*S*-2*S* transition in atomic hydrogen we enhance the 243 nm radiation in a linear cavity consisting of a plane incoupling mirror (transmission
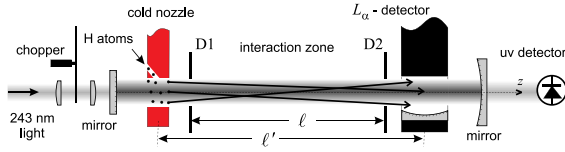
FIG. 1. (Color online) Excitation of cold hydrogen atoms by 243 nm light in the enhancement cavity. Atoms escaping the cold nozzle are collimated by two diaphragms D1 and D2 before entering the detection zone. All parts except the chopper assembly and the uv photodiode are placed in vacuum of 10^{-7}–10^{-6} mbar. The diameters of the nozzle and the diaphragms are not drawn to scale and are much smaller as suggested by this graph.

$T_1 = 2.4 \times 10^{-2}$) and a concave outcoupling mirror (radius $R = -4$ m, $T_2 = 1.36 \times 10^{-4}$) separated by a distance of 29 cm as depicted in Fig. 1. The cavity loss is dominated by the diaphragms D1 and D2 that partially touch the laser mode so that the input coupling mirror roughly corresponds to the impedance matching condition. The radiation leaking out of the cavity is monitored by a silicon photodiode which is periodically calibrated by a power meter (Fieldmaster, Coherent Inc.). The photodiode readout has been averaged over 1 s which is the laser dwelling time when recording the spectra. Dividing the photodiode readout by the transmission of the outcoupler T_2 we get the total power circulating in the enhancement cavity per direction. The averaged power is recorded for each measured spectrum.

Atoms produced in the microwave gas discharge escape a cold nozzle ($T \simeq 5$ K) of 1.2 mm in diameter and enter the interaction zone of length $\ell' = 15.0$ cm, restricted by two diaphragms D1 and D2 of respective diameters $2r_{D1} = 1.3$ mm and $2r_{D2} = 1.4$ mm separated by $\ell = 13.6$ cm. During the flight through the Gaussian profile of the cavity TEM$_{00}$ mode, a part of the atomic hydrogen is excited to the metastable 2S state. Excited atoms are detected by quenching in a dc electric field through the release of a Lyman-alpha photon [9].

To set an upper limit for the velocity of the atoms that contribute to the signal and thus to reduce the influence of the velocity-dependent systematic effects, a time-of-flight detection technique [5,9] is used. All atoms with velocities higher than v_{max} escape the detection zone before the start of the detection and the contribution of these atoms is excluded from the resulting time-delayed spectrum. The cutoff velocity is defined as $v_{max} = \ell'/\Delta\tau$, where $\Delta\tau$ is a delay between closing of the 243 nm laser light and the start of detection.

The 486 nm laser is scanned stepwise across the resonance and for each laser frequency a multichannel scaler records the number of detected Lyman-α photons for 12 different delays $\Delta\tau_i = 10, 210, 410,..., 2210$ μs in the corresponding time windows $\{\Delta\tau, 3$ ms$\}$.

Using this detection technique we simultaneously record 12 lines, each containing the contributions of atoms in the respective velocity range $0 < v < v_{max}(\Delta\tau_i)$ ($i = 1,...,12$), selected from the same initial velocity distribution $f(v)$. As follows from [12], the velocity distribution in a one-dimensional thermal atomic beam effusing from thermalized gas volume through a hole in a thin wall is given by

$$f(v) \propto (v/v_0)^3 \exp[-(v/v_0)^2], \tag{1}$$

where $v_0 = \sqrt{2k_B T/m_H}$ is the most probable thermal velocity for a given temperature T and m_H is the mass of the hydrogen atom. As discussed in Ref. [12] and references therein, expression (1) is valid for perfectly collimated beams and should be further modified in other cases also because the thin wall assumption is not fulfilled in our case. The collimation angle of the atomic beam in our experiment is about 0.01 which justifies the use of the mentioned approximation. The impact of this approximation on the 1S-2S frequency shift will be discussed in Sec. IV C.

The increase of the delay $\Delta\tau$ reduces the maximum velocity $v_{max}(\Delta\tau)$ of atoms contributing to the signal and decreases the Lyman-α count rate. Correspondingly, the contributions of the time-of-flight broadening and the second-order Doppler effect are reduced, which in turn leads to a narrowing and a symmetrization of the 1S-2S transition line shape. Hence, at the cost of a lower signal-to-noise ratio, lines with lower systematics are recorded. Using this experimental approach and the line-shape model [9] one can correct for the second-order Doppler effect which is necessary for the accurate determination of the absolute 1S-2S transition frequency.

In this paper we will study three types of intensity related line broadening effects: Because the 2S state is close enough to the continuum a single additional 243 nm photon is sufficient to ionize the hydrogen atom reducing the effective interaction time. In addition the spatially dependent ac Stark shift and the usual power broadening caused by Rabi flopping are present.

For simplicity, we will analyze only hydrogen lines recorded at a particular delay, $\Delta\tau = 1210$ μs, which corresponds to $v_{max} \simeq 120$ m/s: this is a compromise between simple line shape and sufficient signal-to-noise ratio. At this delay the line shape can be well approximated by a Lorentzian and the maximum second-order Doppler effect does not exceed 200 Hz in modulus, the typical linewidth being 1–2 kHz at 121 nm. Therefore we consider contributions to the width of a Lorentzian line, which provides a much clearer insight into the nature of the different broadenings than the complete line shape model for all $\Delta\tau$.

To correct for another important systematic effect, the dynamic Stark shift, we recorded a number of 1S-2S spectra at different excitation powers during each day of measurement [5]. Here we use the same set of data for the analysis.

All lines recorded at $\Delta\tau = 1210$ μs have been fitted by Lorentzian functions and then the absolute frequencies of the line centers ν_{1S-2S} and linewidths Γ_{tot} were plotted versus the excitation light power P (per direction). The results for the data set recorded on one of the days of measurement and the linear extrapolation to zero intensity are presented in Fig. 2 as an example.

The intensity-dependent line shift $\nu_{1S-2S}(P)$ is mainly caused by the dynamic Stark shift [8] with small contributions of velocity-selective ionization. As in Refs. [5,7] we fit the data with a linear function (since for low intensities the ac Stark shift for the 1S-2S transition is proportional to the intensity), but instead of extracting just the absolute frequency at zero power we also determine the slope of the fit,
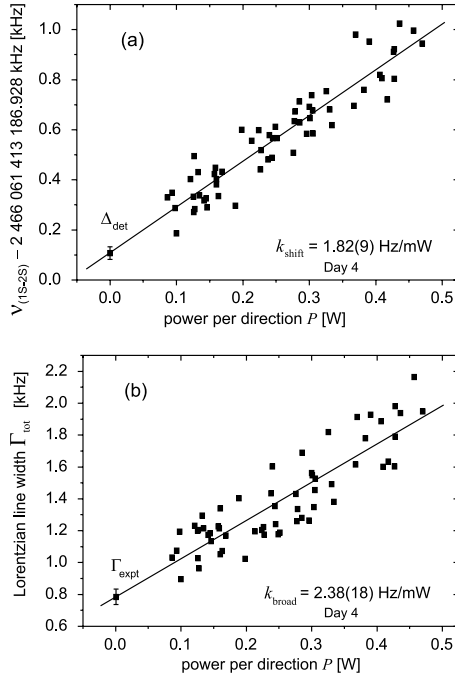
FIG. 2. Results from 59 line scans: (a) center frequencies and (b) linewidths full width half maximum (FWHM) both derived from Lorentzian fits versus the excitation power circulating in the cavity per direction, P. The power of 1 W per direction corresponds to a total on-axis focal intensity of 16 MW/m^2 averaged over one wavelength of the standing wave.

k_{shift}, as shown in the figure. Correspondingly, we consider the slope of the linear fit of the $\Gamma_{tot}(P)$ dependence and call it k_{broad}. It will be shown in the following that this coefficient is formed by three important contributions, namely power broadening, inhomogeneous ac Stark shift in a Gaussian beam profile, and the influence of the ionization of the 2S level.

In the next section we will analyze the structure of these coefficients by the help of a numerical analysis performed for an ensemble of hydrogen atoms excited in the given experimental geometry.

III. EXCITATION OF A BEAM OF ATOMIC HYDROGEN IN THE PRESENCE OF IONIZATION

The calculation of the 2S excitation dynamics is based on the equations of motion for the matrix elements of the density operator ρ' in the rotating wave approximation [8]. The laser field of angular frequency $\omega_L \simeq 2\pi \times 1233$ THz, corresponding to $\lambda = 243$ nm, and intensity I excites the two-photon transition between the ground state $|g\rangle$ (1S) and the excited state $|e\rangle$ (2S). The frequency detuning is defined to be the difference between the doubled laser frequency and the resonance frequency $\Delta\omega = 2\omega_L - \omega'_{eg}$, where $\hbar\omega'_{eg}$ is the energy difference between the 1S and 2S states of a perturbed atom [see Eq. (3)], ignoring the hyperfine structure [2].

In the experiment, the excitation field intensity I depends on the position inside the excitation region, because the laser profile is of Gaussian type. The fact that each atom flies along a certain trajectory with an individual speed through this intensity profile, renders the intensity a time-dependent quantity $I(t)$ in the frame of the traveling atom. Because the dynamic Stark effect is proportional to the intensity, also the total detuning as measured by the atom is a function of time, $\Delta\omega(t)$. In addition the upper state $|e\rangle$ decays to the continuum due to photoionization with a time-dependent rate proportional to the laser intensity. One can write the equations of motion for the density matrix, neglecting spontaneous decay of the 2S state [8]. After factoring out the fast optical oscillations from the components of the density matrix ρ via $\rho' = \rho \exp(-2i\omega_L t)$ we obtain the two-photon Bloch equations,

$$\frac{\partial}{\partial t}\rho'_{gg}(t) = -\Omega(t)\text{Im}(\rho'_{ge}(t)), \tag{2a}$$

$$\frac{\partial}{\partial t}\rho'_{ge}(t) = -i\Delta\omega(t)\rho'_{ge}(t) + i\frac{\Omega(t)}{2}(\rho'_{gg}(t) - \rho'_{ee}(t))$$

$$- \frac{\gamma_i(t)}{2}\rho'_{ge}(t), \tag{2b}$$

$$\frac{\partial}{\partial t}\rho'_{ee}(t) = \Omega(t)\text{Im}(\rho'_{ge}(t)) - \gamma_i(t)\rho'_{ee}(t), \tag{2c}$$

where the time-dependent two-photon Rabi frequency is $\Omega(t) = 2(2\pi\beta_{ge})(m_e/\mu)^3 I(t)$. Here m_e is the electron mass, μ the reduced mass, and the value of β_{ge} is taken from [8]: $\beta_{ge} = 3.681\,11 \times 10^{-5}$ Hz(W/m^2)$^{-1}$ for the 1S-2S transition. In the same paper the ionization rate is given by $\gamma_i(t) = 2\pi\beta_{ioni}(e)(m_e/\mu)^3 I(t)$, where the ionization coefficient reads $\beta_{ioni}(e) = 1.202\,08 \times 10^{-4}$ Hz(W/m^2)$^{-1}$.

Experimentally an ensemble of atoms contributes to the signal, with each individual atom having a different speed and trajectory through the interaction zone. We take into account only those trajectories, which are confined by the diaphragms D1 and D2 (see Fig. 1). It is assumed, that the starting points on the diaphragm D1 and the exit points on the diaphragm D2 defining each trajectory are randomly and independently distributed over the corresponding diaphragm with constant area density. It means, that the angle $\varphi > 0$ between the cavity axis z and each individual trajectory is also randomly and uniformly distributed for r_{D1}, $r_{D2} \ll \ell$: the atom can intersect the excitation light beam as well as fly parallel to its axis. The velocities are also chosen at random according to a Maxwellian distribution as in Eq. (1) at $T = 5$ K; as in the experiment the day-averaged readouts of the temperature sensor, placed on the cold nozzle, ranged between 4.95 and 5.25 K.

After this longitudinal velocity seeding, all atoms which would reach the detector earlier than the time at which the delayed detection started (that is before $\Delta\tau = 1210$ μs), were rejected from the ensemble. For each remaining atom, one can then easily calculate the time-dependent intensity $I(t)$, as well as the total interaction time. The laser is modeled by a
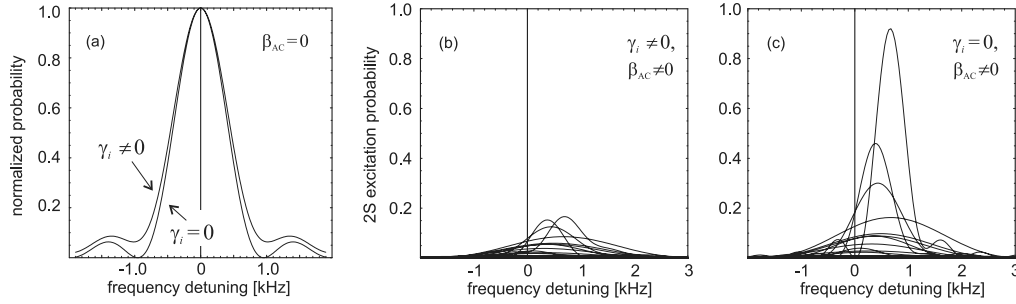
FIG. 3. (a) Normalized responses of a single atom illuminated by a 1 ms rectangular pulse with the intensity of $I=4$ MW/m^2 with ionization channel ($\gamma_i \neq 0$) and without it ($\gamma_i = 0$). For simplicity, neither the ac Stark shift nor the Doppler effect are taken into account. (b), (c) Excitation probabilities for atoms flying along different random trajectories through the Gaussian intensity profile corresponding to $P=300$ mW. (b) Calculations for 50 randomly chosen trajectories in the presence of the ionization channel. (c) Calculation for the same ensemble of trajectories without ionization taken into account.

Gaussian beam profile with parameters defined by the experimental geometry. The radial intensity distribution is therefore given by $I(r)=(4P/\pi w^2)\exp[-2r^2/w^2]$, where $w^2=w_0^2(1+(z\lambda/\pi w_0^2)^2)$. The beam slightly diverges along the z axis, and the beam waist on the incoupler plane equals $w_0=283$ μm. Here P is the power per direction, as used in Fig. 2.

It is necessary to point out that atoms flying through a standing wave in the cavity interact with a highly inhomogeneous laser field consisting of nodes and maxima with the periodicity of 121.6 nm in the z direction. But even for a very slow atom traveling at a longitudinal velocity of $v=v_0/300\simeq 1$ m/s, Eq. (1), the intensity will be modulated at a frequency of about 10 GHz, which is six orders of magnitude higher than the typical Rabi frequency Ω, which governs the population dynamics. Thus for the calculation of the density matrix elements, we can equivalently use a laser field with an averaged intensity, in a similar way as in applying the rotating wave approximation.

The general detuning $\Delta\omega(t)$ along the trajectory can now be expressed as follows:

$$\Delta\omega(t) = 2\omega_L - \omega'_{eg} = 2\omega_L - \omega_{eg} + \frac{\omega_{ge}}{2}\left(\frac{v}{c}\right)^2 - 2\pi\beta_{ac}I(t),$$
(3)

where $\hbar\omega_{eg}$ is the energy between the unperturbed $1S$ and $2S$ states. The other summands take into account the second-order Doppler effect and the intensity-dependent frequency shift caused by the real part of the dynamic Stark effect. In turn, the imaginary part of the dynamic Stark effect is related to ionization. According to [8], $\beta_{ac}=[\beta_{ac}(2S)-\beta_{ac}(1S)]\times(m_e/\mu)^3=1.669\,82\times10^{-4}$ Hz(W/m^2)$^{-1}$.

The time evolution of Eqs. (2) for a specific atom and its corresponding interaction time is calculated numerically for each given laser frequency ω_L which is scanned stepwise across the resonance. The resulting value of ρ'_{ee} is stored together with ω_L to define the contribution of each individual atom to the line profile.

Figure 3(a) illustrates the spectral response of a single

atom at rest to the excitation with the rectangular pulse of 243 nm radiation. This case is analyzed in detail in [8]. One observes that, for moderate excitation intensities of a few MW/m^2 and for short interaction times less then 1 ms, the contribution of the ionization broadening to the total linewidth is practically negligible. Indeed, for a 1 ms rectangular pulse of intensity $I=4$ MW/m^2 the ionization broadening is a very small effect, though the ionization rate itself in this case equals $\gamma_i=480$ Hz.

Figure 3(b) illustrates how individual atoms flying through the excitation region contribute to the observed line shape. Depending on the individual trajectory and the velocity of an atom it will be exposed to a time-varying intensity. The figure shows the resulting individual line shapes, over which the detector integrates to yield the observed line profile. Note the variations in amplitude, shift, and width of the individual lines due to varying speeds (second order Doppler shift), interaction times (excitation and ionization probability, TOF broadening) and sampled intensities (excitation and ionization probability, AC Stark shift, power broadening).

In contrast to the physical case given in Fig. 3(b) with all effects taken into account, Fig. 3(c) shows the excitation probabilities for *the same ensemble* of 50 trajectories calculated without ionization. Apparently the ionization preferably removes the slow atoms from the initial distribution, because they have more time to interact with the field. But these atoms would have contributed the strongest and the narrowest spectral lines to the resulting collective spectrum if no ionization had taken place. As a result, the detected line becomes weaker and broader.

In the results section we will discuss the simulated line profiles in more detail and compare the results with experimental data.

To perform the described Monte Carlo simulation we used the package MATHEMATICA 5 [13]. The simulation has shown good convergence and an arbitrary ensemble of 10 000 atoms has been used to calculate each transition line shape. The input parameters used by the program can be divided into four groups: (i) atomic structure; (ii) geometric parameters (w_0, r_{D1}, r_{D2}, ℓ, ℓ', nozzle radius); (iii) experimental conditions (P, T, $\Delta\tau$); and (iv) two program switches which allowed one to artificially set $\gamma_i=0$ (no ionization) or $\beta_{ac}=0$
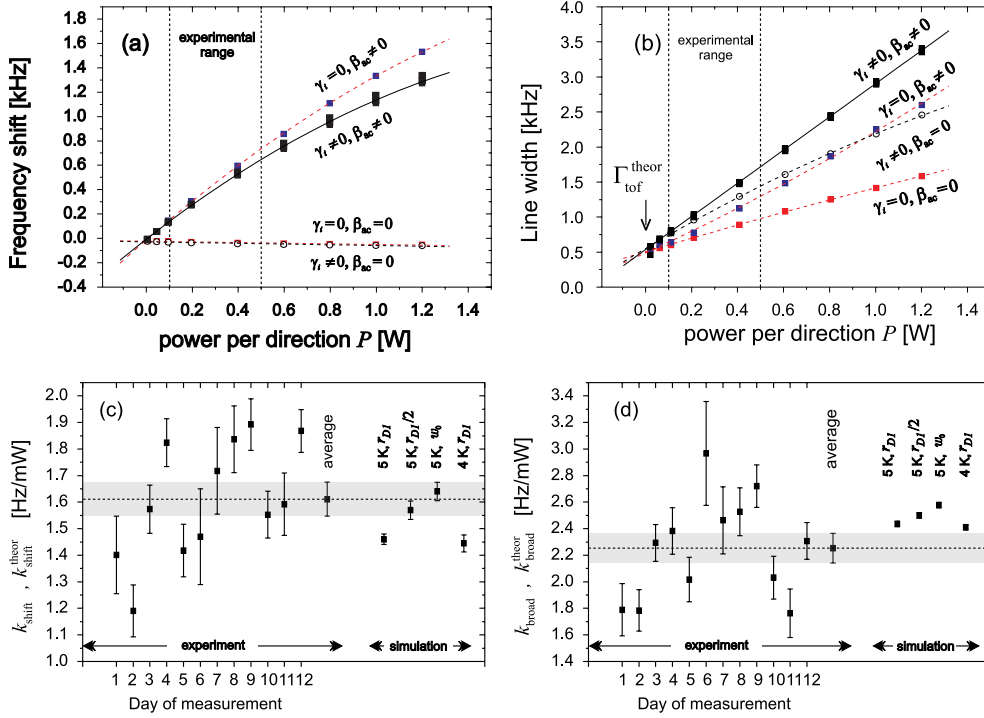
FIG. 4. (Color online) Simulated dependencies of the frequency shift (a) and the linewidth (b) of the 1*S*-2*S* transition vs excitation power per direction, P and a detection delayed by $\Delta\tau=1210$ μs. The set of data marked $\beta_{ac}\neq 0$, $\gamma_i \neq 0$ corresponds to the physical case. The other simulations clarify the separate contributions of ionization, inhomogeneous ac Stark shift, and power broadening [e.g., the data set with $\gamma_i=0$, $\beta_{AC}=0$ in (b) corresponds to pure power broadening]. Note that the contributions cannot be added in any simple algebraic way. The data sets are fitted by parabolic functions. On the left side of (c) and (d) the day-averaged values of k_{shift} and k_{broad} with corresponding uncertainties are presented. The total 12-day average of the data is indicated by the dashed lines and the gray bars for the uncertainties. Simulations for two different beam temperatures (5 and 4 K) and for different radii of the entrance diaphragm D1 (r_{D1}, $r_{D1}/2$, and w_0) are presented on the right part of the lower plots.

(no ac Stark shift). The last option allows one to analyze separately the contributions of ionization, ac Stark shift, and power broadening to the line shape.

Including all contributions to $\rho'_{ee}(\Delta\omega_L)$, we obtain the simulated line shape, which we fit with a Lorentzian profile exactly as in the evaluation of the experimental data for the purpose of this study. In our simulations, we varied the excitation power up to $P=1.2$ W per direction which covers and exceeds the whole experimental range.

IV. RESULTS

In this section the results of the numerical simulation will be compared with experimental results obtained in the measurement [5]. We will analyze the frequency shift and the line shape of the 1*S*-2*S* transition and discuss possible origins of the excess data scattering observed in the frequency measurement experiments.

We would like to point out here that both the frequency shift and the line broadening are *very small* effects of the order of 10^{-12} compared to the optical carrier frequency. Only the improvements of the laser stability and the narrowing of its spectral linewidth along with an improved absolute

frequency measurement have made it possible for the first time to perform a *quantitative* analysis of the line shift and especially of the line broadening as a function of excitation intensity.

Figure 4 illustrates the results of the different simulations (a), (b) and their comparison with experimental observations (c), (d). To evaluate the uncertainty of the simulation for 10 000 atoms due to the random elements of the simulation, we performed the simulation for three different arbitrary ensembles of atoms for the same input program parameters. The variation is on the level of few percent which is sufficient for this analysis.

A. Line center shift

As follows from Fig. 4(a), the main origin of the frequency shift is the ac Stark shift. The physical case is depicted in a solid curve ($\gamma_i \neq 0$, $\beta_{ac} \neq 0$). The line shift reveals an observable nonlinearity at higher powers. It could be explained by the following contributions: (i) the inhomogeneous ac Stark shift; (ii) the influence of ionization; and (iii) the saturation of the transition. In the current analysis we

took the nonlinearity into account by fitting the simulations in Fig. 4(a) with a parabolic function.

For comparison with the full treatment, we performed the same set of calculations for three nonphysical cases: with the ionization channel switched off ($\gamma_i=0$, $\beta_{ac} \neq 0$), the ac Stark shift is switched off ($\gamma_i \neq 0$, $\beta_{ac}=0$), and both these effects are switched off ($\gamma_i=0$, $\beta_{ac}=0$). We see that the main contribution to the frequency shift is due to the real part of the dynamic Stark shift. The ionization reduces the number of atoms undergoing the highest perturbation in the intensive laser field. It also influences the frequency shift, but only if the dynamic Stark shift is present as well. All data sets in Fig. 4(a) converge at zero power to the same value of $-20(1)$ Hz which corresponds to the mean second-order Doppler shift for the given beam temperature of $T=5$ K and the delay time $\Delta\tau=1210$ μs. This value is considerably smaller than the maximal shift of -200 Hz calculated for $v_{max}(\Delta\tau)$. This difference is caused by the fact that the velocity distribution of atoms which contribute to the signal $f'(v)$ is different from the velocity distribution of atoms in the beam $f(v)$: neglecting additional losses it is given by

$$f'(v) \propto f(v)(1-v/v_{max}(\Delta\tau)), \quad v < v_{max},$$

$$f'(v) = 0, \quad v \geqslant v_{max}. \quad (4)$$

Consequently, the Doppler correction must take this weighting into account. A further correction to the effective second-order Doppler effect is invoked by the preferred removal of slow atoms. As seen in Fig. 4(a) (for $\gamma_i \neq 0$, $\beta_{ac}=0$) this preference and thus the associated shift is vastly independent of laser power for our experimental conditions. As it is impossible in our experiment to measure the Stark coefficients β_{ac} and β_{ioni} separately, we analyze the values which can be derived both from the experiment and our numerical analysis, namely the slopes k_{shift} and k_{broad} of the power dependencies given in Fig. 2 and Figs. 4(a) and 4(b).

On the experimental side, we derive these values for each of the 12 days of measurement exactly in the same way as depicted in Fig. 2. The results for each day are presented in Figs. 4(c) and 4(d). One observes a significant scatter of the day-to-day data, with $\chi_r^2 \simeq 3$ (the reduced χ^2 or Birge ratio [14]), which could be partly ascribed to errors on the power axis, coming from both the calibration of the photodiode measuring the 243 nm power and from temporal variations of the transmittance of the curved mirror in Fig. 1. Therefore we average these data without taking into account the individual uncertainties and obtain $k_{shift}=1.61(6)$ Hz/mW and $k_{broad}=2.25(11)$ Hz/mW.

Extracting the coefficient k_{shift} from the results of the numerical analysis, depicted in Fig. 4(a), is not straightforward, since the curves for the shift of the line center are not linear and therefore k_{shift} is not strictly defined. However, since the scatter in the experimental data is larger than the calculated nonlinearities, it is enough on the present level of accuracy to replace the parabolic fit by a linear fit in the case of the frequency shift-intensity dependence (k_{shift}), in order to evaluate the results in the same way as in the experiment. To reduce the error introduced by this procedure, we restrict the

data points taken into account by the fit to those which fall into the experimental range of powers: $0.1 \text{ W} < P < 0.5 \text{ W}$. The value resulting from the Monte Carlo analysis is denoted as k_{shift}^{theor} in analogy to the notation in Fig. 1.

To test the sensitivity of the model to the experimental conditions and to evaluate the corresponding uncertainties we also performed a set of simulations for different beam temperatures, varying between 4 and 6 K, slightly different interaction lengths, and a reduced radius r_1 of the diaphragm D1. All these tests show a low sensitivity of results to these parameters which allows one to compare them with the experimental data. We have performed calculations of k_{shift}^{theor} for different realistic experimental parameters. The results of four selected cases are given in Fig. 4(c): with an atomic beam temperature of 4 and 5 K and for a diaphragm size matched and centered to the laser beam to simulate the nozzle covered with a molecular hydrogen film.

The last case corresponds to a possible situation, where a film of molecular hydrogen symmetrically covers the nozzle from inside in such a way that the nozzle radius equals either $r_{D1}/2$ or $w_0=283$ μm (the film eventually touches the laser beam). The frozen nozzle radially restricts the atomic trajectories on the entrance to the interaction zone, which results in changing the intensity profiles. The growth of the H_2 film was a characteristic feature of the hydrogen spectrometer working at the lowest beam temperature. The measurement cycle lasted about 15 min, after which the nozzle was heated to 20 K to melt the film.

Comparing the averaged value k_{shift} with the results of the numerical simulation, we can establish an agreement on the level of about 15% uncertainty with respect to the absolute values. As follows from the previous analysis, the intensity-dependent frequency shift is mainly caused by the ac Stark shift which contributes to the general detuning (3). Using the linearity of the effect at low powers one can conclude, that this analysis allows one to verify β_{ac} at the same confidence level of 15% and therefore we can experimentally verify the results of the calculations of $\beta_{ac}=\beta_{ac}(2S)-\beta_{ac}(1S)$ presented in [8].

B. Linewidth

The analysis of the linewidth is more complicated in comparison with the analysis of the frequency shift since a number of different effects contribute significantly to the line broadening. The linewidth consists of intensity-independent and intensity-dependent parts. The intensity-independent part includes the laser spectral linewidth and the time-of-flight broadening, while such effects as power broadening, inhomogeneous ac Stark broadening, and ionization broadening contribute to the latter part. In addition, temporal intensity fluctuations of the laser radiation in the excitation region also induce an additional intensity-dependent broadening due to the variable Stark shift. Thus, assuming for simplicity the Lorentzian profiles, one can write

$$\Gamma_{tot}(P) = \Gamma(P) + \Gamma_{tof} + 4\Gamma_{laser}, \quad (5)$$

where $\Gamma_{tot}(P)$ is the total linewidth, Γ_{tof} is the contribution of the time-of-flight broadening, and $\Gamma(P)$ includes all

intensity-dependent effects with $\Gamma(0)=0$. The laser linewidth Γ_{laser} carries a factor of 4 because we measure it at 486 nm, whereas all other transition frequencies correspond to 121 nm. It has been shown experimentally that the spectral linewidth of our laser system doubles for the frequency doubling process. We understand that each of the contributions listed above has a complex spectral shape which can significantly differ from Lorentzian and the expression (5) can be used only for rough estimations. Still, the simulations show that in our case the time-of-flight broadening has near-to-Lorentzian spectral line shape while heterodyne experiments indicate the same for the spectral line of our laser system.

As is evident from Fig. 4(b), the intensity-dependent part of the linewidth is formed by three different processes: (i) the power broadening, (ii) the inhomogeneous ac Stark shift in the laser beam profile, and (iii) the ionization of the 2*S* state. The pure power broadening corresponds to the case ($\gamma_i=0$, $\beta_{\text{ac}}=0$) and is due to Rabi flopping between the ground and the excited states, effectively reducing the lifetime of the population in the excited 2*S* state. The inhomogeneous ac Stark shift in the case ($\gamma_i=0$, $\beta_{\text{ac}}\neq0$) originates from a Gaussian intensity profile in the excitation region. The last significant broadening comes from ionization which contributes in a highly nontrivial way illustrated in Figs. 3(b) and 3(c).

The excessive loss of slow atoms has been taken into account in the line form model [7,9] as an empirical modification of the low-velocity wing of the Maxwellian v^3 dependency in Eq. (1). There it was assumed that the slow atoms are missing from the beam because of collisions with the fast atoms (Zacharias effect). However, now we conclude that no such mechanism is necessary to fit our data and the selective ionization is the most significant effect responsible for this loss. Strictly speaking, one deals with three distinct velocity distributions: (i) the atoms emerging from the nozzle; (ii) the detected 2*S* atoms; and (iii) the ground state atoms. Whereas the first distribution is assumed to be Maxwellian [Eq. (1)], the second is relevant for determining the line shape.

To compare with the experimental results, we also evaluated the contribution of the temporal intensity fluctuations. In principle, this effect is equivalent to the considered inhomogeneous ac Stark shift, but integrated over time, not space. In the experiment, we observed fast intensity fluctuations on the level of ±5% during the excitation cycle. We embedded this process into the simulation by adding white noise with a 5% band to $I(t)$. The effect lies within the uncertainty of the calculations for the given number of atoms used in the simulation.

For the linewidth as a function of laser power, the slope is derived from the fit similar to the case of Fig. 4(a). The value resulting from the Monte Carlo analysis is denoted as $k_{\text{broad}}^{\text{theor}}$. The linewidth, extrapolated to zero power, is $\Gamma_{\text{tof}}^{\text{theor}}$ =550(5) Hz which corresponds to the theoretical value for the averaged time-of-flight broadening for the given delay $\tau=1210$ μs in the absence of other broadening contributions [Fig 4(b)].

The value k_{broad} can be tested in the same way as k_{shift} with an uncertainty of 18% [see Fig. 4(d)]. Due to the complex structure of this value and the number of contributions of different nature which add up to the total line broadening,

it is impossible to disentangle them and to set separate restrictions on the transition matrix element and the ionization cross section. Nevertheless, if we switch off any of the important broadening mechanisms, as illustrated in Fig. 4, the simulation will no longer agree so well with the experimental observation. This means that both the calculations performed in [8] as well as the current analysis adequately describes the excitation dynamics of the hydrogen atom in the presence of photoionization.

For consistency of our analysis, we also performed an evaluation of the laser linewidth Γ_{laser}. Studies of the spectral laser linewidth at 486 nm, based on the investigation of beat signals, resulted in a value of 60 Hz [15]. In the framework of this paper, we can make an estimate of its spectral linewidth with a different, indirect method. To this end, we compare the calculated linewidth at zero laser power $\Gamma_{\text{tof}}^{\text{theor}}$ with the experimentally observed linewidth Γ_{expt}, where the latter is obtained by averaging the extrapolated day values for the linewidth similar to Fig. 2(b), resulting in Γ_{expt} =775(20) Hz. From Eq. (5) we obtain Γ_{laser}=56(5) Hz, which is consistent with the previous independent measurement [15]. The splitting of the $(1S, F=1, m_F=\pm1) \rightarrow (2S, F'=1, m_F'=m_F)$ magnetic components is negligible in the experiment.

An attempt to directly evaluate the expected Lyman-α count rate in the given experimental geometry and thus test the theoretical values more directly fails due to the large uncertainties in the beam density, the fraction of atomic hydrogen in it, and the detection efficiency. The presented indirect analysis happens to be much more sensitive to the absolute values of the transition matrix elements and the ionization cross section than the direct evaluations.

C. Impact on the 1*S*-2*S* absolute frequency determination

At the end of this section we discuss the conclusions of the current analysis regarding the absolute frequency measurement of the 1*S*-2*S* transition in atomic hydrogen.

First of all, we want to point out the nonlinearity of the frequency shift of the line center as a function of the laser power [Fig. 4(a)]. Our analysis shows, that our previous linear fit leads to an error of 10–20 Hz in the determination of the absolute 1*S*-2*S* frequency $\omega_{ge}/2\pi$, if we restrict ourselves to the experimental range of powers $(0.1\text{ W}<P<0.5\text{ W})$. This does not contradict the uncertainty of the line shape model of 20 Hz given in [9]. Moreover, in the derivation of the possible small temporal drift of the 1*S*-2*S* frequency [5] this error cancels out. Still, for a further improvement of the 1*S*-2*S* frequency measurement it is highly desirable to reduce the laser intensity and thus reduce the error and the uncertainty of the extrapolation.

Secondly, the calculations show, that due to the photoionization, the velocity distribution of atoms escaping the nozzle significantly differs from the distribution of atoms contributing to the signal. For the correction of the second order Doppler effect it is more physical to model the initial velocity distribution in the nozzle by a Maxwellian distribution [see Eq. (1)], which is dynamically modified by the ionization process of atoms with long interaction times, instead of mod-

eling an effective velocity distribution at the detector. On the other hand, the magnitude of the Doppler effect, which has been one of the biggest concerns in the last measurements [5,7] is already on the level of −20 Hz for a delay time of $\Delta\tau = 1210$ μs. This opens an opportunity to use a simplified line shape model to correct for this effect.

We have performed an evaluation of the whole data set obtained in the 2003 measurement [5] using such a simplified approach. The 1*S*-2*S* spectral lines detected with the delays $\Delta\tau > 1210$ μs have been fitted by Lorentzian functions. The frequencies of the line centers have been corrected for the second-order Doppler effect by adding the calculated frequency shift. The result of this analysis was consistent with the result of the full line shape model [9] within the uncertainty of the model. The shift should be sensitive to the initial velocity distribution which can differ from (1) due to, e.g., geometrical factors, imperfect thermalization or collisions. The delayed detection modifying the velocity distribution (5) drastically reduces the mean Doppler shift as well as its sensitivity to the initial distribution. We tested numerically, that the substitution of the v^3 dependency (1) by v^4 results in a mean Doppler shift of −23 Hz for $\Delta\tau = 1210$ μs, which is only 3 Hz aside the previous value of −20 Hz. The difference decreases for increasing $\Delta\tau$ and the corresponding uncertainty in the determination the1*S*-2*S* frequency can be reduced to a few hertz. Thus, using such a simplified model we can correct the second-order Doppler effect with an uncertainty on the level of a few parts in 10^{15}.

The last point concerns the influence of the freezing nozzle on the observed absorption line centers, and resulting effects on the absolute frequency, which is obtained by the extrapolation of these line centers to zero laser power. Since the nozzle temperature is lower than its melting point of 14 K, molecular hydrogen effectively freezes on the nozzle walls and reduces its diameter. In the experiment, we had to melt molecular hydrogen approximately once per 20 min to avoid significant losses of laser power and atomic hydrogen flux in the 243 nm cavity. Our simulation allows for different spatial seedings of starting points of the atomic trajectories at the diaphragms, which can be used to model a reduced nozzle diameter or a misalignment of the cavity mode with respect to the atomic beam axis.

We have performed a simulation of a whole day of measurement recording the 1210 μs delayed spectra at 100 different intensities, while varying the nozzle radius randomly in the range from r_{D1} down to w_0. The resulting line center fits as a function of laser power per direction are shown in Fig. 5(b). Figure 5(a) results from the same simulation but with a permanently free nozzle. An uncontrolled freezing leads to an excess scatter of the line centers, increasing for larger exciting powers. Specifically, a smaller radius at the entrance diaphragm results in an upward shift in line center frequency, the shift increasing with excitation power. This is consistent with the observation in Fig. 4(c), where a small nozzle radius results in a larger value for k_{shift}. As a result, a linear fit in the range of 0.1−0.5 W and an extrapolation to zero intensity gives different values for the absolute frequency depending on the amount of nozzle freezing. Typically the scatter is on the level of a few tens of hertz, which can only partly explain the scatter observed in the experi-
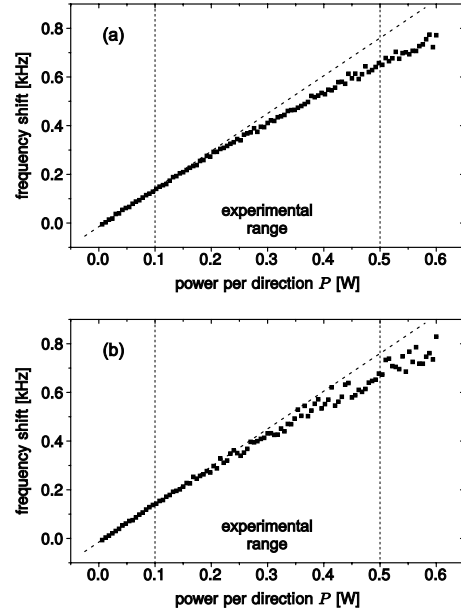

FIG. 5. Monte Carlo simulation: (a) The frequency of the 1*S*-2*S* transition vs laser power for an ensemble of 10 000 atoms for the completely opened nozzle. The residual scatter of the data can be explained by the stochastic nature of the Monte Carlo simulation. (b) The same simulation, but the nozzle radius is randomly varied in the range $\{w_0, r_{D1}\}$. We fit the data at low intensity limit by linear functions (dashed tilted lines) for visualization of nonlinearity of the frequency shift.

ments [5,7]. Other contributions can originate in uncertainties of the power axis and misalignment of the 243 nm enhancement cavity. In future measurements we will aim at increasing the nozzle diameter to avoid restriction of the atomic trajectories, working at lower excitation powers, and improving the stability of the enhancement cavity including power stabilization.

The beam nature of the 1*S*-2*S* spectroscopy of atomic hydrogen imposes certain restrictions on the experimental conditions like high intensity of the excitation field, impossibility of further cooling of the beam, short interaction time, and freezing of the nozzle. The enumerated effects result in a number of systematic shifts and corresponding loss of accuracy. Note, that all optical spectroscopic experiments demonstrating the accuracy better than 10^{-14} deal with cold ions or atoms in traps (see, e.g., [16,17]). All the systematic shifts of the 1*S*-2*S* transition discussed in the paper would be significantly reduced or eliminated if the hydrogen atoms were slowed down by laser cooling or if one used hydrogenlike ions that could be held in a trap [18].

Based on considerations of this section, we can conclude that perturbation of the mode of the enhancement cavity results in a frequency shift via the intensity related shift and broadenings. Though the cavity is not confocal which ensures the suppression factor over 500 for the TEM$_{01}$ mode, the intracavity diaphragms can influence the structure of the TEM$_{00}$ cavity mode. Monte Carlo simulations performed for

the impure TEM_{00} mode show that the results presented in the article remain valid if the power falling into the TEM_{01} mode does not exceed 5%. Thus, special attention should be paid for intensity stabilization, coupling, and alignment of the cavity to avoid any additional nonresonant light. After taking the issues discussed in the paper into account it seems realistic to reduce the uncertainty of the determination of the 1*S*-2*S* frequency to the level of a few parts in 10^{15}.

V. CONCLUSIONS

In this paper we discussed the transient excitation dynamics of the 1*S*-2*S* transition of atomic hydrogen under irradiation by two counterpropagating 243 nm light beams. The main focus of the present analysis has been the inclusion of photoionization of the 2*S* state, power broadening, and the inhomogeneous ac Stark shift in the quantum dynamics and the detailed study of their influence on the transition frequency and its linewidth.

Though photoionization would only insignificantly change the linewidth of each individual atom in the experimental range of excitation powers and interaction times in a laser field of constant intensity, the preferred ionization of slow 2*S* atoms results in a substantial broadening of the observed collective spectrum. The modeling shows, that the resulting intensity-dependent frequency shift is mainly caused by the dynamic Stark shift, while the intensity-dependent line broadening results from power broadening, the dynamic Stark shift in a spatially inhomogeneous laser field, and the influence of photoionization.

For our simulation we used the values of the transition matrix elements, the dynamic Stark shift coefficients, and the ionization rates rederived in [8]. The results of the simulation show a fair agreement with the experimentally observed ones. We can confirm the value of the difference of the dynamic Stark shift coefficients $\beta_{ac}(2S)$-$\beta_{ac}(1S)$ with an accuracy of 15% using the analysis of the 1*S*-2*S* frequency shift. The analysis of the line broadening also shows a good agreement with the experimental values within 18%. Due to the complex structure of the process, the intensity-dependent line broadening does not allow one to make definite conclusions about the ionization coefficient, although it provides evidence that our treatment of the excitation process in the thermal beam is correct.

The uncertainty of the determination 1*S*-2*S* frequency is limited not only by the experimental accuracy, but also by the uncertainty of the line shape model and the correction of the dynamic Stark shift. Taking photoionization into account allows one to build a more accurate line shape model. Factors such as the nonlinearity of the line shift and geometrical factors contribute on a level comparable in magnitude to the second order Doppler effect, which has been of major concern in previous studies [7,9]. The Monte Carlo approach presented in this paper allows one to perform accurate quantitative evaluations of all these effects and to make an accurate evaluation of the final uncertainty.

[1] F. Biraben *et al.*, in *The Hydrogen Atom. Precision Physics of Simple Atomic Systems*, edited by S. G. Karshenboim, F. S. Pavone, G. F. Bassani, M. Inguscio, and T. W. Hänsch (Springer, 2001), pp. 18–41.

[2] N. Kolachevsky, M. Fischer, S. G. Karshenboim, and T. W. Hänsch Phys. Rev. Lett. **92**, 033003 (2004).

[3] Th. Udem, A. Huber, B. Gross, J. Reichert, M. Prevedelli, M. Weitz, and T. W. Hänsch, Phys. Rev. Lett. **79**, 2646 (1997).

[4] A. Huber, Th. Udem, B. Gross, J. Reichert, M. Kourogi, K. Pachucki, M. Weitz, and T. W. Hänsch, Phys. Rev. Lett. **80**, 468 (1998).

[5] M. Fischer *et al.*, Phys. Rev. Lett. **92**, 230802 (2004).

[6] E. Peik, B. Lipphardt, H. Schnatz, T. Schneider, C. Tamm, and S. G. Karshenboim, Phys. Rev. Lett. **93**, 170801 (2004).

[7] M. Niering *et al.*, Phys. Rev. Lett. **84**, 5496 (2000).

[8] M. Haas *et al.*, Phys. Rev. A **73**, 052501 (2006).

[9] A. Huber, B. Gross, M. Weitz, and T. W. Hänsch, Phys. Rev. A **59**, 1844 (1999).

[10] M. Fischer *et al.*, in *Astrophysics, Clocks and Fundamental Constants*, Lect. Notes Phys. Vol. 648 edited by S. G. Karshenboim and E. Peik (Springer-Verlag, Berlin, 2004), p. 209.

[11] Th. Udem, R. Holzwarth, and T. W. Hänsch, Nature (London), **416**, 233 (2002).

[12] G. Scoles, D. Bassi, U. Buck, and D. Laine, *Atomic and Molecular Beam Methods* (Oxford University Press, New York, 1988) Vol. 1.

[13] S. Wolfram, *The Mathematica Book*, 4th ed. (Wolfram Media/ Cambridge University Press, Cambridge, 1999).

[14] R. T. Birge, Phys. Rev. **40**, 207 (1932).

[15] M. Fischer, N. Kolachevsky, S. G. Karshenboim, and T. W. Hänsch, Can. J. Phys. **80**, 1225 (2002).

[16] L. Hollberg *et al.*, J. Phys. B **38**, S469 (2005).

[17] H. S. Margolis *et al.*, Science **19**, 1355 (2004).

[18] M. Herrmann, Th. Udem, C. Gohle, N. Kolachevsky, T. W. Hänsch, D. Leibfried, D. Wineland, M. Haas, U. D. Jentschura, and C. H. Keitel (unpublished).

5.3. XUV frequency combs

The following two manuscripts report on the first demonstration of a high repetition rate XUV frequency comb generated in an external enhancement cavity and a subsequent significantly improved system. The author's contribution to the first manuscript is the verification of the comb structure by a measurement of a beat note between the third ("high") harmonic from the enhancement cavity and the fourth harmonic of an independent mode-locked Nd:YAG laser. The main contributions to the second manuscript are i) the interpretation and comparison of the obtained results to previous measurements by a study of the scaling of the conversion efficiency with experimental parameters and ii) the interpretation of the result in terms of He$^+$ 1S-2S.

LETTERS

A frequency comb in the extreme ultraviolet

Christoph Gohle[1], Thomas Udem[1], Maximilian Herrmann[1], Jens Rauschenberger[1], Ronald Holzwarth[1], Hans A. Schuessler[1], Ferenc Krausz[1,2] & Theodor W. Hänsch[1,2]

Since 1998, the interaction of precision spectroscopy and ultrafast laser science has led to several notable accomplishments. Femtosecond laser optical frequency 'combs' (evenly spaced spectral lines) have revolutionized the measurement of optical frequencies[1,2] and enabled optical atomic clocks[3]. The same comb techniques have been used to control the waveform of ultrafast laser pulses, which permitted the generation of single attosecond pulses[4], and have been used in a recently demonstrated 'oscilloscope' for light waves[5]. Here we demonstrate intra-cavity high harmonic generation in the extreme ultraviolet, which promises to lead to another joint frontier of precision spectroscopy and ultrafast science. We have generated coherent extreme ultraviolet radiation at a repetition frequency of more than 100 MHz, a 1,000-fold improvement over previous experiments[6]. At such a repetition rate, the mode spacing of the frequency comb, which is expected to survive the high harmonic generation process, is large enough for high resolution spectroscopy. Additionally, there may be many other applications of such a quasi-continuous compact and coherent extreme ultraviolet source, including extreme ultraviolet holography, microscopy, nanolithography and X-ray atomic clocks.

For more than three decades, laser physics and laser spectroscopy have evolved along two seemingly opposite and disconnected frontiers, pursued by different communities of researchers. In the field of high resolution spectroscopy, scientists have learned to build ultra-stable continuous wave (c.w.) laser sources and they have perfected spectroscopy of laser-cooled atomic systems to reach extremely high spectral resolution[7]. In the field of ultrafast science, researchers have demonstrated ever-shorter pulses from mode-locked laser systems and ways of amplifying such pulses to very high intensities[8]. By focusing intense amplified pulses into a gas, coherent radiation down to the X-ray region can be generated by high harmonic generation (HHG)[9]. Since this process requires very high intensities ($>10^{13}$ W cm^{-2}), the available laser power had to be concentrated into a small number of ultrashort pulses per second, limiting repetition rates for HHG to typically a few kHz.

To overcome this limitation, we couple the driving laser pulses from the oscillator into a high finesse optical resonator that contains the nonlinear medium. Inside this resonator, the circulating power is enhanced by a factor P (the resonator finesse divided by π) so that it can drive the nonlinear process (HHG) inside a gas target. For c.w. lasers, resonators with a finesse exceeding 100,000 can be constructed[10] and overall nonlinear conversion efficiencies approaching unity can be achieved[11]. In the case of a mode-locked ultrafast laser, however, complying with the extra requirements discussed below is more difficult: the output spectrum of a mode-locked laser contains not just a single c.w. mode but a comb of such modes, with frequencies

$$\omega_n = n\omega_r + \omega_{CE} \qquad (1)$$

Here ω_r is the pulse repetition frequency and ω_{CE} the carrier envelope

(CE) frequency[12]. Both ω_r and ω_{CE} reside in the radio frequency domain, whereas the optical frequencies of the comb are given by ω_n. The two frequency regions are connected by virtue of the large integer $n = 10^5 \ldots 10^6$ that enumerates the modes. An optical resonator for such radiation has to be simultaneously resonant for each mode ω_n that originates from the laser. This can be accomplished with a resonator of appropriate length and zero group velocity dispersion, whose CE frequency is matched to the laser[13,14]. Rephrased into time domain language, coherent pulse addition in a resonator occurs if (1) the round trip time of the pulse is the same as the period of the laser, (2) the pulse envelope does not change its shape during one round trip, and (3) the carrier phase shift with respect to the envelope of the circulating pulse is the same per round trip as the pulse to pulse change from the laser. For increasing finesse, the stored pulse undergoes an increasing number of round trips and therefore dispersion compensation becomes more critical. Nevertheless, such cavities have been demonstrated to enhance nonlinear conversion for 100-fs pulses[15], and recently a resonator for sub-50-fs pulse duration has been demonstrated to provide an enhancement factor of up to 70, resulting in pulse energies of more than 200 nJ (ref. 16).

Instead of dumping the power from the resonator as has been done in earlier experiments[16], we have placed a low-density xenon gas target as the nonlinear medium for HHG inside such a resonator. In contrast to the usual HHG schemes, the power that is not converted into the extreme ultraviolet (XUV) after a single pass through the medium is 'recycled' and can contribute in subsequent passes, so that higher total conversion efficiencies than for conventional schemes can be expected. Moreover, it becomes possible to use the high power at the full repetition rate of the laser. As a result, in addition to the comb of odd laser harmonics that stem from the periodicity of the carrier wave in one pulse, a nested frequency comb with a spacing given by the repetition frequency originates from the periodic pulse train. If the HHG spectrum contains only frequency components that are the sum of the original frequencies from equation (1), as expected from energy conservation, then the XUV comb structure of the kth laser harmonic (that is, the sum of k laser photons) is given by

$$\omega'_n = n\omega_r + k\omega_{CE} \qquad (2)$$

where the integer n now runs over k times larger values than in equation (1). With such a widely spaced frequency comb, single modes that are effectively c.w. lasers may be isolated for high resolution spectroscopy. If a mode ω_n of the comb is tuned into resonance with a two-photon transition, any pair $\omega_{n-\ell} + \omega_{n+\ell}$ (with integer ℓ) is simultaneously resonant. This allows the use of the entire (broadband) power of the comb while maintaining the linewidth of a single mode[17].

Direct frequency comb spectroscopy has been applied to atomic resonances in the infrared[18–20] and in the ultraviolet range[21], and a resolution approaching the natural linewidth with a laser-cooled sample has been reached[18,20]. At the same time, the frequency comb may be phase coherently linked to a Cs atomic clock for accurate
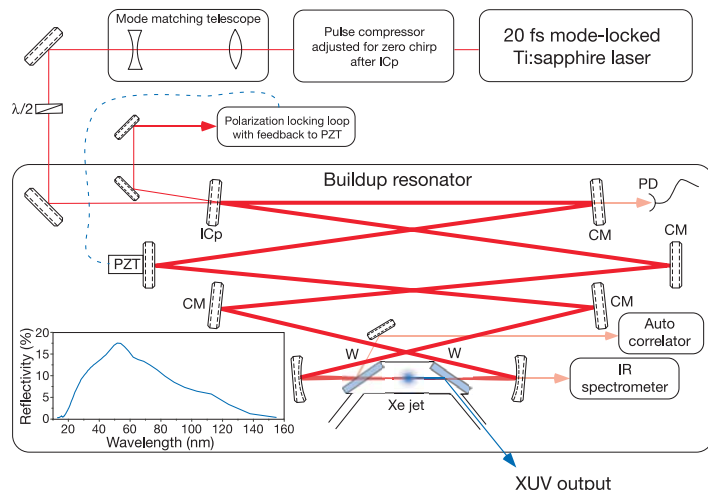
       LETTERS

Figure 1 | The XUV laser set-up. ICp, coupling mirror with 1% transmission; CM, chirped mirrors; PD, photodiode; W, Brewster-angled sapphire window of 1 mm thickness; PZT, piezoelectric transducer. Inset shows the reflectance of sapphire for p-polarized XUV light at an incidence angle of 60.4° (Brewster angle for 800 nm radiation).

determination of the optical frequencies. However, applicability of our XUV frequency comb for high resolution laser spectroscopy relies on the coherence of the generation process. So far there was only indirect evidence that this is indeed the case. For example, it was observed that two independent HHG sources pumped by the same fundamental pulse produce stable interference fringes[22] and that the generated XUV bursts are compressible[23], which both indicate that the phase link between fundamental and XUV is tight. Direct evidence can only be provided by a beat measurement between two independent XUV sources or a spectroscopy measurement. Upconversion of phase noise in the fundamental pulse train that might bury the comb is reduced in our approach, as the enhancement resonator acts as a flywheel for the incoming pulse train.

When the buildup resonator (shown in Fig. 1 and explained in the Methods section) is put into lock and the CE frequency of the laser is adjusted to maximize the power inside the resonator, an optical spectrum as shown in Fig. 2 is observed. The circulating (average) power has been determined to be 38 W. The discrepancy between the calculated ($P = 100$) and observed enhancement ($P = 54$) can mostly be attributed to spectral filtering due to residual dispersion inside the resonator. The autocorrelation of the stored pulse inside the resonator is measured using the residual reflection of the fundamental laser radiation from the first Brewster window
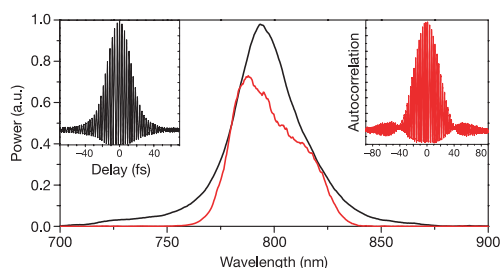
(see Fig. 1). It indicates an approximately chirp-free pulse of about 28 fs duration. With these figures, we estimate a peak power of about 12 MW and intensities in the focus of around 5×10^{13} W cm^{-2}. Turning on the xenon jet has no effect on the cavity lock, which shows that plasma induced phase noise above feedback bandwidth (10 kHz) is negligible.

Given these conditions, an XUV spectrum as shown in Fig. 3 can be observed after the XUV output coupler, which is described in the Methods section. High harmonics up to fifteenth order or 23 eV photon energy (as expected for these intensities) are observed, with an exponential roll-off starting around the ninth harmonic, presumably due to increasing phase mismatch. The cut-off wavelength of our XUV spectrometer around 120 nm prevented us from observing the fifth harmonic. The third harmonic could be observed with the naked eye, even though the outcoupling efficiency was very low for this wavelength. Additionally, we observe a line slightly below the ionization potential of xenon at 103 nm, which to our knowledge has not been reported previously. To test the comb coherence, we performed a beat experiment between the third harmonic from the
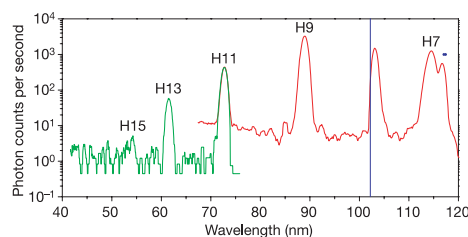

Figure 2 | Normalized spectrum of the pump laser (black) and the circulating pulse in the enhancement resonator (red) when locked. Inset, respective measured autocorrelations.

Figure 3 | Harmonic spectrum obtained with the resonator locked and the xenon jet on. The short-wavelength end of the spectrum (green) is taken with a 0.1 μm aluminium filter in the beam path to reduce stray light from the stronger lower harmonics, and is rescaled to match the peak height at the eleventh harmonic (H11) of the measurement without filter (red). Blue dots indicate the 5P–7S resonance in xenon that modifies the shape of the seventh harmonic (H7), and the vertical line indicates the ionization potential. The spectral feature just below the ionization limit presumably originates from fluorescence of coherently excited Rydberg states.

enhancement cavity and the fourth harmonic of a mode-locked Nd:YVO$_4$ laser. The results are shown in Fig. 4. A similar result[24] is obtained in a beat measurement between third harmonics produced in a nonlinear crystal and a gas jet, which proves equation (2) for this special case.

In order to test the spatial coherence of the harmonic radiation and investigate the possible origin of the feature at 103 nm, we have recorded transverse beam profiles for each feature of the spectrum from the seventh through to the eleventh harmonic by translating the monochromator in the horizontal direction and recording the transmitted intensity for each feature. A gaussian fit to these profiles yields divergence angles of 14, 11 and 10 mrad for the seventh, ninth and eleventh harmonic, respectively. This corresponds approximately to the diffraction limit, which would allow tight focusing. The divergence of the feature at 103 nm could not be determined, as it exceeds the limited viewing angle of the set-up.

We also investigated the generated power of the different spectral features as a function of the fundamental power. The results are shown in Fig. 5. As expected[25], for low intensities before the individual harmonic reaches the plateau, it follows a power law with an exponent close to the harmonic order. As the harmonic reaches the plateau, the exponent decreases to a value that is approximately the same for all harmonic orders. The line at 103 nm exhibits a very high slope for low intensities while it quickly saturates and even decreases at higher powers, which, in addition to the divergence and the frequency not being close to an odd harmonic, suggests that a different process than the usual HHG is responsible for that feature. A possible explanation for this feature would be that during the pulse the Rydberg levels of the atom are Stark-shifted into eight- and even nine-photon resonance with the fundamental laser light. Population can accumulate there, as high-lying Rydberg states are robust against field ionization for such short laser pulses. This long-lived excited dipole can now oscillate for a long time in phase even after the pulse has passed, so that most of the emitted power is directed and has a frequency of the unperturbed Rydberg states just below the ionization limit.
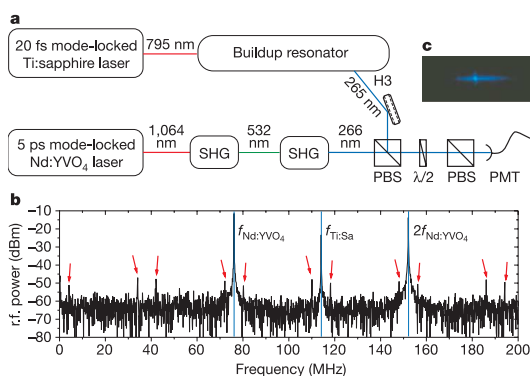
The total power of the spectral range from 120 nm down to 60 nm was determined to be more than 1 nW after the sapphire window. If the calculated coupling efficiency of that window is taken into account, more than 10^{-8} of the power from the laser is converted into photons in the 60–120 nm range. Optimized results with chirped pulse amplifier (CPA) systems reached more than 10^{-5} single pass efficiency in this wavelength range[26]. With the advent of precision dispersion characterization[27], dispersion-compensated resonators with enhancement factors of 1,000 are possible, so that with high energy oscillators[28], intra-cavity pulse energies approaching 100 μJ seem realistic with current technologies. Obviously, at such high pulse energies, special care has to be taken to avoid nonlinear responses of such a resonator, such as self phase modulation in windows, two-photon absorption in the mirror coatings, and the like. In this case optimized single pass conversion efficiencies would allow a total power conversion in the per cent range and XUV output powers in the mW range.

In conclusion, we have shown that efficient high-order harmonic generation directly from a Ti:sapphire oscillator is possible by use of an enhancement resonator of high finesse specifically designed to support ultrashort femtosecond pulses. This not only reduces the complexity of the set-up for the generation of high harmonics compared to a typical CPA system but simultaneously increases the repetition rate of this conversion by several orders of magnitude. At such a high repetition rate, the frequency comb from the fundamental laser will also be usable in the XUV, so that high resolution spectroscopy in the XUV comes into reach. This will enable new high precision tests for fundamental physical theories. For example, the 1S–2S transition of singly charged helium can be probed with the thirteenth harmonic of a Ti:sapphire laser. This would provide an even more sensitive test of quantum electrodynamics than the hydrogen 1S–2S experiment[29]. If these measurements are combined, a new precise value for the proton charge radius and the Rydberg constant may be obtained. It can be expected that the presented method is capable of producing orders of magnitude more intense XUV output than conventional HHG schemes and with excellent spatial coherence, so that other applications like XUV interferometry, holography and lithography come into the realm of reality.

Figure 4 | Frequency comb coherence. a, Set-up for testing comb coherence at the third harmonic (H3). SHG, second harmonic generation; PBS, polarizing beam splitter; PMT, photomultiplier. To synchronize the two lasers, the third harmonic of the Nd:YVO$_4$ laser repetition rate (76 MHz) was phase-locked to the second harmonic of the Ti:sapphire laser repetition rate (changed to 114 MHz). The repetition rates from the two lasers are marked with blue lines in the r.f. spectrum (**b**). The red arrows mark the position of the beat signals observed when the delay between the pulses is adjusted appropriately using an r.f. delay line. **c,** Grating image of the overlapped beams with the narrow bandwidth picosecond laser (bright spot) confined to the centre of the femtosecond spectrum.

Figure 5 | Generated power versus the fundamental intensity *I* for three spectral features. Data are shown for the feature at 103 nm (squares), the ninth harmonic (H9; circles) and the eleventh harmonic (H11; triangles). Solid lines represent fits to the data with a power law with exponents as indicated. The ninth harmonic follows a power law with an exponent of 9.4 for low intensities, as expected from lowest order perturbation theory, whereas for higher powers it decreases to 7. The eleventh harmonic shows a similar behaviour, with the change in exponent occurring at a higher intensity. The line at 103 nm shows a high exponent of 11.5 for low intensities and then quickly saturates (and even decreases).

LETTERS

METHODS

Apparatus. The complete set-up is sketched in Fig. 1, and consists of a Ti:sapphire femtosecond oscillator (Femtolasers Femtosource 20) that delivers 20 fs pulses with 850 mW average power at 800 nm and a repetition rate of 112 MHz, which results in a pulse energy of 7.7 nJ and a peak power around 400 kW. These pulses are sent to the enhancement resonator, which is a bowtie-type ring cavity. It consists of eight mirrors: a 1% transmission coupling mirror; a 1/4-inch mirror mounted on a piezoelectric transducer for electronic control of the cavity length using the polarization lock technique[30]; four plane chirped mirrors for compensation of the dispersion of air; and the two sapphire Brewster windows inside the resonator. Two spherical mirrors with 50 mm focal length produce a tight focus with a diameter of about 5.3 μm inside the harmonic generation chamber. On the way to the resonator, the beam passes through a prism compressor that compensates the dispersion of the coupling mirror substrates and a telescope that matches the beam diameter and focus position to the resonator mode. In this way, nearly transform limited pulses are obtained inside the resonator. For optimal coupling the enhancement resonator input mirror has 1% transmission, so that an enhancement factor of $P = 100$ is expected. The laser resonator includes a pair of thin wedged fused silica plates for manual control of the carrier envelope frequency. No electronic feedback was necessary to control the CE frequency of the laser, because the system was stable enough to operate for hours by feeding back on the resonator length only. The power circulating in the resonator while put into lock was determined by measuring the power leaking through one of the highly reflecting cavity mirrors with accurately known spectral transmission. The intra-cavity spectrum was measured the same way. Amplitude stability was better than 10% r.m.s. with no frequencies higher than 1 MHz limited by photon lifetime.

Procedure. The enhancement resonator contains a small vacuum chamber with Brewster-angled sapphire windows, housing the rare-gas jet. The peak intensity in these windows is smaller than 10 GW cm^{-2}, so that their nonlinear response is negligible. Xenon gas is injected into the focus of the resonator mode in the HHG chamber, using a glass capillary placed right above the focus with approximately 50 μm inner diameter and 1 bar backing pressure. This diameter is approximately matched to the Rayleigh range of the focus of about 110 μm. With this focus geometry and repetition rate, the atoms see about five pulses before leaving the focus. As the coherently generated XUV radiation is emitted collinearly with the fundamental in a well-collimated beam, a crucial component in the scheme is some sort of beam splitter that separates the two. In order not to compromise the resonator finesse, this beam splitter has to have a very low loss for the fundamental laser radiation. The vacuum windows fulfill this requirement through Brewster orientation with losses smaller than 10^{-3} per window, and accomplish the separation by providing total external reflection for the XUV. High Fresnel reflectivity (inset in Fig. 1) is achieved in this range, as the refractive index of sapphire is lower than one for the relevant wavelengths. The generated XUV beam extracted this way was analysed with a grazing incidence XUV monochromator (McPherson model 248/310G) placed at the HHG chamber exit port. A channeltron photodetector (BURLE CEM4751G), sensitive to wavelengths below 150 nm, was installed at the exit slit of the monochromator, and its signal was analysed with (1) a photon counter (Stanford Research SR400) for high sensitivity measurements, and (2) a voltmeter across a 1 MΩ load resistance for XUV photon flux measurements. To determine the total power in the observed XUV spectrum, the channeltron was placed directly in the beam at the XUV port. A photocurrent of 1 μA was detected at 1.36 kV bias, which corresponds to a photon flux of about 0.85×10^9 photons per second, according to the manufacturer's specifications. From the spectrum we know that the major contributions to that flux come from the spectral range between 85 and 115 nm, so that we can assume an average photon energy of about 12 eV, from which the total power can be calculated.

To synchronise the two lasers in the beat experiment, the third harmonic of the Nd:YVO$_4$ laser repetition rate (76 MHz) was phase-locked to the second harmonic of the Ti:sapphire laser repetition rate (changed to 114 MHz). The delay between the pulses from the two lasers was adjusted using an r.f. phase shifter. The beat signal was recorded using a photomultiplier tube.

1. Udem, T., Holzwarth, R. & Hänsch, T. W. Optical frequency metrology. *Nature* **416**, 233–237 (2002).
2. Cundiff, S. T. & Ye, J. Femtosecond optical frequency combs. *Rev. Mod. Phys.* **75**, 325–342 (2003).
3. Diddams, S. A. et al. An optical clock based on a single trapped ^{199}Hg$^+$ ion. *Science* **293**, 825–828 (2001).
4. Baltuška, A. et al. Attosecond control of electronic processes by intense light fields. *Nature* **421**, 611–615 (2003).
5. Goulielmakis, E. et al. Direct measurement of light waves. *Science* **305**, 1267–1269 (2004).
6. Lindner, F. et al. High-order harmonic generation at a repetition rate of 100 kHz. *Phys. Rev. A* **68**, 013814 (2003).
7. Rafac, R. J. et al. Sub-dekahertz ultraviolet spectroscopy of ^{199}Hg$^+$. *Phys. Rev. Lett.* **85**, 2462–2465 (2000).
8. Strickland, D. & Mourou, G. Compression of amplified chirped optical pulses. *Opt. Commun.* **56**, 219–221 (1985).
9. Seres, J. et al. Laser technology: Source of coherent kiloelectronvolt X-rays. *Nature* **433**, 596 (2005).
10. Schoof, A., Grünert, J., Ritter, S. & Hemmerich, A. Reducing the linewidth of a diode laser below 30 Hz by stabilization to a reference cavity with a finesse above 10^5. *Opt. Lett.* **26**, 1562–1564 (2001).
11. Polzik, E. S. & Kimble, H. J. Frequency doubling with KNbO$_3$ in an external cavity. *Opt. Lett.* **16**, 1400–1402 (1991).
12. Reichert, J., Holzwarth, R., Udem, T. & Hänsch, T. W. Measuring the frequency of light with mode-locked lasers. *Opt. Commun.* **172**, 59–68 (1999).
13. Jones, R. J. & Ye, J. Femtosecond pulse amplification by coherent addition in a passive optical cavity. *Opt. Lett.* **27**, 1848–1850 (2002).
14. Petersen, J. C. & Luiten, A. N. Short pulses in optical resonators. *Opt. Express* **11**, 2975–2981 (2003).
15. Yanovsky, V. P. & Wise, F. W. Frequency doubling of 100-fs pulses with 50% efficiency by use of a resonant enhancement cavity. *Opt. Lett.* **19**, 1952–1954 (1994).
16. Jones, R. J. & Ye, J. High-repetition-rate coherent femtosecond pulse amplification with an external passive optical cavity. *Opt. Lett.* **29**, 2812–2814 (2004).
17. Baklanov, Y. V. & Chebotayev, V. P. Narrow resonances of 2-photon absorption of super-narrow pulses in a gas. *Appl. Phys.* **12**, 97–99 (1977).
18. Snadden, M. J., Bell, A. S., Riis, E. & Ferguson, A. I. Two-photon spectroscopy of laser-cooled Rb using a mode-locked laser. *Opt. Commun.* **125**, 70–76 (1996).
19. Eckstein, J. N., Ferguson, A. I. & Hänsch, T. W. High-resolution spectroscopy with ultrashort light-pulses. *J. Opt. Soc. Am.* **68**, 646 (1978).
20. Marian, A., Stowe, M. C., Lawall, J. R., Felinto, D. & Ye, J. United time-frequency spectroscopy for dynamics and global structure. *Science* **306**, 2063–2068 (2004).
21. Witte, S., Zinkstok, R. T., Ubachs, W., Hogervorst, W. & Eikema, K. S. E. Deep-ultraviolet quantum interference metrology with ultrashort laser pulses. *Science* **307**, 400–403 (2005).
22. Bellini, M. et al. Temporal coherence of ultrashort high-order harmonic pulses. *Phys. Rev. Lett.* **81**, 297–300 (1998).
23. López-Martens, R. et al. Amplitude and phase control of attosecond light pulses. *Phys. Rev. Lett.* **94**, 033001 (2005).
24. Jones, R. J., Moll, K., Thorpe, M., Ye, J. Phase-coherent frequency combs in the vacuum ultraviolet via high-harmonic generation inside a femtosecond enhancement cavity. *Phys. Rev. Lett.* **94**, 193201 (2005).
25. Wahlström, C. G. et al. High-order harmonic-generation in rare-gases with an intense short-pulse laser. *Phys. Rev. A* **48**, 4709–4720 (1993).
26. Constant, E. et al. Optimizing high harmonic generation in absorbing gases: Model and experiment. *Phys. Rev. Lett.* **82**, 1668–1671 (1999).
27. Thorpe, M. J., Jason, J. R., Moll, K., Ye, J. & Lalezari, R. Precise measurements of optical cavity dispersion and mirror coating properties via femtosecond combs. *Opt. Expr.* **13**, 882–888 (2005).
28. Fernandez, A. et al. Chirped-pulse oscillators: a route to high-power femtosecond pulses without external amplification. *Opt. Lett.* **29**, 1366–1368 (2004).
29. Fischer, M. et al. New limits on the drift of fundamental constants from laboratory measurements. *Phys. Rev. Lett.* **92**, 230802 (2004).
30. Hänsch, T. W. & Couillaud, B. Laser frequency stabilization by polarization spectroscopy of a reflecting reference cavity. *Opt. Commun.* **35**, 441–444 (1980).

High Harmonic Frequency Combs for High Resolution Spectroscopy

A. Ozawa,[1,*] J. Rauschenberger,[1,2] Ch. Gohle,[1] M. Herrmann,[1] D. R. Walker,[1] V. Pervak,[2] A. Fernandez,[1] R. Graf,[2]
A. Apolonski,[2] R. Holzwarth,[1] F. Krausz,[1,2] T. W. Hänsch,[1,2] and Th. Udem[1]

[1]*Max-Planck-Institut für Quantenoptik, Hans-Kopfermann-Strasse 1, 85748 Garching, Germany*
[2]*Department für Physik der Ludwig-Maximilians-Universität München, Am Coulombwall 1, 85748 Garching, Germany*
(Received 14 December 2007; published 24 June 2008)

We generated a series of harmonics in a xenon gas jet inside a cavity seeded by pulses from a Ti:sapphire mode-locked laser with a repetition rate of 10.8 MHz. Harmonics up to 19th order at 43 nm were observed with plateau harmonics at the μW power level. An elaborate dispersion compensation scheme and the use of a moderate repetition rate allowed for this significant improvement in output power of the plateau harmonics of 4 orders of magnitude over previous results. With this power level and repetition rate, high-resolution spectroscopy in the extreme ultraviolet region becomes conceivable. An interesting target would be the 1S-2S transition in hydrogenlike He$^+$ at 60 nm.

High-resolution laser spectroscopy has provided us with the most precise measurements in atomic and molecular physics. The 1S-2S transition frequency in atomic hydrogen, for example, has attained an uncertainty of 1.8 parts in 10^{14}, allowing for important tests of bound state quantum electrodynamics (QED) [1]. Thus far only neutral variants of the most fundamental hydrogenlike systems such as positronium, muonium, and atomic hydrogen can be excited with lasers from the ground state. Much shorter wavelengths, where no lasers exist, are required for charged systems such as He$^+$, Li^{++}, etc. For the same reason, laser cooling of neutral systems has not been achieved, so that transit time effects are dominating all measurements. On the other hand, hydrogenlike ions, while being more sensitive to higher-order QED contributions, can be held indefinitely at very low temperatures in the virtually undisturbed environment of an ion trap. In fact, the most precise optical frequency measurements are performed this way [2] with complex ions whose properties cannot be predicted from first principles with sufficient accuracy.

Thus far, highly brilliant focusable radiation in the required extreme ultraviolet (XUV) regime can only be generated with large optical bandwidth by synchrotron radiation, free electron lasers or with pulsed four-wave mixing which is notoriously affected by frequency chirps. The process of high harmonic generation (HHG) (see, e.g., [3]) can provide a way out of this dilemma. Even though HHG requires very high laser intensities that can only be reached with pulsed lasers, a coherent XUV pulse train actually consists of a frequency comb of narrow-band laser modes. The mode separation is given by the pulse repetition rate which can be locked to an atomic clock, enabling precise measurement of optical frequencies [4,5]. At the same time the comb modes of the driving laser can be stabilized to a linewidth of a fraction of a hertz [6], just like the best single-mode lasers. Each mode of the frequency comb can therefore be thought of as a continuous wave laser that may be used for high-resolution spectroscopy [7].

In addition, such a frequency comb can cover a large bandwidth with massively parallel acquisition without sacrificing resolution [8,9].

When a two-photon transition, such as the hydrogenlike 1S-2S transition, is driven with a comb, the modes combine in pairs that add to the same energy. With transform-limited pulses, all transition amplitudes are in phase. The resultant excitation rate is then identical to that of a continuous wave laser of the same average power while maintaining the narrow linewidth [10–12]. In addition, the ac Stark shift is dictated by the average power rather than the high peak power of the pulses [13]. Therefore, direct two-photon frequency comb spectroscopy is essentially equivalent to excitation with a continuous wave laser. The mode number of the XUV comb can be identified using results from hydrogen with the well-known scaling laws or by measuring with at least two different repetition rates [14].

This powerful approach can push high-resolution spectroscopy to shorter wavelengths opening a largely unexplored spectral region [15]. For this to become reality, two main problems had to be solved: The high pulse energies necessary to generate high harmonics could only be provided with low repetition rates, typically in the kHz regime. The resulting frequency comb is far too dense for direct frequency comb spectroscopy which requires the separation of the modes, i.e., the repetition rate, to be larger than the observed transition linewidth. Meanwhile, intracavity HHG achieves the required intensity with the repetition rate of the laser oscillator around 100 MHz [16,17]. This significantly overshoots the design goal. The second obstacle was the very low power generated so far with this method. Now we report a dramatic enhancement of the XUV output power by almost 4 orders of magnitude in the high harmonic plateau, capable of producing useful excitation rates on the 1S-2S transition of He$^+$. We achieve this by an elaborate dispersion compensating scheme and by reducing the repetition rate to 10.8 MHz.

Enhancing nonlinear frequency conversion with continuous wave optical cavities is a well-established tech-

nique. To enhance a pulse train in the same way, several additional conditions must be met: (i) Cavity dispersion that is nonlinear in frequency must be minimized so that the pulse shape is preserved upon a round-trip. Interferometric overlap with the driving pulse train is then ensured by (ii) adjusting the cavity length such that the round-trip time matches the repetition period of the laser and (iii) setting the carrier-envelope offset frequency of the laser appropriately. In the frequency domain, the conditions are that the resonant modes of the cavity must be (i) equidistant, (ii) separated by the pulse repetition rate, and (iii) positioned correctly. While the mode spacing and the position of the comb can be adjusted during the experiment, the irregularities of the cavity mode spacing are compensated with chirped dielectric mirrors [18].

We use a Ti:sapphire mode-locked laser that produces a regular comb of continuous wave modes with frequencies $\omega_n = n\omega_r + \omega_{CE}$. There are two radio frequencies involved: the pulse repetition rate ω_r and the carrier-envelope frequency ω_{CE}. Locking these radio frequencies to a precise reference, such as a Cs atomic clock, establishes a phase coherent connection to the $\approx 2 \times 10^6$ optical frequencies ω_n, due to the large integer $n = 3.4 \times 10^7, \ldots, 3.6 \times 10^7$ [4]. Coupling the frequency comb to the enhancement cavity as sketched in Fig. 1, its nth mode experiences a power amplification of [19]

$$U_n = \frac{T_{IC}}{1 + A - 2\sqrt{A}\cos(\phi(\omega_n))}. \quad (1)$$

Here, the transmittance of the input coupling mirror is denoted by T_{IC}. The round-trip power factor A is defined as the product of the mirror reflectivities, the input coupler reflectivity and the infrared transmission of the XUV output coupler. The cavity is assumed to have a round-trip length L leading to a round-trip phase shift of the nth mode of $k(\omega_n)L = \phi(\omega_n)$, where $k(\omega_n)$ is the frequency-dependent wave number. The nth mode resonates as
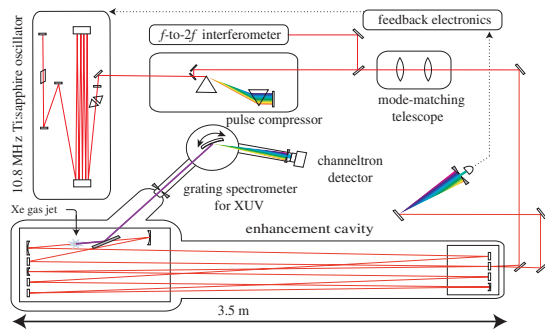

FIG. 1 (color online).   Schematic of the setup as described in the text. The f-to-$2f$ interferometer [4] is used to measure intracavity dispersion [22]. The reflection from the cavity is dispersed by a grating to generate an error signal for locking the comb at a specific wavelength.

$\phi(\omega_n)$ becomes an integer multiple of 2π with a finesse $\mathcal{F} \approx \pi/(1 - \sqrt{A})$. The round-trip phase which we express in terms of a power series expansion about some fixed frequency ω_c

$$\phi(\omega_n) = \phi(\omega_c) + \phi'(\omega_c)(\omega_n - \omega_c) + \Delta\phi(\omega_n) \quad (2)$$

needs to be controlled. Without the higher-order dispersion collected in $\Delta\phi(\omega_n)$, all modes may be readily resonated simultaneously by adjusting ω_r and ω_{CE} so that $\omega_r = 2\pi/\phi'(\omega_c)$ and $\omega_{CE} = \omega_c - \phi(\omega_c)/\phi'(\omega_c)$.

Experimentally these two parameters are controlled by adjusting the laser cavity length and the position of the piezoactuated prismatic wedge in the laser cavity [20]. We find that the drift of ω_{CE} is slow enough that active feedback to the prism position was not necessary for several minutes after optimizing its position manually. The laser cavity length is stabilized by the Pound-Drever-Hall locking method [21]. To generate the necessary modulation sidebands, a small piezoactuated laser mirror is driven at a vibration frequency of 650 kHz avoiding the large dispersion of an electro-optic modulator otherwise used for this purpose. The error signal is processed with a fast proportional and integrating circuit that feeds back on the laser cavity length using two piezoactuators, one with a large bandwidth, the other with a large range. With this approach, a locking bandwidth of more than 100 kHz is achieved.

The phase mismatch $\Delta\phi(\omega_n)$ cannot be controlled by the servo system, so instead we correct it with compensating (chirped) mirrors. The required precision for this dispersion management can be estimated by

$$\Delta\phi(\omega_n) \ll \Delta\phi_{(1/2)} \approx \pi/\mathcal{F}, \quad (3)$$

with $\Delta\phi_{(1/2)}$ being the phase detuning that reduces the power enhancement U_n by one-half. With a constant group delay dispersion (GDD) $\phi''(\omega_c)$ [i.e., $\Delta\phi(\omega_n) = \phi''(\omega_c)(\omega_n - \omega_c)^2/2$], a cavity finesse of $\mathcal{F} = 100\pi$, and a laser bandwidth of 20 THz, $\phi''(\omega_c)$ would have to be smaller than 5 fs^2.

The harmonic radiation is generated at the focus of the cavity in the form of a laserlike beam that propagates collinearly with the infrared laser field. As a consequence, it requires an elaborate outcoupling method. Our solution is to place inside the cavity a sapphire plate, which possesses a refractive index smaller than 1 in the XUV so that total external reflection occurs. By orienting the sapphire plate at Brewster's angle for the fundamental, we introduce minimal cavity loss of about 10^{-3}.

The entire cavity was placed in a vacuum chamber and evacuated to 10^{-2} mbar. This eliminates dispersion and scattering losses from air. The GDD from air amounted to 57 fs^2 in our previous setup [16] and would be 591 fs^2 in our current setup. For the XUV Brewster output coupler, we used a 0.5 mm thick sapphire plate. In our previous setup, the XUV was generated in a tiny vacuum chamber placed at the focus of the cavity with two sapphire win-

dows thick enough to withstand atmospheric pressure. Altogether, we reduced the GDD from 197 fs^2 in our previous 3 m cavity to 34 fs^2 in our 27.8 m cavity. The enhancement cavity consists of 10 mirrors including seven quarter-wave-stack mirrors, four of which are curved, two chirped mirrors, and one input coupler. Asymmetric focusing with two differently curved mirrors (radii of curvature 0.1 and 0.24 m) is used to focus to a waist size of $w_0 = 13$ μm into the gas target. The target is contained within a tube with an inner diameter of 0.4 mm which has been pierced with holes of 200 μm diameter, to allow the laser beam to enter perpendicularly to its axis. At the focus, a peak intensity of $>5 \times 10^{13}$ W/cm^2 is obtained. With a continuous flow of Xe, Ar, or air through the gas nozzle, a fluorescing plasma can be observed. The gas flow is estimated to be 1×10^{-2} mbar l/s.

Two homemade chirped mirrors are used to compensate the dispersion of the Brewster XUV output coupler and the contribution from the other cavity mirrors. First, we designed one chirped mirror by using the estimated total dispersion of the cavity. Then, the residual dispersion is measured by analyzing the spectrally resolved cavity enhancement as described in [22]. Using this information, we generate several different coating designs with the proper dispersion properties. These are optimized by using $\Delta\phi(\omega)$ as a merit function instead of the commonly used GDD. This leaves much more freedom to the actual coating structure, so that more different suitable designs are found. Among these, the one with the smallest sensitivity to coating errors is chosen. To evaluate this sensitivity, we ran a Monte Carlo simulation that adds noise to the layer thickness and recalculates the resulting dispersion properties.

Our mode-locked laser [23] has a 13.9 m long cavity and operates in the positive GDD regime. The cavity is linear and compact due to a Herriott-type multipath delay line. The intracavity GDD of the laser is adjusted by a pair of fused silica prismatic wedges and chirped mirrors. The output of about 1.5 W of average power is compressed by a pair of LaK16 (Schott) prisms. Figure 2 shows the

spectrum of this laser and the spectrum of the enhanced pulses. After optimizing the prism compressor, we obtain pulse durations of 38 and 57 fs for the laser and intracavity pulses, respectively, as measured by an autocorrelator, assuming a Gaussian pulse shape.

The intracavity pulse duration is measured using a small residual reflection from the Brewster XUV output coupler. Figure 2 shows that the spectrally resolved power enhancement covers more than 40 nm. We measure 1 W of laser power in front of the cavity, generating 100 W of circulating power, as determined from residual transmission through one of the highly reflecting cavity mirrors. The total power enhancement is only a factor of 2 smaller than the empty, four mirror cavity in [24]. As shown in Fig. 2, a reduced spectral variation of the enhancement was observed when the input pulses were chirped to about 1 ps. This is explained by nonlinear effects due to the high peak intensity at the Brewster XUV output coupler which has a calculated B integral of 1.8 rad. The peak power is around 160 MW.

The XUV output is analyzed by a scanning grating spectrometer (Jobin-Yvon, LHT30) with an estimated resolution of 1.4 nm and a channeltron detector (Burle, CEM4839). The pulse compressor, gas flow rate, nozzle position, and ω_{CE} are optimized to maximize the XUV signal. In order to independently calibrate the XUV power, the (spectrally unresolved) total power is measured with a calibrated Si photodiode (IRD, AXUV20HS1) placed directly after the Brewster XUV output coupler. A 150 nm thick Al filter (Lebow) is used to remove the residual reflection of the fundamental laser beam. The transmission of the Al filter is measured by comparing the XUV spectra with and without it. Together with the specified wavelength dependence of the grating's diffraction efficiency, we recover the true XUV spectrum. After normalizing to the total power, the absolute spectral power density as shown in Fig. 3 is obtained. High harmonics up to the 19th order (41 nm) are clearly observed, which agrees with the calculated cutoff located between the 13th and 15th harmonic.
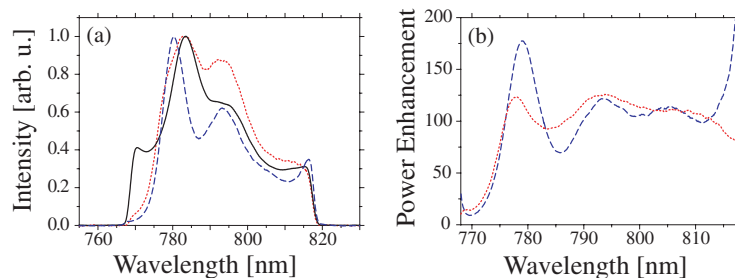
FIG. 2 (color online).   Left: The spectrum of the seed laser (solid black curve) together with the intracavity spectrum of a compressed (dashed blue curve) and highly chirped pulse (dotted red curve). Right: Normalizing the intracavity spectra to the seed spectrum and the laser power measured in front of the cavity yields the spectrally resolved power enhancement U_n for compressed (dashed blue curve) and chirped (dotted red curve) pulses. Because of the intensity dependence of $\Delta\phi(\omega)$, the enhancement varies more strongly for shorter pulses.

FIG. 3. (a) Spectrum of the outcoupled XUV generated in Xe. Higher harmonics (>H15) are measured with an Al filter to suppress stray light. The spectrally integrated powers for the individual harmonics are given in the plot. Compared to previously reported powers, this represents an improvement of 10^4. (b) The single pass conversion efficiency is de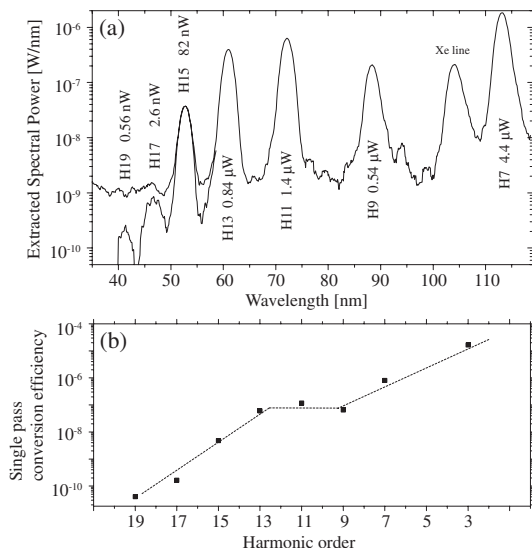rived from the intracavity infrared power for each order of harmonics. The extracted power for H3 is measured with a Si photodiode based power meter.

In addition to the odd harmonics, a broad peak at 104 nm is observed. Its origin is not yet understood but appears to be related to the occupancy of excited bound states of the Xe atom [16].

Two mechanisms are responsible for the drastic improvement over our previous results: larger focal volume and higher peak intensity. The lower repetition rate and the improved cavity lead to a 30-fold increase in pulse energy. The XUV output power scales with large powers of the input power (e.g., $\propto I^9$ for H11 [16]), so even a slightly higher peak intensity leads to significantly higher output power. When saturation is reached, more XUV power is obtained by looser focusing while keeping the peak intensity constant. This lets the interaction volume grow $\propto w_0^4$ and the adverse Gouy phase shift is reduced $\propto w_0^2$. In total, the single pass conversion efficiency for H11 rose from a very low 2×10^{-11} to 10^{-7}. This is a typical value for gas jet HHG without special phase matching measures [3]. We would like to note further that in cavity-assisted HHG the beam quality (due to spatial filtering) is much better than in an amplified system. Therefore, under otherwise identical conditions, we expect higher conversion efficiencies.

With the improvements described here, we obtain μW-level average XUV output power in the plateau region

per harmonic. With this power level, precision spectroscopy in the XUV comes into reach for the first time. As an example, a trapped He ion may be excited to the 2S state by two-photon absorption using the 13th harmonic at 60.8 nm. A third photon can further ionize to He^{2+}, which can be accumulated in the ion trap and detected with unity efficiency. If the entire 0.84 μW generated so far could be focused on the He ion with a waist size of 0.5 μm, an ionization rate close to 1 Hz could be obtained [25,26]. This is a typical rate for high precision spectroscopy experiments on trapped ions. Such tight focusing has indeed been demonstrated [27]. Delivering the XUV beam from the HHG chamber to the trapped ion with high transmission will require special attention. Since there is virtually no background for this type of detection, we believe precision spectroscopy is realistic even with count rates below 1 Hz.

Note added in proof.—Since the submission of this manuscript, a μW power level XUV frequency comb was also generated with an Yb fiber laser based system [28].

*akira.ozawa@mpq.mpg.de

[1] M. Fischer *et al.*, Phys. Rev. Lett. **92**, 230802 (2004).
[2] T. Rosenband *et al.*, Science **319**, 1808 (2008).
[3] J. G. Eden, Prog. Quantum Electron. **28**, 197 (2004).
[4] Th. Udem *et al.*, Nature (London) **416**, 233 (2002).
[5] S. Cundiff *et al.*, Rev. Mod. Phys. **75**, 325 (2003).
[6] A. Bartels *et al.*, Opt. Lett. **29**, 1081 (2004).
[7] V. Gerginov *et al.*, Opt. Lett. **30**, 1734 (2005).
[8] S. A. Diddams *et al.*, Nature (London) **445**, 627 (2007).
[9] Ch. Gohle *et al.*, Phys. Rev. Lett. **99**, 263902 (2007).
[10] Ye. V. Baklanov *et al.*, Appl. Phys. **12**, 97 (1977).
[11] M. J. Snadden *et al.*, Opt. Commun. **125**, 70 (1996).
[12] A. Marian *et al.*, Science **306**, 2063 (2004).
[13] P. Fendel *et al.*, Opt. Lett. **32**, 701 (2007).
[14] R. Holzwarth *et al.*, Appl. Phys. B **73**, 269 (2001).
[15] R. Th. Zinkstok *et al.*, Phys. Rev. A **73**, 061801(R) (2006).
[16] Ch. Gohle *et al.*, Nature (London) **436**, 234 (2005).
[17] R. J. Jones *et al.*, Phys. Rev. Lett. **94**, 193201 (2005).
[18] R. Szipöcs *et al.*, Opt. Lett. **19**, 201 (1994).
[19] J. C. Petersen *et al.*, Opt. Express **11**, 2975 (2003).
[20] A. Apolonski *et al.*, Phys. Rev. Lett. **85**, 740 (2000).
[21] R. W. P. Drever *et al.*, Appl. Phys. B **31**, 97 (1983).
[22] A. Schliesser *et al.*, Opt. Express **14**, 5975 (2006).
[23] A. Fernandez *et al.*, Opt. Lett. **29**, 1366 (2004).
[24] I. Hartl *et al.*, Opt. Lett. **32**, 2870 (2007).
[25] M. Haas *et al.*, Phys. Rev. A **73**, 052501 (2006).
[26] M. Herrmann *et al.* (to be published).
[27] H. Mashiko *et al.*, Opt. Lett. **29**, 1927 (2004).
[28] D. C. Yost *et al.*, Opt. Lett. **33**, 1099 (2008).

A. Mathematica code for absorption spectra of collinearly excited ion strings

Constants

$u = 1.66053886 * 10^\wedge - 27;$
$e = 1.60217653 * 10^\wedge - 19;$
$\epsilon = 8.854187817 * 10^\wedge - 12;$
$\text{kb} = 1.3806505 * 10^\wedge - 23;$
$\hbar = 1.05457266 * 10^\wedge - 34;$
$\text{me} = 9.1093826 * 10^\wedge - 31;$
$\text{mp} = 1.67262171 * 10^\wedge - 27;$

$\text{Mg} = 24 * u;$

Equilibrium Positions of the Ions and Normal frequencies

Enter radial frequency of Helium ion and configuration of ions
Remove[vars, a, pos, dist, eval, evec, u0, nb, conf, i];

ωrad $= 2\pi 1010^\wedge 6;$
conf $= \{\text{Mg}, \text{He}, \text{Mg}\}$
"Radial Frequency"
ωrad$/(2\pi 10^\wedge 6)$"MHz"
nb $=$ Length[conf];
ωax $= \omega$rad$(*\text{Sqrt}[3.2\text{nb}^\wedge - 1.83]; *)$
u0 $=$ Heωax$^\wedge 2;$
"Axial Frequency"
ωax$/(2\pi 10^\wedge 6)$"MHz"
$l = (e^\wedge 2/(4\pi\epsilon\text{u0}))^\wedge(1/3);$
"Length scale"
$l 10^\wedge 6$"μm"

(* Equilibrium Positions *)

vars $=$ Array[a[#]&, nb];
positions $=$
FindRoot[
Table[$a[m] - Sum[1/(a[m] - a[n])^\wedge 2, \{n, 1, m - 1\}]+$
Sum$[1/(a[m] - a[n])^\wedge 2, \{n, m + 1, \text{nb}\}] == 0,$
$\{m, 1, \text{nb}\}]$, Table[$\{a[i], -$Floor[nb/2] $+ (i - 1)\},$
$\{i, 1, \text{nb}\}]];$

```
pos = Table[{Evaluate[a[i]/.positions], conf[[i]]},
{i, 1, nb}];

dist = l * 10^6 * Table[pos[[i + 1, 1]] − pos[[i, 1]],
{i, 1, nb − 1}];
"Length of ion crystal"
lth = Total[dist]"μm"
ListPlot[dist, Frame → True,
PlotRange → {{1, Length[dist]}, {0, Ceiling[Max[dist]]}},
Joined → True, Mesh → All, PlotLabel → "Ion-Ion distance"]

(* Hessian Matrix *)

Do[a[i] = l * a[i]/.positions, {i, 1, nb}]
V = Table[1/(Sqrt[pos[[i, 2]] * pos[[j, 2]]])*
If[i == j,
u0+
2*
Sum[Piecewise[
{{e^2/(4πεAbs[a[i] − a[k]]^3), k ≠ i},
{0, k == i}}], {k, 1, nb}],
−2e^2/(4πεAbs[a[i] − a[j]]^3)], {i, 1, nb},
{j, 1, nb}];

(* Eigenfrequencies and Eigenvectors *)

eval = Sqrt[Eigenvalues[V]];
evec = Eigenvectors[V];

(*Visualisation*)

helium = Tuples[{Cases[pos, {_, He}][[All, 1]], {0}}];
magnesium = Tuples[{Cases[pos, {_, Mg}][[All, 1]], {0}}];
GraphicsColumn[
Table[
Framed[
Graphics[
{Table[Arrow[{{pos[[i, 1]], 0},
{pos[[i, 1]] + evec[[j, i]], 0}}], {i, 1, nb}],
{{Purple, PointSize[Medium], Point[helium]},
{Blue, PointSize[Large], Point[magnesium]}}},
PlotLabel → eval[[j]]/(2π10^6)"MHz"],
FrameMargins → Medium], {j, 1, nb}], ImageSize → 500,
Spacings → 0]
{3.985293264*^-26, 6.64215544*^-27, 3.985293264*^-26}
Radial Frequency
10MHz
```

20000000π
Axial Frequency
10MHz
Length scale
2.06442μm
Length of ion crystal
4.44766μm

Calculate Spectrum

Definitions

$\eta = \text{Compile}[\{\lambda, m, \nu, \beta\}, (2\pi/\lambda) * \beta * \text{Sqrt}[\hbar/(2m\nu)]];$
$\text{Mtx} = \text{Compile}[\{\eta, \text{n1}, \text{n2}\},$
$\text{Piecewise}[$
$\{\{\text{Abs}[\text{Exp}[-(\eta\verb|^|2)/2] * \eta\verb|^|\text{Abs}[\text{n2} - \text{n1}]*$
$\text{Sqrt}[\text{Min}[\text{n1}, \text{n2}]!/(\text{Max}[\text{n1}, \text{n2}]!)]$
$\text{LaguerreL}[\text{Min}[\text{n1}, \text{n2}], \text{Abs}[\text{n2} - \text{n1}], \eta\verb|^|2]]\verb|^|2,$
$\text{n1} \geq 0 \&\& \text{n2} \geq 0\}\}, 0]];$
$\text{nav} = \text{Compile}[\{T, \nu\}, 1/(\text{Exp}[\hbar\nu/(\text{kb}T)] - 1)];$
$\text{Pe} = \text{Compile}[\{n, \omega, T\},$
$(1 - \text{Exp}[-\hbar\omega/(\text{kb}T)]) * \text{Exp}[-n\hbar\omega/(\text{kb}T)]];$
$\text{ListPlot}[\text{Table}[\{n, \text{Pe}[n, 2\pi10\verb|^|7, 10\verb|^| - 3]\}, \{n, 0, 10\}],$
$\text{PlotRange} \to \text{All}, \text{Joined} \to \text{True}, \text{InterpolationOrder->0},$
$\text{Filling} \to \text{Axis}, \text{Frame} \to \text{True},$
$\text{GridLines} \to \{\{\text{nav}[10\verb|^| - 3, 2\pi10\verb|^|7]\}, \text{None}\}]$

$\text{Plot}[\text{Integrate}[\text{Pe}[n, 2\pi10\verb|^|7, 10\verb|^| - 3], \{n, 0, m\}],$
$\{m, 1, 50\text{nav}[10\verb|^| - 3, \text{eval}[[\text{nb}]]]\}, \text{Frame} \to \text{True},$
$\text{PlotRange} \to \text{All}]$

Choose Ion

$\text{ion} = \text{He};$
$T = 1 * 10\verb|^| - 3;$
$\lambda = 30.4 * 10\verb|^| - 9;$
$\text{rec} = \pi\hbar/(\lambda\verb|^|24u10\verb|^|6)$
53.9722
$\text{ion} = \text{Mg};$
$T = 1 * 10\verb|^| - 6;$
$\lambda = 280 * 10\verb|^| - 9;$
$\text{rec} = \pi\hbar/(\lambda\verb|^|24u10\verb|^|6)$
0.636211

Limits of Calculation

```
lower = −25;
upper = 25;
el = −2π100 ∗ 10^6;
eu = 2π200 ∗ 10^6;
int = 10;
```

```
"Total Sidebands"
perm =
Tuples[
Table[Range[Ceiling[eval[[nb]]/eval[[i]]] ∗ lower,
Ceiling[eval[[nb]]/eval[[i]] ∗ upper]], {i, 1, nb}]];
lm = Length[perm]
energ =
Monitor[
Table[{perm[[j]], Sum[perm[[j, i]]eval[[i]],
{i, 1, nb}]}, {j, 1, lm}],
ProgressIndicator[j, {1, lm}]];
energies = Select[energ, #[[2]]>=el&&#[[2]]<=eu&];
Remove[energ]
en = energies[[All, 1, All]];
energies = energies[[All, 2]];
"Selected Sidebands"
lm = Length[en]
"Iterations"
it = nb ∗ lm ∗ Product[Floor[intnav[T, eval[[i]]]] + 1,
{i, 1, nb}] ∗ Count[conf, He]
"Time [s]"
N[72.2 ∗ 10^ − 6 ∗ it, 1]"s"
N[72.2 ∗ 10^ − 6 ∗ it/60, 1]"min"
Total Sidebands
70176
Selected Sidebands
20433
Iterations
367794000
Time [s]
26554.7s
442.579min
7.37631h
```

Spectrum

```
Remove[iter, n]
iter =
Evaluate[
```

```
Sequence@@
Table[{n[i], 0, Floor[intnav[T, eval[[i]]]], 1},
{i, 1, nb}]];
t1 = TimeUsed[];
spectrum = Monitor[Table[{energies[[s]]/(2π10^6),
Sum[Piecewise[
{{Sum[Product[
Mtx[η[λ, ion, eval[[α]], evec[[α, j]]],
n[α] + en[[s, α]], n[α]]*
Pe[n[α], eval[[α]], T], {α, 1, nb}],
Evaluate[iter]], conf[[j]] == ion}}, 0],
{j, 1, nb}]}, {s, 1, lm}],
ProgressIndicator[s, {1, lm}]];
t2 = TimeUsed[];
"Time"
t2 − t1
"Strongest Sideband"
stln = Max[spectrum[[All, 2]]]
spectrum2 = Select[spectrum, #[[2]] > stln/100&];
"Number of Sidebands (1%)"
Length[spectrum2]
"Check total amplitudes [%]"
100 * Total[spectrum, {1}][[2]]/Count[conf, He]
"Check deviation recoil frequency [%]"
rec = πℏ/(λ^2Count[conf, He] * He10^6);
100*
(Sum[spectrum[[i, 1]] * spectrum[[i, 2]], {i, 1, lm}]−
rec)/rec
spectrum2 = DeleteCases[Chop[spectrum, 10^ − 4], {_, 0}];
resultplot = ListPlot[spectrum2, Frame → True,
PlotMarkers → {""}, Filling → Axis, FillingStyle → Black,
PlotStyle → Black, PlotRange → {{−100, 200}, {0, 0.1}},
GridLines → {{53.972}, None}, Axes → False,
LabelStyle → Medium,
FrameLabel → {"Detuning [MHz]", "rel. Matrix Element"},
Epilog → Text[Style["Mg-He-Mg", Medium], {190, 0.09},
{1, 0}]]
```

Bibliography

[1] W. Neuhauser, M. Hohenstatt, P. Toschek, and H. Dehmelt, "Optical-Sideband Cooling of Visible Atom Cloud Confined in Parabolic Well," *Phys. Rev. Lett.*, vol. 41, no. 4, pp. 233–236, 1978.

[2] D. J. Wineland, R. E. Drullinger, and F. L. Walls, "Radiation-Pressure Cooling of Bound Resonant Absorbers," *Phys. Rev. Lett.*, vol. 40, no. 25, pp. 1639–1642, 1978.

[3] T. Rosenband, D. B. Hume, P. O. Schmidt, C. W. Chou, A. Brusch, L. Lorini, W. H. Oskay, R. E. Drullinger, T. M. Fortier, J. E. Stalnaker, S. A. Diddams, W. C. Swann, N. R. Newbury, W. M. Itano, D. J. Wineland, and J. C. Bergquist, "Frequency Ratio of Al+ and Hg+ Single-Ion Optical Clocks; Metrology at the 17th Decimal Place," *Science*, vol. 319, no. 5871, pp. 1808–1812, 2008.

[4] D. Leibfried, B. DeMarco, V. Meyer, D. Lucas, M. Barrett, J. Britton, W. M. Itano, B. Jelenkovic, C. Langer, T. Rosenband, and D. J. Wineland, "Experimental demonstration of a robust, high-fidelity geometric two ion-qubit phase gate," *Nature*, vol. 422, no. 6930, pp. 412–415, 2003.

[5] F. Schmidt-Kaler, H. Häffner, M. Riebe, S. Gulde, G. P. T. Lancaster, T. Deuschle, C. Becher, C. F. Roos, J. Eschner, and R. Blatt, "Realization of the Cirac-Zoller controlled-NOT quantum gate," *Nature*, vol. 422, p. 408, 2003.

[6] A. Friedenauer, H. Schmitz, J. T. Glueckert, D. Porras, and T. Schaetz, "Simulating a quantum magnet with trapped ions," *Nature Physics*, vol. 4, no. 10, pp. 757–761, 2008.

[7] R. Feynman, "Simulating physics with computers," *Int. J. Th. Phys.*, vol. 21, no. 6, pp. 467–488, 1982.

[8] D. Hanneke, S. Fogwell, and G. Gabrielse, "New Measurement of the Electron Magnetic Moment and the Fine Structure Constant," *Phys. Rev. Lett.*, vol. 100, no. 12, p. 120801, 2008.

[9] D. Leibfried, R. Blatt, C. Monroe, and D. Wineland, "Quantum dynamics of single trapped ions," *Rev. Mod. Phys.*, vol. 75, no. 1, pp. 281–324, 2003.

[10] D. J. Berkeland, J. D. Miller, J. C. Bergquist, W. M. Itano, and D. J. Wineland, "Minimization of ion micromotion in a Paul trap," *J. Appl. Phys.*, vol. 83, no. 10, pp. 5025–5033, 1998.

[11] T. Hänsch and A. Schawlow, "Cooling of gases by laser radiation," *Opt. Comm.*, vol. 13, no. 1, pp. 68–69, 1975.

[12] D. J. Wineland and H. G. Dehmelt, "Proposed 10^{-14} $\delta\nu/\nu$ laser fluorescence spectrsocopy on Ti$^+$ mono-ion oscillator III," *Bull. Am. Phys. Soc.*, vol. 20, no. 4, p. 637, 1975.

[13] S. Stenholm, "The semiclassical theory of laser cooling," *Rev. Mod. Phys.*, vol. 58, no. 3, pp. 699–739, 1986.

[14] D. J. Wineland and W. M. Itano, "Laser cooling of atoms," *Phys. Rev. A*, vol. 20, no. 4, pp. 1521–1540, 1979.

[15] D. H. E. Dubin and T. M. O'Neil, "Trapped nonneutral plasmas, liquids, and crystals (the thermal equilibrium states)," *Rev. Mod. Phys.*, vol. 71, no. 1, p. 87, 1999.

[16] F. Diedrich, E. Peik, J. M. Chen, W. Quint, and H. Walther, "Observation of a Phase Transition of Stored Laser-Cooled Ions," *Phys. Rev. Lett.*, vol. 59, no. 26, pp. 2931–2934, 1987.

[17] T. J. Harmon, N. Moazzan-Ahmadi, and R. I. Thompson, "Instability heating of sympathetically cooled ions in a linear Paul trap," *Phys. Rev. A*, vol. 67, no. 1, p. 013415, 2003.

[18] T. Baba and I. Waki, "Sympathetic cooling rate of gas-phase ions in a radio-frequency-quadrupole ion trap.," *Appl. Phys. B*, vol. 74, no. 4/5, pp. p375 –, 2002.

[19] S. Schiller and C. Lammerzahl, "Molecular dynamics simulation of sympathetic crystallization of molecular ions," *Phys. Rev. A*, vol. 68, no. 5, p. 053406, 2003.

[20] P. Blythe, B. Roth, U. Frohlich, H. Wenz, and S. Schiller, "Production of ultracold trapped molecular hydrogen ions," *Phys. Rev. Lett.*, vol. 95, no. 18, p. 183002, 2005.

[21] V. L. Ryjkov, X. Zhao, and H. A. Schuessler, "Sympathetic cooling of fullerene ions by laser-cooled Mg[sup +] ions in a linear rf trap," *Phys. Rev. A*, vol. 74, no. 2, p. 023401, 2006.

[22] L. Deslauriers, S. Olmschenk, D. Stick, W. K. Hensinger, J. Sterk, and C. Monroe, "Scaling and Suppression of Anomalous Heating in Ion Traps," *Phys. Rev. Lett.*, vol. 97, no. 10, p. 103007, 2006.

[23] D. Stick, W. K. Hensinger, S. Olmschenk, M. J. Madsen, K. Schwab, and C. Monroe, "Ion trap in a semiconductor chip," *Nature Physics*, vol. 2, no. 1, pp. 36–39, 2006.

[24] S. Seidelin, J. Chiaverini, R. Reichle, J. J. Bollinger, D. Leibfried, J. Britton, J. H. Wesenberg, R. B. Blakestad, R. J. Epstein, D. B. Hume, W. M. Itano, J. D. Jost, C. Langer, R. Ozeri, N. Shiga, and D. J. Wineland, "Microfabricated Surface-Electrode Ion Trap for Scalable Quantum Information Processing," *Phys. Rev. Lett.*, vol. 96, no. 25, p. 253003, 2006.

[25] D. Leibfried, D. Wineland, R. Blakestad, J. Bollinger, J. Britton, J. Chiaverini, R. Epstein, W. Itano, J. Jost, E. Knill, C. Langer, R. Ozeri, R. Reichle, S. Seidelin, N. Shiga, and J. Wesenberg, "Towards scaling up trapped ion quantum information processing," *Hyperfine Interactions*, vol. 174, no. 1, pp. 1–7, 2007.

[26] Q. A. Turchette, Kielpinski, B. E. King, D. Leibfried, D. M. Meekhof, C. J. Myatt, M. A. Rowe, C. A. Sackett, C. S. Wood, W. M. Itano, C. Monroe, and D. J. Wineland, "Heating of trapped ions from the quantum ground state," *Phys. Rev. A*, vol. 61, no. 6, p. 063418, 2000.

[27] J. Labaziewicz, Y. Ge, P. Antohi, D. Leibrandt, K. R. Brown, and I. L. Chuang, "Suppression of Heating Rates in Cryogenic Surface-Electrode Ion Traps," *Phys. Rev. Lett.*, vol. 100, no. 1, p. 013001, 2008.

[28] V. Letchumanan, G. Wilpers, M. Brownnutt, P. Gill, and A. G. Sinclair, "Zero-point cooling and heating-rate measurements of a single [sup 88]Sr[sup +] ion," *Phys. Rev. A*, vol. 75, no. 6, p. 063425, 2007.

[29] F. Diedrich, J. C. Bergquist, W. M. Itano, and D. J. Wineland, "Laser Cooling to the Zero-Point Energy of Motion," *Phys. Rev. Lett.*, vol. 62, no. 4, pp. 403–406, 1989.

[30] L. Deslauriers, P. C. Haljan, P. J. Lee, K.-A. Brickman, B. B. Blinov, M. J. Madsen, and C. Monroe, "Zero-point cooling and low heating of trapped $^{111}Cd^+$ ions," *Phys. Rev. A*, vol. 70, no. 4, p. 043408, 2004.

[31] D. Cubric, B. Lencova, F. H. Read, and J. Zlamal, "Comparison of FDM, FEM and BEM for electrostatic charged particle optics," *Nucl. Inst. Meth. Phys. A*, vol. 427, no. 1-2, pp. 357–362, 1999.

[32] H. Dehmelt *Adv. At. Mol. Phys.*, vol. 3, p. 53, 1967.

[33] D. R. Denison, "Operating Parameters of a Quadrupole in a Grounded Cylindrical Housing," *J. Vac. Sci. Tech.*, vol. 8, no. 1, pp. 266–269, 1971.

[34] W. Lorenz, "Dimensionierung einlagiger Zylinderluftspulen mit optimaler Güte," *Frequenz*, vol. 24, p. 20, 1970.

[35] F. Markert, "Ein UV Festkörperlasersystem zur Kühlung von Mg$^+$ Ionen," Master's thesis, Ludwig-Maximilians-Universität München, 2005.

[36] A. Friedenauer, F. Markert, H. Schmitz, L. Petersen, S. Kahra, M. Herrmann, T. Udem, T. W. Hänsch, and T. Schätz, "High power all solid state laser system near 280 nm," *Appl. Phys. B*, vol. 84, no. 3, pp. 371–373, 2006.

[37] T. W. Hänsch and B. Couillaud, "Laser frequency stabilization by polarization spectroscopy of a reflecting reference cavity," *Opt. Comm.*, vol. 35, no. 3, pp. 441–444, 1980.

[38] J. C. Bergquist, W. M. Itano, and D. J. Wineland, "Recoilless optical absorption and Doppler sidebands of a single trapped ion," *Phys. Rev. A*, vol. 36, no. 1, pp. 428–430, 1987.

[39] M. Zakova, C. Geppert, A. Herlert, H.-J. Kluge, R. Sanchez, F. Schmidt-Kaler, D. Tiedemann, C. Zimmermann, and W. Nörtershäuser, "Towards a nuclear charge radius determination for beryllium isotopes," *Hyperfine Interactions*, vol. 171, no. 1, pp. 189–195, 2006.

[40] L. Lorini, N. Ashby, A. Brusch, S. Diddams, R. Drullinger, E. Eason, T. Fortier, P. Hastings, T. Heavner, D. Hume, W. Itano, S. Jefferts, N. Newbury, T. Parker, T. Rosenband, J. Stalnaker, W. Swann, D. Wineland, and J. Bergquist, "Recent atomic clock comparisons at NIST," *Eur. Phys. J.*, vol. 163, no. 1, pp. 19–35, 2008.

[41] J. K. Webb, M. T. Murphy, V. V. Flambaum, V. A. Dzuba, J. D. Barrow, C. W. Churchill, J. X. Prochaska, and A. M. Wolfe, "Further Evidence for Cosmological Evolution of the Fine Structure Constant," *Phys. Rev. Lett.*, vol. 87, no. 9, p. 091301, 2001.

[42] M. T. Murphy, J. K. Webb, and V. V. Flambaum, "Further evidence for a variable fine-structure constant from Keck/HIRES QSO absorption spectra," *Mon. Not. R. Astron. Soc.*, vol. 345, no. 2, p. 609, 2003.

[43] V. A. Dzuba, V. V. Flambaum, and J. K. Webb, "Space-Time Variation of Physical Constants and Relativistic Corrections in Atoms," *Phys. Rev. Lett.*, vol. 82, no. 5, pp. 888–891, 1999.

[44] J. C. Berengut, V. A. Dzuba, and V. V. Flambaum, "Isotope-shift calculations for atoms with one valence electron," *Phys. Rev. A*, vol. 68, no. 2, p. 022502, 2003.

[45] T. Steinmetz, T. Wilken, C. Araujo-Hauck, R. Holzwarth, T. W. Hänsch, L. Pasquini, A. Manescau, S. D'Odorico, M. T. Murphy, T. Kentischer, W. Schmidt, and T. Udem, "Laser Frequency Combs for Astronomical Observations," *Science*, vol. 321, no. 5894, pp. 1335–1337, 2008.

[46] T. Ashenfelter, G. J. Mathews, and K. A. Olive, "Chemical Evolution of Mg Isotopes versus the Time Variation of the Fine Structure Constant," *Phys. Rev. Lett.*, vol. 92, no. 4, p. 041102, 2004.

[47] T. Nakamura, M. Wada, K. Okada, A. Takamine, Y. Ishida, Y. Yamazaki, T. Kambara, Y. Kanai, T. M. Kojima, Y. Nakai, N. Oshima, A. Yoshida, T. Kubo, S. Ohtani, K. Noda, I. Katayama, V. Lioubimov, H. Wollnik, V. Varentsov, and H. A. Schuessler, "Laser spectroscopy of ^{7,10}Be$^+$ in an online ion trap," *Phys. Rev. A*, vol. 74, no. 5, p. 052503, 2006.

[48] R. Drullinger, D. Wineland, and J. Bergquist, "High-Resolution Optical Spectra of Laser Cooled Ions," *Appl. Phys.*, vol. 22, no. 4, p. 365, 1980.

[49] A. L. Wolf, S. A. van den Berg, C. Gohle, E. J. Salumbides, W. Ubachs, and K. S. E. Eikema, "Frequency metrology on the 4s ^{2}S$_{1/2}$–4p^{2}P$_{1/2}$ transition in ^{40}Ca$^+$ for a comparison with quasar data," *Phys. Rev. A*, vol. 78, no. 3, p. 032511, 2008.

[50] T. Udem, R. Holzwarth, and T. W. Hänsch, "Optical frequency metrology," *Nature*, vol. 416, no. 6877, pp. 233–237, 2002.

[51] B. Bernhardt, "Aufbau und Charakterisierung eines stabilen optischen Frequenzverteilungssystems," Master's thesis, Ludwig-Maximilians-Universität München, 2006.

[52] W. Ansbacher, Y. Li, and E. H. Pinnington, "Precision lifetime measurement for the 3p levels of Mg II using frequency-doubled laser radiation to excite a fast ion beam," *Phys. Lett. A*, vol. 139, no. 3-4, pp. 165–169, 1989.

[53] H. J. Metcalf and P. van der Straten, *Laser Cooling and Trapping*. Springer, Berlin, 2001.

[54] I. I. Sobelman, *Atomic Spectra and Radiative Transitions*. Springer, Berlin, 1996.

[55] D. E. Kelleher and L. I. Podobedova, "Atomic Transition Probabilities of Sodium and Magnesium. A Critical Compilation," *J. Phys. Chem. Ref. Data*, vol. 37, no. 1, pp. 267–706, 2008.

[56] M. Aldenius, S. Johansson, and M. T. Murphy, "Accurate laboratory ultraviolet wavelengths for quasar absorption-line constraints on varying fundamental constants," *Mon. Not. R. Astron. Soc.*, vol. 370, no. 1, pp. 444–452, 2006.

[57] J. C. Pickering, A. P. Thorne, and J. K. Webb, "Precise laboratory wavelengths of the Mg I and Mg II resonance transitions at 2853, 2803 and 2796 Å," *Mon. Not. R. Astron. Soc.*, vol. 300, p. 131, 1998.

[58] V. DeGiorgio and M. O. Scully, "Analogy between the Laser Threshold Region and a Second-Order Phase Transition," *Phys. Rev. A*, vol. 2, no. 4, pp. 1170–1177, 1970.

Coauthored Publications

1. A phonon laser
K. Vahala, M. Herrmann, S. Knünz, V. Batteiger, G. Saathoff, T. W. Hänsch& Th. Udem
In preparation (2008)

2. Feasibility of coherent xuv spectroscopy on the 1S-2S transition in singly ionized helium
M. Herrmann, M. Haas, U. D. Jentschura, F. Kottmann, D. Leibfried, G. Saathoff, C. Gohle, A. Ozawa, V. Batteiger, S. Knünz, N. Kolachevsky, H. A. Schüssler, T. W. Hänsch& Th. Udem
Phys. Rev. A **79**, 052505 (2009)

3. Frequency metrology on single trapped ions in the weak binding limit: The $3s_{1/2} - 3p_{3/2}$ transition in ^{24}Mg$^+$
M. Herrmann, V. Batteiger, S. Knünz, G. Saathoff, T. W. Hänsch& Th. Udem
Phys. Rev. Lett. **102**, 013006 (2009)

4. High harmonic frequency combs for high resolution spectroscopy
A. Ozawa, J. Rauschenberger, C. Gohle, M. Herrmann, D. R. Walker, V. Pervak, A. Fernandez, R. Graf, A. Apolonski, R. Holzwarth, F. Krausz, T. W. Hänsch& Th. Udem
Phys. Rev. Lett. **100**, 253901 (2008)

5. Photoionization broadening of the 1S-2S transition in a beam of atomic hydrogen
N. Kolachevsky, M. Haas, U. D. Jentschura, M. Herrmann, P. Fendel, M. Fischer, R. Holzwarth, Th. Udem, C. H. Keitel& T.W. Hänsch
Phys. Rev. A **74**, 052504 (2006)

6. Two-photon excitation dynamics in bound two-body Coulomb systems including ac Stark shift and ionization
M. Haas, U.D. Jentschura, C.H. Keitel, N. Kolachevsky, M. Herrmann, P. Fendel, M. Fischer, Th. Udem, R. Holzwarth, T. W. Hänsch, M. O. Scully& G. S. Agarwal
Phys. Rev. A **73**, 052501 (2006)

7. High power all solid state laser system near 280 nm
A. Friedenauer, F. Markert, H. Schmitz, L. Petersen, S. Kahra, M. Herrmann, Th. Udem, T.W. Hänsch& T. Schätz
Appl. Phys. B **84**, 371-373 (2006)

8. A frequency comb in the extreme ultraviolet

C. Gohle, Th. Udem, M. Herrmann, J. Rauschenberger, R. Holzwarth, H.A. Schüssler, F. Krausz& T.W. Hänsch

Nature **436**, 234-237 (2005)

9. Precision spectroscopy of hydrogen and femtosecond laser frequency combs

T. W. Hänsch, J. Alnis, P. Fendel, M. Fischer, C. Gohle, M. Herrmann, R. Holzwarth, N. Kolachevsky, Th. Udem& M. Zimmermann

Phil. Trans. Royal Soc. A **363**, 2155-2163 (2005)

10. First laser-controlled antihydrogen production

C. H. Storry, A. Speck, D. Le Sage, N. Guise, G. Gabrielse, D. Grzonka, W. Oelert, G. Schepers, T. Sefzick, H. Pittner, M. Herrmann, J. Walz, T. W. Hänsch, D. Comeau& E.A. Hessels

Phys. Rev. Lett. **93**, 263401 (2004)

11. Cold antihydrogen atoms

J. Walz, H. Pittner, M. Herrmann, P. Fendel, B. Henrich& T. W. Hänsch

Appl. Phys. B **77**, 713-717 (2003)

12. Towards laser spectroscopy of antihydrogen

J. Walz, P. Fendel, M. Herrmann, M. König, A. Pahl, H. Pittner, B. Schatz& T. W. Hänsch

J. Phys. B **36**, 649-654 (2003)

Thank You

Looking back, a thesis is a long and challenging endeavour which is not conceivable without the support of many individuals for which I am deeply grateful.

First and foremost I wish to thank **Prof. Hänsch** for welcoming me in his group. The working conditions at MPQ couldn't have been any better - well equipped and a great, inspiring atmosphere to work in. Thank You for Your contagious passion for physics, the great freedom granted and the trust the freedom arose from.

When I was desperately seeking a referee **Prof. Habs** spontaneously grabbed my thesis and read and corrected it in no-time despite his tight schedule - thus enabling my defense before Christmas. What should I say - thank You very much!

Thomas! Although our interactions were sometimes accompanied by some friction I am always fully aware of how much You taught me. Your healthy disrespect for apparently well-known facts often led to valuable new insights - that was an important lesson and certainly made me a better physicist. Also, thanks a lot for many great tours in the mountains! I hope the "great spooner" wasn't our last one and stay clear of avalanches!

Hans Schuessler, Didi Leibfried and **Tobias Schätz** - with no experienced ion trapper in our group my efforts would have been futile without Your support! Thanks for getting me started and answering all my stupid questions along the road. Special thanks to Tobias and his great team (especially Axel and Hector) for a countless number of equipment loans that kept us going. Hans, thank You so much for the great time we had in Texas and I will never forget our trips to the Wiesn! Didi, thanks for being a tough and knowledgable discussion partner, I certainly learned a lot.

Tino and **Sebastian** - As Prof. Hänsch once put it, physics is a team sport, and without Your support much of my thesis wouldn't have been possible. Sebastian, how many times did we bake the 6 rod trap? I can't remember. But I will always remember Your awful music! Thanks for all the software that orchestrated our experiments. Tino, by resurrecting the dye laser and making it fit for the Mg measurement You did nothing less but rescue my thesis. Thank You. And keep flying the pirate flag!

Guido! Despite my share of bad luck I occasionally was very lucky - especially that You joined our group. Your constant support in every field was pivotal for the success of this thesis and Your ataraxia helped me stay sane in the darkest moments. Thank You for so much: for countless long measurement nights, for continuous patient proof-reading (especially of my thesis), for introducing our pub quiz Thursday (!) and for excellent east frisian tea!

Many others made this thesis a great experience inside and outside the lab and I hope I won't miss anybody: I was lucky to share my office with **Christoph** (yes, THE Chris G.!) from whom I learned a lot from, especially that it is great fun to celebrate a birthday in December (!) with an open-air BBQ! **Marcus** and I share a passion for mountainbiking and rode two amazing transalps (Gamp!). Come back to munich, damnit! **Peter** is an exceptional guy - I am happy to have met You and keep up the good work in Boston! **Nikolai**, it was a great pleasure to work with You - I'm looking forward to our next trip to the Dammkar! The muonic guys, **Tobi, Aldo** and **Randolf** made it much more bearable *not* to see a line...just

kidding... I know 2009 will be the year and all the hard work will pay off! **Akira**, a 24/7 worker and a shining example of cultural integration: A japanese savouring Leberkas and Weißwurst and a robust beergarden visitor ("One Maß is enough!"). Thanks for introducing me to japanese cuisine, I never thought I would enjoy raw fish. **Gitti** and **Katha** made the institute a much more fun place to be. Your Christmas movies made the other attempts look pathetic - keep it up! And last, but not least, **Andreas** (aka Freddy Krueger, aka the pale Kenyan...), who runs faster than his shadow and who helped establish our office as the MPQ party headquarters. Und Marzipan!

While I'm at it: I was lucky to receive the most awesome Doktorhut of all times (sorry, all-others, but face it). Thanks to everybody who participated!

The MPQ is famous for its excellent infrastructure and support, and indeed my thesis wouldn't have been possible without the team in the background.

Being an electronics bungler I would have had a really hard time without **Helmut**'s support. Thank You very much and I will always remember the fun we had with the video camera attached to Your RC helicopter!

Much of the apparatus that fills our labs has been hand-built by **Charly** and **Wolfgang** and the importance of their support can hardly be over-estimated. Thank You for everything, especially the design of the endcap trap together with Wolfgang was great fun and I learned a lot.

Without our administrative assistants **Gabi Gschwendtner** and **Ingrid Hermann** in the background nothing would work as it should - thank You for Your support.

I am deeply saddened that I can't thank **Rosi Lechner** for all her support personally anymore. I wish we could have toasted after my defense with a glass of Prosecco!

Finally, I would like to thank my beloved **parents** and **family** for teaching me everything that is really important. And without You, **Melanie**, a lot would be much less meaningful.

Thank You!